https://doi.org/10.15388/vu.thesis.185
https://orcid.org/0000-0001-8505-5067

VILNIUS UNIVERSITY
STATE RESEARCH INSTITUTE
CENTER FOR PHYSICAL SCIENCES AND TECHNOLOGY

Lina
GRINEVIČIŪTĖ

Nanostructured optical coatings for the manipulation of laser radiation

DOCTORAL DISSERTATION

Technological sciences,
Material engineering (T 008)

VILNIUS 2021

This dissertation was prepared between 2016 and 2020 at Optical coatings laboratory of the Center for physical sciences and technology.

Academic supervisor:
dr. Ramutis Drazdys (Center for Physical Sciences and Technology, Technological Sciences, Material Engineering – T 008).

This doctoral dissertation will be defended in a public meeting of the Dissertation Defense Panel:
Chairman – Prof. Habil. Dr. Valdas Sirutkaitis (Vilnius University, Technological Sciences, Material Engineering – T 008).
Members:
Assoc. Prof. Renata Butkutė (Center for Physical Sciences and Technology, Technological Sciences, Material Engineering – T 008);
Prof. Dr. Saulius Juodkazis (Swinburne University of Technology, Technological Sciences, Material Engineering – T 008);
Prof. Dr. Giedrius Laukaitis (Kaunas University of Technology, Natural Sciences, Physics – N 002);
Dr. Andrejus Michailovas (Center for Physical Sciences and Technology, Technological Sciences, Material Engineering – T008).

The dissertation shall be defended at a public meeting of the Dissertation Defense Panel at 10:00 on 9th of July 2021 in the hall of FTMC Institute of Physics.
Address: Savanoriu Ave. 231, LT-02300 Vilnius, Lithuania
Tel. +370 5 264 8884; e-mail: office@ftmc.lt

The text of this dissertation can be accessed at the libraries of Vilnius university and Center for Physical Science and Technology, as well as on the website of Vilnius University: www.vu.lt/lt/naujienos/ivykiu-kalendorius

https://doi.org/10.15388/vu.thesis.185
https://orcid.org/0000-0001-8505-5067

VILNIAUS UNIVERSITETAS
VALSTYBINIS MOKSLINIŲ TYRIMŲ INSTITUTAS
FIZINIŲ IR TECHNOLOGIJOS MOKSLŲ CENTRAS

Lina
GRINEVIČIŪTĖ

Nanostruktūrizuotos optinės dangos, skirtos lazerio šviesos valdymui

DAKTARO DISERTACIJA

Technologijos mokslai,
Medžiagų inžinerija (T 008)

VILNIUS 2021

Disertacija rengta 2016 – 2020 metais Optinių dangų laboratorijoje, Valstybiniame mokslinių tyrimų institute Fizinių ir technologijos mokslų centre.

Mokslinis vadovas:
dr. Ramutis Drazdys (Valstybinis mokslinių tyrimų institutas Fizinių ir technologijos mokslų centras, technologijos mokslai, medžiagų inžinerija, T008)

Gynimo taryba:
Pirmininkas – **prof. habil. dr. Valdas Sirutkaitis** (Vilniaus universitetas, technologijos mokslai, medžiagų inžinerija – T008);
Nariai:
Doc. dr. Renata Butkutė (Fizinių ir technologijos mokslų centras, technologijos mokslai, medžiagų inžinerija – T008);
Prof. dr. Saulius Juodkazis (Swinburne University of Technology, technologijos mokslai, medžiagų inžinerija – T 008);
Prof. dr. Giedrius Laukaitis (Kauno technologijos universitetas, gamtos mokslai, fizika N002);
Dr. Andrejus Michailovas (Fizinių ir technologijos mokslų centras, technologijos mokslai, medžiagų inžinerija – T008);

Disertacija ginama viešame Gynimo tarybos posėdyje 2021 m. liepos mėn. 9 d. 10 val. FTMC Fizikos instituto salėje.
Adresas: Savanorių pr. 231, LT-02300 Vilnius, Lietuva
Tel. +370 5 264 8884; el. paštas: office@ftmc.lt

Disertaciją galima peržiūrėti Fizinių ir technologijos mokslų centro, Vilniaus universiteto bibliotekose ir VU interneto svetainėje adresu: https://www.vu.lt/naujienos/ivykiu-kalendorius

CONTENTS

List of abbreviations

Abbreviation	Phrase
PVD	Physical Vapor Deposition
CVD	Chemical Vapor Deposition
ALD	Atomic Layer Deposition
IBS	Ion Beam Sputtering
E-beam	Electron Beam
OAD	Oblique Angle Deposition
GLAD	GLancing Angle Deposition
SBD	Serial Bi-Deposition
SEM	Scanning Electron Microscopy
AFM	Atomic Force Microscopy
XPS	X-Ray photoelectron spectroscopy
LIDT	Laser Induced Damage Threshold
AOI	Angle Of Incidence
FS	Fused Silica
MD	Molecular Dynamics
FDTD	Finite-Difference Time-Domain
AR	Anti-reflective
HR	High-reflective
QWOT	Quarter Wavelength Optical Thickness

INTRODUCTION

People have always admired the ripples of different colors on the surfaces of soap bubbles, or in oily ponds on a sunny day. However, very few people have ever observed that the same charming physical phenomenon could be applied to the formation of complex optical elements. As early as 1935, Alexander Smakula (a member of the Zeiss company) invented anti-reflective coatings that improved light transmission by using the principle of interference in thin films. These were formed on the surfaces of binocular lenses, and until 1940 such coatings were considered to be military secrets [1].

Huge demand for novel and high-quality dielectric optical elements appeared after the invention of the laser. The first laser was built in 1960 by Theodore H. Maiman at Hughes Research Laboratories, using a high-power flashlamp-pumped ruby rod with silver coated surfaces [2]. The main drawback of this early invention occurred when the laser radiation that was generated burned holes in the silver layers – the first example of laser-induced damage [3]. In the modern world, there are a wide range of different lasers: from huge and powerful laser systems for fundamental science applications [4] to micro-laser systems applicable in various novel technological solutions [5]. Obviously, laser technologies have drastically improved since their inception, and they are now widely used in research, telecommunications, medicine, and many other fields.

Various optical elements are used to control laser-generated radiation, such as: high reflective mirrors, polarizers, and spectra filters. Thus, considering the requirements of constantly improving technologies and the need for novel optical elements, a deep understanding of the manufacturing principles involved in producing optical coatings is necessary. Standard thin-film deposition technological processes allow for the fabrication of optical coatings with controllable refractive indexes, extinction coefficients, and precise thicknesses. An additional degree of freedom – control over the internal nanostructure of individual layers – opens new possibilities for the formation of elements that are even more complex. However, studying the internal compositions of layers is not an easy task due to their miniscule dimensions – the sizes of the individual features are much smaller than the wavelength of light.

In 1955, C. W. Oatley's group demonstrated a scanning electron microscope with a resolution of around 20 nm. Such a high resolution paved the way for the study of nanometer-sized structures, but these microscopes only later became commercially available to the scientific community.

Although impressive results have been achieved in the study of various nanostructures over the last 30 years, many incomprehensible mechanisms involved in the formation of physical structures remain. Thus, the nanoengineering of materials has become one of the most significant fields of science in the 21st century.

Sculptural thin films formed by oblique angle deposition technology are a well-known class of nanostructures. Such coatings are already applied in the fabrication of phase retardation elements [6], filters of circular polarization [7], biological sensors [8], and a range of other applications. The ability to control all of the deposition parameters makes it possible to create elements with novel optical properties, and with high resistances to powerful laser radiation. The nanoengineering of the material significantly influences the laser-induced damage thresholds of optical coatings, even in the UV spectral range. Porous layers are known to withstand higher laser-generated radiation energies [9]; however, for the most part, only homogeneous layers have been applied and demonstrated to be highly resistant, such as anti-reflective (AR) or high-reflective (HR) coatings [10,11].

The engineering of the internal properties of thin films by periodically oriented structure modifications is a very attractive and prospective area of science and technology. It opens new technological possibilities for the creation of novel elements, such as photonic crystals for the visible range, which has previously been impossible due to the need for features smaller than the wavelengths [12]. Photonic crystal is the composition of periodic dielectric or metal-dielectric nanostructures that are designed to affect the propagation of light in the same way as the periodic potential in a semiconductor crystal affects the movement of electrons [13]. By periodically repeating high- and low-refractive index regions, the allowed and forbidden electronic energy bands are created. One-dimensional photonic crystals are already popular in the optical coating industry (multilayer interference coatings) with various applications that utilize AR or HR properties. However, a great deal of interest lies in two- and three-dimensional photonic crystals in both fundamental and applied science. Such structures are attractive for application in medicine and biosensors [14], and in controlling and manipulating the flow of light [15].

This thesis is focused on improving the properties of optical elements by changing the thin film's internal structure. Firstly, nanostructured all-silica anisotropic layers were investigated in detail, and their advantages in phase retardation plates (these will be referred to as "waveplates", for simplicity) and polarizer formation were demonstrated. Secondly, the possibility of

forming 2D photonic crystals based on periodically pre-patterned substrates coated in a multilayer structure was established. Such methods allow for the creation of nanostructured optical elements as coatings, which can be applied to microlasers and to high-power complex systems.

The objective of the thesis

To investigate the possibility of forming thin films with controllable internal structures by using physical vapor deposition technologies, and to extend these methods to the manufacture of optical elements used in the manipulation of laser light.

The scientific tasks of the thesis

1. To develop a novel method of glancing angle deposition technology for the precise formation of low loss multilayer coating, highly robust to the laser radiation.
2. To develop a fabrication method of all-silica waveplates and polarizers operating at zero angle of incidence using glancing angle deposition technology.
3. To investigate the formation process of multilayer films deposited on periodically modulated surfaces by ion beam sputtering technology using different materials, and to compare the method with other thin film formation technologies.
4. To develop a method of depositing a multilayer coating on a periodically modulated surface for an element with high angular selectivity of optical transmittance.
5. To investigate the control of the geometry of nanostructured columnar coatings fabricated on the pre-patterned surface by glancing angle deposition method.

Scientific novelty and practical value

Permanent research in material science is of crucial importance to develop novel optical components with complex functionalities and novel optical characteristics. The main novelty of this dissertation from both sides, scientific and practical, is the demonstration of the new possibilities to control the internal structure of the deposited layer by: i) selecting the appropriate

technology, ii) optimizing deposition parameters, and iii) choosing substrates of suitable profiles. Specifically, scientific novelty and practical value of this dissertation can be summarized in following statements:

- The conceptually novel method of formation of porous anisotropic and dense all-silica multilayer coatings featuring low optical losses was developed. The method enables fabrication of high optical quality waveplates as a coating on virtually any type of substrate featuring a superior laser-induced damage threshold (~40 J/cm^2).
- The new formation method of polarizing coatings was proposed, made of different silica anisotropic layers with orthogonally crossed anisotropy axes. Those coatings feature a superior laser-induced damage threshold (39.0 J/cm^2 and 48.5 J/cm^2 for the reflected and transmitted radiation of orthogonal polarizations, respectively), as measured in the nanosecond regime by 355 nm wavelength radiation.
- The multilayer thin-films depositions on modulated surfaces by different technologies were investigated for the first time. The most promising technologies for conformal deposition were compared. As a result, ion beam sputtering technology was found optimal.
- For the first time, the growth of structured layers of different materials fabricated by ion beam sputtering on the modulated substrate was investigated in detail. High refractive index periodically modulated dielectric thin layer, surrounded by a low refractive media featured Fano-resonant coupling of the electromagnetic radiation, and manifested in angular and frequency selectivity of light reflection.
- Selecting suitable materials with high and low refractive indexes for the multilayer stack's conformal deposition on the modulated surface a compact 5 μm thickness spatial filter was manufactured. Such elements could be integrated into resonators of compact microlasers for performing spatial selection of the generation transverse modes.

Statements to defend

1. The dense, ultrathin silica interlayers in porous nanostructured anisotropic silica film minimize optical losses by reducing the coalescence and bundling effects of the columnar structure.

2. The combination of silica layers with different porosities and anisotropies allows for the formation of multilayer coating structures, with controllable phase retardation properties, high transmittance (up to 99%), and enhanced (up to 40 J/cm^2) laser induced damage thresholds in the nanosecond regime due to the use of only silica as a constituent material.
3. The cross-alignment of the optical axes of different anisotropic layers with effective refractive indices that match for only one polarization allows for the formation of a coating with different optical properties and polarizing effects for the normal angle of light incidence, with a high laser-induced damage threshold in the nanosecond regime.
4. The periodically modulated dielectric thin layer of a high refractive index in a low refractive index surrounding allows Fano resonances, and shows high angular and frequency selectivity of light reflection and transmission.
5. The conformal deposition of multilayer optical coatings on a pre-patterned surface using physical vapor deposition technology has been shown to be a 2D photonic crystal with spatial filtering functionality (< 2° half-width pass-band).

Approbation

*Scientific papers **directly related** to the thesis (peer-reviewed and indexed in Clarivative Analytics WoS):*

1. **L. Grineviciute**, H. Badorreck, L. Jensen, D. Ristau, M. Jupé, A. Selskis, T. Tolenis "Impact of deposition conditions on nanostructured anisotropic silica thin films in multilayer interference coatings" Applied Surface Science, 562, 150167, 2021
2. **L. Grineviciute**, M. Andrulevičius, A. Melninkaitis, R. Buzelis, A. Selskis, A. Lazauskas, T. Tolenis "Highly Resistant Zero-Order s Based on All-Silica Multilayer Coatings", Phys. Status Solidi A, 1700764, 2017
3. **L. Grineviciute**, L. Ramalis, R. Buzelis, T. Tolenis "Highly resistant all-silica polarizing coatings for normal incidence applications" Optics letters, Vol. 46, No. 4, 2021
4. **L. Grineviciute**, C. Babayigit, D. Gailevičius, E. Bor, M. Turduev, V. Purlys, T. Tolenis, H. Kurt, K. Staliunas "Angular filtering by Bragg

photonic microstructures fabricated by physical vapour deposition", Applied Surface Science, 481, 353-359, 2019

5. **L. Grineviciute**, C. Babayigit, D. Gailevičius, M. Peckus, M. Turduev, T. Tolenis, M. Vengris, H. Kurt, K. Staliunas "Nanostructured Multilayer Coatings for Spatial Filtering", Adv. Optical Mater. 2001730, 2021
6. **L. Grineviciute**, J. Nikitina, C. Babayigit, K. Staliunas "Fano-like Resonances in Nanostructured Thin Films for Spatial Filtering", Applied Physics Letters 118, 131114, 2021

*Scientific papers **directly related** to the thesis (conferences proceedings)*

1. **L. Grineviciute**, K. Gricius, R. Buzelis, T. Tolenis "Anisotropic Optical Coatings for Polarization Control in High-power Lasers", OIC 2019, OCIS codes: 230.0230 Optical devices, proc. OSA, 2019
2. **L. Grineviciute**, K. Gricius, R. Buzelis, T. Tolenis "Optical anisotropic coatings for polarization control in high-power lasers", Proc. SPIE 11033, High-Power, High-Energy, and High-Intensity Laser Technology IV, 1103300, 2019
3. **L. Grineviciute,** L. Ramalis, K. Gricius, R. Buzelis, T. Tolenis, "Anisotropic coatings for normal incidence applications", Proc. SPIE 10691, 1069120, 2018
4. **L. Grineviciute**, R. Buzelis, M. Andrulevičius, A. Lazauskas, A. Selskis, R. Drazdys, T. Tolenis "Advanced design of UV waveplates based on nanostructured thin films", Proc. SPIE, Nanostructured Thin Films X, Vol. 10356, 103560Q, 2017

Other scientific papers (peer-reviewed and indexed in Clarivative Analytics WoS):

1. **L. Grineviciute**, R. Buzelis, L. Mažulė, A. Melninkaitis, S. Kičas, T. Tolenis, "Enhancement of high reflectivity mirrors using the combination of standard and sculptured thin films" Optics & Laser Technology, Vol. 129, 106292, 2020
2. E. Buzavaite-Verteliene, A.Valavicius, **L. Grineviciute**, T. Tolenis, R. Lukose, G. Niaura, and Z. Balevicius "Influence of the graphene layer on the strong coupling in the hybrid Tamm-plasmon polariton mode", Optics Express, Vol. 28, No. 7/30 March, 2020

3. H. Badorreck, M. Steinecke, A. Farid, M. Jupé, D. Ristau, J. Müller, R. Tonneau, P. Moskovkin, S. Lucas, **L. Grineviciute**, A. Selskis, and T. Tolenis, "Correlation of structural and optical properties using Virtual Materials analysis", Optics Express, Vol. 27 Issue 16 p.p. 22209-22225, 2019
4. T. Tolenis, **L. Grineviciute**, L. Smalakys, M. Ščiuka, R. Drazdys, L.Mažulė, R.Buzelis, A. Melninkaitis "Next generation highly resistant mirrors featuring all-silica layers", Scientific reports, 7(10898), 2017
5. T. Tolenis, **L. Grineviciute**, R. Buzelis, L. Smalakys, E. Pupka, S. Melnikas, A. Selskis, R. Drazdys, and A. Melninkaitis "Sculptured anti-reflection coating for high power lasers", Optical Material Express, 7(4), 2017

Conferences directly related to the thesis:

1. **L. Grineviciute,** D. Gailevicius, C. Babayigit, L. Ramalis, J. Nikitina, K. Staliunas, T. Tolenis "Deposition of multilayer optical coatings on corrugated surfaces for 2D photonic crystals formation", FM&NT, Vilnius, Lithuania, 23-26 November, 2020, Oral-Online
2. **L. Grineviciute**, R. Buzelis, R. Drazdys, T. Tolenis "The capabilities to form multilayer nanostructured coatings and their applications for waveplates production", ICTON, Angers, France, 9-13 July 2019, Oral pr.
3. **L. Grineviciute**, K. Gricius, R. Buzelis, T. Tolenis, "Anizotropic optical coatings for polarization control in high-power lasers", OSA Optical interference coatings, New Mexico, US, June 2-7, 2019, Oral/poster pr.
4. **L. Grineviciute**, K. Gricius, R. Buzelis and T. Tolenis "Optical anisotropic coatings for polarization control in high-power lasers", SPIE Optics and optoelectronics, Prague, Czech Republic, 1-4 April, 2019, Oral pr.
5. **L. Grineviciute**, L. Ramalis, R. Buzelis, A. Melninkaitis, T. Tolenis "Anisotropic optical interference coatings for polarization control in high-power lasers", ICLO, St.Petersburg, Russia, 4-8 June,2018 – Oral pr.
6. **L. Grineviciute**, A. Melninkaitis, A. Jasinskas, R. Buzelis, T. Tolenis "HR and AR nanostructured optical coatings for high-power applications", ICLO, St.Petersburg, Russia, 4-8 June,2018 – Poster pr.

7. **L. Grineviciute**, L. Ramalis, K. Gricius, R. Buzelis, T. Tolenis "Anisotropic coatings for normal incidence applications", Frankfurt, Germany, 14-17 May, 2018 – Poster pr.
8. **L. Grineviciute**, L. Petronis, R. Buzelis, T. Tolenis "Evaporated anisotropic nono-structured coatings for polarization control in high-power lasers", Nanophotonics and micro/nano optics international conference, Rugsėjo 13-15, 2017, Barcelona, Spain – Poster pr.
9. **L. Grineviciute**, R. Buzelis, M. Andrulevičius, A. Lazauskas, A. Selskis, R. Drazdys, T. Tolenis, "Advanced design of UV waveplates based on nanostructured thin films", SPIE, Nanostructured Thin Films X, August 9-10, 2017, San Diego, California, JAV – Oral pr.
10. **L. Grineviciute**, R. Buzelis, A. Melninkaitis and T. Tolenis "High resistive UV waveplates based on nanostructured anisotropic coatings" International Conference Nanotechnology and Innovation in the Baltic Sea Region, June 14 – 16, 2017 – Poster pr.
11. **L. Grineviciute**, T. Tolenis, R. Buzelis, A. Selskis, R. Drazdys; "Investigation of serial bi-deposited nanostructured thin films for polarization control" 18-th International Conference-School ADVANCED MATERIALS AND TECHNOLOGIES August 27-31, 2016, Palanga, Lithuania – Poster pr.
12. **L. Grineviciute**, A. Valavičius, T. Tolenis, R. Drazdys "Characterization of Nb_2O_5 and Ta_2O_5 coatings produced by electron beam evaporation with plasma source assistance" OPEN READINGS 2016, Vilnius, Lithuania, March 15-18, 2016 – Poster pr.

Contribution of the author and others

The contribution of the thesis author and main co-authors is noted following the sections of the results presented:

ANISOTROPIC NANOSTRUCTURED COATINGS

The author personally designed, or actively participated in designing, all experiments and devised the idea of multilayer phase retardation waveplate fabrication. The author also performed or supervised all experimental thin film depositional processes, performed spectrophotometric and AFM measurements, and conducted the analysis of nanostructured films.

Dr. T. Tolenis participated in designing of all the experiments and devised the waveplate and the polarizer fabrication ideas.

PhD stud. L. Ramalis performed part of experiments and of measurements of polarizers.

K. Gricius, supervised by the author, performed part of deposition processes and measurement of anisotropic single layers.

Dr. M. Andrulevičius performed XPS measurements.

Dr. R. Buzelis and dr. A. Melninkaitis performed LIDT measurements.

Dr. H. Badorreck and dr. M. Jupé performed MD simulations.

COATINGS ON CORRUGATED SURFACES

The author devised and designed experimental procedures for single- and multilayer formation. She fabricated master samples with the modulated surface, also performed or supervised all spectrophotometric and AFM measurements, performed the analysis of the results.

Prof. dr. K. Staliūnas proposed the idea for the fabrication of spatial filters based on multilayer coating and supervised theoretical calculations.

PhD stud. C. Babayigit performed FDTD simulations.

Dr. D. Gailevičius performed measurements of spatial filtering with a probe laser beam, also replicated substrates from the modulated surface.

J. Nikitina, supervised by the author, performed part of spectrophotometric and AFM measurements.

J. Bliūdžius, supervised by the author, performed depositions with IBS.

Dr. A. Selskis performed all SEM measurements (provided in both sections of the results).

1 THE LITERATURE OVERVIEW

1.1 Optical elements for light manipulation

The demand for novel and high-quality dielectric optical elements exists as a result of the constant improvement of laser systems. Various optical elements are used to control the characteristics of laser-generated radiation, including: high reflective mirrors; waveplates; polarizers; and intensity and spectra filters. In this chapter, waveplates, polarizers, and spatial filters will be discussed in detail.

Optical elements for the control of polarization are some of the common parts of advanced laser systems. High-power laser system parameters such as polarization state and peak intensity are often controlled by polarization optics, including waveplates and polarizers. With the combination of these two elements, it is possible to effectively control the polarization properties of light and the intensity of radiation. Such a combination is also widely used in laser systems, various spectroscopic systems, ellipsometers, and a host of other applications.

Waveplates (or phase retardation plates) are optical elements used to control the polarization state of light. These elements are widely used in optical and laser systems where polarized light is used. The application of waveplates can fulfill various roles: changing polarization state, controlling light intensity, identifying polarization, etc. The physical principle of operation is based on the birefringence of the anisotropic material. Phase retardation occurs because the index of refraction is different for linearly polarized light along two specific perpendicular anisotropy axes. To produce a waveplate, it is important to select the right anisotropic material and to know its birefringence Δn. Phase retardance, δ, can be calculated by the formula [16]:

$$\delta = \frac{2\pi D \Delta n}{\lambda}, \qquad (1)$$

where D is the thickness of the birefringent media, Δn is the difference between the refractive indexes of the fast and slow axes, and λ is the wavelength.

The two types of waveplates most widely used are quarter and half-wavelength plates. These are so named due to their phase shift amounts – a quarter of the wavelength (90°) or a half of the wavelength (180°), respectively – which change the state of light polarization. Such elements can be made of natural crystals, polymers, liquid crystals, and other anisotropic layers featuring optical anisotropy [17,18]. Most of these elements are challenging to fabricate, fragile, unstable when environmental conditions change, difficult to apply in microsystems, or have low resistance to laser radiation.

Polarizers are standard optical elements designed to convert ordinary unpolarized light into polarized light. Polarization control in modern laser systems is essential in a variety of different kinds of applications such as: interference lithography [19]; refractive index modulations in transparent materials [20]; and absorption enhancement in laser-matter interactions [21]. In the case of solid-state lasers, birefringent crystals (such as YVO_4) can be used as gain media and can generate linear polarization [22]. For microchip lasers, however, isotropic materials are preferable due to their entirely superior properties [23].

In modern science, polarizers are produced using various polymeric or metallic grids with absorption properties. In addition, polarizers can be employed as spectral dividers, where the radiation of s-polarized light (perpendicular to the plane of incidence) is reflected, and p-polarized light (parallel to the plane of incidence) is transmitted.

A number of problems inevitably occur when using polarizers. In the case of polarizers that absorb at normal incidence, a low laser-induced damage threshold occurs. Isotropic multilayer dielectric polarizers with higher LIDTs can only be designed as elements that must be installed in systems at a certain angle, typically Brewster's angle [24], leading to the light beam shifting from a straight line.

The insertion of anisotropic layers – namely nanostructured thin films – into dielectric multilayer coating can be used to design both waveplates and polarizers. Such all-silica elements can be applicable for zero angles of incidence and exhibit superior LIDTs [25,26].

A spatial filter is an optical element which "cleans" the spatial structure of a laser beam. When a beam passes through a complex system of optical elements, dust in the air, or a turbulent environment, the beam structure can be detreated, and the wave front of transmitted/reflected light distorted. Some "imperfect" lasers also emit beams with poor spatial quality (large beam quality factor m^2). The spatial structure of these beams can be improved by

spatial filtering outside of the laser resonator. Spatial filters can also be installed in the laser resonator, providing intracavity filtering and forming a high spatial quality beam directly within the laser.

The standard multi-lens arrangement with pinholes is typically used for both intracavity and extra-cavity filtering. Many important laser systems, including high power and ultrashort pulse lasers, use conventional intracavity filtering [27]. Such an arrangement, however, is not especially compact, and can be inconvenient for applications requiring a compact design. Therefore, conventional filtering is extremely problematic for use in micro lasers.

A different commercially available solution – reflective volume grating – was proposed for use in spatial filtering. This solution is based on using holographic methods to write refractive index modulation into the volume of a photosensitive glass. A narrow acceptance angle enables the filtering of laser beams with a single element, thus replacing pinhole assemblies. However, such an element must be used as an external optical element and installed into the system at a particular angle, and is therefore not applicable for zero-angle of incidence [28].

With micro-lasers in high-power emission regimes, the spatial quality of laser light beams also deteriorates. This high power requires a large amplification area, and for short cavities the natural spatial filtering mechanisms are absent. High-power micro-lasers typically emit light in a multi-transverse mode regime. However, the methods mentioned above cannot be applied in this case due to the lack of space in the laser resonator. Recently, a new physical principle of spatial filtering was proposed based on beam propagation through a compact photonic crystal structure [29]. Such a spatial photonic crystal filter is fabricated by periodically modulating refractive index media in a glass volume using a tightly focused femtosecond laser beam [30]. In optics, for visible frequencies, the realization of such a form of spatial filtering remains a challenging technological task, as the period of refraction index modulation must be of the order of the wavelength. Moreover, in the case of direct laser writing, the difference between the refractive indexes of the exposed and unexposed sites in glass is in the order of 10^{-3}. This means that the structures must be written deeply into the glass to achieve a strong filtering effect, which presents a significant technological challenge [31,32].

In this thesis, the angular filtering of light in the photonic structures fabricated by physical vapor deposition was proposed and experimentally manufactured. The thickness of such elements was reduced to 5 μm due to the high refractive index contrast of using different materials. Moreover, such a

filter can be formed directly onto a crystal surface and is suitable for zero-angle of incidence. [33,34]

1.2 Thin film deposition methods

Most modern optical elements used in solid-state laser systems are based on interference coatings [35,36]. Such coatings consist of thin sub-wavelength thickness dielectric multilayer structures, which meet the conditions of interference phenomena. The fabrication methods of such thin films can be divided into three main groups: physical, chemical, or combination of both of them. Each process is different, but the main evolution during the thin-layer growth consists of several main stages: vapor transport from material to substrate, condensation and nucleation, the formation of nucleation points, their expansion, bonding, and further layer growth. Each of these stages affects the final properties of the coating. [37] The most common techniques for optical coatings production of dielectric layers are Physical vapor deposition techniques (PVD), such as electron beam evaporation and sputtering. PVD became very popular in laser optics fabrication due to high quality and high purity layers, high yield and deposition rate, low deposition errors [38].

Deposition of thin films consists of three different steps: i) Transition of the condensed phase into the gaseous state, ii) The vapor transport between the vapor source and the substrate, iii) Material condensation on the substrate (deposition of evaporated atoms on the substrate).

1.2.1 Electron beam evaporation method

The fabrication of thin films by evaporation is comparatively simple and convenient and is the most widely used technique. However, reaching the excellent quality of deposited layers requires high-vacuum conditions, high purity of materials, and precise control of technological parameters. Moreover, there are several methods of evaporation: evaporation from resistive boats, electron beam (e-beam) evaporation, e-beam evaporation with plasma assistance, etc. During the resistive evaporation, process material is placed in the heated boat. Despite the fast and straightforward procedure, this method is limited by the selection of materials. The sublimation or evaporation temperature of depositing material must be much lower than the resistive boat's material. In this respect, e-beam evaporation overcomes this issue by cooling the crucible and heating only evaporated material with a focused

electron beam. In this way, a vast number of materials can be evaporated, e.g., metals, metal-oxides, fluorides, etc. [39]

The properties of coatings deposited during electron beam evaporation depend on many parameters: vacuum level in the chamber, the substrate temperature, the substrate material, the evaporation rate, the incidence angle of material atoms on the substrate, etc. [40].

The atoms of the material deposited during the electron beam evaporation do not acquire much energy; it is not exceeding 0.4 eV. For this reason, the deposited particles form a porous, low-density layer. Such coatings absorb moisture from the environment, creating internal stresses, and often do not achieve the desired optical characteristics. An additional energy source can be introduced into the system to eliminate those problems (see Fig.1). [41,42]

The additional energy sources could be an ion source or plasma source, which generates ions that is directed towards the surface to be coated. High energy ions increase the mobility of deposited molecules, which can diffuse on the surface some distance before settling. This results in a much denser thin film and increases adhesion to the substrate.

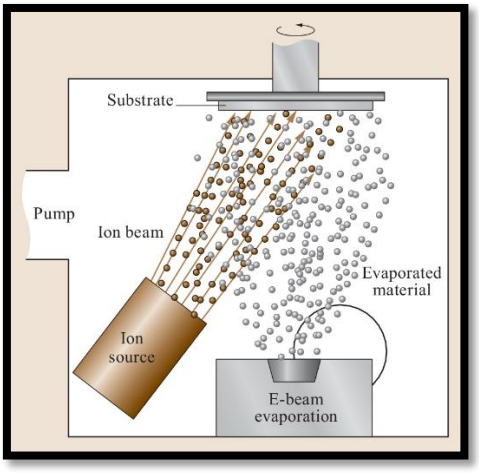

Figure 1. The schematic representation of e-beam evaporation with Ion Assisted Deposition method [43].

Increased density reduces moisture absorption and increases the refractive index. Depending on the selected plasma source parameters for energetic particles and evaporation parameters, it is possible to change the optical properties of materials and the thin film stresses, which are especially important for the evaporation of multilayer structures of different materials.

Due to internal tension, the probability of cracking or peeling the coating off the substrate increases. If an optical element is fabricated on a very thin and fragile substrate, it can bend along with the layer and distort the light wave fronts of transmitted/reflected light. [44].

1.2.2 Ion beam sputtering method

Ion-beam sputtering (IBS) technology is based on a different physical principle than the previously described evaporation method. IBS is based not on the evaporation of material but on the destruction of a solid surface by bombarding it with a flux of energetic ions (Fig. 2).

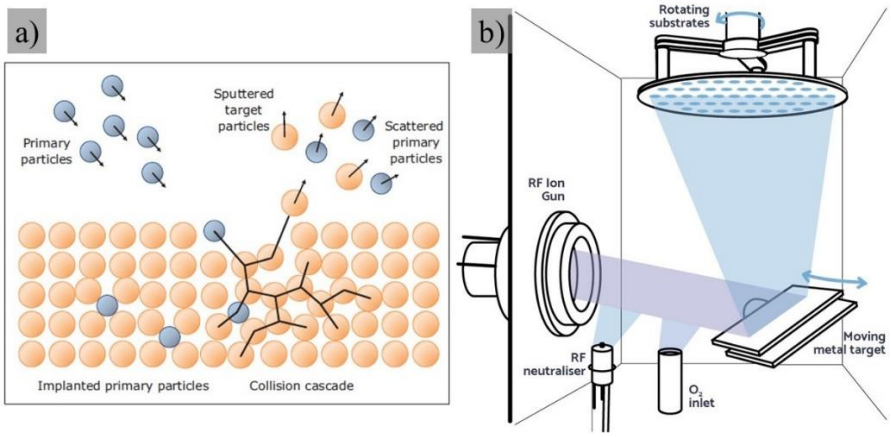

Figure 2. IBS a) The schematic representation of a) the basic principle of the sputtering method [45], b) Ion Beam Sputtering technology [46].

The gas discharge plasma and acceleration at high voltage is used to generate the directional ion beam. Primary energetic particles (usually Ar ions with energy larger than 100 eV) transfer their energy to the target atoms as a quantity of momentum. If the transferred energy exceeds a bulk material's atoms' chemical bonding energy, atoms are sputtered and form a vapor flux that flows freely in a vacuum chamber towards the substrates. The surface of the deposited material, especially in the case of dielectrics, may be charged due to the accumulation of positive ions. An additional electron source is used to neutralize ion flux and eliminate the charging effect during the sputtering process. Also, the target is being cooled during the process with the water-cooling system, which prevents the material from overheating. Ion-beam sputtering is a high-energy process suitable for virtually any material. Sputtered atoms acquire significantly higher energies (1 - 40 eV or even more)

than in the case of evaporation. The high energy of the deposited particles results in better optical and mechanical properties of the layers. Coatings produced in this way are very dense, with low loss of scattering and absorption. However, it is worthy of mentioning that the coatings formed by this technology have very high internal stress, in most cases compressional ones. Also, sputtering has a lower deposition rate than e-beam evaporation, resulting in an increased process time, i.e., production costs [47,48].

1.2.3 The basic principle of thin film formation

Examining the layer deposition process, it is convenient to divide it into three stages, separated in time and space:

i) the conversion of the condensed matter to individual atoms, ions (vapor or plasma phase);
ii) the transfer of atoms and ions from the source to the substrate where the particles settle (condensation);
iii) the condensation and layer formation on the substrate.

Mainly the third stage of the process will be explained in this section, how thin films condense on the substrate and how this affects the properties of the films.

The optical properties of sputtered dielectric layers mainly depend on deposition parameters during fabrication, such as vacuum level, deposition rate, temperature, etc. However, in general, the theoretical models that consist of homogeneous distribution of layer properties do not fully agree with the experimental results. In reality, there is neither an ideal crystal nor an ideal amorphous layer without defects. Even the perfect crystal will have some defects, usually atoms that are not in their intended places. Such internal defective atoms do not change the stoichiometry of the material itself. External defects can change both the stoichiometry of the layer and its properties (optical, electrical, etc.). Therefore, various theoretical models are needed to help to identify the coating's actual internal structure, optical or other properties.

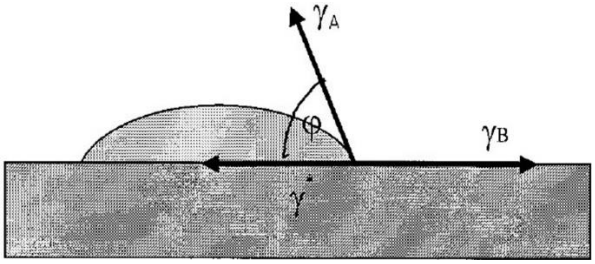

Figure 3. The wetting angle φ of a liquid phase nucleus on a substrate is described by Young's equation. Υ_B is the surface energy of the substrate, Υ_A - the energy of coating material, Υ^* - the energy of the interface between the film and the substrate [49].

One of the most critical steps in the deposition of thin films is the nucleation of material atoms on the substrate. The nucleation of the particles occurs differently depending on the bonding energies between the materials of the interface. The interaction between depositing atoms and substrate can be described by the contact or wetting angle φ (see Figure 3).

The wetting angle φ of the material deposited on the substrate is defined by Young's equation [49]:

$$\Upsilon_B = \Upsilon^* + \Upsilon_A \cos(\varphi), \qquad (2)$$

where Υ_B is the surface energy of the substrate, Υ_A – the energy of coating material, Υ^* - the energy in the interface between the film and the substrate

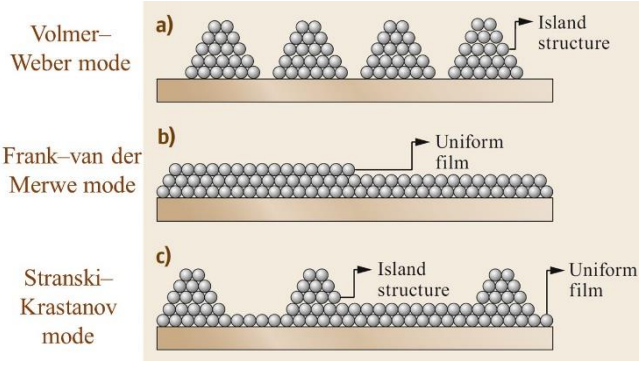

Figure 4. The schematic representation of Volmer-Weber, Frank-van der Merwe, and Stransky-Krastanov models [43].

The film formation on the substrate can be divided into three main models, depending on the energy Υ values: layer growth with islands, continuous

layer, or mixed. The best-known models are Volmer-Weber, Frank-van der Merwe, and Stransky-Krastanov models, describing islet, continuous, and mixed-layer growth, respectively (see Figure 4).

Volmer-Weber model. This is a model of layer formation with individual islets. For the layer to grow in three-dimensional islands, the condition must be met:

$$\Upsilon_B < \Upsilon^* + \Upsilon_A \quad (3)$$

In this case, the interaction energy between the coating atoms Υ_B is stronger than the interaction of the coating atoms with the substrate atoms.

Franc-van der Merwe model. This is a model of continuous layer (layer-by-layer) formation. For a coating to grow in a continuous layer, the energy of its atomic bond with each other must be less than the energy of interaction with the substrate atoms:

$$\Upsilon_B > \Upsilon^* + \Upsilon_A \quad (4)$$

Stranski-Krastanov model. The continuous formation of the layer together with the islands begins when the energy of the bond between the atoms of the interlayer and the substrates increases as the layer grows. This growth model is described not only by the energy at the interface between the substrate and the coating but also by the coverage of the substrate surface.

Coalescence is a crucial stage in the formation of coatings. It is a step of individual feature formation, in this case, coalescence of islands. The layer begins to form islands that grow and expand individually until there is no enough space for expansion, and they begin to connect. This coalescence process is essential for coatings that require particular properties. After merging two islands, one double derivation can be formed with a clear junction boundary between the former individual islands. However, in the case of a continuous layer formation, the junction zone disappears by mixing liquid substances – simply, a larger island is formed. The diffusion, not only on the surface but also in the volume, of the material depends on surface energy and surface filling. A threshold of percolation can characterize the transition from isolated individual islands to the continuous solid layer. The percolation threshold is the thickness at which a cluster of infinite size appears. Percolation refers to the passage or forced movement through a porous material. This term can be explained in the example of measuring electrical

conductivity between two macroscopically isolated contacts formed by a metal layer on a dielectric substrate. As the percolation threshold (thickness) is reached, the coalescence of the individual islands creates a continuous path for electrons to flow from one contact to another. This creates a network connecting the islands, and the electrical conductivity increases at several orders of magnitude. The characteristics of the optical coating are also changing intensively. For most metals, the percolation thickness of the coating is between 1 nm and 20 nm of effective coating thickness. For the production of metal mirrors or dielectric quarter-wavelength optical element systems, the layer thicknesses are much larger than this value. However, low atom mobility and the self-shadowing effect can completely change the structure of the growing films. Few processes can describe the formation of a layer:

Shading effect. This is a relatively simple geometric interaction between the deposited atoms (or the surface roughness) and nucleation centers of the growing layer. This phenomenon occurs when the substrate temperature *Ts* is low and comparable to room temperature. It is also of the essence for shading that the flux of depositing atoms is sufficiently collimated.

Surface diffusion of deposited atoms can occur when atoms or molecules have sufficiently high energies: kinetic energy or high substrate temperature. During it, a denser coating is formed, and the phenomenon of shading becomes less significant.

Bulk diffusion. Molecules and atoms in the coating volume can move and enter the most stable position only when the substrate temperature is high and provides sufficient energy for diffusion to take place, which helps to reach energetically favorable site.

Recrystallization. A phase transition such as crystallization or a final change in the orientation of the crystallites can only occur at very high substrate temperatures, often only after crossing the percolation threshold or at higher coating thicknesses.

For most metals and dielectrics, the diffusion activation energy is related to the material's melting temperature T_m. Thus, accordingly, different processes may be more likely to occur than others during the deposition of layers, depending on the value of T_s/T_m. The actual coating internal structure and properties of the layer depend on the dominant growth processes. This is the basic concept behind which structural zone models were devised. In the

simplest case, the actual coating structure can be divided into three zones. The first model of such structural zones was proposed by B. A. Movchan and A. V. Demchishin [50]. They studied layers made by electron beam evaporation method ranging in thickness from 300 μm to 2 mm. The evaporated materials were metals (Ti, Ni, W, Fe) and oxides (ZrO_2 and Al_2O_3), and the deposition rate of the coating ranged from 12 to 18 kÅ/min. The resulting coating structures were divided into three zones (see Figure 3):

- Zone I – $T_s/T_m < 0{,}3$ (low mobility, admolecules and adatoms settle as soon as they reach the substrate). The coating is obtained as a porous, internal structure consisting of crystallites (granules).
- Zone II – $0{,}3 < T_s/T_m < 0{,}5$ (the surface diffusion occurs with an activation energy equal to 0.1-0.3 eV). In this process, layers consisting of columnar shape crystals are formed. In this case, the distribution of the crystallites is denser, and the surface is smoother. In this temperature range, the crystallites increase with increasing substrate temperature. The formation of columnar crystallites is determined by the low mobility of the adatoms and the shadowed areas for depositing particles as the crystallites grow.
- Zone III – $T_s/T_m > 0{,}5$ (begins bulk diffusion with activation energy greater than 0.3 eV). Layers are formed with chaotically oriented crystallites. The recrystallization process determines the structure of such layers.

J. A. Thornton extended this three-zone structure model to study the layers that are deposited using the ion sputtering process. In this case, the microstructure of the layers is determined not only by the substrate temperature but also by the gas pressure during the deposition of the layers. In this model, an intermediate T-zone between the first and second zones is introduced. The depositing particles' energy changes explain the influence of gas pressure on the microstructure due to thermalization. In the J. A. Thornton model, the structure of the first zone is obtained when the adatoms do not have enough energy to diffuse into the gaps formed by shadowing. This occurs during the formation of both amorphous and crystalline coatings.

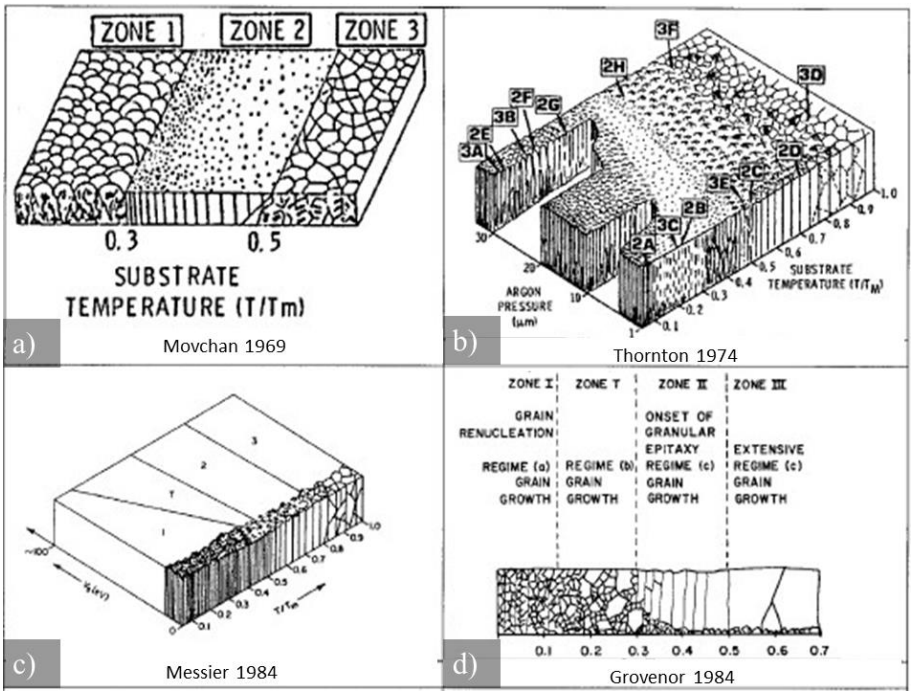

Figure 5. Structure zone models: a) B. A. Movchan, b) J. A. Thornton, c) R. Messier and d) C. R. M. Grovenor. [49]

High substrate roughness of the nucleation area causes the shading phenomenon – higher sites reach a higher proportion of the deposited particle flow than lower sites. J. A. Thornton observed that the influence of shading increases significantly when the substrate is held at a large angle to its surface normal. The transition zone (Zone T) consists of denser but difficult-to-define internal structure. Surface diffusion is higher than in the first zone, so the shading effect is less dominant.

R. Messier also applied the zone model to coatings made by sputter deposition with an ion-assistance [51]. C. R. M. Grovenor additionally evaluated the influence of substrate morphology [52]. All of these models are shown in Figure 5.

A. Anders, based on J. A. Thornton structure zone model, supplemented it by estimating the influence of plasma and ions on coating formation the diagram shown in fig. 6 is made by analyzing coatings deposited by high-energy pulsed magnetron sputtering. [53]

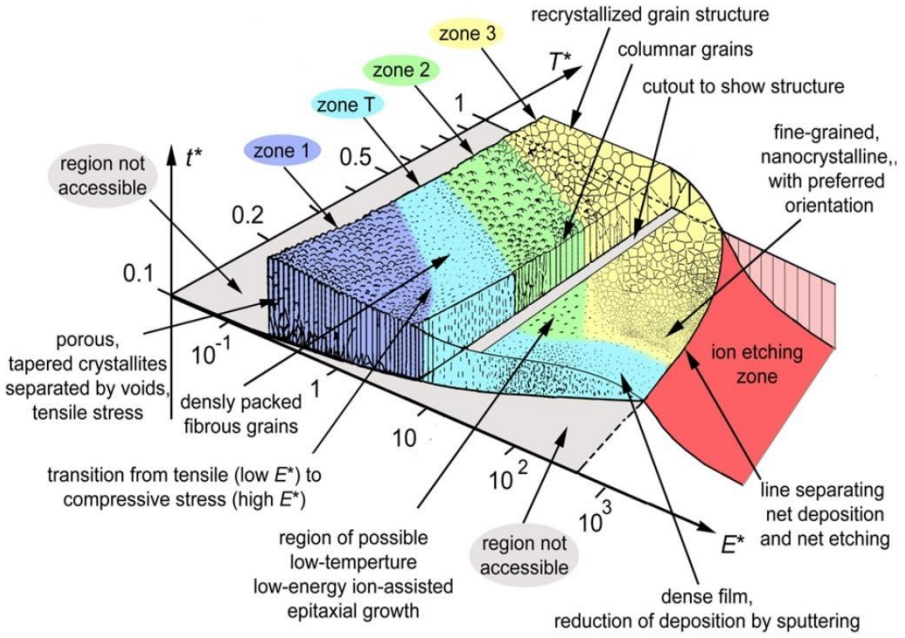

Figure 6. Anders structure zone diagram applicable to energetic deposition processes (Figures on the axes are for rough estimation only. Actual values depend on the specific material and the primary deposition parameters.). [53]

It shows three axes: temperature, normalized kinetic energy, and coating thickness, which can have a negative value if high ion energy causes etching of the coating (or substrate). While this model is one of the most applicable in most cases, it should be kept in mind that the properties of layers also depend on many primary parameters such as target voltage, vacuum level, base distance from the target, etc.

1.3 Sculptured thin films

About 70 years ago, the study of the internal structures of deposited film layers, which have dimensions smaller than the wavelength of light, started. Only in 1955, the group of C.W. Oatley demonstrated the scanning electron microscope with a resolution of about 20 nm [54], which finally led to the marketing of the first commercial SEM instrument by Cambridge Scientific Instrument Company. It was impossible to see the individual features with an optical microscope until then due to light diffraction limits. Only when electron microscopes with much higher resolutions emerged, it was possible

to see that the coatings formed under certain conditions had a neat structure at the nanometer level. When the substrate is tilted during the process, the coating is formed with a structured volume - columns smaller than a few hundred nanometers. This is how Oblique Angle Deposition (OAD), or also so-called Glancing Angle deposition (GLAD) technology emerged (Fig. 7) [55,56]. During the process, the substrate is tilted at a certain angle χ (the angle between the normal of the substrate surface and the flow of evaporated atoms). Using a stepper motor, this angle can be manipulated, and the coating begins to form a more porous structure with neat columns. By introducing another stepper motor into this system, which would change the angle around the normal of the substrate surface, it is possible to form coatings with complex three-dimensional structures - spiral, chevron, etc. [56,57]

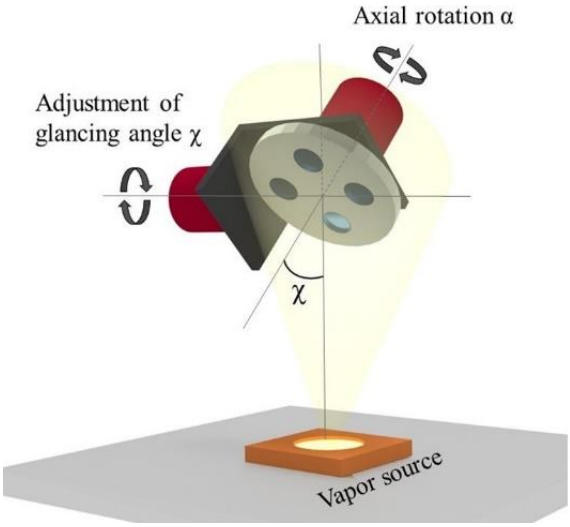

Figure 7. The schematic representation of the Oblique angle deposition method.

The formation of a specific nano-structure by oblique angle deposition is due to the shadowing effect of the atoms of the evaporated material (see Fig. 8). Atoms deposited during evaporation do not have much energy (it does not exceed 0.4 eV). As a result, if the substrate is not additionally heated, the atoms settle on the substrate as soon as it reaches it, and there is almost no surface migration of particles. The formation of nucleation centers (nuclei from which columns begin to form) is a random process that depends on evaporation parameters such as vacuum conditions, evaporation rate, material, etc.

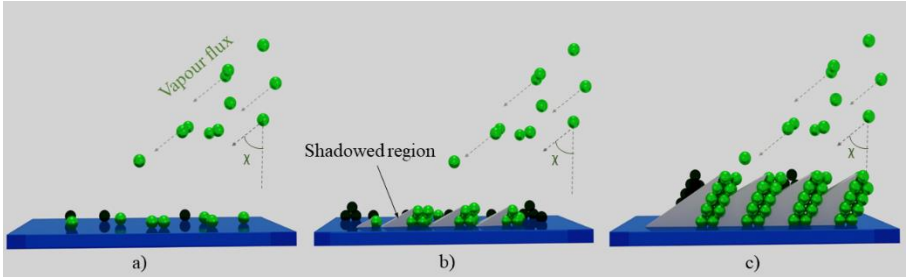

Figure 8. Principal scheme of glancing angle deposition method.

When the first atoms settle on the substrate, primary nucleation sites are formed, which creates a shadow (Fig. 8 a). The atoms of the nuclei, embedded in the surface of the substrate, certain obscure areas (shading areas) that cannot be reached by particles coming at an angle χ (Fig. 8 b). Because the atoms of the material evaporated by the electron beam form a collimated flux, and the atoms themselves do not have much energy, they immediately settle on the nearest, already established, atoms and create columns (Fig. 8 c). The width and the shape of the formed column depend on the evaporation parameters and the evaporation angle [58].

For the effective shadowing effect and column formation, the substrate must be tilted at an angle of more than 30 degrees, but not more than 90 degrees. Also, the column's inclination angle does not coincide with the angle of evaporation and is slightly smaller. The relationship between the evaporation angle χ and the column tilt angle β (see Fig. 8 c) was determined at low evaporation angles [56]:

$$\tan\beta = \frac{1}{2}\tan\chi \qquad (5)$$

When the evaporation angle is greater than 30 degrees, the tilt angle of the column can be calculated using the formula [56]:

$$\beta = \chi - \arcsin\left(\frac{1-\cos\chi}{2}\right) \qquad (6)$$

By manipulating the angle between the normal of the substrate surface and the vapor flux of evaporated material and the angle around the normal of the substrate surface, complex three-dimensional structures can be formed. When the substrate is fixed at a specific, constant evaporation angle χ, and the substrate itself is rotated during the process, spiral structures are formed, as shown in Figure 9.

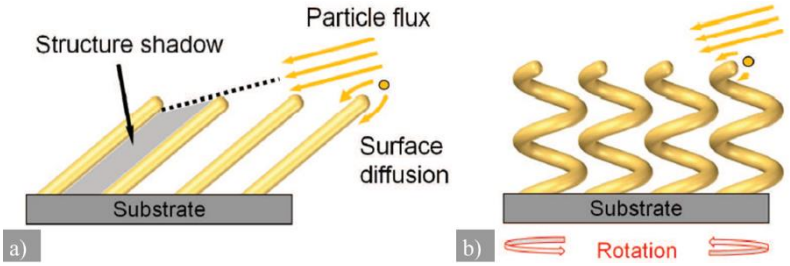

Figure 9. The shadowing phenomenon during coating formation – scheme of a) columnar structure formation and b) scheme of formation of spiral structure. [59]

Number of scientific works has been accomplished, demonstrating creation of various structures: columnar (I-shaped), chevron (V-shaped), C-shaped, spiral, etc., perpendicular to the substrate. In Fig. 10, various geometric shape structures formed by manipulating evaporation angles are presented. [59]

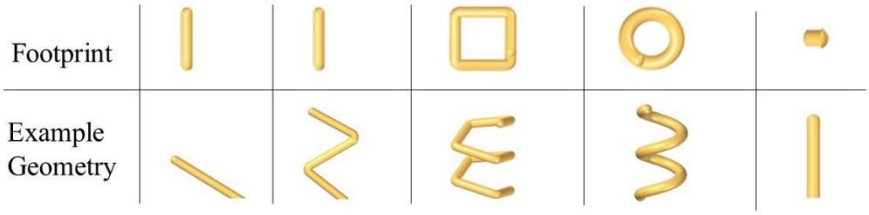

Figure 10. Coating structures of various geometric shapes. [60]

Some of the first complex two-dimensional and three-dimensional structures were formed using MgF_2 material [61,62]. Evaporation of MgF_2 at an angle of 60 degrees resulted in the formation of a coating with a columnar structure (Fig. 11 a). By evaporating the same material but periodically turning the substrate around its surface normal by small-angle, screw-shaped structures are formed (Fig. 11 b). It is also possible to combine two or more layers of different geometries to form the multilayer coating (Fig. 11 c). The geometry of the fragment of the internal structure of sculptural coatings can be changed by varying the evaporation angles and the evaporation parameters - evaporation rate, temperature.

A slightly higher temperature initiates a more significant surface migration of the adatoms, which changes the nucleus and column width of the resulting material. In order to form structures with the shape of all the columns to be the same and at certain constant distances from each other, it is possible to use

specially prepared substrates with the primary structure already formed on the surface.

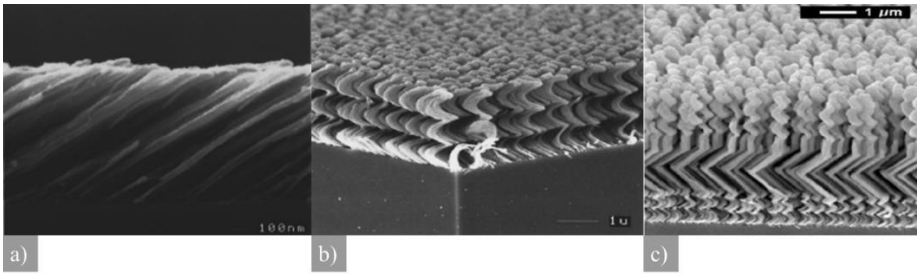

Figure 11. SEM images of fabricated sculptured coatings: a) columnar structure of MgF_2, b) structure of screw-shaped MgF_2 [61], c) the combination of spiral and chevron shape layers. [18]

As discussed earlier, the internal structure of coatings of the surface depends on various physical deposition parameters such as temperature, pressure, roughness, etc. Different structure zone models have been developed for normal to the substrate surface material deposition. However, if we want to analyze sculptural coatings, these standard models do not allow it precisely.

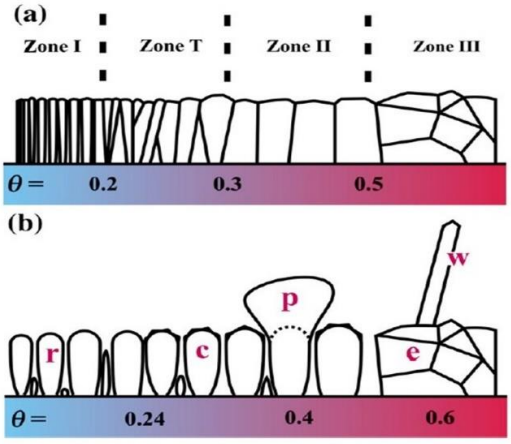

Figure 12. a) Structure zone model for thin films deposited by physical vapor deposition in the normal direction. The x-axis shows the ratio of the evaporation temperature Ts to the melting temperature Tm of the material ($\theta = Ts/Tm$), b) Corresponding schematic for layers deposited by glancing angle deposition with continuous substrate rotation, showing rods (r), columns (c), protrusions (p), equiaxed grains (e), and whiskers (w). [63]

In the case of sculptural coatings, i.e., layers deposited on a substrate that is tilted at a glanced angle (often $\alpha > 80$ degrees), the structural zone model looks slightly different from the standard case (see Figure 12). This figure shows a structural model of the zones when the coating is deposited on the substrate at a certain angle and a constant substrate rotation. Structures with various geometric shapes are shown: rods (r), columns (c), protrusions (p), equiaxed grains (e), and whiskers (w). The lower axis shows the ratio of the evaporation temperature Ts to the melting temperature Tm of the material (θ = Ts/Tm). At low evaporation temperatures, the internal structure of the coatings deposited at the angle of evaporation consists of rod-shaped elements. Those rods have a high height to width ratio. Increasing the evaporation temperature when $\theta > 0.24$ increases the surface diffusion, which results in slightly wider rods, in this case, columns. As the temperature is increased further, at $\theta > 0.35$, various protrusions begin to dominate, forming above the mean level of the coating. If the temperature is so high as $\theta > 0.5$, the layer will consist of homogeneous grains. Long and thin rods may be formed above the mean level of the coating, similar to filaments called whiskers. [63]

Most research is related to sculptural films, which were fabricated at low temperatures. At low (room) temperatures, there is no significant surface diffusion, and there is an opportunity to form structures that enable various geometric shapes.

Coatings formed by oblique angle deposition are currently receiving a lot of attention and are being applied in many areas. Porous coatings formed with this technology are used in the production of solar cells, electronic devices, where electrically conductive but light-transmitting coatings are required. Due to their porosity, optical and electrical properties, OAD coatings are used to manufacture sensors, biosensors, or optical elements. [64]

Optical (laser) and electron beam lithography currently dominate in the formation of more complex 3D structures in thin layers. One of the main disadvantages of these methods is that these technologies are very expensive. The processes take a long time and are realized only in materials that can be etched. An alternative to creating these three-dimensional structures is coatings fabricated by OAD methods. It is superior to the methods listed above by having the capability to grow three-dimensional structures instead of etching them (*bottom-up* instead of *top-down*). During the deposition process, by choosing the right deposition angle, rotation angles, and the frequency of rotation around the substrate surface, it is possible to form very complex three-dimensional structures - spirals perpendicular to the substrate, screw-shaped

structures, etc. This technology takes advantage over lithography not only in that the process is fast, applicable for big areas (from mm to tens of cm) but also that structures can be formed from a wide variety of materials from which standard thin films are formed by evaporation or sputtering techniques. [65]

1.3.1 Serial bi-deposition method

Ever since the earliest studies of oblique deposition, it has been known that the tilted columnar microstructure of obliquely deposited films generates a corresponding optical anisotropy, where film properties depend on the geometrical shape and the orientation between the microstructure and the polarized electromagnetic radiation direction. While the column material in GLAD films is generally isotropic, an anisotropic optical response is created when shaped into an elongated, asymmetric columnar structure. Light propagation through such a film exhibits polarization-sensitive properties atypical of isotropic materials, often exploited in optical devices such as polarizers and waveplates. Optical anisotropy is typical in the natural world, with the birefringent and double refractive properties of quartz and calcite being classic examples. In these natural examples, the anisotropy is intrinsic to the material, typically created by the crystal structure. In GLAD films, however, the anisotropy is a consequence of the structure and not of the material itself, and the induced anisotropy is thus frequently termed form birefringence.

In Figure 13, a structure made by OAD with a constant substrate position (a and b) with an elliptical shape is compared to the structure fabricated as the substrate is constantly rotating (d and e). The constant rotation helps to form vertically orientated columns with a neat structure indicating uniaxial anisotropy (the ellipsoid of the refractive index indicates only two different values). The deposition with atoms descending from one particular direction allows to form vertical columns with an elliptical cross-section with biaxial anisotropy (the ellipsoid of the refractive index have three different values). The main disadvantage of OAD technology is that the tilted substrate without the rotation around the normal to the surface during evaporation, results in an uneven physical coating thickness. More material is evaporated on the area of the substrate closer to the evaporation source. This problem is solved by SBD (Serial Bi-Deposition) technology, where the substrate is periodically rotated 180 degrees around the surface normal.

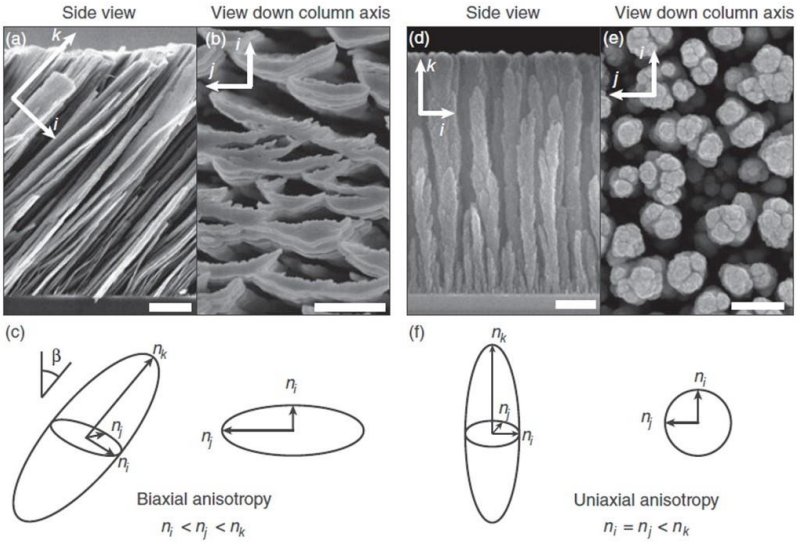

Figure 13. Thin-film internal microstructures and their corresponding refractive index ellipsoids. a, b) tilted columns made by oblique angle deposition without any movement around substrate normal, and c, d) vertically oriented columns made by oblique angle deposition with constant rotation around substrate normal. The scale bars in a) and b) are 2 μm, and in d) and e) are 200 nm. [66,67]

The internal structure of the coating formed by this methodology is chevron and indicates anisotropic optical properties (see Figure 14). Coatings formed by SBD technology have not only higher uniformity but also indicate higher optical response to electromagnetic radiation than columnar structures formed by OAD. It is known, coatings formed by oblique angle deposition have a difference of 0.04 - 0.3 in effective refractive indices between fast and slow axis. Such anisotropy is higher than most natural anisotropic substances but can be further enhanced by selecting the appropriate evaporation parameters. The layer with an internal structure consisting of such perpendicular to the surface columns, also the chevron structure has three principal refractive indexes. This phenomenon results from a different effective refractive index in the direction of column growth and in a plane perpendicular to these columns. Depending on the height, density, and evaporation parameters of the chevron structure, twice the phase retardance and effective refractive index difference can be achieved using SBD technology compared to standard evaporation at an angle of OAD [68,69].

In oblique angle deposition technology, the optical response is greatly influenced by the evaporation angle, and the maximum anisotropy is achieved

by selecting an evaporation angle close to 70 degrees. The optical response can be further increased by setting the optimal evaporation angle and chevron step (height) h (see Fig. 14).

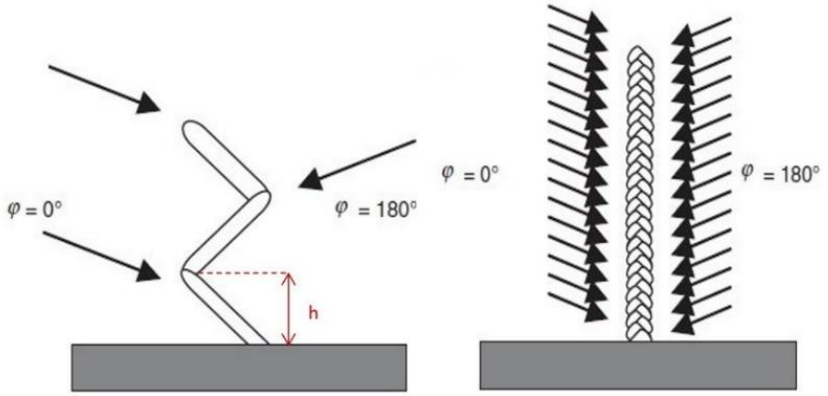

Figure 14. Structures of coatings formed by SBD technology: on the left - the height of the sub-deposit is much larger than the width of the column, on the right - the height of the sub-deposit is smaller than the width of the column (φ indicates the angle around the normal of the sample surface). [70]

Using SBD technique and selecting the proper time delay during the half-turns of the sample around its surface normal, such that the height of the column is smaller than the width, results in columns that are more similar to columns perpendicular to the substrate rather than chevron structure. Each column has an elliptical shape that causes the difference in effective refractive indices in the shadowing direction and perpendicular to it. In terms of optical properties, the shadowing direction corresponds to the fast axis of the layer due to the lower effective refractive index towards this direction. The dependency of the effective refractive index on the number of zigzags is shown in Fig 15. Here, the film, deposited at 70° angle, with a total thickness of 1 μm was divided into 1, 2, 4 and 8 identical zigzag alternations of opposite β angles (+57° and −57°), and authors derived the optical indices from the transmission spectra by the Swanepoel's method. Experimental and simulated indices n as a function of the number of zigzags are compared (in Fig. 15 on the right) for λ = 550 nm. [71]

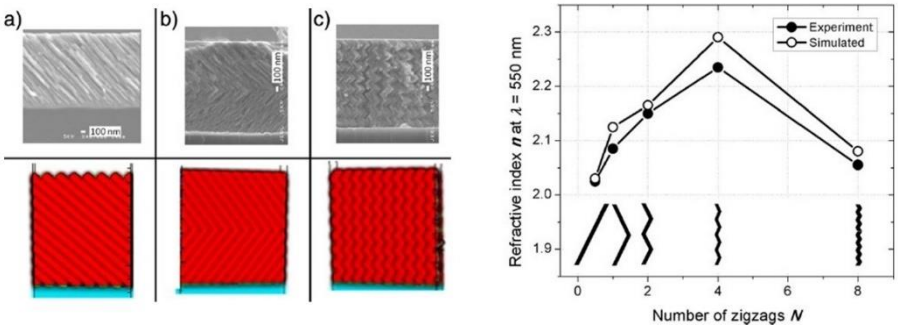

Figure 15. Cross-sectional SEM images of the WO_3 films fabricated at $\chi = 70°$ and their corresponding models below for the simulation for overall 1μm thickness: a) inclined columnar structure, b) 1 zigzag and c) 8 zigzags. On the right: Comparison between experimental and simulated refractive indices n at λ = 550 nm for zigzag structures with N = 0.5, 1, 2, 4 and 8 zigzags. [71]

As specified above, if the layer with a total thickness of 1 μm divided in 1, 2, 4, and 8 identical zigzag alternations, the highest effective refractive index was found for the case with 4 zigzags. However, if we look for the best parameters, not for the refractive index, but for maximal birefringence, the heights of the zigzag must be decreased. Other studies have shown that when the column step height h is higher than 20 nm, the layer indicates optical characteristics as coatings formed by the OAD method. If h is less than 20 nm, the birefringence increases strongly and reaches maximum values when h does not exceed 5 nm. [70]

It should be kept in mind that all these parameters, e.g., deposition angle, the height of zigzags, etc., can be just partly applied to all materials (fabricated by PVD technologies). Although, the exact values and optimal parameters should be found individually for each material. The dependence of the differences of effective refractive indexes on deposition angle for different materials can be seen in Fig. 16. The most significant values of Δn recorded for the three materials studied in detail were 0.11 for zirconium oxide bi-deposited at 70°, 0.15 for tantalum oxide bi-deposited at 70°, and 0.15 for titanium oxide at 65°. All values are at least twice as large as the values recorded for optimized tilted-columnar films of the same materials. [68]

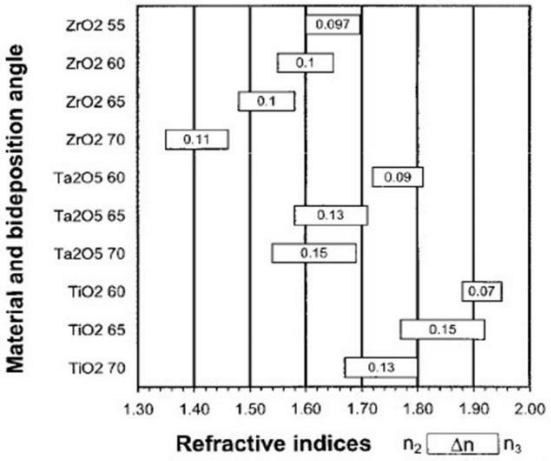

Figure 16. Values of n_2, n_3, and Δn were measured for the layers of different materials. [68]

1.4 Coatings on nanostructured surfaces

When it comes to forming multilayer coatings on periodically modulated surfaces, it is worth distinguishing two different goals: i) the formation of periodic nano- and microstructures with various geometries and ii) the conformal deposition and the primary modulation repeatability. In the first case, the aim is to control the nucleation site of the nuclei by artificially creating the desired "pattern" on the pre-coated surface.

1.4.1 Non-conformal deposition

In order to form sculptural coatings with the periodic internal structure, a pre-patterned substrate can be used. Such a substrate should consist of desired period nucleation sites which could serve as a base on which columns will grow [72], [73]. Such topography consists of periodically arranged nuclei, which are usually formed using lithographic technologies. Depending on the topography of the modulated surface and various parameters during deposition (the angle of inclination, step of rotation around surface normal), a wide range of shapes of the internal structure can be obtained. [67, 74]

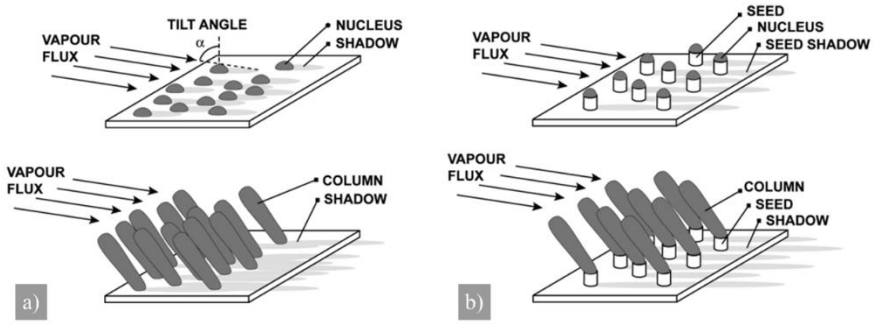

Figure 17. (a) GLAD is performed on a flat substrate, the initial flux nucleates randomly on the surface, resulting in a film with randomly distributed columns. (b) As GLAD is performed on a substrate with a pre-patterned surface, the seeds and their shadows enforce periodic nucleation and yield a periodic columnar film structure. [75]

The difference between the formation of films on a periodic and on a flat surface can be seen when examining the GLAD method (Fig. 17) [75]., The size and location of individual columns are random as the deposition is performed at a particular angle. As a result of this disorder, the competitive growth begins as the film thickness increases – slower-growing columns fall into the shadow of an adjacent column and stop growing since the depositing atoms do not reach them [76]. Thus, in order to create neatly arranged uniform columns, a "pattern" can be created on the surface, indicating the desired places for the formation of columns (see Fig.18).

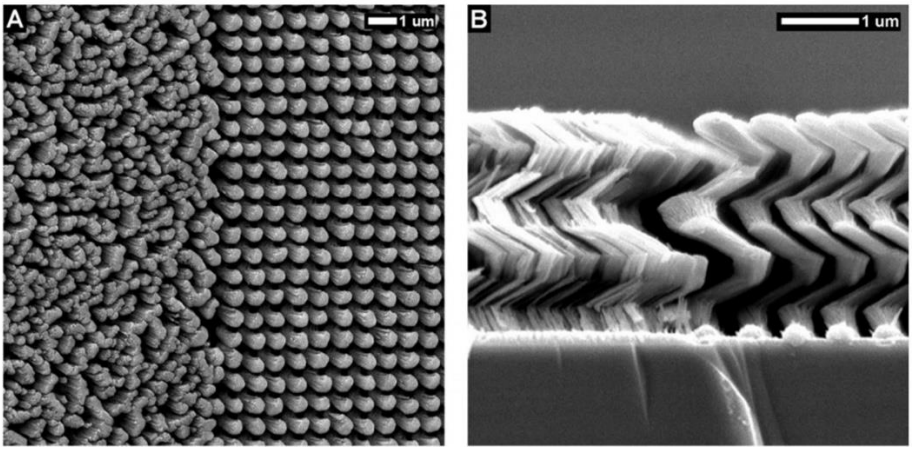

Figure 18. (a) Top- and (b) cross-sectional images comparing non-periodic and periodic GLAD silicon film growth on silicon substrates at a deposition angle of 84. [75]

Such periodically structured GLAD films are much more uniform than randomly nucleated GLAD films with nearly no column diameter variation parallel to the substrate, less column broadening as the film grows, and no column competition or extinction. The size, shape, and distance between the nucleation sites are essential parameters that determine the geometry of the final nanostructured coating.

1.4.2 Conformal deposition

Over the last decades, the coatings community has sufficiently mastered the basic technologies of thin-film formation and came up with a vast number of their variations. The numerous scientific works and books dedicated to the description of these technologies were created [77, 78] and the same amount of literature on the products created by these technologies [76–80]. However, this literature focuses on the possibilities and achievements of modern methods of coating production on flat surfaces. With the development of etching and lithography technologies, the idea of coating periodically modulated surfaces has attracted attention. As this is a relatively new branch of coating methods employing standard technologies, there are still many unsolved issues in this field.

One of the desirable capabilities is to cover the coating on a structured surface by repeating the geometry of the original surface. The form of modulation can be various on a micro- or nano-scale, such as rectangular or sinusoidal gratings. Experimental attempts to uniformly coat modified surfaces have recently emerged by J. Oliver group [81,82]. They experimented with different deposition techniques on the grating of different modulation depths, but the results revealed the main emerging problems: flattening of the initial modulation and formation of cracks due to modulation.

It has been shown that the internal structure of a multilayer coating deposited on a nanostructured surface is determined by several factors [82,83], such as the modulation depth. For comparison, deposited multilayer coatings were demonstrated on two gratings of different modulation depths (180 nm and 350 nm). In the first case, the smoothening of the initial modulation is visible with an increasing number of deposited layers (Fig. 19). The smoothing of the modulation can be explained by each feature of the grating growing along with the deposited film, and it will grow in a manner as a coated defect [84]. There is a competitive growth between the neighboring protruding points, significantly reducing the initial modulation after several deposited layers.

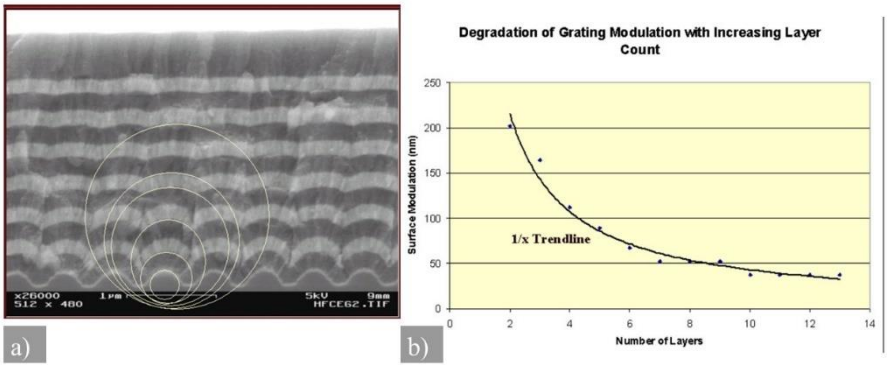

Figure 19. a) SEM image of the coating deposited on the grating with a modulation depth of ~180 nm; b) the dependency of modulation depth on the number of deposited layers. [82]

In the case of high modulation, another problem arises - the formation of cracks. The accumulating material on the neighboring grooves restricts the incoming flux, which results in a shading effect - separate columns are formed on each grating line. As a result – the modulation practically disappears after several deposited layers.

Another critical factor determining the internal geometry of the structured coating is the choice of PVD technology. Different technologies can produce layers with various characteristics, depending on depositing atoms' energies. In the case of evaporation, the energies are low, so the diffusion of surface particles is limited and does not allow filling empty spaces what causes relatively porous layer formation. Therefore, it can be assumed that as a result of the sputtering technology, where much more energetic particles are depositing, the denser and more conformal layer can be formed. In Fig. 20, some works from J. Oliver group are summarized. In Fig.20 a), multilayer interference coating is deposited on diffraction grating surface (period around 600nm) by electron beam evaporation technique. Such coating was planarized within eight layers. The use of a collimated IBS process makes it possible to deposit a similar number of layers on an identical surface with a much higher degree of conformal repeatability. The SEM image in Fig. 20 b) results from a deposition without oscillation of the substrate, showing greater deposited thickness in the minima of the grating profile and leading to sharper peaks in the maxima. The grating in Fig. 20 c) appears to have relatively sharp peaks also when ±26° substrate oscillations are employed. The same sharp peaks appear in Fig.20 d) when honeycomb filtration of depositing atoms was used.

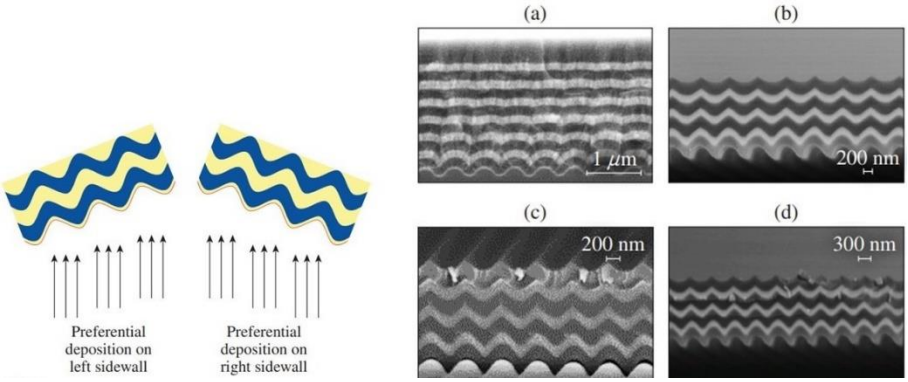

Figure 20. Scanning electron micrographs of multilayer interference coatings deposited sinusoidal diffraction-grating surfaces. The coating deposited by (a) electron-beam evaporation, (b) the IBS, (c) the IBS with the addition of an aluminum honeycomb to improve vapor flux collimation, (d) ±26° substrate oscillation (as shown in the schematic representation on the left). [82]

Thus, in order to evenly replicate the initial modulation of the substrate, similar problems emerge during both the evaporation and sputtering technologies – the modulation gradually disappears as the coating thickness increases. In the case of deeper modulation, the appearance of cracks is also observed.

1.4.3 Ion-assisted conformal deposition

The autocloning can be an ideal technique for the deposition of conformal layers on modulated surfaces. Frequently, the autocloning term can be found in literature, which means that the growing structure repeats itself. Actually, the grow/etch method is employed for implementing this technique, for example, electron-beam evaporation with high energy ion-assisted deposition (IAD). Authors use this technology to conformally repeat the modulated substrate as the multilayer coating is deposited on top. This technology was proposed by Kawakami group as a perspective way to form photonic crystals from dialectical materials [60]. However, it is a very sensitive and high precision-requiring method. First of all, the etching must be thoroughly investigated to control the shape of the surface features. Despite the difficult procedure, autocloning is used for various element fabrication, e.g., space-variant optical elements [85,86], spectral filters [87,88], omni-directional [89], high-reflection mirrors [88], etc.

The autocloning process can involve thin-film deposition, etching by energetic ion flux, and additional material deposition. In this way, the primary surface shape keeps stationary geometry when films are formed. However, in the beginning, the adjusting layer must be deposited between the modulated substrate and the multilayer coating. The coating will repeat the shape of the surface of the adjusting layer. The group from Taiwan has analyzed the influence of the various parameters on autocloning, including the depths of the modulation, the ion-beam voltage, and the ion-etching time [90,91]. The primary grating was made in a silicon wafer by electron beam lithography, and then the adjusting layer was fabricated on top of it made from SiO_2 material.

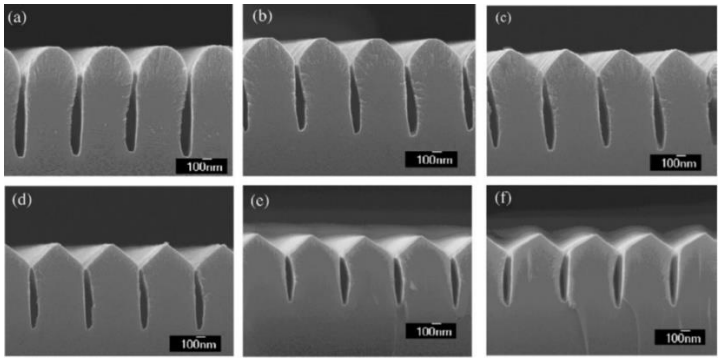

Figure 21. The change of the grating lines with adjusting layer shape after different ion-etching times (a) 0 min, (b) 20 min, (c) 40 min, (d) 60 min, (e) 80 min, and (f) 100 min.

The shape of the adjusting layer is changed by ion-beam etching and can be formed closer to a desirable zigzag structure. Ion-beam etching can also be used to modify the slope of the corrugation by controlling the ion etching time (see Fig.21 and Fig.22). Also, the quality of the slopes depends on ions energy – the lower the ion-beam voltage, the more unstable the ion beam flux, and the higher the ion-beam voltage, the more absorption the film would have. Authors have shown the structure shape dependency on the ion-beam voltage, which was controlled between 300 V and 600 V. In the case of 300 V, the ion-beam voltage was too low to provide enough energy for the ion beam to etch the structured film. In the case of maximum voltage, ridges of the adjusting layers eroded, and the surface became plainer. So, 400 V was shown as an optimal value for the ion beam, which had enough energy to etch the film without distortions.

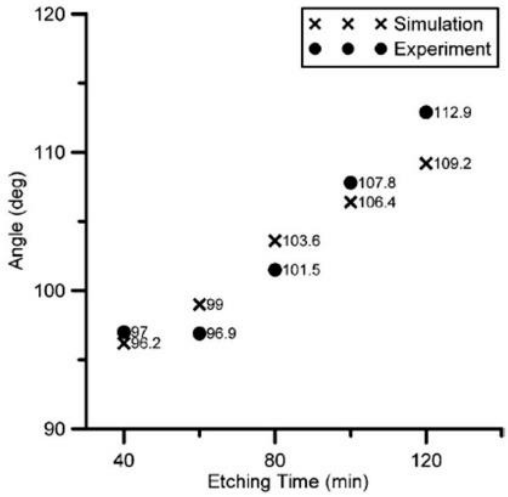

Figure 22. The dependency of the angle of the individual grating line top of adjusting layers on etching time (experiments together with the simulated results) [90].

After optimal parameter selection, the authors fabricated the complete coating consisted of 17 alternating Ta_2O_5/SiO_2 layers. Figure 23 shows a cross-section of the fabricated structure. The angle of the corrugation slope was about 102°, about the same as the adjusting layer. The results show that the periodic surface corrugation was very well preserved even after the deposition of the multilayered structures [90].

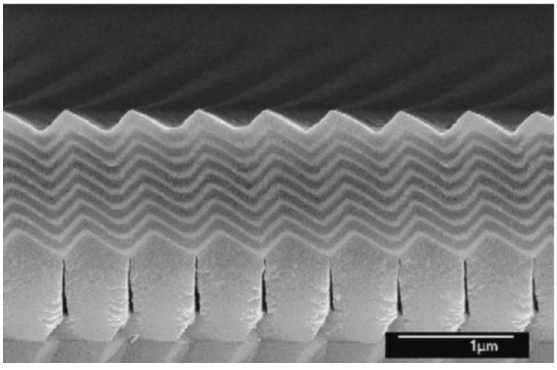

Figure 23. Cross-sectional SEM image of the Ta_2O_5/SiO_2 multilayer deposited on the grating surface with adjusting layer [90]

By carefully selecting deposition parameters, autocloning method allows the precision photonic crystals fabrication simply by changing the substrate periodicity and the structure of the stacking materials.

2 ANALYSIS AND EXPERIMENTAL SET-UPS

2.1 Determination of optical properties

2.1.1 Spectrophotometric measurements

Spectroscopic measurements were performed by spectrophotometer Photon RT (Essent Optics, Belarus). It was employed to measure the transmission and reflection of linearly polarized light. For anisotropic coatings the measurements were performed at 0° incident angle in two perpendicular polarizations/directions: F polarization – fast axis, which is aligned with the shadowing plane, S polarization – slow axis.

In the case of coatings on gratings-substrate, spectra were generated from -30° to +30° incident angles for standard S and P polarizations. Perpendicular (S) polarization is the polarization where the electric field is perpendicular to the plane of light incidence, while parallel (P) polarization is the polarization where the electric field is parallel to the plane of light incidence. During all measurements S polarization was parallel to grating stripes, P – perpendicular.

2.1.2 Ellipsometric measurements

Ellipsometric measurements were performed by spectroscopic ellipsometer (RC2, J.A. Woollam Co, Inc.). The dispersions of phase retardance measurements in all deposited anisotropic films were performed in transmission mode at 0° incident angle.

2.1.3 Laser-induced damage threshold measurements

Two different set-ups were used for the determination of laser-induced damage threshold (LIDT) of anisotropic coatings. Both of them were operated according to the 1-on-1 method described in ISO standard (ISO 21254:2011 [92]).

The basic measurement system equipped with the third harmonics (pulse duration 3.1 ns) Nd:YAG laser (NL 120 model Ekspla) was used only for comparative measurements. The wavelength of 355 nm and a beam diameter of 60 μm was used.

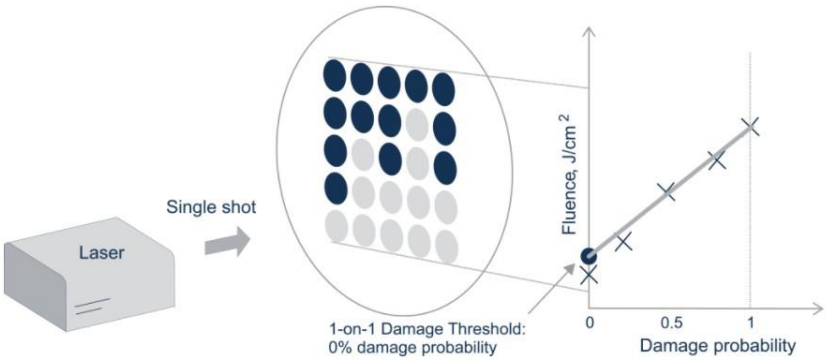

Figure 24. The schematic illustration of ISO certified 1-on-1 LIDT test method. *[93]*

The absolute values of LIDT were measured by using the third harmonic of pulsed Nd:YAG InnoLas Laser: SpitLight Hybrid laser (linear polarization, pulse duration 5.4 ns). The absolute value was measured according to the 1-on-1 and S-on-1 test procedures, which is in obedience to ISO 21254-2 standard. Two different diameters of the laser beam were used for testing: 220 μm, as specified in ISO standards, and a microfocus approach with a focused beam diameter of 60 μm were chosen in order to separate damages on local defects from intrinsic resistance of investigated surfaces. The final evaluation of LIDT consisted of online scattered light damage detection and offline inspection of damage sites using Nomarski microscopy.

2.2 Determination of structural properties

2.2.1 Atomic force microscopy

Atomic force microscopy (AFM) is one of the most widely used types of scanning probe microscopy. The principle of operation of this microscope is based on the interaction of the probe tip with the atoms on the surface of the analyzed sample. When scanning a sample and maintaining a constant distance between the probe and the surface, the probe cantilever bends up or down, depending on whether there is a peak or valley on the surface. The curvature of the cantilever is detected using a laser (wavelength of 650 nm) which is directed to the probe. The laser beam is reflected at a certain angle, which changes with the probe movements, and enters the four-section photodetector. Depending on the distribution of laser intensity in four

segments, the surface height distribution is recorded, and a three-dimensional image of the morphology can be further analyzed. [94]

The surface roughness of the anisotropic coatings and the surface morphology of corrugated samples were measured using an atomic force microscope Dimension Edge of Bruker. Measurements were accomplished in tapping (dynamic) mode and in ambient conditions, using diamond-coated silicon tips with tip radius < 10 nm.

2.2.2 Scanning electron microscopy

A scanning electron microscope (SEM) was used to produce the top view and cross-sectional images of the anisotropic coatings and layers on corrugated samples. After the coating process, samples were fractured and deposited with 20 nm of Cr layer by magnetron sputtering to avoid charging effect. The morphology of the samples was characterized using SEM workstation Helios Nanolab 650 (USA). The imaging of nanostructure was carried out under an accelerating voltage of 3 kV.

2.2.3 X-Ray photoelectron spectroscopy

X-Ray photoelectron spectroscopy (XPS) measurements were made by Thermo Scientific ESCALAB 250Xi spectrometer and monochromatized Al Kα radiation (hν=1486.6 eV) as the excitation source. Base pressure in the analytical chamber was greater then 2.7 x 10^{-7} Pa. The energy scale of the system was calibrated according to Au 4f7/2, Ag 3d5/2 and Cu 2p3/2 peaks position. A charge neutralizer was used during the analysis of all samples. Relative atomic concentrations calculations were performed using original ESCALAB 250Xi Avantage software and relevant sensitivity factors.

2.3 Sample preparation

An electron beam evaporation technique was used to form all anisotropic thin films. Coating deposited on Fused silica (FS) substrates with a diameter of 24,5 mm were used for measurements by spectrophotometer, XPS, AFM, and LIDT. Si wafers were used as substrates for structural analysis by SEM. All the processes were executed in Sidrabe (Latvia) vacuum chamber. During the process, a crystal quartz monitor was used to control the growth rate and maintained at 3 Å/s. Depositions were started in a vacuum chamber at the pressure of 1.5×10^{-5} mbar, at room temperature. During the evaporation

process, 2 sccm of oxygen gas flow rate was used (which corresponds to partial pressure in the chamber – $1.5 \cdot 10^{-4}$ mbar) to ensure the oxidation of evaporated silica (or alumina) material.

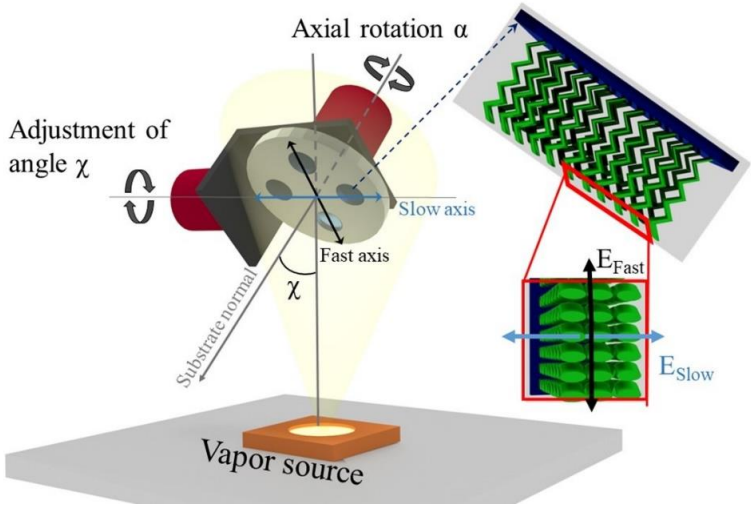

Figure 25. The principal scheme of oblique angle deposition with two-step motors: χ indicates the angle between the vapor flux and the normal of the substrate, α indicates axial rotation of the substrate.

A birefringent layer was obtained by using one particular oblique angle deposition (OAD) method – serial bi-deposition (SBD) [68]. During this process, the substrate was set at oblique angle χ and rotated in half-turns (axial rotation α) around the surface normal with constant time delays (see Figure 25). The proper time between rotation was selected to form structures, similar to chevrons, with 1 – 2 nm thickness sub-deposits.

A dense silica layer was manufactured in the same vacuum chamber with identical deposition conditions as birefringent layers but with the angle χ set at 0 angle. Moreover, the constant axial rotation α was used to reach high thickness uniformity. In this manner, the dense homogeneous layer was formed.

The method mentioned above is eligible for all materials which can be evaporated for thin-film production, e.g., metals, metals oxides, etc. Therefore, the full-scale investigation was accomplished with three eligible materials-candidates for laser applications, particularly UV spectral zone – LaF_3, Al_2O_3, and SiO_2. All these materials have low absorption for the wavelength of 355 nm due to their wide bandgaps (9.4 eV [95], 7.0 eV [96] and 8.9 eV [97], respectively) and are widely used in optical coatings for UV spectral region.

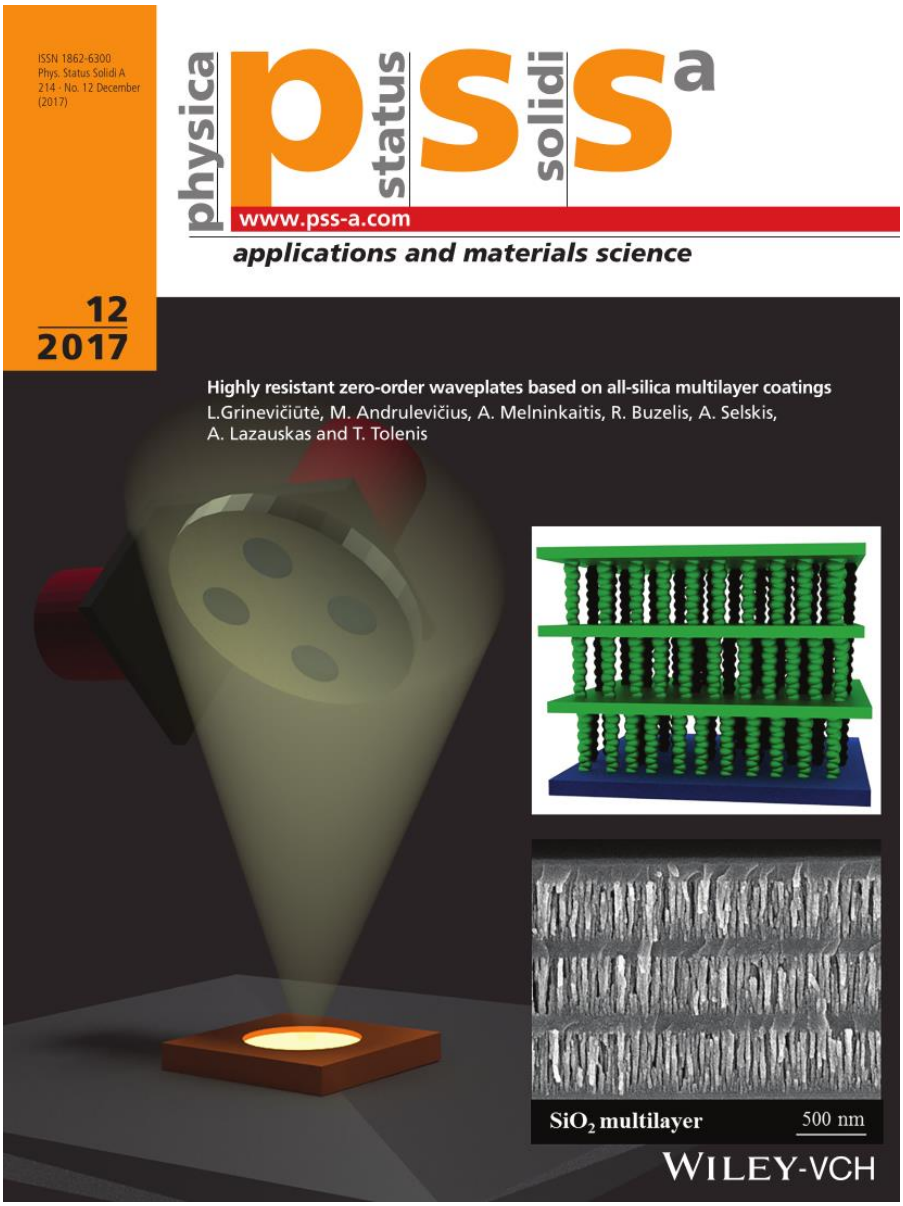

BACK COVER:

Lina Grinevičiūtė, Mindaugas Andrulevičius, Andrius Melninkaitis, Rytis Buzelis, Algirdas Selskis, Algirdas Lazauskas, Tomas Tolenis, "*Highly Resistant Zero-Order Waveplates Based on All-Silica Multilayer Coatings"* (Phys. Status Solidi A 12/2017)

RESULTS

Due to the complex nature of both the research and the implementation of different approaches to the control of the nanostructure of the coating, it was decided to divide the results into two sections: **anisotropic nanostructured coatings**, and **coatings on corrugated surfaces**.

3 ANISOTROPIC NANOSTRUCTURED COATINGS

A series of experiments were performed in order to develop glancing angle deposition technology for the low loss and high robustness of laser radiation coatings. Firstly, three different materials (SiO_2, Al_2O_3, and LaF_3) were selected as primary candidates for forming anisotropic UV coatings. The second investigation involved detailed analysis of SiO_2: samples were coated using the SBD method at the χ angles of 66°, 70°, 72°, 74°, 76°, 78°, 80°, and 84° in order to select the layer with the highest optical anisotropy. Later, various 2-layer and 6-layer structures were fabricated and analyzed in detail. The investigation of optical and structural properties was performed for single- and multi-layer silica in order to determine optimal deposition parameters for achieving the highest optical anisotropy within the film.

3.1 The analysis of single layers of different materials

The investigation of optical and structural properties was performed for single layers made of LaF_3, Al_2O_3, and SiO_2 in order to determine the depositional conditions necessary for low-loss waveplates with high optical resistivity. Dispersions of phase delay difference between two perpendicular polarizations – namely on the shadowing plane (the fast axis) and perpendicular to it (the slow axis) – were measured by a spectrophotometric ellipsometer. The dispersions of phase retardance, normalized to an individual film thickness, for LaF_3, Al_2O_3, and SiO_2 nanostructured anisotropic layers are presented in Fig. 26 a). LaF_3 and Al_2O_3 columnar thin films exhibit similar phase retardances of 0.043° and 0.042°/nm, respectively, at a wavelength of 355 nm for the one-nanometer physical thickness of the layer. An SiO_2 film of the same physical thickness indicates slightly smaller retardance – 0.038°/nm.

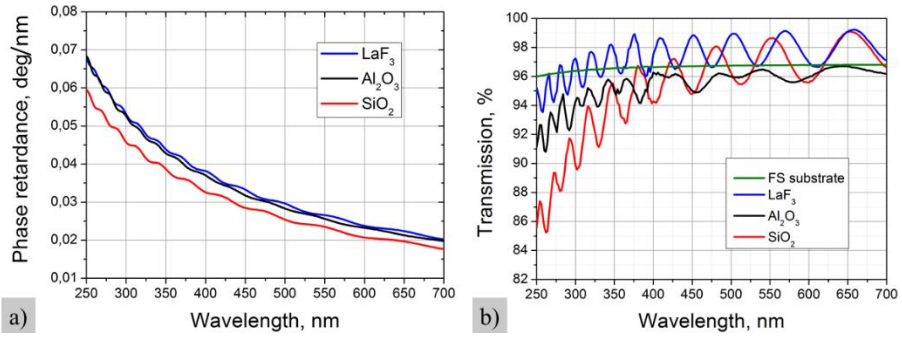

Figure 26. The dispersions of a) phase retardance and b) transmission spectra of LaF_3 (blue line), Al_2O_3 (black line), and SiO_2 (red line) single layer anisotropic thin films for linear polarization, oriented parallel to the fast axis.

For comparison, natural crystal quartz has a birefringence in the range of 0.01 at a wavelength of 355 nm [98]. Such a difference of refractive indexes in perpendicular directions would result in a phase retardance of 0.01°/nm. The deposited nanostructure layers exhibited significant differences in phase delay. According to these results, all three materials can be considered for the formation of λ/4 waveplates by depositing 2.09 μm, 2.14 μm, and 2.37 μm thickness films of LaF_3, Al_2O_3, and SiO_2, respectively. Furthermore, analysis of optical transmission was performed by measuring all three experimental coatings at 1.5 μm thickness. Transmission spectra are shown in Fig. 26 b), where the reflection from the backside of the fused silica substrate was neglected. The solid green line shows the modeled transmission of the bare fused silica substrate with a refractive index of 1.48 at a wavelength of 355 nm (reflection from one side is also neglected here). The OptiLayer program was used to model transmission and determine the effective refractive indexes of single anisotropic layers deposited at an oblique angle of 70°. Modelling results indicate that the effective refractive indexes for LaF_3 are 1.364 in the fast axis plane and 1.321 perpendicular to it. For SiO_2, these indexes were 1.211 and 1.231, respectively. It is already known that materials with higher bulk refractive indexes indicate more significant differences in phase delay in columnar structures, as was also demonstrated experimentally by Hodgkinson [68]. The transmission value of the single-layer and the substrate system both increase when the film's refractive index is lower than the index of the substrate, and there are no optical losses in the film itself [99]. The spectrophotometric measurements show that only the transmission of the LaF_3 film is at the same level as the bare substrate, which also has no optical losses

in the UV spectral range. Despite the relatively low effective refractive index, the transmission of the silica layer is lower than the transmission of the substrate, indicating optical losses throughout all of the spectral regions measured. The difference between substrate and alumina transmission with varying levels of maximal and minimal interference indicate optical losses and the inhomogeneity of the effective refractive index in alumina thin film. Therefore, efforts to characterize the optical properties of this material were not effective.

The next step was to investigate the chemical compositions of the materials deposited. Deviations from ideal stoichiometry can induce absorption and inhomogeneity in thin films. Therefore, X-ray photoelectron spectroscopy (XPS) measurements were used to determine the elemental compositions and possible chemical bonds of all deposited layers. The atomic concentrations of the films analyzed are shown in Table 1.

Table 1. The atomic concentrations of SiO_2, Al_2O_3, and LaF_3 nanostructured thin films, obtained from XPS measurements.

Sample	Atomic concentration				
	Si (%)	Al (%)	La (%)	O (%)	F (%)
Silica	38.6	–	–	61.4	–
Alumina	–	41.1	–	58.9	–
Lanthanum fluoride	–	–	33.2	8.2	58.6

A small amount of carbon contamination on the film surfaces was detected for all experimental samples (2.2 %, 4.8 %, and 2.6 % atomic concentrations for SiO_2, Al_2O_3, and LaF_3, respectively) because of the exposure to the atmosphere after the deposition processes. Therefore, during stoichiometry determination, it was neglected and is not included in Table 1. The silica film XPS spectra analysis showed the composition of Si and O elements with atomic concentrations equal to 38.6% and 61.4 %, respectively. This is similar to the theoretical stoichiometric ratio of SiO_2, which is equal to 33.3 % and 66.6 % for Si and O, respectively. However, the measured and theoretical stoichiometry discrepancy can occur

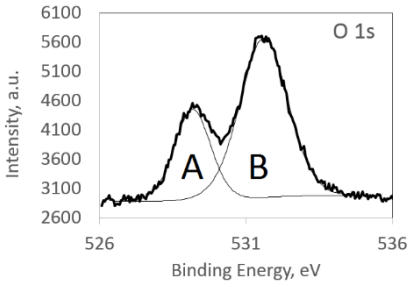

Figure 27. High-resolution O 1s spectrum for LaF_3 film.

due to the minor inclusions of SiO material or the errors of the measurement procedure. The composition in alumina film consisted 41.1 % of Al and 58.9 % of O elements. Measured ratio also agrees with its theoretical value for Al_2O_3, where Al:O is 40 % and 60 %, respectively. The analysis of lanthanum fluoride film reveals an unexpected result - additional lanthanum composition with oxygen. Fitting procedure results (Fig. 27) in O 1s region for LaF_3 film demonstrated that a significant part of the oxygen bounds (Fig. 27., "B" peak) could be attributed to adsorbed atmospheric contaminants since its position at 531.6 eV (FWHM = 2.0 eV) suggest typical adsorbed atmospheric contaminants (O_2, OH, O-C). On the other hand, the position of "A" peak at 529.2 eV (FWHM = 1.5 eV) indicates oxygen bonds to lanthanum. In the latter analysis, the influence of oxygen in LaF_3 film to optical parameters will be explained in more detail.

Analysis of thin nanostructured layers cross-sections indicates that internal structures consist of vertical columns with different features depending on each material (see Figure 28). Characteristic feature sizes of relatively densely packed columns (width ~40 nm) remain constant only during the LaF_3 growth. SiO_2 and Al_2O_3 layers consist of a columnar structure with gradually increasing diameters of individual columns as the film grows. At the beginning of the film growth, the average widths of the columns were equal to 29 nm for silica and 20 nm for alumina. When film thicknesses reached 400 nm, the coalescence of columns has been started, and the width of the individual element extended to 31 nm and 88 nm for SiO_2 and Al_2O_3, respectively. Near the top of the layer (at 1.5 μm thickness), the width of the structural element increases to 70 nm for silica and 120 nm for alumina.

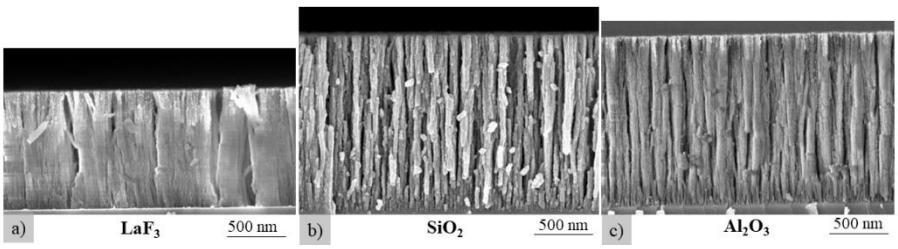

Figure 28. SEM images of cross-sections of nanostructured a) LaF_3, b) SiO_2, and c) Al_2O_3 thin layers, deposited by serial bi-deposition method at 70° angle.

Both, the expansion and later the coalescence of such columns could lead to inhomogeneity of film's refractive index and light scattering. This

phenomenon also was shown by another scientific group who conclude that photometric measurements of silica OAD films indicated poor performance, because of optical scattering, with losses of 10% to 15% [100].

Optical resistivity to laser radiation was analyzed by measuring the laser-induced damage threshold (LIDT) for nano-sculptured films of each material deposited on fused silica substrates. Comparative laser damage testing measurements were performed in the single-shot mode for SiO_2, Al_2O_3, and LaF_3 thin films and indicated thresholds of 6.5 a. u., 3.0 a. u., and 3.0 a. u., respectively, at the wavelength of 355 nm (see Figure 29). The silica layer exhibited the largest optical resistivity: LIDT was more than two times larger compared to lanthanum fluoride or alumina. In a pulsed nanosecond regime, the LIDT is closely related to thermal properties (thermal capacity, heat conduction, and melting point) and dielectric breakdown effects (multiphoton absorption and avalanche ionization) of materials. [101] It is known from the literature that materials with larger bandgap are less efficient absorbers (by means of multiphoton absorption) and thus are more resistant to laser damage. [102] The bandgap of bulk SiO_2 is ~9 eV, which is higher than that of Al_2O_3 (~7 eV). Pure LaF_3 material has an even higher band-gap value than silica. However, from an earlier analysis of the chemical composition, it was shown that deposited LaF_3 film consisted not only of pure LaF_3 but also contains La_2O_3, which has a bandgap value of 5.3 eV. [103] La2O3 inclusions in LaF3 film initiate defected areas with lower effective bandgap value compared with pure LaF3, thus significantly reducing LIDT values.

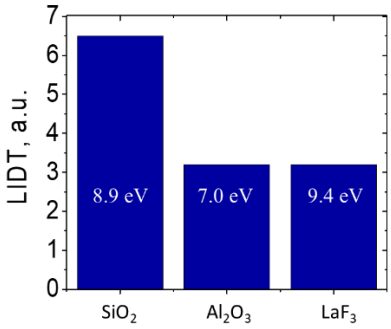

Figure 29. Laser-induced damage threshold in nanostructured SiO_2, Al_2O_3, and LaF_3 films measured at the wavelength of 355 nm.

LID threshold measurements of single-layer experimental samples indicate better optical resistance of silica thin films if compared to alumina or lanthanum fluoride. However, nanostructured silica films exhibited significant

optical losses in UV spectral range in transmittance, which must be addressed before using such waveplates in practice.

3.2 Analysis of silica single-layers

A detailed investigation of optical and structural properties has been performed for anisotropic nanostructured silica single-layers in order to determine the optimal deposition parameters for reaching the highest birefringence. SEM images have been analyzed for the nanostructured thin films with thicknesses of 250 nm, deposited at different angles. The surface filling dependency on deposition angle is presented in Figure 30. Analysis indicates the decrease of the surface filling when depositing at larger angles.

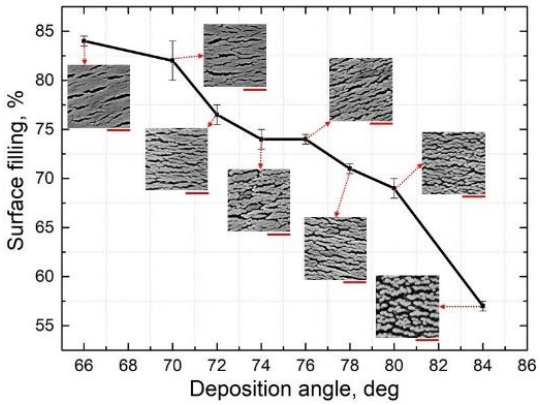

Figure 30. Surface filling dependency on deposition angle and SEM images of single layer anisotropic coatings top view, deposited at different angles by SBD method. (Red bar indicates 250 nm).

Increasing the deposition angle χ, the influence of self-shadowing becomes more prominent, leading to more porous layer formation and resulting in a lower effective refractive index of the film. As the shadowing effect dominates in one direction, such nanostructured layers indicate elliptical/oblong shape in cross-section when observing from growth direction. Optical anisotropy appears with a slow and fast axis as in natural anisotropic crystals due to oblong geometrical shape, which allows the birefringent layer formation.

Deposition at larger angles changes not only the internal structure of thin films but also optical characteristics. Transmission of light of two perpendicular linear polarizations, namely with the electric field oscillating in the shadowing plane (fast axis) and perpendicular to it (slow axis), are measured by a spectrophotometer and and phase raterdance is measured with

spectrophotmetric ellispometer. The dispersions of the refractive indices of silica thin films for fast and slow axis were modeled by using the "Optilayer" software [104] by fitting measured transmission spectra of each sample (see Figure 31). Gradually increasing the deposition angle between the vapor flux and the substrate normal reduces the effective refractive index values due to increasing self-shadowing effect, which has a major effect to films porosity in low energy deposition processes. Since the shadowing effect occurs only in one direction, the birefringence of films also depends on the deposition angle. Silica anisotropic layers exhibited the highest phase retardance of 0.032°/nm at the deposition angles of 70° and 72°. A similar tendency was reported in other scientific research conducted for sculptured films made from other materials (Ta_2O_5, WO_3, and BiO_3) [105]. As stated above, optical analysis indicates that two deposition angles, namely 70° and 72°, are the most effective for the formation of anisotropic coatings, waveplates in our case. Additionally, surface structural investigations show that thin films deposited at an angle of 70° have a higher surface filling by 5.5 %. This is preferable for multilayer elements and for gaining better environmental stability.

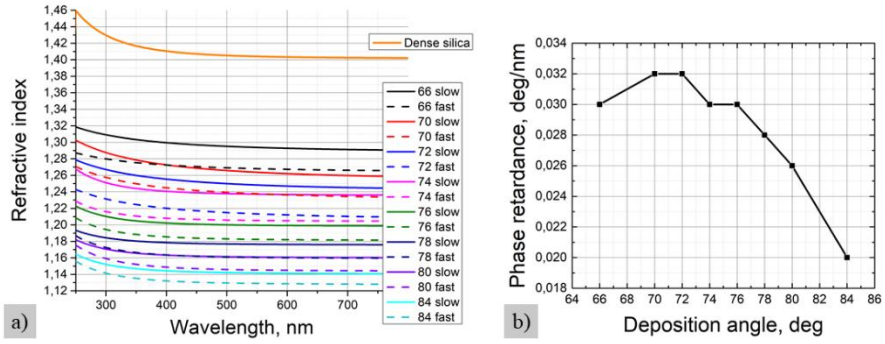

Figure 31. a) Refractive index dispersions for fast and slow axes and b) normalized phase retardance (@355 nm) of silica layers evaporated at different angles by SBD method.

For estimation of the optical anisotropy - dependence of the effective refraction index on polarization direction in nanostructured silica layers Bruggeman Efficient Media Theory (EMT) for anisotropic composites was applied. Analyzing SEM images, surface nanostructures were considered as the anisotropic inclusions in air. The anisotropy factor of the structure was estimated from the autocorrelation function described in [106].

The initial SEM image and its autocorrelation contour map together with its` cross-sections at the center in x (fast) and y (slow) directions are shown in Figure 32.

The anisotropy parameter *k* can be calculated from the ratio of the full widths at half maxima of the x and y cross-sections of the autocorrelation contour map at the central part. Such procedure was repeated for the structures made at different deposition angles in order to determine the structural anisotropy dependence on deposition angle (see Figure 33).

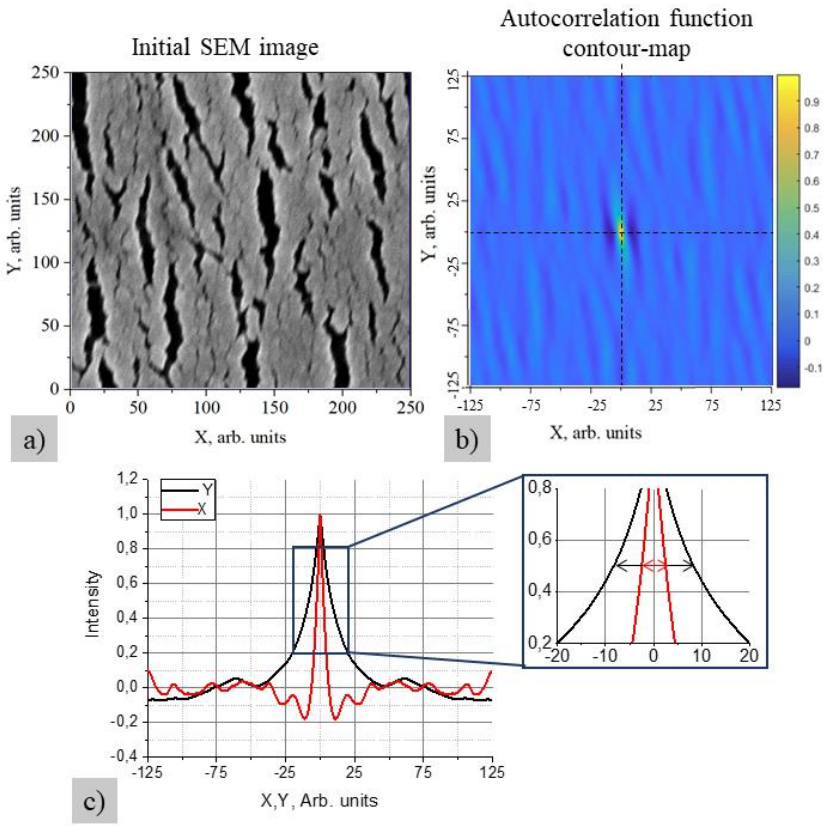

Figure 32. The steps of autocorrelation procedure: a) the initial SEM image, b) its autocorrelation function contour map, c) the cross-sections of X and Y axis of the autocorrelation contour map at the central part for determination of anisotropy *k* factor (the ratio of widths of x and y cross-sections at FWHM).

The top views of layers fabricated at various deposition angles ranging from 66° to 84° were analyzed in detail. As shown in Fig.34), the structural anisotropy *k* varies from 3.77 to 1.98 when the angle changes from 66° to 84°,

respectively, and indicates the highest value (k= 4.11) for the layer deposition angle of 70°. According to experimental results, the layer fabricated at this angle showed the highest phase retardance value and the one deposited at 72° angle. However, thin films deposited at an angle of 70° have a higher surface filling of 5.5 % what is essential for the further deposition process on such layer.

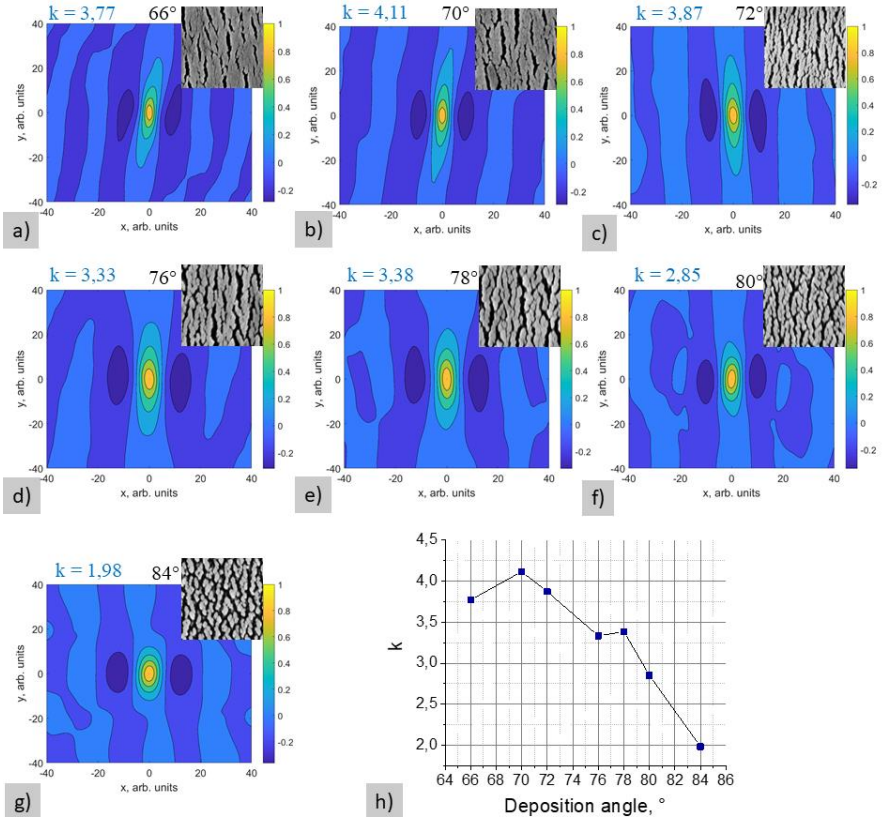

Figure 33. The evaluation of structural anisotropy of silica layers: a-g) the autocorrelation function contour maps together with initial SEM images of nanostructured films fabricated at different deposition angles, h) k factor dependence on deposition angle.

According to the accomplished results, mainly, the anisotropy *k* and the surface filling fraction *f*, the refractive index and the birefringence were evaluated theoretically. The refraction indices of anisotropic composites can be calculated using quite general Maxwell-Garnett approach, and specifically applying Bruggeman Efficient Media Theory (EMT) theory for 2D media [107]:

$$\frac{f(\varepsilon_1 - \varepsilon)}{(\varepsilon_1 + k\varepsilon)} + \frac{(1-f)(\varepsilon_2 - \varepsilon)}{(\varepsilon_2 + k\varepsilon)} = 0, \qquad (7)$$

where k is the anisotropy factor of the structure; f is the filling fraction; ε_1=1 stands for the permittivity of air with fraction $1-f$ for porous media, and ε_2 for the media with fraction f; ε is the total permittivity of the mixture.

Generally, the light of two orthogonal polarizations propagates with *k* and *1/k* (in Bruggeman formula (7) for anisotropic medium described above) through the composite. It is the implicit relation for calculating the birefringence of the composite media. The ordinary (*o*) and extraordinary (*e*), which in the dissertation are named – fast and slow axis, respectively, refraction indices follow from, $n_{o,e}=\varepsilon_{o,e}^{1/2}$, with anisotropy factors *k* and *1/k* for *o* and *e* polarizations, respectively. The calculated refractive index and the birefringence (difference between n_{slow} and n_{fast}) for different deposition angles are shown in Fig.34 a) and b).

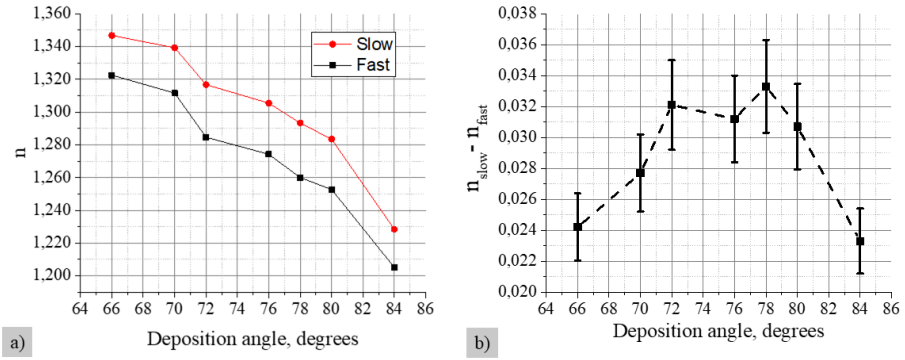

Figure 34. a) The effective refractive index and the b) difference of refractive indices of the fast and slow axis, calculated using filling fraction *f* and structural parameters *k* extracted from experimental results.

Calculated results show the dependences of the effective refractive index on the deposition angle for slow and fast axis: the refractive index decreases with increasing the angle for evaporated particles (Fig. 34 a). To calculate the birefringence, the refractive indices for the slow and fast axis were subtracted one from another. The deposition angles between 70° to 80° indicate the highest birefringence values (0.027 – 0.033) within error limits. The error was defined from the error of filling factor determination by analyzing SEM images with ImageJ software (~ 3%).

For further analysis, the deposition at 70° angle was chosen as an optimal for anisotropic layer formation due to the high optical anisotropy and comparatively high surface filling.

Due to the competitive growth between fractions in the nanostructured layer, the expansion and coalescence of columns are present during the film growth [25]. The evolution of the film surface filling and dispersions of the retardance with increasing film thickness is shown in Figure 35. The birefringence is influenced by the internal geometry and differs with the thickness of the layer. The structural inhomogeneity – the spread and bundling effect of columns, leads to optical inhomogeneity. Additionally, the increased size of the features can cause some negative side effects, such as optical scattering.

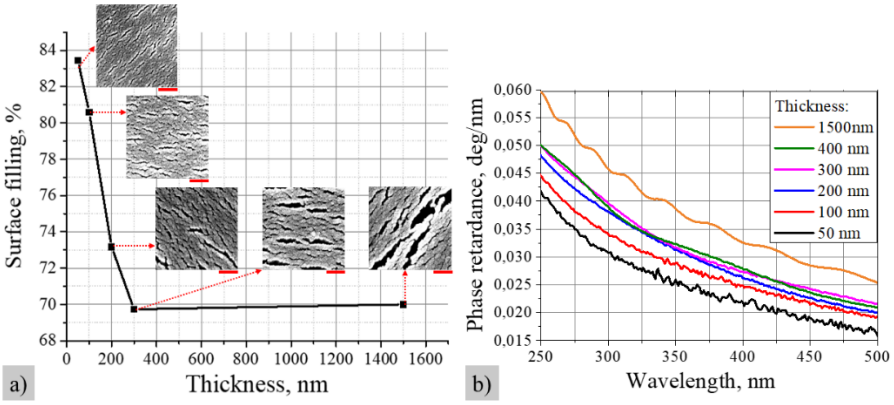

Figure 35. Surface filling dependency on a thicknesses of single layer anisotropic coating deposited at 70° angle by SBD method (together with top-view SEM images, where the red bar is set at 200 nm), and b) normalized phase retardance of layers with different thicknesses.

It was mentioned earlier that nanostructured silica films exhibited significant optical losses in UV spectral range in transmittance, which must be addressed before using such waveplates in practice (Fig.36). During the structural analysis, the spread of the features of the internal structure was noticed.

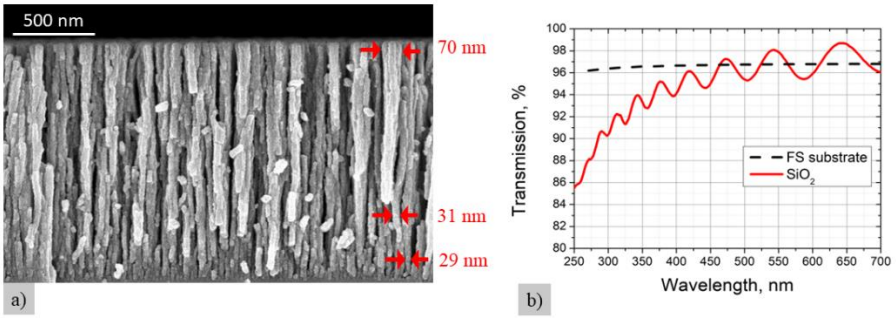

Figure 36. a) Cross-sectional SEM image of nanostructured silica layer and b) its transmission spectra.

At the beginning of layer growth, the average width of the columns was about 29 nm. When film thickness reached 400 nm, the width of the columns increased up to ~31 nm. Moreover, when film thickness reached 1.5 μm, the width of the feature becomes about 70 nm. To suspend the spread of cone-like structure, a dense SiO_2 capping layer is introduced after 400 nm of columnar film growth (see the principle scheme in Fig. 37). This capping layer serves two purposes: suppressing the bundling of columns and serving as the new flat base for the next layer with a columnar structure formation. The growth of anisotropic structure on such dense layer is continued in the same way as the growth on a substrate. The average width of the columns is kept at about 29 nm and expands only by two nanometers when film thickness reaches 400 nm.

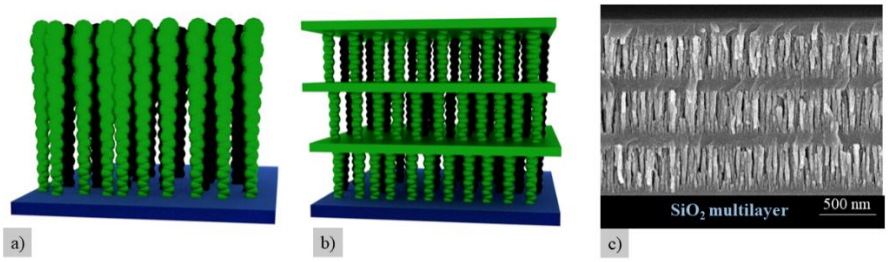

Figure 37. The schematic representation of the formation mechanism during the evolution of nanosculptured SiO_2 thin film: a) the spread and coalescence of the columns with 1.5 nm thickness sub-deposits during single layer growth, b) capping layer approach using dense interlayers. c) SEM image of deposited multilayer SiO_2 coating.

Deposition on top of such layers can be highly influenced by open pores. Structural morphology, and therefore optical characteristics, can be changed not only for the second layer but also for the first one. Open crack formation

is induced due to this SBD process and the self-shadowing effect at larger oblique angles. During low energy deposition, the surface morphology of the surface is the main factor for the formation of the secondary film.

3.3 Multi-layer analysis

Fresnel reflections between interfaces of materials with different refractive indexes are unavoidable in optical systems. Even reducing the columnar broadening in anisotropic nanostructured silica film (using fully chevronic thin-film structure [108] with, possibly, lower birefringence [109] would result in interference between the porous silica layer and the fused silica substrate. Furthermore, the final waveplate must contain at least two layers: birefringent volume for retardance and a dense layer on the top for mechanical protection. It is difficult to obtain a transparent optical element with deposited relatively thick film (~4 μm) due to intense interference oscillations. Therefore, the multilayer approach allows more freedom in varying the thickness of individual layers resulting in a broad spectral region of transmittance.

As the first step of multilayer analysis, the 2-layer structures were fabricated and investigated in detail. The first layer (the base) is deposited at optimal deposition angle – 70° with a thickness of 250 nm and is kept the same in all 2-layer coating experiments. The second layer is deposited with changed GLAD conditions: different deposition angles of incidence (χ) or different vapor flux directions (Figure 38). A second layer with a thickness of 50 nm is deposited for three samples using constant substrate rotation and setting the deposition angle at 0, 30, and 50 degrees. The second layer is deposited by the SBD method for the fourth sample with an angle of $\chi = 50$ ° and a time delay of 6 s between the half-rotations around the substrates normal is maintained.

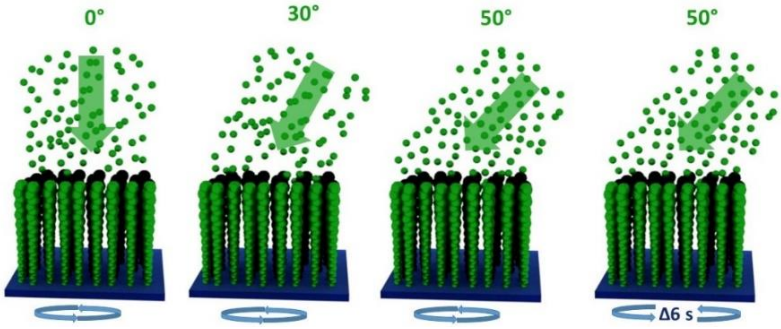

Figure 38. The schematic representation of deposition conditions to form the second (dense) layer.

The detailed SEM analysis was performed for the base layer and all 2-layer coating samples. As shown in Figure 39, the base anisotropic layer surface structure consists of open cracks. As the second layer is deposited on such base structure, some of the particles are penetrating inside the open voids and influence the optical properties of the first layer, therefore generating a transition zone. Furthermore, it is required for the dense layer to close the voids and serve as a solid base for the subsequent porous layer deposition. Depositing the secondary film at 0° and 30° closes most of the cracks (Fig. 39 b) and c)), and it can be considered as a dense layer.

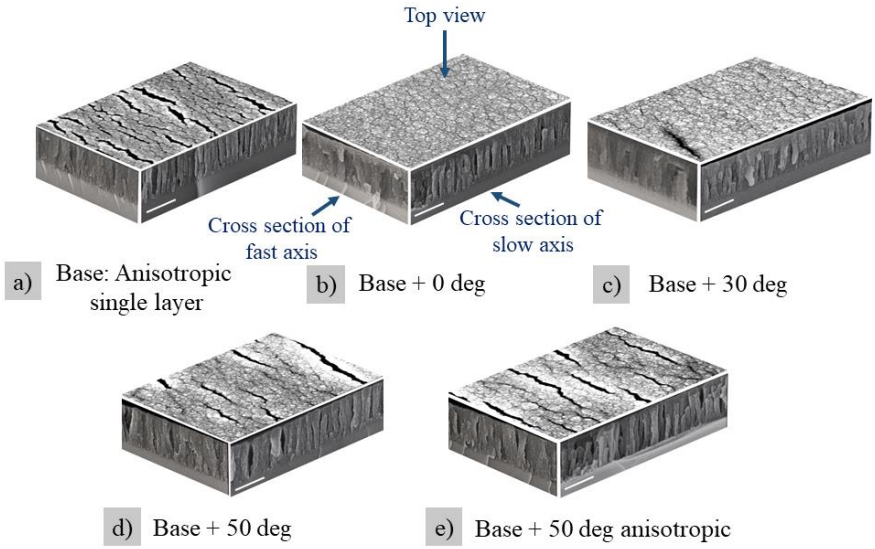

Figure 39. 3D representation of SEM images of a) single layer with 250 nm thickness, deposited at an angle of 70° and 2-layers structures with the second layer deposited at b) 0°, c) 30°, d) 50° and e) 50° anisotropic case. (Red bar is set at 250 nm).

In order to enhance the spectral response to the multilayer, consisting of nanostructured porous and dense layers, two 6-layer coatings were deposited. The anisotropic layers were the same in both designs, but the dense layers were deposited with constant rotation at different angles – 0° and 30° (see Fig. 40 a). Both coatings are measured with the spectrophotometer and the ellipsometer (see Fig. 40 b) and c), respectively) for transmittance and phase retardance analysis. The multilayer structure, which contains a dense layer deposited at a normal angle, exhibited a spectral difference in transmission of 3.9 nm (see Fig.40 b)). For the dense layer deposited at 30 ° incidence, the spectral difference extended 1.6 times to 6.2 nm, indicating a larger optical

anisotropy in the multilayer coating. Additionally, the phase retardance is also evaluated for both experimental samples (see Fig. 40 c).

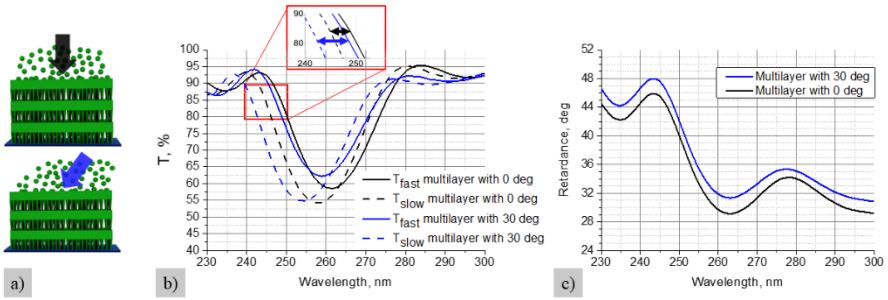

Figure 40. a) The schematic representation of deposition conditions, b) transmission spectra of fabricated multilayers for perpendicular polarizations (slow and fast axis), c) The normalized retardance of the fabricated multilayer.

Again, the multilayer, which contains dense layers deposited at 30 °, exhibits larger phase retardance values throughout all UV spectra. Since dense films, coated at both angles, are formed using constant substrate rotation, no birefringence is expected when light is irradiated at a normal angle. Therefore, phase retardance is present only due to the anisotropic layers deposited at the same conditions in both cases. The difference in optical properties can be explained by considering the larger open cracks in anisotropic films surface. Deposition at a normal angle has a lower shadowing effect comparing to deposition at an incidence of 30 °. Therefore, some part of the initial vapor flux can penetrate into the pores and condensate in the initial film, and reduce its structural anisotropic properties. In order to confirm this hypothesis, the growth of the coating was simulated and analyzed.

3.3.1 Molecular dynamics simulations

For the growth simulations of silica two-layer structures consisting of anisotropic and dense films, the interaction potential from Zhang et al. [110] is used for the classical molecular dynamics (MD) performed with LAMMPS [111], [112]. Graphics are generated with VMD [113]. The simulation is performed for a substrate area size of x = 16 nm and y = 7 nm with lateral periodic boundary conditions. The first layer simulates a SBD film (Fig. 41) under an angle of $\chi = 70$ °, where the substrate is flipped by 180 ° around its surface normal for every 1.5 nm of structure height.

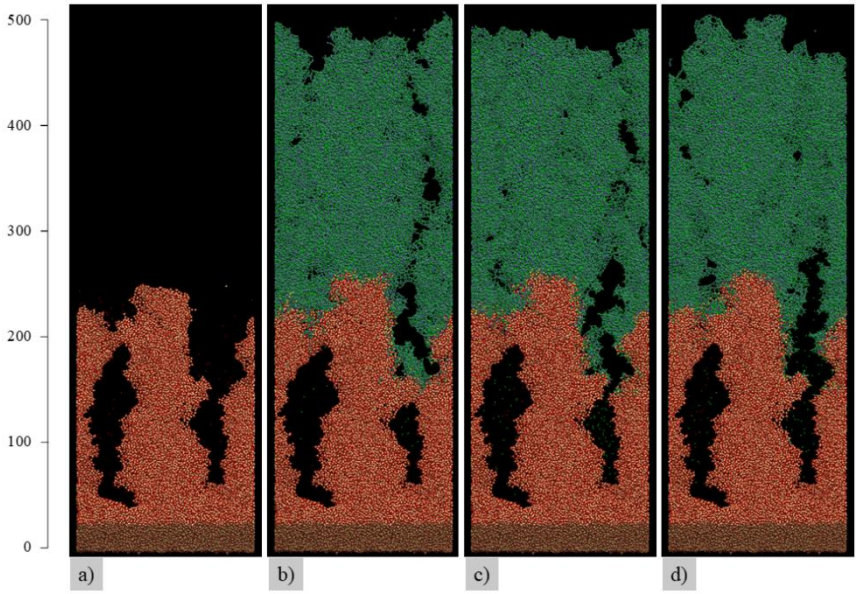

Figure 41. Side view of simulated coatings (y-axis normal to paper plane), a) the initial base layer zig-zag structure grown like SBD (red-yellow). And the 2-layer structures with the second layer in blue-green continuing the first layer with different incidence angles: b) $\chi = 0$ °, c) $\chi = 30$ °, d) $\chi = 50$ °. The height scale is given on the left in angstrom.

As deposition energy 0.3 eV is used throughout the simulation for silicon, while oxygen is deposited with no energy, i.e., it is adsorbed only in case of an attractive local potential on the surface. This method for oxygen serves as a simplified simulation of the common process of saturation in physical vapor deposition. The continuation on top of the zig-zag structure is done with comparatively dense layers, deposited with an incidence of $\chi = 0°$, 30°, and 50° during the constant rotation of the substrate. The rotating speed is 2.5 turns/nm. Therefore, these simulations represent the digital twin of the experimental coatings shown in Fig. 41 a) - d).

As can be seen from Fig. 41a a), the zig-zag layer exhibits a columnar structure. Although the simulation yields only two columns here due to the limited structure size and taking the periodic boundary into account, two major effects can already be observed. That is the beginning coalescence on the left side, while an open pore and crack are built upon the right. With the continuation in Fig. 41 b) – d), the closed pore on the left of each structure is nearly unchanged. In contrast, the open pore on the right is filled with additional material, which even leads to a closed small pore for 0°, while the

impact on the initial layer decreases with increasing deposition angle as shown in Fig. 41 c) and d). However, the second layer qualitatively changes the structure morphology, including only pores much smaller than the first layer. This is also viewed by the density profiles in the growth direction in Fig. 42.

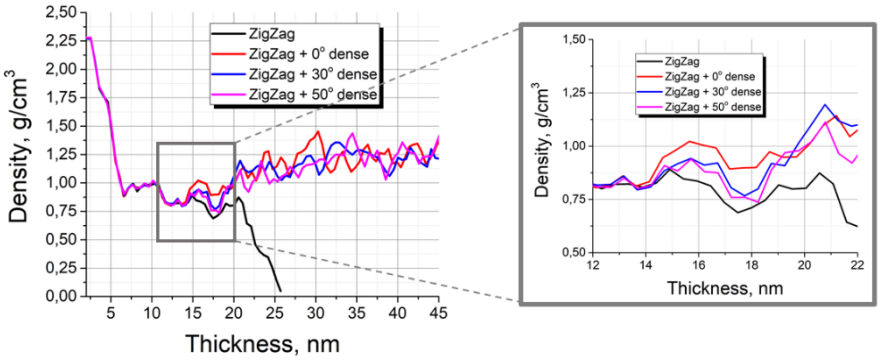

Figure 42 Density profiles of anisotropic zig-zag single layer and its continuation with dense layers deposited with constant rotation at $\chi = 0$ °, 30 ° and 50 °.

While the density does not change up to a height of about 14 nm, the range up to 19 nm for the 0 ° deposition shows a higher increase of the density than 30 ° and 50 ° due to filling of the open pores with material from the second layer. The same initial structure reduces the high fluctuation in density seen for regions above 19 nm, therefore, here the higher density can be considered significant, as also supported by the similar initial density for 30° and 50°, which is lost for 19 nm and above. For this region, the density grows by about 0.4 g/cm³, while fluctuating by a non-negligible amount on the overall growth, but with no significant difference between the second layers. Due to the structure morphology, an anisotropy for the first layer is expected and confirmed in the following by performing an anisotropic effective medium approximation analysis as described in [114].

Table 2. The anisotropic effective medium approximation analysis for the first layer, i.e., the structure height region between 7 and 20 nm, with the impact of the second layer.

	ZigZag	ZigZag + 0°	ZigZag + 30°	ZigZag + 50°
Volume distribution: material, pores	43.0%, 57.0%	46.6%, 53.4%	45.2%, 54.8%	44.8%, 55.2%
Refractive index of fast and slow axis	1.1925, 1.2080	1.2128, 1.2251	1.2055, 1.2184	1.2029, 1.2166
Δn	0.0155	0.0123	0.0129	0.0137
Normalized phase retardance @ 266nm	0.0207 °/nm	0.0167 °/nm	0.0176 °/nm	0.0185 °/nm

The results are shown in Table 2 for a bulk refractive index of 1.5 for silica (at 266 nm). The analysis of the first layer is taken for the growth height region of 7 – 20 nm. It excludes the substrate structure and upper surface region of the first layer but includes the height region impacted by the second layer. For this region, corresponding with the highest porosity, the highest birefringence for normal light incidence is observed for the solely first layer of Δn = 0.0155. Adding the second layer, the porosity decreases, leading to a raise of the value of the refractive index ellipsoid. Additionally, due to the non-directional deposition of the second layer, the birefringence decreases to 0.0123 for 0 ° and increasing again for larger deposition angles of 30 ° and 50 ° with 0.0129 and 0.0137, respectively, where the impact on the first layer is decreasing. The birefringence, i.e., the difference of the refractive indices of the slow and fast axis, mainly resembles the refractive index ellipsoid in x and y, because the ellipsoid is nearly aligned with the coordinate axes.

Deposition of dense silica thin films on top of nanostructured anisotropic layers induces inhomogeneity of optical properties. Birefringence is reduced in films with columnar structure, and, therefore, the deposition of a dense coating at angles of 0°, 30 °, and 50 ° with substrate rotation were tested.

Both, simulations and experimental results indicate that to fully exploit optical anisotropic properties of nanostructured silica thin films in multilayer coatings, the parameter of dense layer formation should be carefully selected. For example, dense layers should be deposited at a 30° angle or similar angles to induce a minor shadowing effect.

3.4 Applications

The combination of anisotropic and dense layers, or even a combination of two anisotropic layers with different optical constants, can be used for unique optical elements formation: all-silica waveplates and polarizers. Such elements can be applicable for high power applications in both: large laser systems or microsystems.

3.4.1 Zero-order wave-plates

The technological solution – the combination of porous and dense layers with different internal structures allows to create an interference coating using only one material. As it is shown in the previous section (in Figure 32 a), depending on the deposition parameters, the same layers of SiO_2 can exhibit

different effective refractive indices in a wide range (from 1.41 to 1.13). Tailoring the nanostructures for individual layers induces Fresnel reflections in multilayer coatings due to the difference in refractive indices, and therefore, various optical designs can be realized.

Simple antireflection or high-reflection optical coatings are formed by combining iterative pairs of high and low refractive index materials films with an optical thickness equal to quarter-wave or half-wave [115]. To reach the highest optical transmission of the waveplate, the great care must be intended to model the design of interference coating, consisting of dense and porous anisotropic silica layers. The dispersions of refractive indexes were characterized using "OptiLayer" program for dense silica layer and anisotropic layer for two perpendicular polarizations: fast and slow axis. For the wavelength of 355 nm the refractive index of dense SiO_2 layer is equal to 1.41, of anisotropic layer for fast and slow polarization – 1.211 and 1.231, respectively. Therefore, maintaining the evaporation structure design, dense and porous anisotropic films can be approached as high and low refractive index materials. In the case of the waveplate design, it is important to have the smallest number of layers in order to reach the highest transmission and to keep thicknesses of individual anisotropic layers less than 400 nm to avoid the coalescence of individual columns, which can cause optical scattering effect. Moreover, the orientation of the fast and slow optical axes of all anisotropic layers must be perfectly aligned with each other throughout the thickness of the coating. In this way, the coating itself can serve as a thick antireflective layer and, by keeping the sum of anisotropic layers at the proper thickness, necessary phase retardance can be achieved. The modeled design of the quarter-wavelength waveplate, where the distribution of electromagnetic field $|E|^2$ is presented along with the coating, is shown in Figure 43 a). One of the methods for obtaining higher LIDT values is the optimization of the electric field, which passes through the multilayer coating [116]. In our case, most of the intensity peaks lay on the porous silica coating, however, one peak appears on the last dense layer. This encourages us to extend future work in optimizing E-field in nano-sculptured coatings for even better LIDT results. The presented evaporation design in Fig. 43 a) was implemented, and the transmission and phase retardance dispersions are shown in Figure 43 b). The transmittance of almost 99 % was reached event the physical coating thickness is larger than 4 μm. Also, the phase retardance was accomplished to be 89 degrees, what corresponds well to standard quarter-wavelength waveplate.

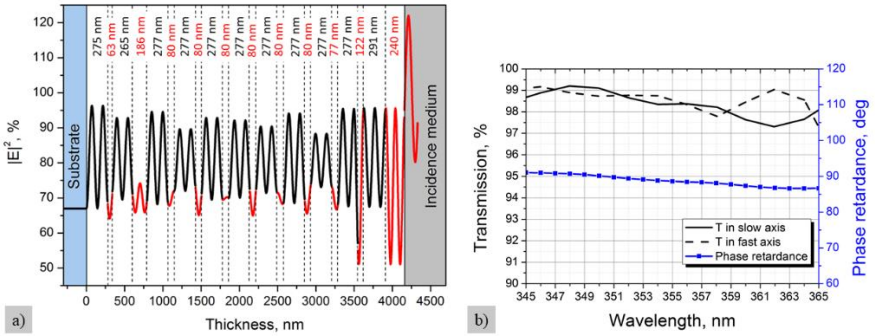

Figure 43. a) The modeled design of multilayer waveplate with E-field distribution along with the film thickness. b) Optical measurements of fabricated waveplate: optical transmission spectra of the element in slow and fast axes are plotted in black solid and dashed curves, respectively; the dispersion of phase retardance is indicated by the solid blue curve.

Laser induced damage threshold of the fabricated waveplate was measured for the wavelength of 355 nm in the nanosecond regime. Using a laser beam diameter of 220 μm, the damage threshold reached 11.5 J/cm2 in a 1–on–1 method and slightly decreased in the S-on-1 test method. Compared with the results of other scientific groups, the LIDT value of 10.4 J/cm2 was obtained for silica nano-sculptured single layer [100]. However, this value possibly is restricted by contamination by various defects and surface cleanliness. The same evaporated waveplate was damage tested with a laser beam diameter of 59 μm to reduce the irradiated area and possibility of interaction with defects within the coating or between it and the substrate. The LIDT value was equal to 24.4 J/cm^2 using 1–on–1 test method and slightly decreased by using S-on-1 test method (Figure 44a).

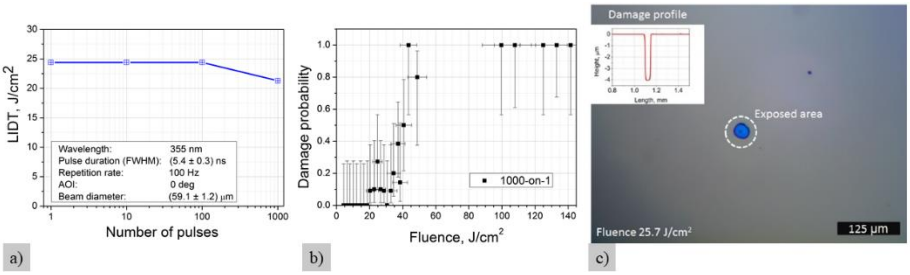

Figure 44. The results of laser induced damage tests of the fabricated waveplate: a) the characteristic damage curve, b) the damage probability curve, c) microscopy image of typical damage morphology at the fluency level of 25.7 J/cm^2 after 1 pulse.

According to the damage probability curve (Figure 44b), this value is still restricted by the layer defects and has more potential to be raised even till 40 J/cm^2. The morphology of the damaged site is presented in Figure 44c, which was initiated by the defect. Profiler measurements, shown in the legend, indicate the depth of the damage to reach 4 μm. This value matches with the total thickness of the multilayer coating, confirming that the defect in the interface of the substrate and the coating is partly responsible for the damage initiation.

Although bulk fused silica indicates LIDT about 23 J/cm^2 for the wavelength 355 nm, the tendency was shown that nano-sculptured evaporated silica layers indicate higher LIDT values due to increasing porosity while evaporating at a glanced angle [117], [118]. Porous structures are less restricted in density when the material is expanding in volume due to the thermal effects. However, as it was shown earlier in the modeled design of multilayer waveplate with E-field distribution along with the film thickness (Figure 43 a), one of the intensive peaks of the E-field coincided with dense silica layer. It encourages to extend future work in optimizing E-field distribution in nano-sculptured coating layers for even better results.

3.4.2 Polarizers for zero angle of incidence

Modern polarizers have a few problems: light beam displacement in Brewster-type polarizers and lower laser-induced damage threshold in normal incidence polarizers due to their absorbing materials. Unfortunately, using standard deposition techniques, isotropic multilayer dielectric polarizers with higher LIDT value, only as elements, which must be installed in the systems at a certain angle, typically Brewster or 45 degrees, can be designed. The technological solution for this issue could be the insertion of anisotropic nanostructured layers in a dielectric multilayer coating design.

Layers fabricated by the OAD method can virtually exhibit any refractive index ranging from bulk material to almost air [119]. Additionally, the birefringence of the layers can also be tuned by changing the deposition angle and the thickness of zig-zag subdeposits [120]. Both these features were shown in the previous section (3.3. Single-layer analysis of silica) for silica thin films, formed by OAD together with SBD method.

The primary idea was to use the combination of porous birefringent and dense isotropic layers to form two spectrally separated Bragg reflection zones for two perpendicular polarizations. The modeled spectrum of multi-layer

design for normal incidence is shown in Fig.45. Due to the anisotropic layer, which indicates two different refractive indexes for perpendicular polarizations, two high-reflective zones appear in spectra. Marked transmission district perfectly indicates polarizer properties: high transmission for one polarization and high reflection for perpendicular polarization.

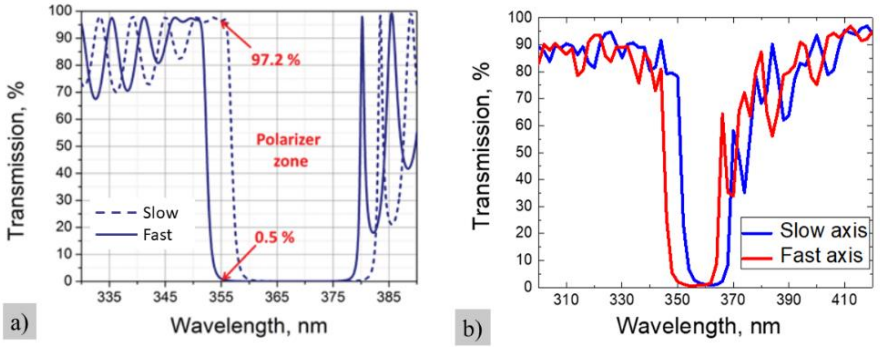

Figure 45. The polarizer for zero angle of incidence: a) modeled transmittance spectra by "OptiLayer" program, b) transmittance of fabricated polarizer

Unfortunately, because of the very sensitive design for fabrication and the lack of precision, it was hard to reach the modeled characteristics with experimental samples (see Figure 45 b).

In further research, a different idea was conceived. Instead of anisotropic and dense layers combination for high-reflective coating, the formation of two different anisotropic films were performed. The effective refractive indexes of silica thin films, deposited at 0°, 66°, and 70° angles, are presented and highlighted in Figure 46 b). A relatively dense silica layer, deposited at 0° angle, exhibits the isotropic effective refractive index of 1.41. The effective refractive indexes of anisotropic layers for the plane between vapor flux and substrate normal has lower values compared to the perpendicular plane due to the self-shadowing effect during thin film growth. Therefore, the plane mentioned above performs a function of the "fast axis" and plane in a perpendicular direction – "slow axis". As shown in Fig. 46 b), refractive indexes match in fast and slow direction for thin films deposited at 66° ($n_{fast}^{66} = 1.27$) and 70° ($n_{slow}^{70} = 1.27$) angles, respectively. For perpendicular directions of the films, the same layers have a difference in refractive indexes of 0.054. Therefore, deposition of both single layers sequentially and aligning their optical axis by 90° with respect to each other would result in a difference in spectral performance. The principal scheme of

crossed layers with elliptically shaped cross-sections is presented in Figure 46 a). Presented multilayer coating will result in two different spectral performances for two perpendicular linear polarizations. For “T Pol” the refractive indexes match, and minimal Fresnel reflections occur between the coating interfaces. For perpendicular polarization, namely “R Pol”, indexes differ by 0.054, and spectral performance depends on thicknesses of individual layers.

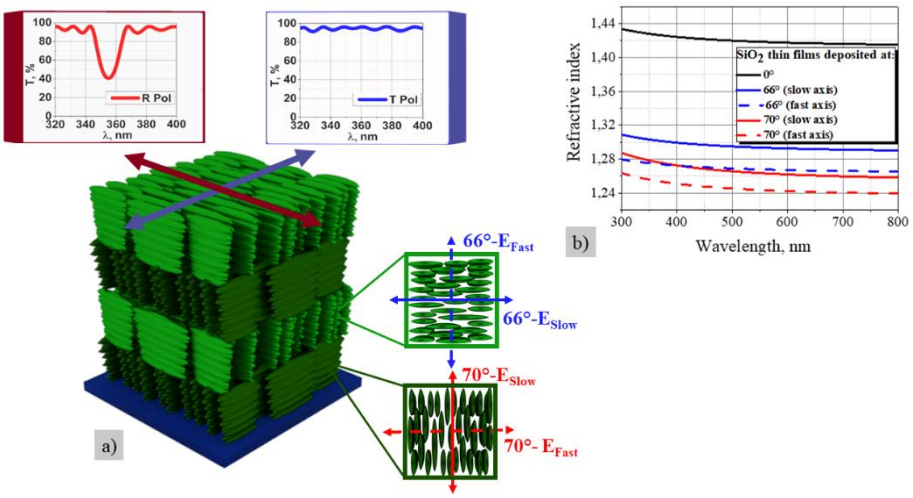

Figure 46 a) The principal scheme of a cross-section of polarizer multilayer coating consisting of anisotropic layers with perpendicularly aligned optical axes. b) effective refractive index dispersions of silica films deposited by the SBD method at different angles

Obtained dispersions of effective refractive indexes of nanostructured silica layers were used in modeling multilayer coatings. Multilayer coating consists of layers sequentially deposited at 66° and 70° angles and changing the orientation of the film’s optical axis by 90°. As mentioned before, such a design results in matched refraction indexes for “T Pol”. Therefore, optical thicknesses of individual layers have a low impact on transmittance for this linear polarization. For perpendicular “R Pol”, indexes have the largest difference and, therefore, optical thicknesses have a high impact on optical performance. In order to gain the highest reflectance at the wavelength of 355 nm, each layer was set at one-quarter wavelength optical thickness (QWOT). Choosing 12 layers (six pairs of films, deposited at 66° and 70° angles) as one stack, several designs were modeled to demonstrate high contrast polarizers' main idea (see Fig. 47 a). Modeled transmission spectra indicate high transmission for “T Pol”, which is independent of the number of stacks in the

coating. As for the “R Pol”, reflectivity increases by increasing the number of stacks within the coating to virtually any value. It is worth mentioning that dense layers (deposited at 0° angle) were inserted between the stacks to strengthen the coating structure and increase the mechanical resistivity. Since the optical thickness of each dense thin film was two QWOTs, it had minimal influence on spectral performance. As can be seen from the figure, the presented approach allows to gradually control the transmittance of the “R Pol” and stabilize it for “T Pol” at the same time. In order to gradually vary the transmittance of “T Pol”, additional modifications were added to the design. The modification means that three pairs of anisotropic layers are removed for the multilayer design, and one pair with high reflectivity (of 70° and dense silica layer of QWOT) is added. Figure 47b) indicates gradual changes in transmittance for “T Pol” while “R Pol” remains almost stable. The presented approach indicates how transmittance for each polarization can be tuned independently to perpendicular polarization by choosing one of the two paths.

Both designs were deposited using SIDRABE electron-beam evaporation plant and measured with a spectrophotometer with polarized light at 0° (AOI). Measured transmittance graphs are presented in Figure 47c). The high-contrast sample consisted of four stacks and exhibited the transmission of 40.4% and 85.3% for R ant T polarizations, respectively. The middle-contrast experimental sample of three stacks and three modifications exhibited the transmission of 35.1% and 62.5% for R ant T polarizations, respectively. The difference in transmission values differs by almost ten percent from the theoretical due to experimental errors in coatings' physical thicknesses and refractive indexes. Also, nano-sculptured layers can exhibit inhomogeneities in structure and optical properties as a consequence [121]. However, such a discrepancy between modeled and experimental results does not preclude the demonstration of the concept.

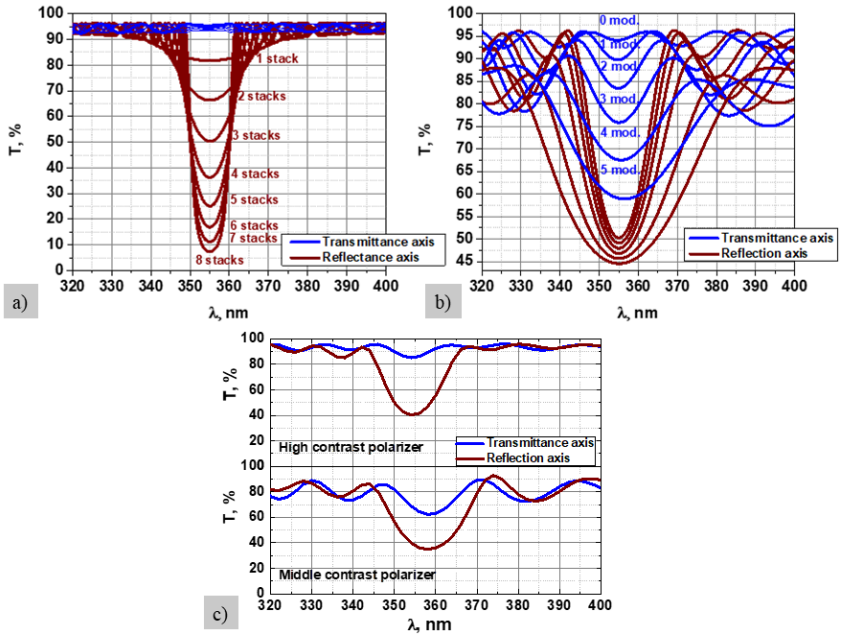

Figure 47. a) Modelled optical transmittances for R and T axes of high-contrast design depending on the number of the stacks (including the back side of the component). b) Modelled transmittances of middle-contrast design depending on the number of modifications. c) Measured transmittance for R and T axes at zero AOI.

High contrast polarizer was treated by high power laser radiation in order to determine the laser induced damage threshold. 1-on-1 test method was used for evaluation of damage probability at the wavelength of 355 nm. The pulse duration of ~3 ns and microfocus approach with a focused beam diameter of 60 μm were chosen to separate damages on local defects from intrinsic resistance of investigated surfaces. Damage probability versus radiation fluence for the R and T axes is presented in Figure 48 a). The lowest fluence level at which damage initiation occurred was 29.5 J/cm^2, when the experimental sample was irradiated in R polarization (higher reflectance value). For T polarization, the lowest fluence at which the damaged site was observed was at the level of 35.5 J/cm^2. In order to evaluate the intrinsic resistivity of the coating more accurately, damage thresholds were also evaluated at a 50% probability level, therefore, neglecting the influence of low resistivity defects [122]. Re-evaluated values were 39.0 J/cm^2 and 48.5 J/cm^2 for the R and T polarizations, respectively. All of the damaged sites were inspected with optical microscopy and measured by profilometer to determine the possible causes for induced damage. Two typical damaged sites are

presented in Fig. 48 b). Several spots are visible in both cases, indicating the defect-based damage morphology. Both images were taken of damaged spots at the fluency level with a probability of 100%. Afterward, damaged sites were measured by profilometer for a depth determination. For R polarization, the depth of the damaged sites increases from 234 nm to 523 nm when the energy fluence was changed from 42.7 J/cm^2 to 65.1 J/cm^2. For T polarization, no tendency for depths of the damaged sites was found. Measured depths varied from around 500 nm to 3000 nm at similar levels of fluency.

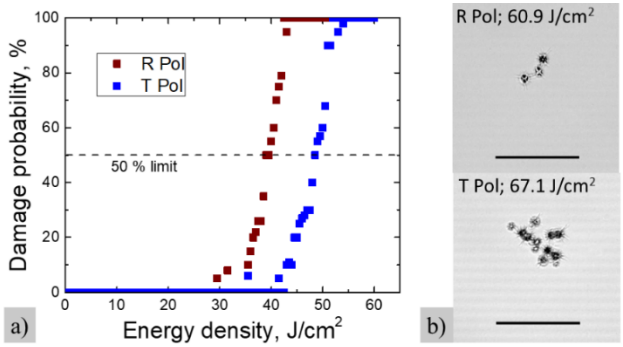

Figure 48. The evaluation of resistivity to laser radiation of the high contrast polarizer: a) damage probability for T and R polarizations and b) Optical microscopy (black bars represents 100 μm) images representing typical damage morphologies.

Presented research demonstrates the polarizer, which is highly resistive to laser radiation. Instead of forming Brewster type design, GLAD technology enabled to form anisotropic layers which allows operating at zero angle of incidence. Accordingly, instead of isotropic films with high and low refractive indexes, only silica material has been used by varying the internal structure of individual layers and, therefore, obtaining necessary birefringence for achieving polarizing properties at zero angle of incidence. However, few issues still have to be addressed for technological implementation in microlaser systems.

The main concern regarding the presented component is its porous structure. The coating is sensitive to environmental changes due to open voids of silica structure. Several investigations indicate the adsorption of water on the structures of silica films [123]. One of the main applications of presented polarizers is to deposit them on the active medium. Typically, such components are sealed or otherwise protected from the environment. Therefore, only the handling throughout the transportation must be addressed.

3.5 The main results and conclusions

In this section, nanostructured all-silica anisotropic single- and multilayers were investigated in detail. The conceptually novel method of formation of porous anisotropic and dense all-silica multilayer coatings featuring low optical losses was developed. The method enables fabrication of high optical quality waveplates as a coating on virtually any type of substrate featuring a superior laser-induced damage threshold (~40 J/cm^2). Also, novel formation method of polarizing coatings was proposed, made of two different silica anisotropic layers with orthogonally crossed optical axes. Those coatings also feature a superior laser-induced damage threshold (39.0 J/cm^2 and 48.5 J/cm^2 for the reflected and transmitted radiation of orthogonal polarizations, respectively), as measured in the nanosecond regime by 355 nm wavelength radiation. Both coatings excel superior resistivity to laser radiation as made only from silica material, which has wide band-gap, and consists of porous layers.

Three statements to defend were formulated according to accomplished results:

- The dense, ultrathin silica interlayers in porous nanostructured anisotropic silica film minimize optical losses by reducing the coalescence and bundling effects of the columnar structure.
- The combination of silica layers with different porosities and anisotropies allows for the formation of multilayer coating structures, with controllable phase retardation properties, high transmittance (up to 99%), and enhanced (up to 40 J/cm^2) laser induced damage thresholds in the nanosecond regime due to the use of only silica as a constituent material.
- The cross-alignment of the optical axes of different anisotropic layers with effective refractive indices that match for only one polarization allows for the formation of a coating with different optical properties and polarizing effects for the normal angle of light incidence, with a high laser-induced damage threshold in the nanosecond regime.

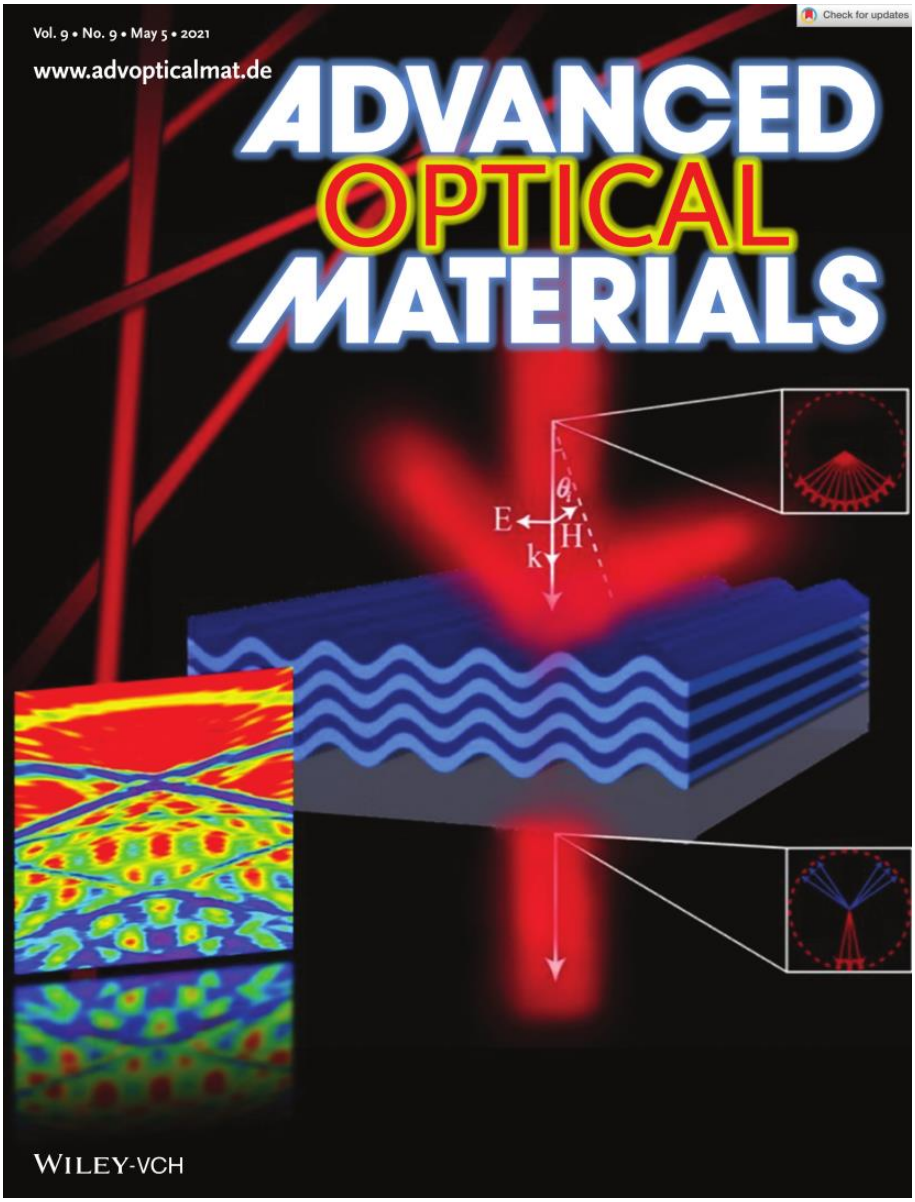

INSIDE COVER:

Lina Grineviciute, Ceren Babayigit, Darius Gailevičius, Martynas Peckus, Mirbek Turduev, Tomas Tolenis, Mikas Vengris, Hamza Kurt, Kestutis Staliunas, *"Nanostructured Multilayer Coatings for Spatial Filtering",* (Advanced Optical Materials 9/2021)

4 COATINGS ON CORRUGATED SURFACES

The use of physical vapor deposition in the fabrication of optical elements with periodically modulated internal nanostructures is presented in this chapter. Two possible variations of the deposition of dielectric coatings on corrugated surfaces are described: conformal growth by repeating the primary surface, and non-conformal growth by forming layers with individual controllable microstructures.

4.1 Conformal coating growth

4.1.1 The target structure of the spatial filter

In modern micro-lasers, especially in high power emission regimes, the spatial quality of the laser light beam deteriorates – i.e., the energy distribution deviates from the Gaussian form. In other words, the broad aperture microlasers operate in a multi-transverse mode regime. Due to the small dimensions of the laser, standard multi-lens spatial filtering arrangements cannot be used for intracavity beam correction. Recently, the idea of angular filtering using photonic crystal-like structures was proposed. For filtering functionality, these photonic structures must be modulated in both the longitudinal and transverse directions to the propagation of the light beam. The first spatial filtering photonic crystals were made in bulk material using direct laser writing techniques. A promising alternative is a structure consisting of alternating multilayers on a substrate, where the interfaces between the layers are modified into a periodic array of sinusoidal "wavy" curves. The geometry of the photonic structure is shown schematically in Fig. 49. The curved thin films replicate the surface modulation of the substrate, providing refractive index modulation in both the longitudinal (*z*-axis) and transverse (*x*-axis) directions. Hence, the proposed structure can be considered a 2D photonic crystal structure.

It is important that the refraction of such a structure can be classified as a generalized Bragg one, since the refracted components propagate backwards. The condition for back-refraction requires that the longitudinal component of the index modulation should have a periodicity of $\lambda/2 < d_z < \lambda$. This results in very compact dimensions of the filtering structure. For instance, 15 periods (30 layers) of modulation result in layered coatings with thicknesses of approximately 10 λ, which, for the near IR – considering the refractive index of the material – is around 5 μm. This is a

significant advantage of our filtering principle compared to the spatial filters in the Laue configuration, where the thickness of the spatial filter is of the order of 1 mm [124].

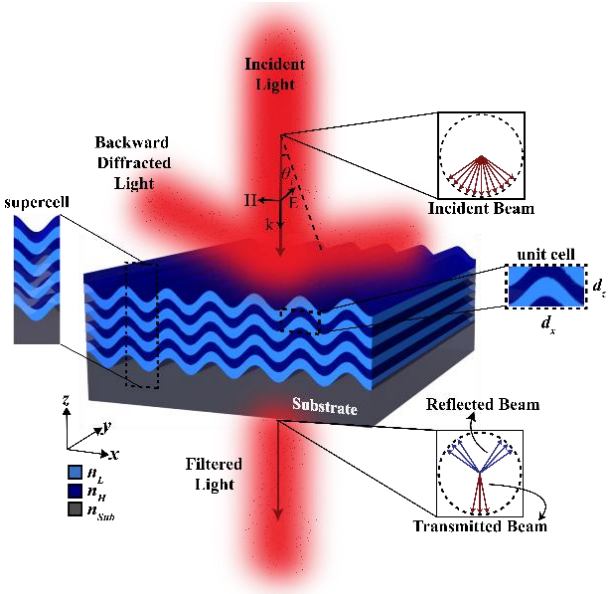

Figure 49. The schematic representation of the photonic structure consisting of a self-repeating curved multilayer coating on a periodically corrugated substrate. The insets show the supercell used to calculate (angle, wavelength) diagrams of field transmission through the structure. The insets also illustrate the double refraction-based angle selectivity of the transmission, providing spatial filtering.

In the design phase, the transmission of the plane waves through the photonic structure depending on their incidence angle and wavelength was modeled. Due to transverse periodicity, we used the supercell analysis of the field propagation using the FDTD method, with a Bloch-periodic boundary condition on the lateral boundaries of the supercell. The results of this are summarized in Fig. 50 a). Here, we present only the results of the s polarized incident wave (where electric field orientation is parallel to the direction of the grating lines – i.e., parallel to the y-axis).

Furthermore, analytically calculated angular-frequency bandgaps are presented and superimposed over the maps in Fig. 50 b). Also, the angular profiles of the transmittance maps are extracted for wavelengths of $\lambda = 1051$ nm and $\lambda = 972$ nm in Figs. 50 c) and 50 d), respectively. Additionally, a vertical cross-section of the map indicating frequency band gaps at the

incidence angle of θ_i =0° is presented in Fig. 50 e). As can be seen from Figs. 50 c) and d), almost perfect transmission occurs for small incidence angles, whereas waves at slightly larger incidence angles are strongly suppressed in the transmitted light.

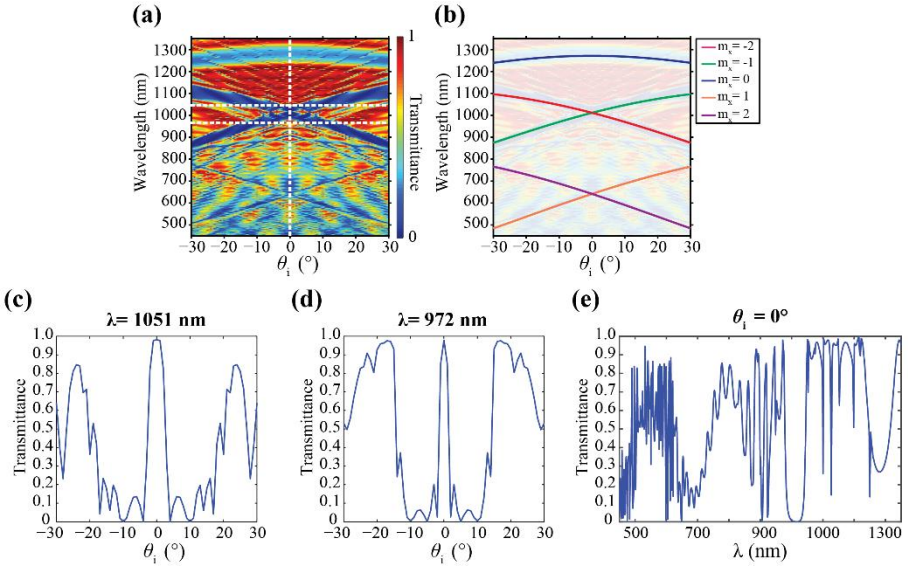

Figure 50. a) Map of transmission dependence on incidence angle and the wavelength extracted from the FDTD numerical calculations. Two dashed lines indicate cross-sectional transmission profiles of λ = 1051 nm and λ = 972 nm. b) Analytically calculated Bragg bandgap positions. c) and d) Angular dependences of transmissions at different wavelengths (horizontal cross-sections of the transmission map) showing efficient spatial filtering. (e) Vertical cross-section at the incidence angle θ_i =0° at the transmission map.

However, to achieve the targeted characteristics of the structured element, it is necessary to have both a proper background profile of the substrate and precise control over the growth of the deposited layers. The deposited layers should repeat the primary profile, or even, as an additional degree of freedom, modify (i.e., increase or decrease) the modulation amplitude of the initial structure. Consequently, the possibility of forming such multilayer structures using physical vapor deposition techniques and control over layer growth was analyzed in detail.

The simulated target parameters for experimental demonstration were as follows: the transverse period (the grating period) – 600 nm; half of the longitudinal period (the optical thickness of each layer) – 310 nm; the number of layers – 33; and the difference between refractive indexes – < 0.2.

For simplicity, the angular selectivity of transmitted/reflected light penetrating through the coating is referred to as **spatial filtering**.

4.1.2 Fabrication of modulated substrate

The substrates with periodically-transversally modulated surfaces were fabricated by laser interference lithography and nanoimprint technology. A chain of technological processes was applied to fabricate the samples. The fabrication process consists of the following steps: i) preparation of the master copy using the interference method in a photoresist, ii) the stamp preparation of the master structure, iii) imprinting of the master structure on the substrate (using the UV imprint polymer).

The laser interference lithography (or also called holographic lithography), employing the third harmonics of Nd:YAG laser radiation, was used to form the master grating onto the photoresist surface.

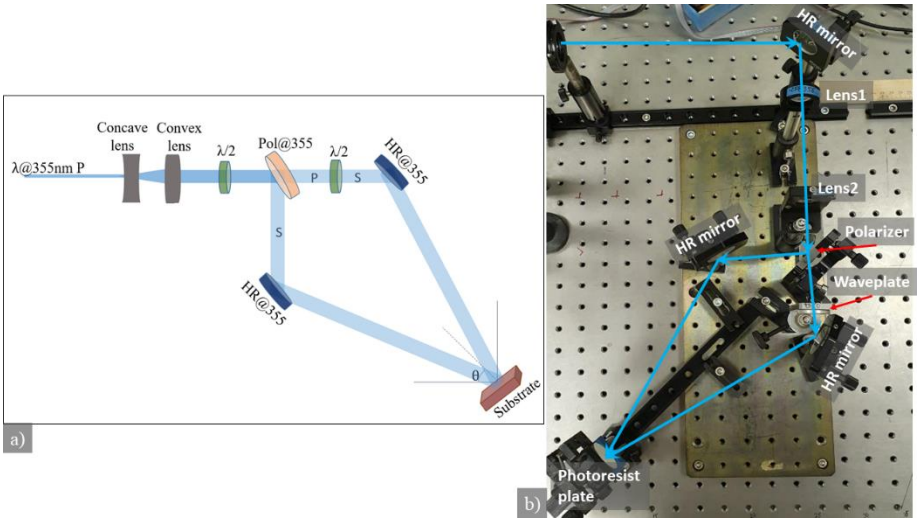

Figure 51. a) The schematic of a laser setup and b) a real laser set-up for the interference lithography process.

The angle between two coherently interfering light beams relates with the fringe-to-fringe spacing (grating period) in the following way:

$$d = \frac{\lambda}{2 * \sin(\theta)}, \qquad (8)$$

where λ – wavelength of the light source, θ – angle between interfering beams.

In our case, angle θ was equal to ~16 degrees to form the grating with ~600 nm periodicity. The total energy for the photoresist exposure (the sum of both beams) was 0,44 mJ. After the exposure, samples were developed in KOH (Potassium hydroxide mixture with distilled water) solution for a different time. As shown in Figure 52, the depth of the grating modulation depends on development time in the KOH solution. The depth can be changed from 350 nm to 50 nm when development time varies from 15 s to 150 s, respectively.

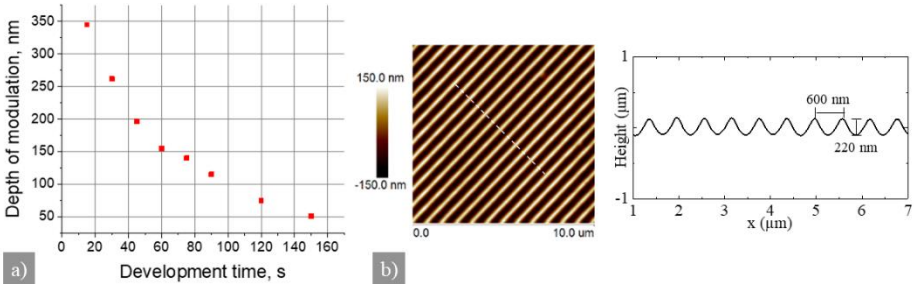

Figure 52. Measured results of fabricated gratings: a) The depth of the grating modulation dependency on the development time in KOH solution. b) AFM measurements of the typical grating surface.

The typical grating surface geometry is shown in Figure 52 b). According to the target design of the structure (provided in 4.1.1. section), an optimal grating with a period of 600 nm and a depth of 200 – 220 nm was chosen for further experiments.

Subsequently, the master structure was used in a typical soft nano-imprint lithography process, where an intermediate soft polydimethylsiloxane imprint was taken from it and used for UV cured polymer (OrmoComp®, n_{ref} = 1.52) copies production.

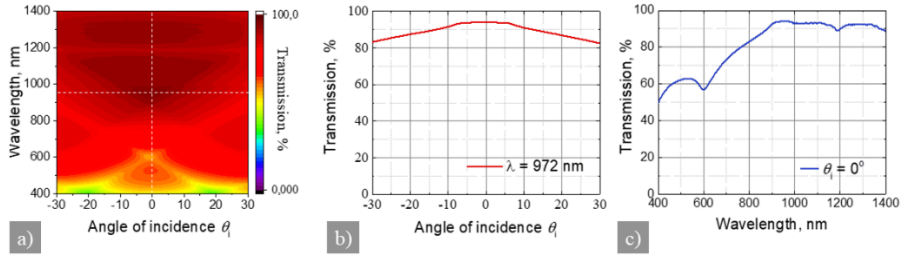

Figure 53. Measured results of fabricated gratings: a) Transmission map (transmission depending on the angle (horizontal axis) and wavelength (vertical axis)); cross-sections of the map: b) angular transmission curve for the wavelength of 972 nm, c) transmission for 0th angle of incidence.

Replicas of the master structure were made in Ormocomp hybrid polymer material, which is transparent even in UV spectral range. The LIDT was measured for thin Ormocomp film spin-coated on FS glass and UV cured for 90 s (as standard procedure for hardening). The sample was measured at the wavelength of 355 nm in a nanosecond regime using a laser beam diameter of 55 μm. The damage threshold reached 11.4 J/cm^2 in 1–on–1 method. Such a result indicates comparatively good quality for optical elements production. The resulting samples with sinusoidally modulated surfaces were used as the substrate for multilayer coating.

4.1.3 The investigation of different technologies

Many different technologies are used to produce high-quality multilayer dielectric coatings, which nowadays are used in modern laser systems. However, most of them are used to deposit the multilayer structures on flat or sometimes evenly bent substrates. In order to evaluate and choose the most perspective technology for coatings deposition on micron-scale modulated surfaces, very few experiments with different available technologies were performed. We explored evaporation by e-beam with different modifications, ion beam sputtering, and atomic layer deposition techniques. The cross-sectional SEM images of fabricated samples are shown in Figure 54.

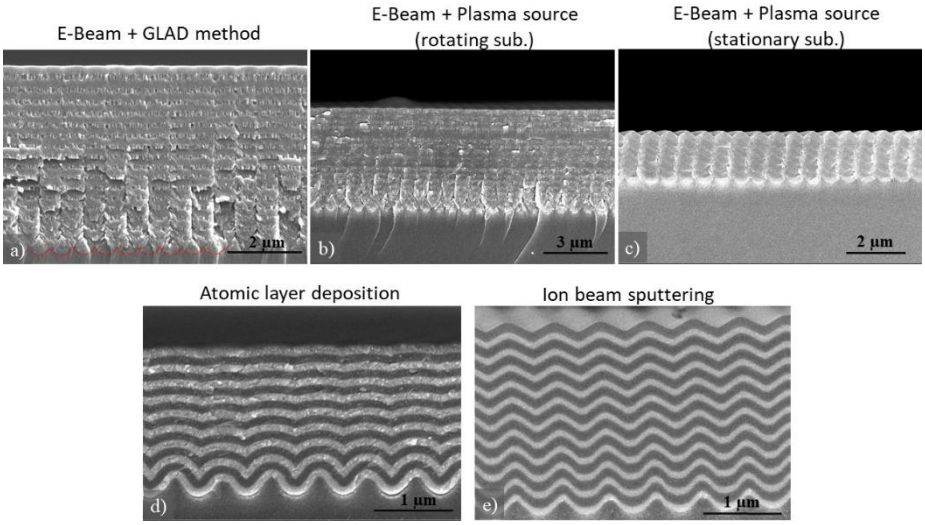

Figure 54. The deposition of multilayer dielectric coating on a miro-scale corrugated substrate by different technologies: a) e-beam evaporation with Glancing Angle Deposition method (red dashed line marks the interface between the substrate and the coating), b) e-beam evaporation with plasma

source when the substrate is rotating in the calotte, c) e-beam evaporation with plasma source when substrate placed stationary above the plasma flux, d) Ion beam sputtering, e) Atomic layer deposition.

The electron beam evaporation. First, a low energetic process - e-beam evaporation with glancing angle deposition method, was employed for the multilayer formation using only silica material. Such a method was used to repeat/replicate the primary modulated structure in [125]. In our experiment, two deposition angles (0° and 70°) were chosen for silica layers formation with different effective refractive index (1.41 and 1.25, respectively). The substrate was subjected to constant speed rotation during the deposition process. However, as shown in the SEM image in Fig. 54 a), layers do not repeat the modulation of the substrate, and after 4,5 μm of film thickness, modulation decreases from the primary 200 nm to barely noticeable 10 nm. Such evanescence of the modulation is caused by the low energy of the deposited atoms during thermal evaporation, which results in the formation of a porous coating structure.

Next, the e-beam evaporation with the assistance of energetic oxygen ions was used to increase the energy of deposited atoms. Two different methods were used: first, when the sample was placed into the constantly rotating calotte, it means that the sample is just briefly interacting with energetic particles of oxygen and argon ion flux. Secondly, the sample was placed straight over the plasma source – for the constant interaction with ions during the deposition process. For both processes, Al_2O_3 and SiO_2 were chosen for multilayer structure growth. In Fig. 54 b), as the sample is just periodically interacting with energetic ions, the result is similar to evaporation with the GLAD method – after ~4 μm of film thickness, the modulation decreases from the primary 230 nm to 20 nm. More perspective result was noticed while analyzing the structure (see Fig. 54 c) of the second method of evaporation with the assistance of energetic particle as the sample is placed straight over the plasma source. If we look more closely at the fabricated structure (Figure 55), after 1.7 μm thickness, the modulation has been changed from primary 220 nm depth to even slightly higher 250 nm. However, it is a comparatively hot process due to the evaporation and plasma source what leads to cleavage of the sample made of hybrid polymer, and the process was suspended after just 1.7 μm thickness coating.

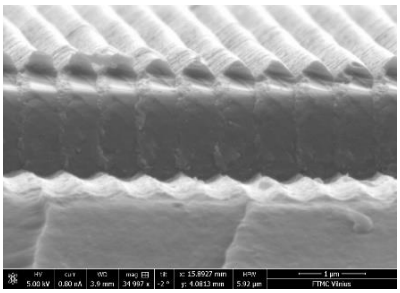

Figure 55. The deposited multilayer Al_2O_3 - SiO_2 coating by e-beam evaporation with plasma source when substrate placed stationary above the plasma flux.

The atomic layer deposition (ALD) was also explored as an experimental method for multilayer formation. This method is known as the deposition technique based on a gas-phase chemical process and is a subclass of chemical vapor deposition. ALD is considered a method with great potential for producing very thin, conformal layers with control of the thickness and composition possible at the atomic level. A unique feature of ALD is its ability to conformally coat very high-aspect-ratio structures, like nanoscale holes and trenches [126]. Due to this feature, it was decided to try ALD for comparatively thick coating deposition on the modulated surface. The coating consisted of 17 layers of HfO_2 and Al_2O_3 materials (total physical thickness was about 1.7 μm) and was deposited by ALD as the temperature of the process was ~120°C. However, as can be seen from the SEM image in Fig. 55 d), only the first layer repeats the modulation of the substrate, and after about 1 μm of film thickness, modulation becomes barely noticeable. Also, high internal stress in the fabricated coating leads to cleavage of the sample due to the comparatively sensitive and mechanically non-resistant sample. Therefore, due to the slow and expensive fabrication process and the high internal stress of the coating made by the ALD process, it was decided to abort further experiments with this technique.

The ion beam sputtering (IBS) method is well known for the capability to form dense and low-loss optical coatings. In this work, the IBS method was also chosen to fabricate multilayer coating on the modulated surface. One of the standard coatings for high-reflective mirrors consisting of Ta_2O_5 and SiO_2 materials (total physical thickness was about 2.4 μm) was fabricated on the periodically corrugated substrate. From the analysis of the SEM cross-sectional image (see Fig. 54 e), the slight smoothening of the structure was noticed – from 200 nm modulation depth to 100 nm. Also, after the process, the sample was not damaged or cracked. Based on these results, the IBS

technology was selected as the most perspective technology for further experiments to grow the multilayer coating without the degradation of primary modulation.

4.1.4 Structural analysis of IBS single-layers

After the preliminary experiments with different thin-film deposition technologies, the IBS method was chosen for further exploration to fabricate conformal optical coatings on periodically modulated surfaces. Four different dielectric materials, highly transparent in visible and infrared spectral range, were chosen for multilayer production – high refractive index materials - HfO_2, Ta_2O_5, Nb_2O_5, and low refractive index material – SiO_2. The parameters which were used for all single-layers fabrication are summarized in the table below.

Table 3. The summarized IBS reactive process parameters for HfO_2, Ta_2O_5, Nb_2O_5, and SiO_2 single-layers formation.

Material	**Refractive index@980nm**	**O_2 flux, sccm**	**Partial pressure, mbar**	**Physical thickness, nm**
HfO_2	2.01	5	$5.0 \cdot 10^{-5}$	1000
SiO_2	1.48	80	$1.4 \cdot 10^{-4}$	1000
NbO_2	2.24	80	$1.4 \cdot 10^{-4}$	1000
Ta_2O_5	2.09	40	$8.0 \cdot 10^{-5}$	900
Ta_2O_5	2.09	40	$8.0 \cdot 10^{-5}$	700
Ta_2O_5	2.09	40		500
Ta_2O_5	2.09	40		350
Ta_2O_5	2.09	40		200
HfO_2	1.94	80	$1.4 \cdot 10^{-4}$	1000

To evaluate the growth of different materials on the nanostructured surfaces, single-layers with a thickness of ~1 μm were deposited with optimal deposition parameters, known from standard layer formation procedures on flat substrates (highlighted lines in table 3). The topographies of the sample surfaces before and after layer growth were measured with an atomic force

microscope, and also the change of the modulation geometry was determined from SEM cross-sectional images (see Fig. 56 and 57).

Comparing the depths of modulation of the initial corrugated substrate and the coating surface, in the case of hafnium oxide, the modulation decreases by 4.5 %. In the case of tantalum oxide, the modulation decreases by 3.2%. The determined change in niobium oxide surface modulation was 10%. The most significant decrease of the modulation depth was found for a structured layer of silica where the surface modulation reduced by 35 % after one μm thickness coating. The measured surface topographies by AFM after layer deposition can be seen in Figure 56.

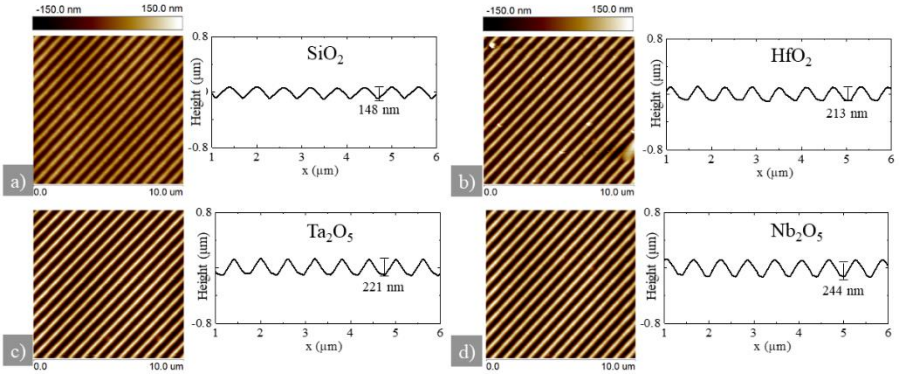

Figure 56. AFM measurements of single-layer surfaces fabricated from different materials: a) SiO_2, b) HfO_2, c) Ta_2O_5, and d) Nb_2O_5.

Accomplished results from AFM measurements were supplemented by SEM cross-sectional images. The observation of different smoothening of the structure was confirmed. In the case of HfO_2, Ta_2O_5, Nb_2O_5, the surface geometry was similar to the triangle shape, and in the case of SiO_2 – the shape was more rounded (Fig. 57).

These metal oxide materials were sputtered on modulated substrates using calibrated parameters known from standard interference coatings production. One of the main parameters for optimal deposition is the amount of oxygen that was inflated into the vacuum chamber to ensure the oxidation of the metal particles. As shown in Table 3, 80 sccm of oxygen is required for the reactive deposition of silicon and niobium oxides, which is several times more than for tantalum and hafnium oxides.

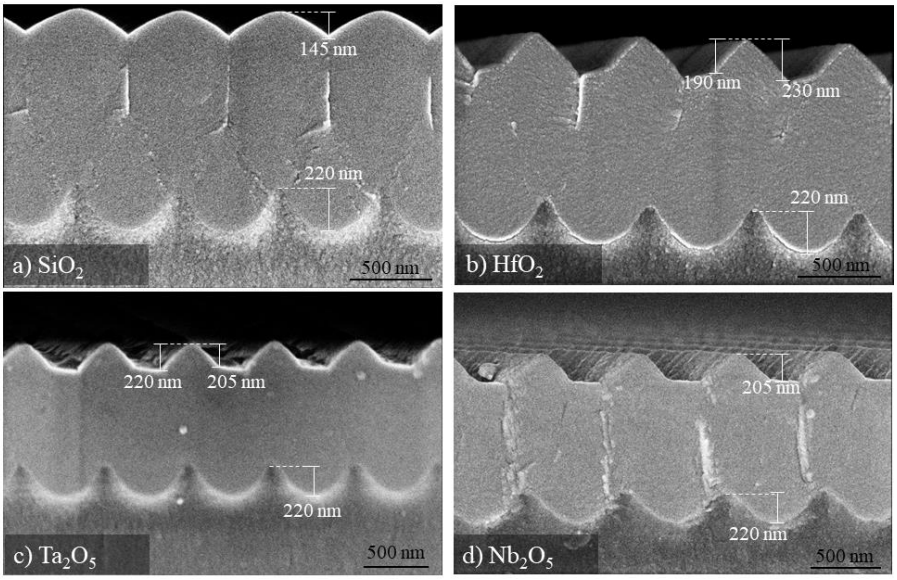

Figure 57. SEM images of cross-sections of fabricated single-layers from different materials: a) SiO_2, b) HfO_2, c) Ta_2O_5, and d) Nb_2O_5 materials.

To assess whether the amount of oxygen inflated into the chamber affects the deposition quality of the coating, HfO_2 material was used to fabricate single-layers with different amount of O_2. 5 sccm and 80 sccm of oxygen were chosen, which correspond to the partial pressure in the chamber of $5 \cdot 10^{-5}$ and $1.4 \cdot 10^{-4}$ mbar, respectively. The cross-sections of the HfO_2 single layers deposited with the standard process and with the increased oxygen content are compared in Figure 58.

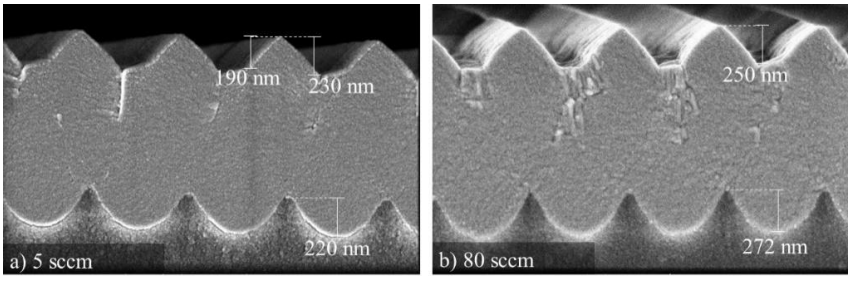

Figure 58. SEM images of cross-sections of the fabricated samples of HfO_2 material by using different amounts of oxygen during the deposition process: a) 5 sccm and b) 80 sccm.

As shown earlier, in the case with 5 sccm O_2, the modulation decreases by 4.5 %. In an oxygen over-saturated environment, a slight change in the shape of surface modulation to the triangular shape is observed, and a decrease in

modulation depth of 8.1% nm is determined. The influence of oxygen flux was also determined to optical constants of single layers fabricated on flat FS substrate during the same deposition processes.

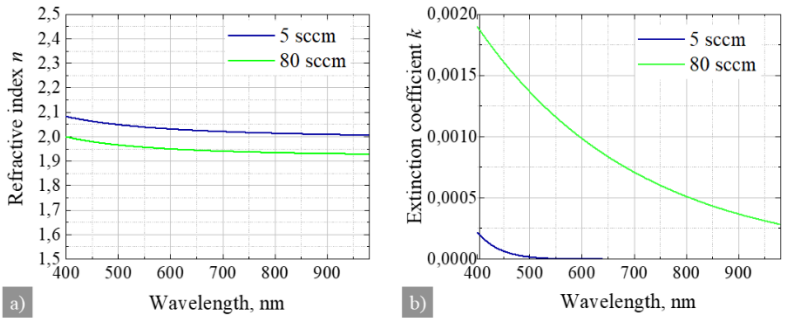

Figure 59. a) Refractive index and b) extinction coefficient dispersions of HfO_2 layers fabricated using different amounts of O_2 during the deposition process.

In Figure 59, refractive index dispersions of HfO_2 material by using different amounts of oxygen during the deposition process can be seen. The layer fabricated with 5 sccm of oxygen indicates a refractive index of 2.02 at the wavelength of 900 nm. If the amount of oxygen is increased to 80 sccm, the refractive index decreased by 3.5 % (n – 1.93) together with increased optical losses. According to observations from structural and optical analysis, we can state that the oxygen-saturated environment during deposition has a minor effect on the conformal deposition of HfO_2 coating on a structured surface.

However, the faster decrease of the modulation with an increasing film thickness of the silica layer compared to the remaining materials can not be explained by different amounts of oxygen (different partial pressure). So, such behavior can be related to the chemical properties of the material itself.

Table 4. The molecular weight and density of different materials

Material	**Molecular weight, g/mol**
Si	28.09
Hf	178.49
Ta	180.95
Nb	92.90

The molecular weight of the materials used in deposition processes is shown in Table 4. We compare the weight of the pure materials instead of their oxides because sputtered atoms are metals and oxidized only on the substrate surface. Values of a silica material are several times lower compared with other metals. Thus, this material consists of relatively "light" atoms, which are easier scattered by residual gasses and form low-density layers, leading to a rapid smoothening of modulation.

4.1.5 Optical analysis of IBS single-layers

The optical transmittances were also evaluated of fabricated single-layer structures. Measurements were accomplished for vertically orientated grating lines with linear polarization parallel to grating lines. The transmission maps (transmission depending on the angle (horizontal axis) and wavelength (vertical axis) together with vertical cross-sections are shown in Figure 60. Three of four spectral maps show low-bandwidth “crosses” (Fig. 60 b-d). Spectral crosses, which can be attributed to Fano-type resonant, can be seen only for single-layers made from materials with high refractive index (HfO_2, Ta_2O_5, Nb_2O_5). There are no such resonance lines in the spectra of the silica modulated layer, which is related to the low refractive index of the material (n_{SiO2} = 1.48, $n_{substrate}$ = 1.52). It means the condition for excitation of waveguide modes in the layer is not satisfied, and radiation is not coupled into the modulated layer.

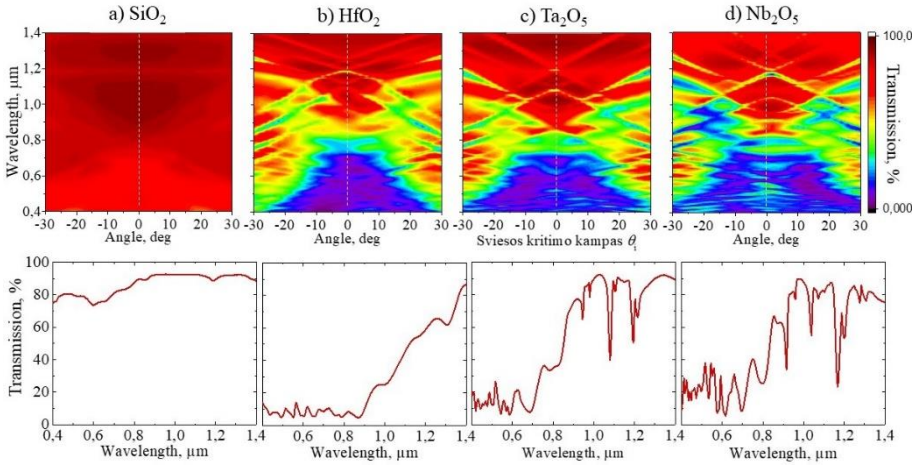

Figure 60. Transmission maps together with characteristic vertical cross-sections (placed below) for 0th angle of incidence of samples made of different materials: a) SiO_2, b) HfO_2, c) Ta_2O_5, d) Nb_2O_5.

The idea of Fano-like coupling in a nanostructured thin film is explained in Fig. 61 b). Fano resonances can be interpreted within a simple model of two coupled oscillators: a driven oscillator with a broad (continuous) spectrum coupled to the second oscillator with a narrow (discrete) spectrum. When the frequency of the driving force is tuned around the resonance frequency of the second oscillator, sharp changes occur in the response of the first driven oscillator. In our case, the radiation incident in a near-to-normal direction to the film excites the Fabry–Perot (FP) modes of the film with the refraction index larger than that of the environment. Moreover, the optically transparent oxide film can be considered as a flat waveguide when the high refractive index layer is surrounded by areas of lower refractive index on both sides. The optical characteristics of coupled Fabry–Perot and waveguiding modes also depend on the coating thickness.

One of the materials with a high refractive index – tantalum oxide (n_{Ta2O5} – 2.09), was selected for more detailed investigation. The layer with the minimum thickness of tantalum oxide deposited on the periodic modulated surface is shown in Figure 61 a. The surface modulation of the grating was ~ 220 nm. The film deposited with 200 nm thickness does not change the depth of the primary modulation.

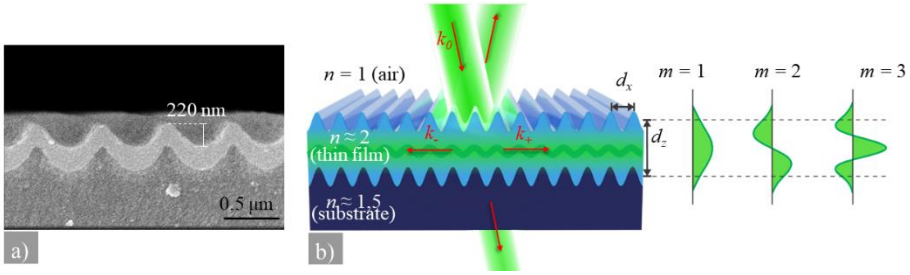

Figure 61. a) Ta_2O_5 single-layer fabricated on modulated substrates with thicknesses of 200 nm and b) The schematic representation of the geometry for the resonant coupling between the Fabry–Perrot and planar waveguiding modes, where the incident radiation couples with left/right propagating waveguiding mode with k_- and k_+.

Later, the influence of structured layer thickness on spectral characteristics was explored. The transmittance of modulated single-layer coatings in thicknesses of 200, 350, 500, 700, and 900 nm was investigated, and the experimental data were compared with the numerical simulation data.

As the nanostructured layer with the thickness of 200 nm is irradiated by light at incidence angle θi = 0°, in the spectrum, the peak of reflection (at λ = 970 nm transmittance value $T \approx 1\%$) occurs due to the excitation of the waveguide mode in the tantalum oxide film (Fig. 63). At a perpendicular incidence of light to the surface plane, the resonant conditions are satisfied equally for both modes propagating in different directions in the fabricated structure, corresponding to m = + 1 and m = - 1 mode. In transmittance maps, this corresponds to the center of the intersecting crosses. The resonant conditions can be satisfied for different wavelengths for higher waveguide modes when the film thickness is increased. Thus, the light propagating through the structure can interfere with several waveguide modes, leading to higher-order resonant frequency crosses appearing on the transmission maps, i.e., the overlap of which gives a complex image.

Experimentally obtained transmission maps with resonance wavelength dependence on irradiation angle and FDTD (Finite difference time domain) simulated spectral maps of the corresponding coatings are shown in Figure 62.

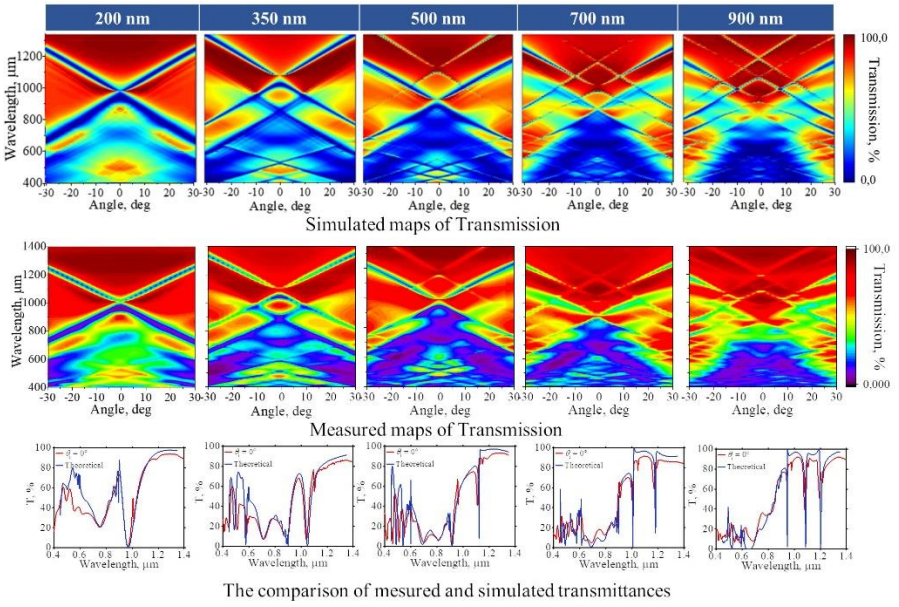

Figure 62. Simulated (first row) and measured (second row) transmittance maps for Ta_2O_5 single layers with different thicknesses. In the third row, the comparison of simulated and measured cross-sections of transmittances maps is shown.

The maps of transmittance are in good accordance with the theoretical relation (more details described [127]):

$$T = \frac{1}{\left(1 - r^2 exp(i\varphi)\right)/t^2 + i\sum_m s_m^2/(\Delta\omega_m t^2)}, \qquad (9)$$

where, r – the reflection, $t = \sqrt{2n}/(n+1)$ is the transmittance through the interface, φ – the phase, $s_m \approx h_0(n-1)/\lambda$ with h_0 – the amplitude of the surface modulation of the film, $\Delta\omega_m$ – the normalized detuning of each excited mode from its resonance frequency. The Eq (9) coincides with the Fano scattering function with the Fano factor equal to zero, i.e., in the absence of the internal losses of the secondary oscillator.

The first line of Figure 62 shows the transmission function considering the left- and right propagating lowest order modes with $m = \pm 1$.

From the comparison (third line in Fig. 62), it can be seen that the spectrophotometric measurements of experimental samples are in good agreement with the theoretical calculations. The main difference is the discrepancy between the minimum and maximum intensities and the broadening of the resonance lines in the results of spectrophotometric measurements. These discrepancies appear due to the imperfection of the periodic structure itself – the fabricated hybrid-polymeric substrate with the modulated surface was somewhat corrugated, and that corrugation is also repeated in the deposited coating. AFM and SEM analysis indicate a weak large-scale corrugation of the surface: on top of the main modulation with the 600 nm period and 220 nm amplitude, some weak random modulation with a spatial scale of about 10 μm and the maximum depth of 50 nm is visible.

4.1.6 The application of the nanostructured single-layer

Examining the spectral maps in more detailed manner, two interesting demonstrations of optical characteristics can be distinguished: frequency and spatial/angular selectivity of light. Fig. 63 shows a transmission map of the coating with 200 nm thickness and corresponding vertical and horizontal cross-sections. From the horizontal cross-section of the transmittance map, it was observed that spatial filtering characteristics are satisfied for specific wavelengths. The spatial filtering properties are satisfied for the wavelength of 910 nm: at 0 degrees of incidence, the transmittance reaches 68 %, the spectral width at half maximum (FWHM) corresponds to 8.7°, and the minimum value of transmittance at 8˚ corresponds to ~ 5.9 %. A similar property is also observed for the wavelength λ = 1050 nm, the intensity of

which reaches 61 % at the angle θi = 0˚, the minimum values (θi = ± 6˚) are ~ 17 % and the width of the FWHM is ~ 7.8˚.

Fano resonance results in a sudden drop in transmittance, theoretically up to 0% (or 100% reflection in the narrow range of the spectrum) for resonant wavelengths. Fig. 63 in the presented vertical cross-section at θi = 0˚, the sudden drop in transmission can be seen at λ = 970 nm. For this wavelength, the transmittance value reaches only ~ 1%. Depending on the angle of incidence, the resonant conditions are satisfied for different wavelengths individually for each mode. Therefore, in the second vertical cross-section, at θi = 10˚, the spectrum shows two sharp decreases in intensity: at λ = 891 nm, the transmittance is 5.45%, and at λ = 1090 nm the transmittance is 12.7%.

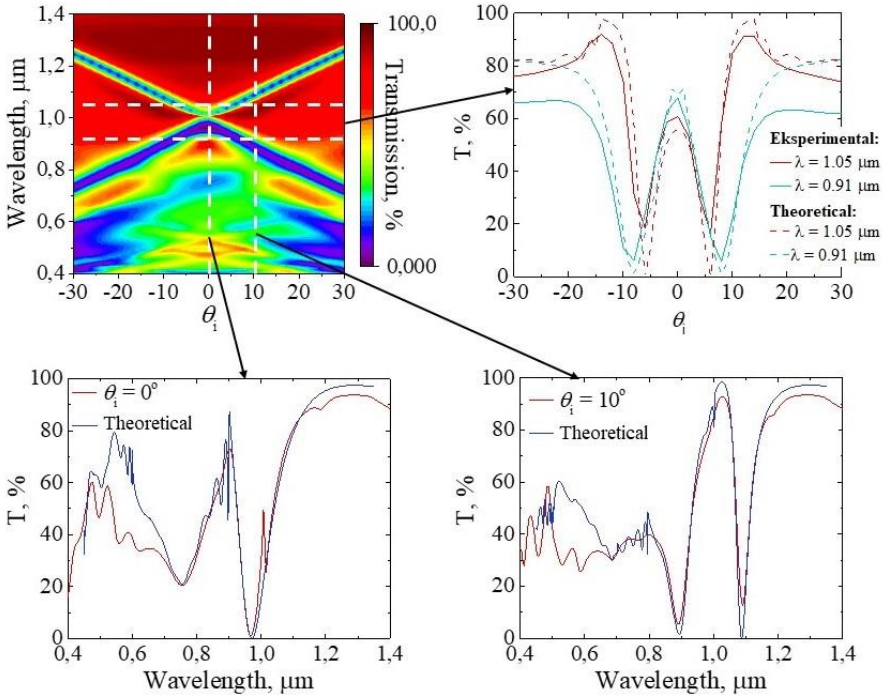

Figure 63. Transmission map in a plane (Θ, λ) and corresponding vertical and horizontal cross-sections are compared with numerical calculations.

The results promise efficient and narrow-band filters both in wavelength and angle domain. It should be noted that in the case of Bragg structures, the resonances are always of flat-top and flat-bottom shape (not of a type of single zero), which result in substantially broadened filtering lines.

Moreover, the width of the Fano resonant lines $\Delta\omega$ depends primarily on the coupling coefficient between the Fabry-Pero modes and the planar

waveguide modes: $\Delta\lambda \sim s^2$. FDTD supercell numerical simulations were performed to evaluate the predicted scaling for different amplitudes of the modulations. The calculated dependencies in Fig.63 are in good agreement with the analytically estimated scaling in the limit of shallow modulations.

Simulations also allowed to calibrate the proportionality coefficient in scaling, since the analytically predicted dependence of $\Delta\lambda$ on the amplitude of the surface modulation h_0 is indicative due to the absence of knowledge of the exact waveguiding mode shapes and exact couplings between FP and waveguiding mode. In terms of the wavelength, the estimation reads: $\Delta\lambda = c\, h_0^2/d_z$.With the calibration constant on the order of unity (c=0.5, and 0.2, for two different planar modes with m=1 and 2).

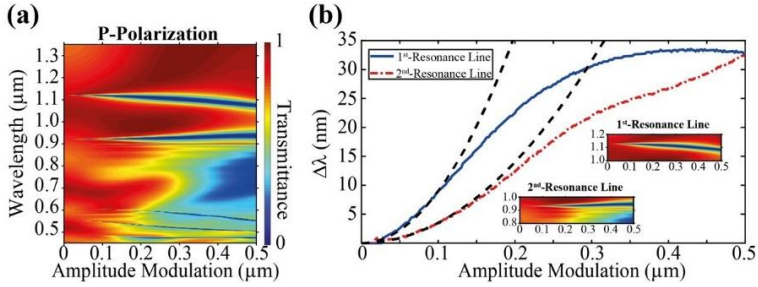

Figure 64. The dependence of the width of the resonance on the modulation height h: obtained from the supercell FDTD calculations (blue and red lines) for 1st and 2nd planar modes together with the analytically proposed scaling (dashed lines). The parameters: $s = 0.1$, $d_x = 0.6\,\mu m$, $d_z = 0.5\ \mu m$, $h_0 = 0.2\ \mu m$, and $n = 2$

This means that shallow modulation could allow extremely narrow transmission gaps in terms of the wavelength. For instance, modulation amplitude $h_0 = 30\ nm$ should result in a transmission gap with the width on the order of $\Delta\lambda \approx 1\ nm$ at around $\lambda = 1\ \mu m$. In terms of the incidence angle, the width of the gap reads: $\Delta\theta = \Delta\lambda/d_x\ (1 + (md_x/(2d_z))^2)$. For shallow modulation the above relation simplifies to: $\Delta\theta = c\, h_0^2/(d_x d_z)$, with the same calibration constant c. The modulation amplitude $h_0 = 30\ nm$ should result in angular transmission gap with the width on the order of $\Delta\theta \approx 1\ mrad$

The above estimations were performed when a single Fano resonance is considered. This occurs away from the cross point of the resonance lines, i.e., for the incidence angle $\theta \neq 0$. What is interesting is the case around the cross of two resonance lines, when two Fano resonances are in action simultaneously. In the wavelength domain, this results in the double width of the gap, comparing with the single Fano resonance case, for the angle $\theta = 0$,

i.e., does not lead to quantitative differences. However, in the angle domain, the width of the transmission gap (and the width of the reflection peak, respectively) becomes:

$$\Delta\theta^2 \approx \frac{s^2\lambda_0^2\Delta\lambda}{2\pi t^2 d_z d_x^2} \qquad (10)$$

which is valid close to the center of the cross of the resonance lines. Having in mind that $d_x \approx \lambda_0$ for the first cross, the following estimation can be obtained: $\Delta\theta \sim s\sqrt{\Delta\lambda/d_z}$, which shows the singular character concerning the wavelength detuning $\Delta\lambda$. This predicts a principal possibility to obtain extremely narrow angular transmission gaps (and reflection peaks) even for finite modulation depth h_0 by tuning the wavelength close to the double resonance point.

4.1.7 Multilayer analysis

In section 4.1.1. target parameters for spatial filter design based on optical coatings were numerically simulated: transverse period (grating period) – 600 nm, modulation depth – 220 nm, longitudinal period (optical thickness of each layer) – 310 nm, the difference of indexes of materials with high and low refraction index – < 0.2, number of layers – 33. The formation of such multilayer coatings for the production of a two-dimensional filter prototype was performed using ion beam sputtering technology, which was analyzed in detailed in previous section of single-layer coatings. HfO_2 and Nb_2O_5 materials with refractive indices of 2.02 and 2.24, respectively, were chosen as the most perspective candidates due to the feature to replicate the primary modulation with increasing layer thickness. Also, higher refractive indices for the IR spectral range are more suitable because, in this case, the physical thicknesses of the formed layers are smaller, which will result in a better replication of the initial modulation.

The multilayer coating consisting of 33 layers of alternative HfO_2 and Nb_2O_5 materials was deposited on flat and modulated substrates for comparison. Cross-sectional SEM images and maps of transmittances are shown in Figure 65. The total thickness of the fabricated coating was 5080 nm (see Fig. 65 a). However, such a thick coating does not ideally conformally settles on the modulated surface.

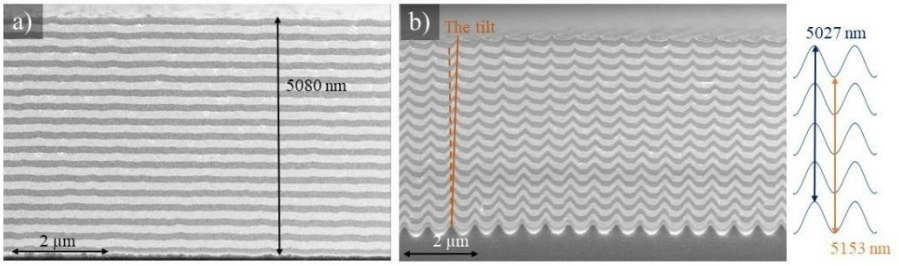

Figure 65. SEM images of the same HfO_2-Nb_2O_5 multilayer coating deposited on a) flat surface, b) modulated surface.

The coating is formed by 50 nm thicker on the valleys of modulated surface and almost 50 nm thinner on peaks. This leads to the modulation degradation by almost 100 nm from the primary depth of modulation of ~220 nm. AFM measurements also confirm this result accomplished from SEM images (See Fig. 66), showing the smoothening of modulation amplitude by 100 nm.

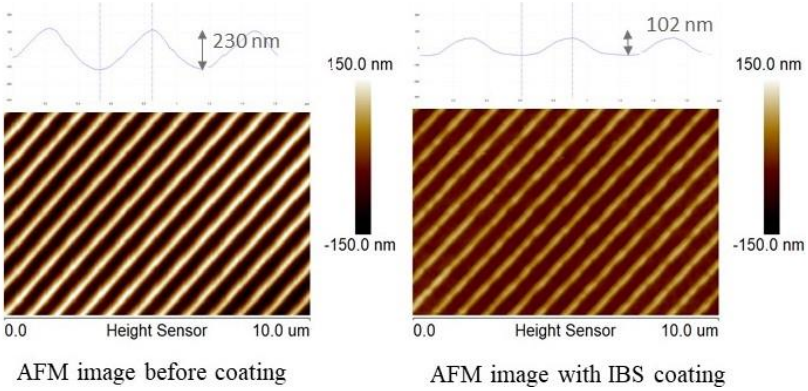

Figure 66. AFM measurements of the modulated surface a) before deposition process and b) after the deposition of multilayer HfO_2-Nb_2O_5 coating

Maps of the transmittance of corresponding coatings deposited on flat and modulated substrates are shown in see Fig. 67 a and b. In the case of the coating deposited on the flat substrate, only a single gap of transmittance appears, which corresponds to the Bragg zone at the wavelength around 1250 nm. In case of modulated coating, in addition to slightly weaker Bragg zone, two more gap of transmittance appears at the wavelengths around ~1000 nm and 650 nm.

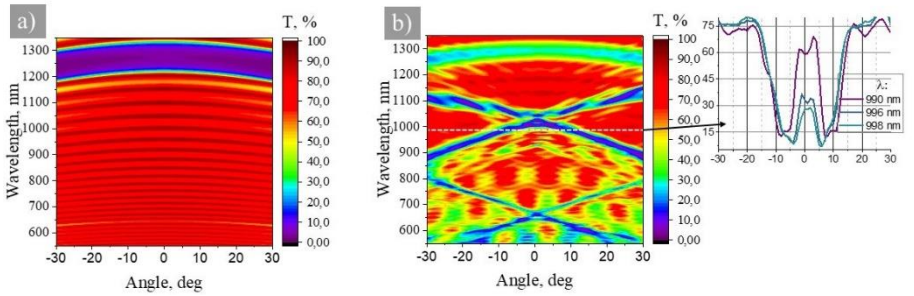

Figure 67. Maps of the transmittance of HfO_2-Nb_2O_5 multilayer coating deposited on a) flat surface, b) modulated surface.

The schematic representation to explain the origin of the Bragg zone and the apparent cross in the transmission map is shown in Figure 68. The multilayer coating deposited on the corrugated substrate can be considered as a 2D photonic crystal. As the light irradiates such structure as in Fig. 68, the optical response, i.e., the transmission map (the dependence of the transmittance on the incidence angle and the wavelength), may look very complicated. However, it can be interpreted by considering such a structure as a crystal with many axes of translational symmetry. In Fig. 68 a), the SEM image of 2D photonic crystal is shown.

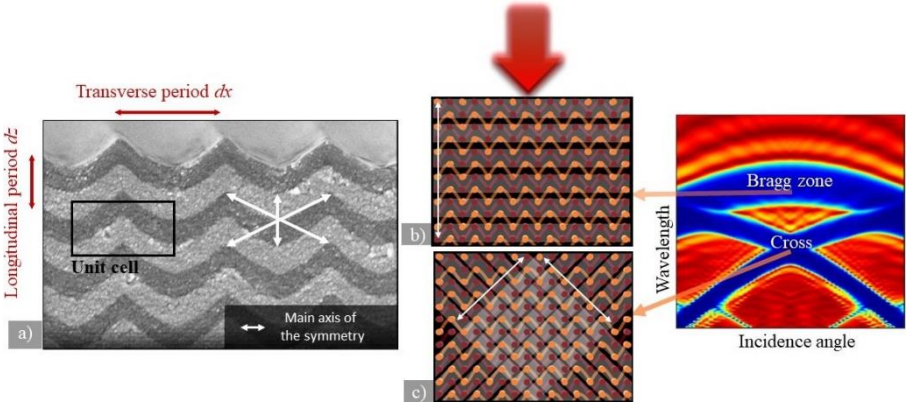

Figure 68. The schematic representation of the origin of the apparent Bragg zone and the cross in transmission map of the 2D periodic structure: a) SEM image with marked unit cell and the principal axes of translational symmetry, b) marked planes of symmetry in a vertical direction corresponding to the main Bragg zone, c) marked tilted planes of crystal symmetry corresponding to the formation of Cross zone. (in b and c yellow dots indicating low refractive index sites in minima and maxima of modulated structure, dark red – high refractive index sites).

The unit cell of such crystal, which was used in FDTD calculations, is indicated. Also, white arrows indicate the main axis of discrete translational symmetry. Multiple planes with the variation of low and high refractive indexes in marked directions are responsible for band-gap formations. In the case of vertically orientated translational symmetry, periodically orientated planes, and light irradiation from the top, the standard Bragg zone appears as the condition for optical thickness to be at one-quarter wavelength is satisfied (Fig.68 b). Due to two tilted axes of symmetry in 2D crystal (Fig.68 c), the corresponding Bragg zones appear as a cross for shorter wavelengths.

Optical response is highly sensitive to geometric parameters of the structure; therefore, it is essential to select the proper deposition parameters for high quality and precision coating fabrication. Additionally, it was noticed that even if the calotte is constantly rotating, the deposition on the modulated substrate is very sensitive to the orientation of the grating according to the vapor flux. Experiments of multilayer depositions were performed to eliminate structural shear (tilt), which appears due to the shadowed flux of atoms by grating features (Fig.69).

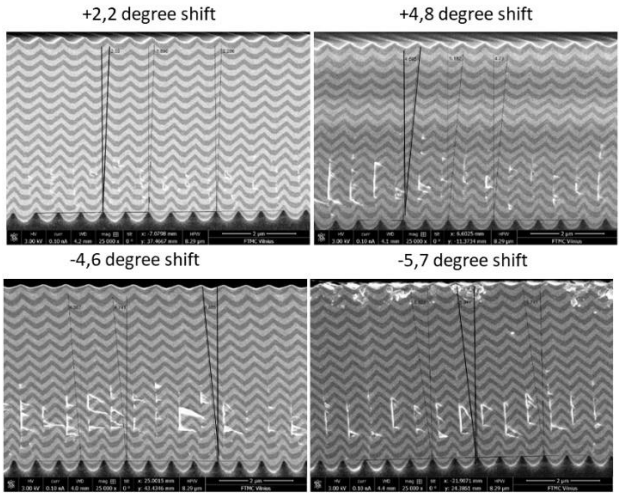

Figure 69. SEM images of cross-sections of multilayer HfO_2-Nb_2O_5 coating deposited on modulated surfaces at different orientated positions in the IBS calotte.

After rough estimations of the orientation, to control the structure tilt more precisely, several processes were performed by simultaneously depositing the coating on differently oriented gratings, rotated by a small angle (Fig 70). Due to the structure shear, the filtering lines in the transmission spectrum become

asymmetric. It is needed to find the optimal position for the deposition process to reach the symmetric transmission of the light.

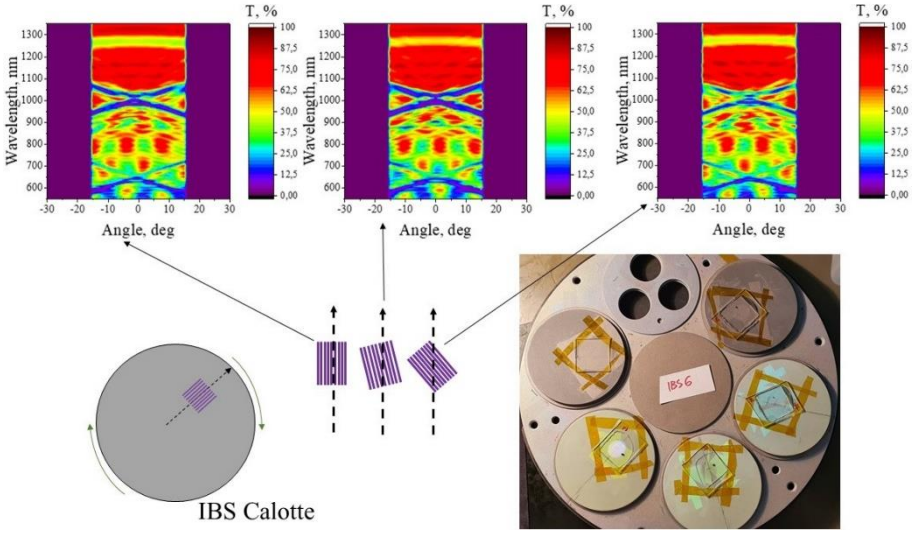

Figure 70. Maps of the transmittance of HfO_2-Nb_2O_5 multilayer coating deposited on modulated surfaces at different orientations in the IBS calotte.

After a detailed analysis of the proper position in IBS calotte and the layer growth dynamics, the multilayer structure consisting of HfO_2 and Nb_2O_5 materials was fabricated on a modulated substrate and characterized. First, SEM image of the sample cross-section is shown in Figure 71. The modulation height decreases from 230 nm to 150 nm after 5 μm coating thickness.

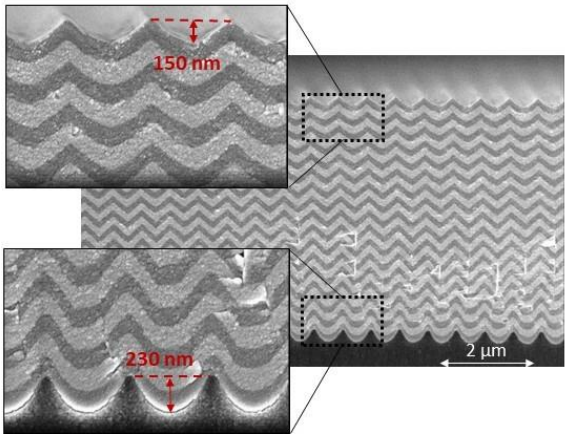

Figure 71. SEM images of the cross-section of the multilayer HfO_2-Nb_2O_5 coating deposited on the modulated surface.

Transmission maps (transmission depending on the angle (horizontal axis) and wavelength (vertical axis)) together with cross-sections of the map (angular transmission curve) for characteristic wavelengths in the insets are shown in Figure. 72. Two maps of transmittance are shown in the figure: right – linear polarization parallel to grating lines, left – linear polarization perpendicular to grating lines.

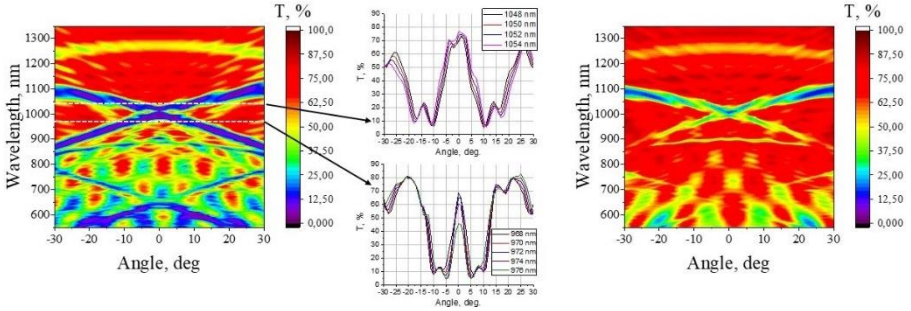

Figure 72. Transmission map (transmission depending on the angle (horizontal axis) and wavelength (vertical axis)), together with cross-sections of the map (angular transmission curve) for characteristic wavelengths in the insets.

The overall filtering pattern (i.e., angular band gaps positions presented in Figure 72 a) corresponds quantitatively well with the simulated and analytically calculated ones (see section 4.1.1. Figure 50 a and b). However, additionally, the transmission spectrum in the map was overlaid by the fringed structure. Vertical fringing is related to the Fabry-Perot resonances of the coating structure, as the frequency separation between the fringes corresponds to the resonances of the structure of 5 μm physical thickness (10 μm optical thickness thus mean refractive index is around 2). The origin of the horizontal part of fringing is more sophisticated. It was identified as the resonances of the first-order diffracted modes trapped in the planar structure of a relatively high refraction index.

The main quantitative difference between numerical results and spectroscopic measurements of the fabricated structure is that the filtering lines were less deep and more blurred. This can be attributed to the imperfections of fabricated structure – the corrugation of the substrate modulation on a range of around 10 μm and, subsequently, the corrugation of the whole structure (see Fig. 73.)

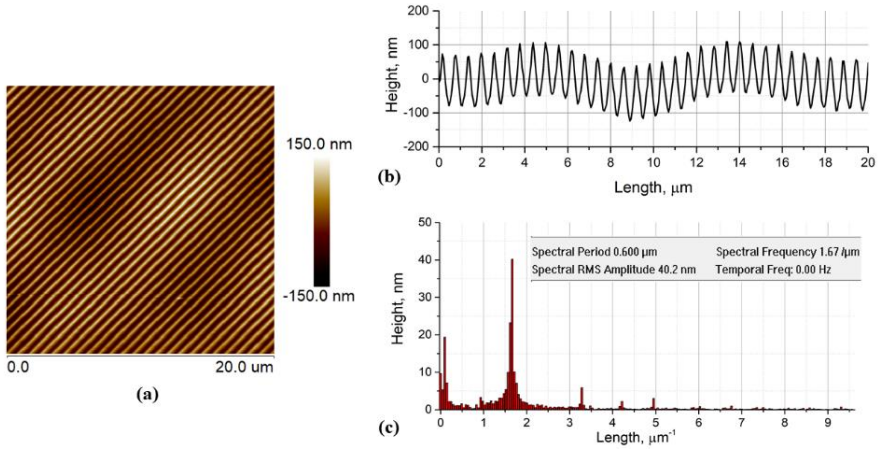

Figure 73. a) Atomic force microscopy measurements of the surface showing the corrugation. b) Height distribution of the surface on a cross-section indicated c) spectrum of the surface coordinate, showing the broadening of spectra around main harmonics (period corrugation), the spectral components around zero frequency (background corrugation), and higher harmonics (non-sinusoidal modulation).

4.1.8 Spatial filters

The fabricated sample was illuminated by a cylindrically focused laser beam of a tunable picosecond laser (tuned in the wavelength range of 958 nm $\leq \lambda \leq$ 980 nm, angular divergence of the beam of ~ 9.7° at FWHM). Figures 74 a) and b) compare the far-field (angular) profiles of the incident probe beam and the resulting filtered beam for slightly different wavelengths. The narrowing of the angular spectra in the transmission is evident – angular divergence of the beam at FWHM is ~ 2°. This is the specifically direct experimental proof for the spatial filtering effect by nanostructured multilayer coating.

For a more detailed analysis, a transmission map was reconstructed by dividing the measured angular intensity profile of the filtered beam by the reference (unfiltered) one. For comparison, we show the reconstructed transmission map in Fig. 74 c) together with the obtained one from spectrophotometric data in Fig. 74 d). Angular transmission spectra for two wavelengths of λ = 968 nm and λ = 972 nm are shown in Figs. 74 e) and f) for an additional comparison. The first case shows a transmission curve for a more bell-shaped profile with a higher transmission loss at the low angle values. On the other hand, the second case shows a lower loss case with a flat top resembling a case. It is notable that the transmission through the structure did

not exceed 80 % whereas 100% would be preferable for practical use at the angular intensity transmission bands. Here, both components of fabricated photonic structure: the substrate and the multilayer coating, are made of transparent, non-absorbing materials for Vis-IR range. Since optical losses arise from the scattering and reflections, it can be controlled by using an optimized design of multilayer coating (including anti-reflective properties).

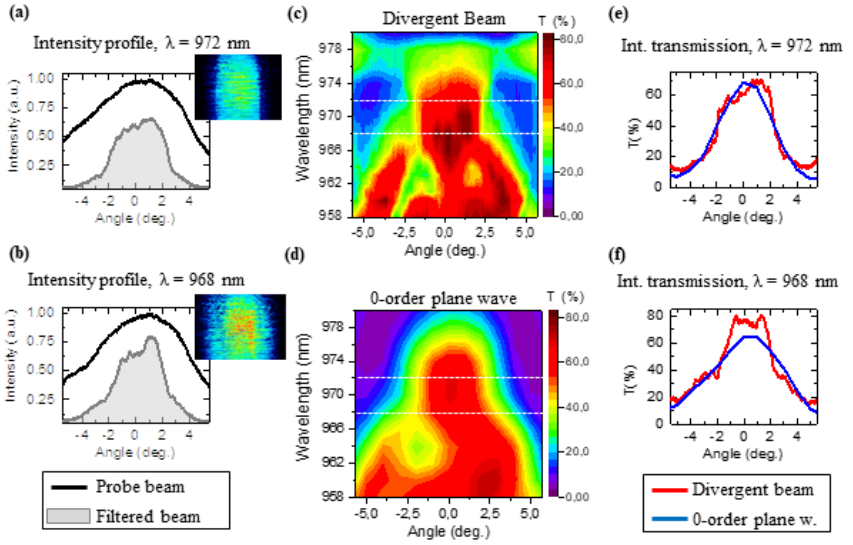

Figure 74. Experimental data for spatial filtering of a divergent probe beam. a, b) Transmission of a reference beam and filtered beam evidencing 1D (cylindrical) spatial filtering for two different wavelengths. Insets show the 2D intensity profiles of the filtered beam registered on a CMOS camera. c) Shows the corresponding transmission map, where the sample was illuminated with a divergent probe beam. Wavelengths of interest are marked with dotted lines. d) Shows the zoomed-in range from the transmittance map corresponding to a 0-order plane wave transmission spectral-angular map. e) and f) show the intensity transmission profiles for wavelengths 972 and 968 nm for both measurement methods.

The main result of this work with coatings on modulated substrates is the demonstration of pronounced functional spatial filtering of light. However, some imperfections still prevent the filter from technical applications, which should be tackled in future work. Although such an element would be the perfect solution for microlaser systems even in high power regimes, thus all structure in future perspectives can consist only of dielectric, resistant to laser radiation materials.

4.2 Non-conformal growth on a corrugated surface

4.2.1 Motivation

In previous sections, two different methods for nanostructured coatings were introduced: evaporation with glancing angle deposition, and deposition of a multilayer coating on periodically modulated surfaces using the IBS energetic process. The combination of those two approaches – evaporation with the GLAD method on periodically orientated surfaces – could generate very promising results. The possibility of controlling the growth of the non-conformal layer is presented in this section.

4.2.2 The control of non-conformal coating growth

The formation of the coating on a periodically modulated surface was performed using electron beam evaporation technology with one particular GLAD (glancing angle deposition) method – SBD (serial bideposition). At this stage, the process was implemented with the deposition of low-energy particles (not exceeding 0.5 eV). The GLAD method allows for the formation of layers with internal periodic nano- and micro-structures if the substrate with periodically orientated nucleation sites is used. In our experiments, we decided to use the SBD method to grow vertically-orientated straight columns and to investigate the dependency of the orientation of grating lines. The same gratings, with a 600 nm period and ~220 nm modulation depth, were used during depositions. In each layer growth process, two differently orientated gratings were used. The schematic representation of vertically- and horizontally-orientated gratings according to the vapor flux is shown in Fig. 75. The orientation of the grating determines the shadowing region for depositing atoms. The length of the shadowing zone can also be controlled by the deposition angle χ, i.e., the angle between the substrate normal and the vapour flux.

The experiment was accomplished via the detailed analysis of SiO_2: modulated samples were coated using the SBD method at the χ angles of 50°, 60°, 70°, and 80° to investigate the formation of the microstructure of a single layer. One depositional process was also accomplished for a multilayer structure consisting of alternating layers deposited at 30° and 50°.

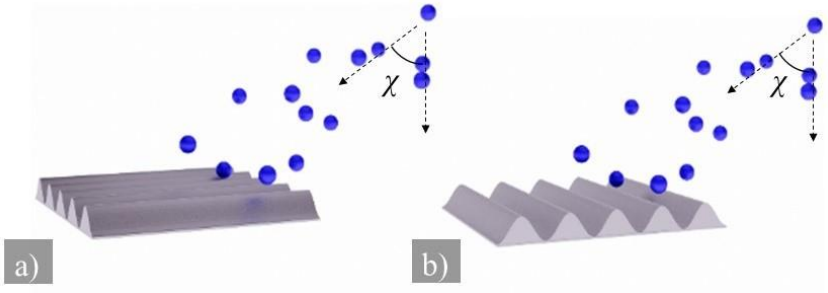

Figure 75. The schematic representation of a) vertically and b) horizontally orientated gratings according to the vapour flux χ.

The influence of the orientation of the grating on the formation of the microstructure during the deposition process can be seen in Fig. 76. As the vapor flux is directed parallel to the grating grooves, shadowing occurs only at the atomic level and is almost unnoticeable at the micro-scale. Since the shadowing phenomenon caused by the grating lines limits growth only in the parallel plane, there is no limitation on the transverse growth of the columns. Due to this asymmetrical shadowing and the structure of the porous coating (as a result of the small energy levels of the deposited particles), the growing features expand along the transverse direction and connect to each other. Thus, after a film thickness of around 200 nm, a continuous layer is observed on a periodically modulated substrate (see Fig. 76 a).

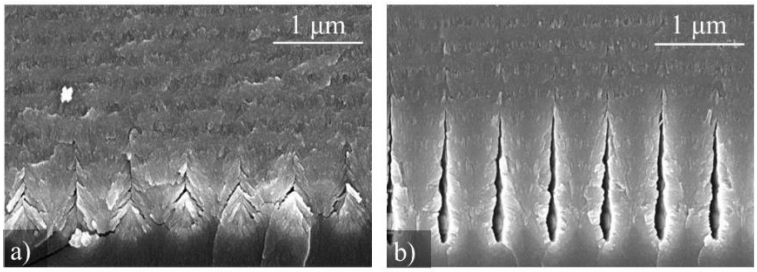

Figure 76. SEM images of cross sections perpendicular to grating lines as the gratings were a) vertically and b) horizontally orientated according to the vapor flux during SBD process for alternating layer growth at 30 and 50 degrees.

As the vapor flux is directed perpendicular to the grating lines, the neighboring grooves limit the incoming particles, resulting in shadowing zones and gaps between the peaks of the structure being formed (Fig. 76 b). The material that accumulates further on the elevated lines also forms a shadow, which determines the growth of the individual columns. Because the

layers are deposited at relatively small angles (30° and 50°), and as the thickness of the coating increases, the deposited columns widen promptly. The height of the columns was ~1.3 μm until they formed a continuous layer.

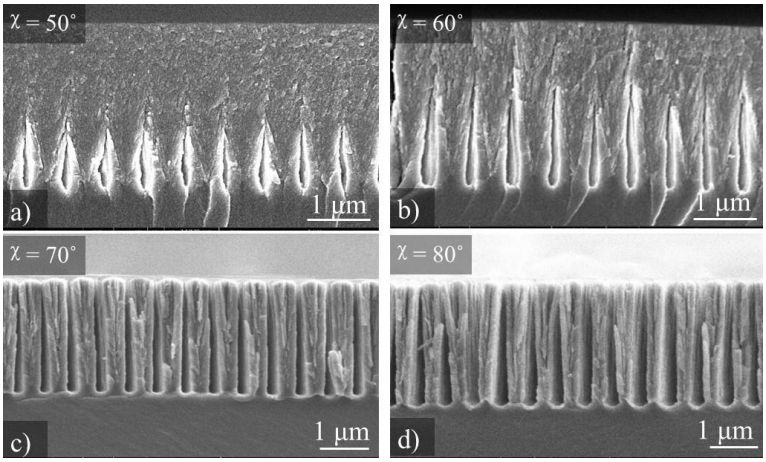

Figure 77. SEM images of cross-sections perpendicular to grating lines as the gratings were orientated horizontally according to the vapor flux during SBD deposition process at the angles of χ a) 50°, b) 60°, c) 70° and d) 80°.

The area of the resulting shadowing zones depends directly on the deposition angle. By changing the deposition angle, χ, it is possible to control the internal geometry of the growing micro-structure. SEM images of cross-sections of single-layer silica coatings deposited at different χ angles on horizontally orientated gratings are presented Fig. 77.

In the case of the smallest angle (50°), comparatively short zones of shadow appear, due to which a continuous layer is formed after ~1.3 μm (Fig. xx a)). When the deposition angle is increased to 60°, columns merge after a thickness of ~1.7 μm. In the case of the largest deposition angles (θ = 70°, 80°), the coating still consists of separated columns even after a thickness of 3 μm.

As can be seen from Fig. 78, at all deposition angles the width of columns increases while film thickness increases. The initial width of the column depends on the angle between the substrate surface and the direction of particle flux. As this angle increases, wider shadow areas are formed, resulting in columns with smaller widths. Thus, when the angle of deposition is changed from 50° to 80°, the initial width of the columns decreases from 0.55 μm to 0.24 μm.

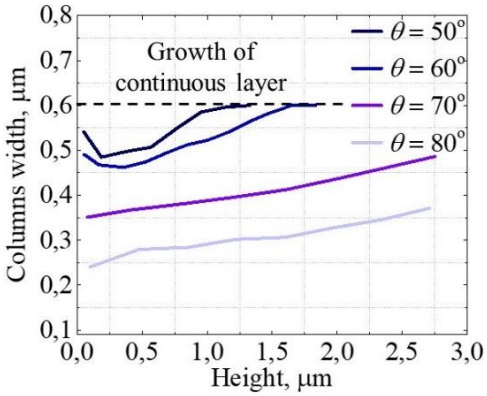

Figure 78. The evolution of the mean width of the columns with increasing film thickness as layers are fabricated at different deposition angles by SBD method.

However, when the deposition angle is ≥ 80°, extremely large shadow zones are formed, which are strongly dependent on any change in the deposition angle – also known as the extreme shading effect [76]. In this case, extremely porous, mechanically unstable structures are formed, which result in a slight variation in the shape of the structures. In order to form a neat microstructure with minimal structural expansion of the column, a deposition angle of 70° is optimal for formation on the modulated substrate with a periodicity of 600 nm.

4.2.3 Perspectives in application

The growth of a neat sculptured coating by the deposition of low-energy particles, i. e., evaporation, strongly depends on parameters such as the orientation of the modulated substrate according to the vapor flux and the deposition angle. From the analysis of the formed SiO_2 coatings, it was determined that in order to form periodic micro-structure on a one-dimensional periodically structured surface like a grating, the direction of modulation lines must coincide with the direction of the shadowing zone. When the latter condition is satisfied, the deposition angle initially determines the threshold thickness of the coating, till which the internal structure consists of columns completely separated from each other. As χ continues to increase, the microstructure consists of completely separated periodically arranged columns. In the case of very large angles, such as $\chi = 80^{\circ}$, the structural elements become disheveled.

Periodic nanostructures, with a large surface area and controlled internal geometry/porosity, are sensitive to changing environmental conditions. For example, moisture or other gases absorbed into the porous structure from the environment will cause detectable changes in the dielectric constants of the effective refractive index of the structure [128,129]. By recording the change in these constants, periodic GLAD structures can serve as humidity/gas sensors. However, such statements and future perspectives will be validated in other works and are out of this theses' scope.

4.3 Main results and conclusions

The growth of different materials deposited by variouse methods on periodically modulated substrates was investigated. Ion beam sputtering technology was found to be optimal due to the high energy of its deposited atoms, which leads to dense and conformal layer growth.

The growth of structured layers of different materials fabricated by ion beam sputtering on the modulated substrate was investigated in detail. It was shown that high refractive index periodically modulated dielectric thin layer, surrounded by a low refractive media featured Fano-resonant coupling of the electromagnetic radiation, and manifested in angular and frequency selectivity of light reflection.

Moreover, selecting suitable materials with high and low refractive indexes for the multilayer stack's conformal deposition on the modulated surface allows for the formation of 2D photonic crystals with spatial filtering functionality (< 2° half-width pass-band).

In the last experimental part of this thesis, the possibility of controlling the geometry of periodical nanostructured columnar coatings on a pre-patterned surface using the glancing angle deposition method is presented.

Two statements to defend were formulated according to accomplished results:

- The periodically modulated dielectric thin layer of a high refractive index in a low refractive index surrounding allows Fano resonances, and shows high angular and frequency selectivity of light reflection/transmission.
- The conformal deposition of multilayer optical coatings on a pre-patterned surface using physical vapor deposition technology has been shown to be a 2D photonic crystal with spatial filtering functionality (< 2° half-width pass-band).

MAIN RESULTS AND CONCLUSIONS OF THE THESIS

Measurements of the laser induced damage threshold of nanostructured single-layers indicated better optical resistance of silica thin films than alumina or lanthanum fluoride. Optical and structural analysis indicates a deposition angle of 70° to be optimal in forming anisotropic silica coatings.

The dense silica layer inserted into the columnar structure can serve two purposes: suppressing the bundling of columns and serving as the new flat base for the next layer with a columnar structure formation. This allows for the forming of optically low-loss interference coating, which operates as a waveplate, indicating a laser induced damage threshold of 40 J/cm^2 in the ns regime due to it being comprised solely of silica.

The perpendicular alignment of the optical axes of two different anisotropic layers with only one matching effective refractive index allows the formation of polarizing elements for the normal angle of incidence. Such an all-silica element indicates a high laser-induced damage threshold in the nanosecond regime: 39.0 J/cm^2 and 48.5 J/cm^2 for the reflected and transmitted polarization, respectively.

Different technologies – namely e-beam evaporation, ion beam sputtering, and atomic layer deposition – were investigated for multilayer coating conformal deposition on periodically modulated substrates. A high-energetic deposition process – ion beam sputtering – showed the most promising results, as after depositing a multilayer structure with a physical thickness of 2.4 μm, surface modulation depth changed from 200 nm to 100 nm.

A dielectric periodically modulated Ta_2O_5 layer with a high refractive index in a low refractive index environment allows Fano resonant coupling of the electromagnetic radiation originating from the planar waveguiding modes.

A novel method of compact spatial filter fabrication based on the deposition of a multilayer coating on a modulated surface was developed. It was demonstrated that a laser beam passed through such a 2D photonic crystal indicates that the angular divergence of the transmitted beam at FWHM is ~2°.

The possibility of controlling the geometry of periodical nanostructured columnar coatings on a pre-patterned surface using the glancing angle deposition method was investigated. As the vapor flux is directed perpendicular to the grating lines with a periodicity of 600 nm, and the deposition angle is changed from 50° to 80°, the initial width of the columns can be changed from 0.55 μm to 0.24 μm due to the shadowing of the incoming particles by neighboring grooves.

SANTRAUKA

SANTRUMPŲ SĄRAŠAS

Santrumpa	Frazė (lietuviškai/angliškai)
PVD	Fizinis garų nusodinimas, Physical Vapor Deposition
CVD	Cheminis garų nusodinimas, Chemical Vapor Deposition
IBS	Dulkinimas jonų pluoštu, Ion Beam Sputtering
E-beam	Elektronų pluoštas, Electron Beam
ALD	Atominio sluoksnio nusodinimas, Atomic Layer Deposition
GLAD	Nusodinimas slystančiu kampu, GLancing Angle Deposition
SBD	Serijinis dvipusis nusodinimas, Serial Bi-Deposition
SEM	Skenuojantis elektronų microskopas, Scanning Electron Microscope
AFM	Atominių jėgų mikroskopas, Atomic ForceMicroscope
XPS	Rentgeno spindulių fotoelektronų spektroskopija, X-Ray photoelectron spectroscopy
LIDT	Lazerio indukuotas pažaidos slenkstis, Laser Induced Damage Threshold
AOI	Kritimo kampas, Angle Of Incidence
FS	Lydytas kvarcas, Fused Silica
MD	Molekulinė dinamika Molecular Dynamics
FDTD	Baigtinio skirtumo laiko srities, Finite-Difference Time-Domain

ĮVADAS

Šviečiant saulei žmonės visada žavėjosi skirtingų spalvų raibuliais muilo burbulų paviršiuose. Tačiau tik mažuma susimąsto, kad tas pats žavus fizikinis reiškinys, sukeliantis spalvų žėrėjimus, taikomas kuriant sudėtingus optinius elementus. 1935 m. pradžioje, Aleksandras Smakula („Zeiss“ įmonės narys), taikydamas interferencijos principą plonose plėvelėse, sukūrė skaidrinančias dangas, pagerinančias optinių paviršių pralaidumą spinduliuotei. Tokios dangos buvo suformuotos ant žiūronų lęšių paviršių, o iki 1940 m. buvo laikomos karine paslaptimi [1].

Didžiulė naujų ir aukštos kokybės dielektrinių optinių elementų paklausa atsirado išradus lazerį. Pirmąjį lazerį 1960 m. sukūrė Theodoras H. Maimanas Hugheso tyrimų laboratorijoje, kai galinga šviesa apšvietė rubino strypą sidabru padengtais paviršiais [2]. Tačiau pirmuosiuose eksperimentiniuose lazeriuose atsirado problemos dėl spinduliuotės sukeltų defektų sidabro sluoksniuose. Taip buvo užfiksuoti pirmieji lazerio sukelti pažeidimai [3]. Šiais laikais yra daugybė įvairių lazerių: pradedant didžiulėmis ir galingomis lazerinėmis sistemomis, skirtomis fundamentaliajam mokslui [4], ir baigiant mikrolazerinėmis sistemomis, kurios taikomos įvairiems naujiems technologiniams sprendimams [5]. Šiuolaikiniai lazeriai ir lazerinės technologijos yra ženkliai patobulėję ir plačiai naudojami mokslinių tyrimų, telekomunikacijų, medicinos ir daugelyje kitų sričių.

Valdyti lazerio generuotai šviesai naudojami įvairūs optiniai elementai: aukšto atspindžio veidrodžiai, poliarizatoriai, intensyvumo ir spektro filtrai ir kt. Taigi, atsižvelgiant į naujų optinių elementų poreikį ir nuolat tobulinamų technologijų reikalavimus, būtina detaliai išnagrinėti ir suprasti optinių dangų, dengiamų ant optinių paviršių, formavimo principus. Pagrindinės charakteristikos, kurias galima keisti vykdant standartinius optinių dangų nusodinimo procesus yra jų optiniai ir fiziniai parametrai – lūžio rodiklis, sugerties koeficientas ir storis. Vidinės plonų sluoksnių nanostruktūros valdymas atveria naujas galimybes formuoti naujus, dar sudėtingesnius kompleksinius optinius elementus. Taikymai gali būti įvairūs: fazę keičiantys elementai [6], apskritiminės poliarizacijos filtrai, biologiniai jutikliai ir kt. [6–8]. Gebant tiksliai valdyti visus nusodinimo parametrus, galima sukurti ne tik elementus su naujomis optinėmis savybėmis, bet ir atsparius galingai lazerio spinduliuotei. Medžiagų nanoinžinerija daro didelę įtaką didinant elementų lazerio indukuotą optinių dangų pažeidimo slenkstį plačiame spektriniame diapazone, įskaitant ir UV spektro sritį. Yra žinoma, kad porėti

sluoksniai atsparesni didesnei lazerio spinduliuotės energijai nei tankios medžiagos [9]. Tačiau didžioji dalis pademonstruotų tyrimų buvo paremti naudojant tik homogeniškų sluoksnių kombinacijas, kurios buvo pritaikytos įvairių konstrukcijų optinių dangų gamybai: atsparių lazerinei spinduliuotei skaidrinančių (AR) arba aukšto atspindžio (HR) dangų [10,11].

Plonų sluoksnių vidinės struktūros periodiškas modifikavimas yra labai patraukli ir perspektyvi mokslo ir technologijų sritis kurti novatoriškus elementus, tokius kaip fotoniniai kristalai regimajam šviesos diapazonui. Iki šiol to pasiekti nebuvo įmanoma dėl mažesnių nei bangos ilgiai periodiškų struktūrų formavimo poreikio [12]. Fotoninis kristalas - tai dielektrinių arba metalo-dielektrinių periodiškai išdėstytų nanostruktūrų visuma įtakojančių šviesos sklidimą panašiai kaip puslaidininkiniame kristale esantis periodinis potencialas veikia elektronų judėjimą [13]. Dėl periodiškai kristale pasikartojančių aukšto ir žemo lūžio rodiklio sričių atsiranda leidžiamos ir draudžiamos energijos juostos.

Vienos dimensijos (1D) fotoniniai kristalai yra populiarūs optinių dangų (daugiasluoksnių interferencinių dangų) pramonėje, formuojant įvairias AR, HR dangas. Tačiau didžiulis susidomėjimas dviejų (2D) ir trijų (3D) matmenų kristalais yra tiek fundamentiniame, tiek taikomajame moksle. Tokios struktūros yra patrauklios medicinoje ir biosensoriuose [14], valdant šviesos sklidimą [15], ir kt.

Pateikta disertacija orientuota į optinių elementų savybių tobulinimą bei kūrimą keičiant sluoksnių vidinę struktūrą. Pirmoje dalyje pateikti išsamūs nanostruktūrizuotų anizotropinių sluoksnių, pagamintų vien tik iš silicio dioksido medžiagos, tyrimai. Pademonstruota šių dangų pritaikymo privalumai formuojant fazines plokšteles ir poliarizatorius. Antroje dalyje, pademonstruota galimybė formuoti 2D fotoninius kristalus tolygiai nusodinant daugiasluoksnes optines dangas ant iš anksto periodiškai modifikuotų padėklų. Tokie naujoviški metodai leidžia sukurti nanostruktūrizuotus optinius elementus kurių galimi taikymai yra tiek didelės galios kompleksinėse lazerinėse sistemose, tiek mikrolazeriuose.

Disertacijos tikslas

Ištirti plonų sluoksnių su kontroliuojama vidine nano- ir mikro struktūra formavimo galimybes, taikant fizikinio garų nusodinimo technologijas, ir išplėsti lazerinės spinduliuotės valdymui naudojamų optinių elementų gamybos metodus.

Disertacijos moksliniai uždaviniai

1. Pritaikant garinimo kampu technologiją skurti naują nanostruktūrizuotų plonų sluoksnių, pasižyminčių mažais optiniais nuostoliais ir dideliu atsparumu lazerio spinduliuotei, formavimo metodą .

2. Sukurti fazinių plokštelių ir poliarizatorių nulio laipsnio kampui gamybos metodą, pritaikant garinimo kampu technologiją.

3. Ištirti dulkinimo jonų pluoštu technologijos galimybes tolygiam daugiasluoksnių optinių dangų nusodinimui ant periodiškai moduliuotų padėklų bei palyginti su kitomis plonų sluoksnių formavimo technologijomis.

4. Sukurti elemento, pasižyminčio kampiniu selektyvumu ir dideliu optiniu pralaidumu, formavimo metodą, pagrįstą daugiasluoksnių optinių dangų nusodinimu ant periodiškai moduliuoto paviršiaus.

5. Ištirti garinimo kampu technologijos galimybes valdyti nanostruktūrinių plonų sluoksnių, suformuotų ant periodiškai moduliuoto padėklo, geometriją.

Mokslinis naujumas ir praktinė vertė

Nuolatiniai medžiagų mokslo tyrimai tampa labai svarbūs siekiant suformuoti naujų ir nestandartinių optinių charakteristikų komponentus. Pagrindinis šios disertacijos naujumas tiek moksline, tiek praktine prasme – pademonstruota galimybė valdyti vidinę nusodinamų sluoksnių struktūrą i) parenkant tinkamą technologiją, ii) optimizuojant nusodinimo parametrus ir iii) parenkant tinkamą padėklą. Konkrečiai, mokslinis naujumas ir praktinė vertė gali būti apibendrinti šiais teiginiais:

- Sukurtas konceptualiai naujas porėtų anizotropinių bei tankių silicio dioksido plonų sluoksnių formavimo metodas, leidžiantis projektuoti daugiasluoksnes struktūras su mažais optiniais nuostoliais. Tai atveria galimybę pagaminti itin atsparias lazeriniam spinduliavimui (~40 J/cm^2) aukštos kokybės fazines plokšteles formuojant jas ant praktiškai bet kokio pagrindo.
- Pristatytas naujas poliarizatorių nulio laipsnio kampui formavimo metodas, statmenai sulygiuojant skirtingus silicio dioksido anizotropinius sluoksnius. Toks elementas pasižymi aukštu lazerio indukuotu pažaidos slenksčiu (~40 J/cm^2) veikiant nanosekundiniam režimui, 355 nm bangos ilgiui.
- Pirmą kartą buvo atliktas daugiasluoksnių optinių dangų, nusodintų ant padėklų su periodiškai moduliuotu paviršiumi, tyrimas naudojant

skirtingas dengimo technologijas (garinimą elektronų pluoštu, IBS, ALD). Tai leido atsirinkti perspektyviausią tolygaus sluoksnių nusodinimo technologiją – dulkinimą jonų pluoštu.

- Pirmą kartą buvo išsamiai ištirtas įvairių medžiagų (SiO_2, Ta_2O_5, Nb_2O_5 ir HfO_2), pagamintų jonapluoščio dulkinimo technologija ant periodiškai moduliuotų paviršių, augimas. Pademonstruota, kad moduliuotas dielektrinis plonas sluoksnis, turintis aukštą lūžio rodiklį, ir esantis mažo lūžio rodiklio aplinkoje, sudaro sąlygas rezonansiniam elektromagnetinės spinduliuotės surišimui. Tokia danga pasižymi optinio pralaidumo kampiniu ir dažniniu selektyvumu.
- Buvo pademonstruota, kad tinkamai parinkta medžiagų su dideliu ir žemu lūžio rodikliu 5 μm storio struktūra, tolygiai nusodinta ant periodiškai moduliuoto paviršiaus, gali būti prilyginta dvimačiam fotoniniam kristalui. Toks elementas galėtų būti integruotas į kompaktiškų mikrolazerių rezonatorius, erdviniam sugeneruotų skersinių modų selektyvumui.

Ginamieji teiginiai

1. Tankių ultra-plonų silicio dioksido sluoksnių įterpimas į porėtų nanostruktūrizuotų anizotropinių silicio dioksido sluoksnių struktūrą sustabdo kolonų plėtimąsi ir jungimąsi.
2. Kombinuojant skirtingo porėtumo ir anizotropiškumo silicio dioksido sluoksnius galima formuoti fazines plokšteles, pasižyminčias dideliu optiniu pralaidumu ir aukštu lazerio indukuoto pažaidos slenksčiu – 40 J/cm^2 veikiant 355 nm bangos ilgio spinduliuote nanosekundiniam režime.
3. Sukryžiuojant skirtingo anizotropiškumo silicio dioksido sluoksnių, turinčių vienodą efektyvųjį lūžio rodiklį abiem sluoksniams vienoje iš krypčių, optines ašis galima formuoti dangas, pasižyminčias skirtingomis optinėmis bei poliarizacinėmis savybėmis veikiant nulio laipsnio kampu ir turinčias aukštą lazerio indukuotą pažaidos slenkstį nanosekundiniam režime.
4. Periodiškai moduliuotas dielektrinis aukšto lūžio rodiklio plonas sluoksnis esantis žemo lūžio rodiklio aplinkoje sudaro sąlygas Fano rezonansui ir pasižymi šviesos kampiniu ir dažniniu selektyvumu.
5. Dvimatis fotoninis kristalas, pagrįstas periodiškai išdėstytų didelio ir mažo lūžio rodiklio sluoksnių, suformuotų fizikinio garų nusodinimo būdu ant periodiškai moduliuoto paviršiaus, pasižymi erdviniu spinduliuotės selektyvumu (< 2° pralaidumo juostos pusės pločio).

Aprobacija

Mokslinės publikacijos, tiesiogiai susijusios su disertacijos tema (žurnaluose, referuojamuose CA WoS duomenų bazėje):

1. **L. Grineviciute**, H. Badorreck, L. Jensen, D. Ristau, M. Jupé, A. Selskis, T. Tolenis "Impact of deposition conditions on nanostructured anisotropic silica thin films in multilayer interference coatings", Applied Surface Science, 562, 150167, 2021
2. **L. Grineviciute**, M. Andrulevičius, A. Melninkaitis, R. Buzelis, A. Selskis, A. Lazauskas, T. Tolenis "Highly Resistant Zero-Order Waveplates Based on All-Silica Multilayer Coatings", Phys. Status Solidi A, 1700764, 2017
3. **L. Grineviciute**, L. Ramalis, R. Buzelis, T. Tolenis "Highly resistant all-silica polarizing coatings for normal incidence applications" Optics letters, Vol. 46, No. 4, 2021
4. **L. Grineviciute**, C. Babayigit, D. Gailevičius, E. Bor, M. Turduev, V. Purlys, T. Tolenis, H. Kurt, K. Staliunas "Angular filtering by Bragg photonic microstructures fabricated by physical vapour deposition", Applied Surface Science, 481, 353-359, 2019
5. **L. Grineviciute**, C. Babayigit, D. Gailevičius, M. Peckus, M. Turduev, T. Tolenis, M. Vengris, H. Kurt, K. Staliunas "Nanostructured Multilayer Coatings for Spatial Filtering", Adv. Optical Mater. 2001730, 2021
6. **L. Grineviciute**, J. Nikitina, C. Babayigit, K. Staliunas "Fano-like Resonances in Nanostructured Thin Films for Spatial Filtering", Applied Physics Letters 118, 131114, 2021

Mokslinės publikacijos tiesiogiai susijusios su disertacijos tema (konferencijų publikacijos)

1. **L. Grineviciute**, K. Gricius, R. Buzelis, T. Tolenis "Anisotropic Optical Coatings for Polarization Control in High-power Lasers", OIC 2019, OCIS codes: 230.0230 Optical devices, proc. OSA, 2019
2. **L. Grineviciute**, K. Gricius, R. Buzelis, T. Tolenis "Optical anisotropic coatings for polarization control in high-power lasers", Proc. SPIE 11033, High-Power, High-Energy, and High-Intensity Laser Technology IV, 1103300, 2019

3. **L. Grineviciute,** L. Ramalis, K. Gricius, R. Buzelis, T. Tolenis, "Anisotropic coatings for normal incidence applications", Proc. SPIE 10691, 1069120, 2018
4. **L. Grineviciute**, R. Buzelis, M. Andrulevičius, A. Lazauskas, A. Selskis, R. Drazdys, T. Tolenis "Advanced design of UV waveplates based on nanostructured thin films", Proc. SPIE, Nanostructured Thin Films X, Vol. 10356, 103560Q, 2017

Kitos mokslinės publikacijos (žurnaluose, referuojamuose CA WoS duomenų bazėje):

1. **L. Grineviciute**, R. Buzelis, L. Mažulė, A. Melninkaitis, S. Kičas, T. Tolenis, "Enhancement of high reflectivity mirrors using the combination of standard and sculptured thin films" Optics & Laser Technology, Vol. 129, 106292, 2020
2. E. Buzavaite-Verteliene, A.Valavicius, **L. Grineviciute**, T. Tolenis, R. Lukose, G. Niaura, and Z. Balevicius "Influence of the graphene layer on the strong coupling in the hybrid Tamm-plasmon polariton mode", Optics Express, Vol. 28, No. 7/30 March, 2020
3. H. Badorreck, M. Steinecke, A. Farid, M. Jupé, D. Ristau, J. Müller, R. Tonneau, P. Moskovkin, S. Lucas, **L. Grineviciute**, A. Selskis, and T. Tolenis, "Correlation of structural and optical properties using Virtual Materials analysis", Optics Express, Vol. 27 Issue 16 p.p. 22209-22225, 2019
4. T.Tolenis, **L. Grineviciute**, L.Smalakys, M.Ščiuka, R.Drazdys, L.Mažulė, R.Buzelis, A. Melninkaitis "Next generation highly resistant mirrors featuring all-silica layers", Scientific reports, 7(10898), 2017
5. T.Tolenis, **L. Grineviciute**, R.Buzelis, L.Smalakys, E.Pupka, S.Melnikas, A.Selskis, R.Drazdys, and A.Melninkaitis "Sculptured anti-reflection coating for high power lasers", Optical Material Express, 7(4), 2017

Konferencijos, tiesiogiai susiję su disertacijos tema:

1. **L. Grineviciute,** D. Gailevicius, C. Babayigit, L. Ramalis, J. Nikitina, K. Staliunas, T. Tolenis "Deposition of multilayer optical coatings on corrugated surfaces for 2D photonic crystals formation", FM&NT, Vilnius, Lithuania, 23-26 November, 2020, Oral-Online

2. **L. Grineviciute**, R. Buzelis, R. Drazdys, T. Tolenis "The capabilities to form multilayer nanostructured coatings and their applications for waveplates production", ICTON, Angers, France, 9-13 July 2019, Oral pr.
3. **L. Grineviciute**, K. Gricius, R. Buzelis, T. Tolenis, "Anizotropic optical coatings for polarization control in high-power lasers", OSA Optical interference coatings, New Mexico, US, June 2-7, 2019, Oral/poster pr.
4. **L. Grineviciute**, K. Gricius, R. Buzelis and T. Tolenis "Optical anisotropic coatings for polarization control in high-power lasers", SPIE Optics and optoelectronics, Prague, Czech Republic, 1-4 April, 2019, Oral pr.
5. **L. Grineviciute**, L. Ramalis, R. Buzelis, A. Melninkaitis, T. Tolenis "Anisotropic optical interference coatings for polarization control in high-power lasers", ICLO, St.Petersburg, Russia, 4-8 June,2018 – Oral pr.
6. **L. Grineviciute**, A. Melninkaitis, A. Jasinskas, R. Buzelis, T. Tolenis "HR and AR nanostructured optical coatings for high-power applications", ICLO, St.Petersburg, Russia, 4-8 June,2018 – Poster pr.
7. **L. Grineviciute**, L. Ramalis, K. Gricius, R. Buzelis, T. Tolenis "Anisotropic coatings for normal incidence applications", Frankfurt, Germany, 14-17 May, 2018 – Poster pr.
8. **L. Grineviciute**, L. Petronis, R. Buzelis, T. Tolenis "Evaporated anisotropic nono-structured coatings for polarization control in high-power lasers", Nanophotonics and micro/nano optics international conference, Rugsėjo 13-15, 2017, Barcelona, Spain – Poster pr.
9. **L. Grineviciute**, R. Buzelis, M. Andrulevičius, A. Lazauskas, A. Selskis, R. Drazdys, T. Tolenis, "Advanced design of UV waveplates based on nanostructured thin films", SPIE, Nanostructured Thin Films X, August 9-10, 2017, San Diego, California, JAV – Oral pr.
10. **L. Grineviciute**, R. Buzelis, A. Melninkaitis and T. Tolenis "High resistive UV waveplates based on nanostructured anisotropic coatings" International Conference Nanotechnology and Innovation in the Baltic Sea Region, June 14 – 16, 2017 – Poster pr.
11. **L. Grinevičiūtė**, T. Tolenis, R. Buzelis, A. Selskis, R. Drazdys; "Investigation of serial bi-deposited nanostructured thin films for polarization control" 18-th International Conference-School ADVANCED MATERIALS AND TECHNOLOGIES August 27-31, 2016, Palanga, Lithuania – Poster pr.
12. **L. Grinevičiūtė**, A. Valavičius, T. Tolenis, R. Drazdys "Characterization of Nb_2O_5 and Ta_2O_5 coatings produced by electron beam evaporation with plasma source assistance" OPEN READINGS 2016, Vilnius, Lithuania, March 15-18, 2016 – Poster pr.

Autoriaus asmeninis ir bendraautorių indėlis

Disertacijos autoriaus ir pagrindinių bendraautorių indėlis pateiktas atsižvelgiant į rezultatų skyrius:

ANIZOTROPINĖS NANOSTRUKTŪRIZUOTOS DANGOS

Autorė pati atliko arba aktyviai dalyvavo planuojant visus eksperimentus. Taip pat atliko pati arba kuravo visus eksperimentinius plonų dangų nusodinimo procesus, atliko spektrofotometrinius, AFM matavimus ir nanostruktūrinių dangų analizę.

Dr. T. Tolenis dalyvavo planuojant visus eksperimentus, pasiūlė fazinių plokštelių ir poliarizatoriaus gamybos idėjas.

PhD stud. L. Ramalis atliko dalį eksperimentinių poliarizatorių garinimų bei matavimų.

K. Gricius, kuruojant autorei, atliko dalį anizotropinių vienasluoksnių dangų garinimų bei spektroskopinių matavimų.

Dr. M. Andrulevičius atliko XPS matavimus.

Dr. R. Buzelis and dr. A. Melninkaitis atliko LIDT matavimus.

Dr. H. Badorreck, dr. M. Jupé atliko MD simuliacijas.

DANGOS ANT MODULIUOTŲ PAVIRŠIŲ

Autorė pati planavo vienasluoksnių ir daugiasluoksnių dangų formavimo eksperimentus. Pati pagamino pagrindinį bandinį su periodiškai moduliuotu paviršiumi. Taip pat pati atliko arba kuravo visus spektroskopinius ir AFM matavimus, atliko rezultatų analizę.

Prof. dr. K. Staliūnas iškėlė erdvinių filtrų, pagrįstų daugiasluoksnių dangų formavimu, idėją ir kuravo visus teorinius skaičiavimus.

PhD stud. C. Babayigit atliko FDTD simuliacijas.

Dr. D. Gailevičius atliko erdvinio filtro matavimus lazerinėje sistemoje, pagamino pagrindinio struktūrizuoto bandinio kopijas.

J. Nikitina, kuruojant autorei, atliko dalį spektrofotometrinių ir AFM matavimų.

J. Bliūdžius, kuruojant autorei, atliko dangų nusodinimo procesus IBS.

Dr. A. Selskis atliko SEM matavimus (pateiktos SEM nuotraukos abiejuose skyriuose).

Literatūros apžvalga

Pirmajame disertacijos skyriuje pateikta literatūros apžvalga. Pradžioje trumpai aprašyti elementai, kurių savybės analizuojamos disertacijoje – fazinės plokštelės, poliarizatoriai ir erdviniai filtrai. Kitame poskyryje aprašomi įvairūs plonų sluoksnių nusodinimo metodai – garinimas elektronų pluoštu, jonapluoštis dulkinimas bei aprašomi bendri optinių dangų formavimosi principai. Taip pat literatūros apžvalgoje supažindinama su garinimo kampu metodika bei optinių dangų formavimu ant struktūrizuotų paviršių. Aprašant nusodinimą ant struktūrizuotų paviršių išskiriami du pagrindiniai atvejai – kai danga tolygiai atkartoja paviršių, ir kai danga formuojama su valdoma vidine struktūra (su kontroliuojamos geometrijos individualiais dariniais).

Eksperimentinės metodikos

Antrame disertacijos skyriuje pateikiami visų disertacijos darbe naudotų eksperimentinių metodikų aprašymai. Skyrius padalintas į tris dalis: optinių charakteristikų nustatymas, struktūros tyrimai bei eksperimentinių bandinių gamyba. Pirmame poskyryje trumpai aprašomi matavimams naudoti prietaisai – spektrofotometras, elipsometras bei lazerinės spinduliuotės indukuoto pažaidos slenksčio matavimo metodas. Antrame poskyryje aprašomi vidinės struktūros ir morfologijos matavimo metodai: atominių jėgų mikroskopija, skenuojanti elektronų mikroskopija ir rentgeno spindulių fotoelektronų spektroskopija. Trečiame poskyryje aprašoma eksperimentinė anizotropinių sluoksnių formavimo metodika, paremta garinimo kampu technologija.

Rezultatai

Dėl kompleksinių tyrimų ir skirtingų eksperimentinių metodų, skirtų valdyti nusodinamų dangų nanostruktūrą, buvo nuspręsta padalinti rezultatų skyrių į dvi dalis: anizotropines nanostruktūrizuotas dangas ir dangas ant moduliuotų paviršių.

ANIZOTROPINĖS NANOSTRUKTŪRIZUOTS DANGOS

Pirmiesiems disertacijos darbo eksperimentams kaip pagrindinės kandidatės, tinkamos plonų dangų formavimui regimajam ir UV spektriniams

diapazonams, buvo pasirinktos trys skirtingos medžiagos – SiO_2, Al_2O_3 ir LaF_3. Po išsamios analizės tolesniems eksperimentus buvo pasirinkta silicio dioksido medžiaga, pasižyminti sąlyginai didesniu lazerio indukuotos pažaidos slenksčiu. Eilė eksperimentų buvo atlikti dangas formuojant SBD metodu 66, 70, 72, 74, 76, 78, 80 ir 84 laipsnių kampais, siekiant nustatyti plonų sluoksnių su didžiausia optine anizotropija optimalų garinimo kampą. Atlikus išsamią elipsometrinių, spektrometrinių matavimų bei struktūros anizotropijos įvertinimo autokoreliacijos metodu analizę, buvo nustatyta, kad 70 laipsnių kampas yra optimalus norint pasiekti didžiausią dvejopalaužiškumą – didžiausią efektinių lūžio rodiklių skirtumą.

Sekančiam etape buvo atlikti dviejų ir šešių sluoksnių optinių dangų struktūrų detalūs tyrimai ir analizė siekiant išsiaiškinti kolonų plėtimosi ir optinių nuostolių atsiradimo efektus, o taip pat nustatyti optimalius parametrus tankaus sluoksnio formavimui išsaugant anizotropinio porėto sluoksnio savybes.

Anizotropinių dangų taikymas optinių elementų formavimui

Kombinuojant nusodinamus vienos medžiagos sluoksnius su skirtingu porėtumu bei anizotropiškumu, galima formuoti dangas pasižyminčias tiek dvejopalaužiškumu, tiek poliarizacinėmis savybėmis. Tokios dangos gali būti naudojamos unikaliems optiniams elementams formuoti: fazinėms plokštelėms ir poliarizatoriams. Šie elementai pagaminti optinių dangų pagrindu vien tik iš silicio dioksido medžiagos gali būti formuojami ant praktiškai bet kokios medžiagos, pvz., stiklo, metalo, kristalų, plokščio paviršiaus ir taikomi tiek didelės galios kompleksinėse lazerinėse sistemose, tiek mikrosistemose.

Nulinės eilės fazinės plokštelės

Šiame skyriuje pristatomas naujas interferencinių optinių dangų, pasižyminčių dvejopalaužiškumu, formavimo metodas naudojant amorfinę medžiagą. Tai garinimo kampu metodas, kuris naudojamas nusodinti anizotropinius skirtingo porėtumo sluoksnius. Kombinuojant šiuos anizotropinius sluoksnius su tos pačios medžiagos tankiais sluoksniais, galima formuoti interferencines dangas. Atsižvelgiant į nusodinimo procesų parametrus sluoksniai, suformuoti iš silicio dioksido medžiagos, dėl skirtingo dangos porėtumo, gali pasižymėti skirtingais nuo 1,41 iki 1,13 efektyviaisiais lūžio rodikliais plačiame spektro diapazone .

Modeliuojant fazinės plokštelės dangos struktūrą būtina atkreipti dėmesį į kelis aspektus: i) siekiant maksimalaus optinio pralaidumo svarbu turėti mažiausią sluoksnių skaičių, ii) siekiant išvengti atskirų kolonų susijungimo, galinčio sukelti optinę sklaidą atskirų anizotropinių sluoksnių storis privalo būti mažesnis nei 400 nm, iii) bendras anizotropinių sluoksnių storis turi užtikrinti fazinės plokštelės ketvirčio arba pusės bangos ilgio įnešamą vėlinimą.

Sumodeliuota ketvirčio bangos ilgio fazinės plokštelės struktūra, kurios elektromagnetinio lauko pasiskirstymas $|E|^2$ pavaizduotas atitinkamai sluoksnių išsidėstymui, parodytas 1 Pav. a). Vienas iš būdų siekiant didesnės optinės dangos LIDT vertės yra elektrinio lauko, praeinančio per daugiasluoksnę dangą, optimizavimas. Mūsų atveju dauguma maksimalaus elektrinio lauko intensyvumo smailių sutampa su porėtais silicio dioksido sluoksniais, tačiau viena smailė sutampa su paskutiniuoju tankiu sluoksniu, mažiau atspariu lazerinei spinduliuotei. Tai skatina mus ateityje tęsti darbą optimizuojant elektrinį lauką nanoskulptūrinėse dangose norint gauti dar geresnius LIDT rezultatus. Sumodeliuota dangos struktūra buvo eksperimentiškai suformuota, o jos pralaidumo ir fazės vėlinimo skirtumo dispersijos parodytos 1 Pav. b paveiksle.

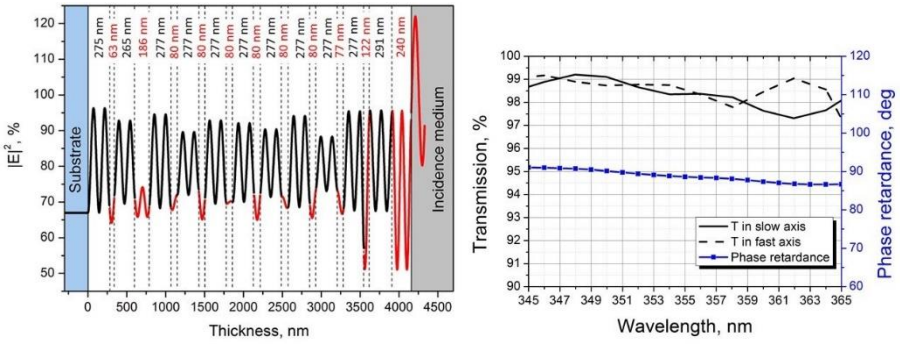

1 Pav. a) Sumodeliuota daugiasluoksnės fazinės plokštelė struktūra su elektrinio lauko pasiskirstymu išilgai dangos storio. b) Suformuotos fazinės plokštelės optiniai matavimai: lėtos ir greitos ašies optiniai pralaidumo matavimai (juodos kreivės); fazės vėlinimo skirtumo matavimas (mėlyna kreivė).

Suformuotos fazinės plokštelės lazerio indukuotas pažaidos slenkstis buvo išmatuotas nanosekundiniame režime 355 nm bangos ilgiui. Lazerio pluošto diametrui esant 220 μm, LIDT buvo gautas 11.5 J/cm^2, matuojant 1–į–1 metodu. Tačiau šis matavimas buvo įtakotas įvairių defektų, esančių dangoje. Siekiant įvertinti defektų įtaką ta pati danga buvo testuojama dar kartą su

mažesnio diametro spinduliu – 59 μm. Matuojant tokiu pačiu metodu buvo gauta 24.4 J/cm^2 LIDT vertė. Detaliai išanalizavus pažaidos tikimybės grafiką, buvo pastebėta, kad, suformavus tokį elementą be defektų, galima būtų pasiekti 40 J/cm^2 vertę.

Poliarizatoriai nulio laipsnių kampui

Dviejų skirtingo anizotropiškumo sluoksnių su skirtingais efektiniais lūžio rodikliais kombinacija leidžia formuoti dangas su poliarizacinėmis savybėmis, veikiant šviesai krentančiai statmenai (nulio laipsnių kampu). Principinė poliarizatoriaus vidinė struktūra ir skirtingais nusodinimo kampais – 0°, 66° ir 70° suformuotų SiO_2 sluoksnių efektiniai lūžio rodikliai pavaizduoti 2 Pav.

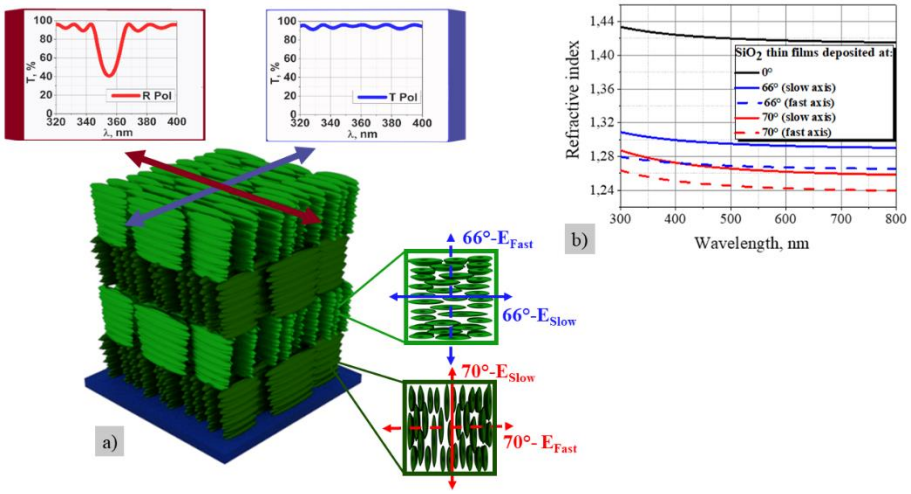

2 Pav. a) Principinė schema, vaizduojanti poliarizatoriaus struktūrą, kurią sudaro anizotropiniai sluoksniai su statmenai sulygiuotomis optinėmis ašimis. b) Dangų, suformuotų skirtingais nusodinimo kampais, efektiniai lūžio rodikliai.

Nusodinant silicio dioksido anizotropines dangas su skirtingu porėtumu ir sukryžiuotomis optinėmis ašimis, tačiau su vienu vienodu efektyviuoju lūžio rodikliu abiem sluoksniams vienoje iš ašių, sukuriamas skirtingas optinis atsakas (skirtingas poveikis elektromagnetinei spinduliuotei) statmenoms poliarizacijoms. Kaip pavaizduota 2 Pav. b), greitosios ir lėtosios ašies lūžio rodikliai sutampa sluoksniams užgarintiems esant 66° ($n_{fast}^{66} = 1.27$) ir 70° ($n_{slow}^{70} = 1.27$) kampams. Taigi, nusodinant šiuos sluoksniu taip, kad jų

optinės ašys sukryžiuojamos (n_{fast}^{66} sutampa su n_{slow}^{70}), gaunama dangos kombinacija, prilyginama ištisiniam storam sluoksniui – efektyvieji lūžio rodikliai yra vienodi. Tačiau statmenai poliarizacijai efektyviųjų lūžio rodiklių skirtumas tarp sluoksnių yra 0.054. Tokia struktūra atitinka sluoksnių su dideliu ir mažu lūžio rodikliu interferencinę atspindinčią dangą. Taigi, poliarizacija, kuri dangą „mato“ kaip vieną sluoksnį – disertacijoje pavadinome „T Pol“ (didesnis pralaidumas), o jai statmena poliarizacija „R Pol“ (didesnis atspindys). Sumodeliuoti įvairūs dangų optinio pralaidumo spektrai, atitinkantys skirtingas konstrukcijas, pavaizduoti 3 Pav.

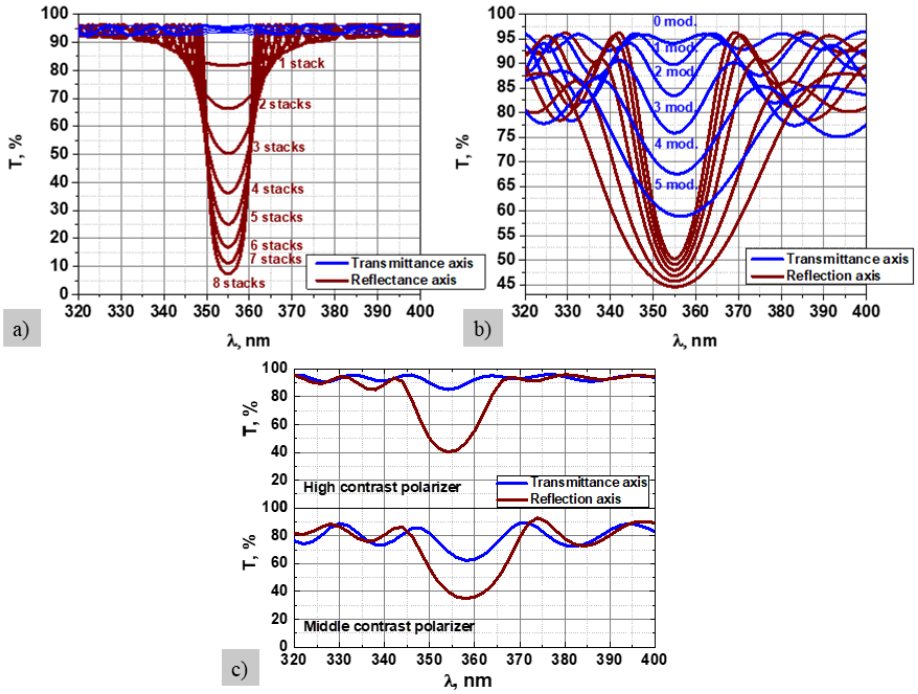

3 Pav. Sumodeliuoti ir pamatuoti optiniai pralaidumai T ir R poliarizacijoms: a) didelio kontrasto poliarizatorius, kai T poliarizacija visiškai praleidžiama, b) vidutinio kontrasto poliarizatorius, kai abi poliarizacijos dalinai atspindimos/praleidžiamos, c) suformuotų poliarizatorių eksperimentiniai matavimai nulio laipsnių kampu, R ir T poliarizacijoms.

Lazerio indukuotas pažaidos slenkstis, nanosekundiniame režime 355 nm bangos ilgiui buvo išmatuotas suformuotam didelio kontrasto poliarizatoriui. Esant spindulio diametrui ~ 60 μm, LIDT vertės buvo 39.0 J/cm^2 and 48.5 J/cm^2, atitinkamai R ir T poliarizacijoms. Šios vertės buvo nustatytos

atsižvelgiant į pažaidos tikimybių grafiką, kai tikimybė pažeisti dangą yra 50 %.

DANGOS ANT STRUKTŪRIZUOTŲ PADĖKLŲ

Šiame disertacijos skyriuje pristatomi optinių elementų su periodiškai moduliuota vidine nanostruktūra tyrimai. Pateikiami du dielektrinių optinių dangų nusodinimo ant moduliuotų paviršių, naudojant fizikines garų technologijas, metodai: tolygus dangos nusodinimas atkartojant pradinę paviršiaus geometriją ir netolygus augimas – formuojant sluoksnį su individualia periodiška mikrostruktūra.

Tolygus sluoksnių nusodinimas

Pirmajame poskyryje pateikiama temos motyvacija, paaiškinanti periodiškai nanostruktūrizuotų optinių elementų, suformuotų optinių dangų pagrindu, reikalingumą. Taip pat pateikiama FDTD simuliacijos pagalba sugeneruota tikslinė elemento konstrukcija, pasižyminti kampiniu prasklindančios šviesos selektyvumu – erdvinio filtravimo savybėmis.

Pateikiami konkretūs tikslinės struktūros parametrai: skersinis periodas (moduliuoto padėklo paviršiaus periodas) – 600 nm, išilginis periodas (individualus kiekvieno sluoksnio optinis storis) – 310 nm, sluoksnių skaičius – 33, naudotinų medžiagų lūžio rodiklio skirtumas – < 0,2.

Sekančiame poskyryje pristatomi pagrindų su moduliuotu paviršiumi gamybos rezultatai. Pagrindinis bandinys (gardelė) su 600 nm periodu buvo suformuotas lazerinės interferencinės litografijos metodu. Kadangi šiuo metodu struktūra buvo užrašoma polimerinio fotorezisto paviršiuje, kuris sugeria šviesą ir yra jautrus aplinkos pokyčiams, eksperimente naudotos struktūros pagamintos replikavimo būdu. Kopijos buvo pagamintos iš “Ormocomp” optiškai skaidraus hibridinio polimero.

Pirmieji optinių dangų ant struktūrizuotų paviršių nusodinimo procesai buvo atlikti naudojant kelias skirtingas plonų sluoksnių dengimo technologijas: garinimo elektronų pluoštu (E-beam), jonapluoštį dulkinimą (IBS) ir atominio sluoksnio nusodinimo (ALD) technologiją. IBS technologija buvo atrinkta kaip pati perspektyviausia pradinės struktūros atkartojimui, nes padengus 2,4 μm storio dangą, paviršiaus moduliacijos gylis pasikeitė mažiausiai – nuo 200 nm iki 100 nm.

Būtent IBS technologija ir buvo pasitelkta tolimesniems vienasluoksnių ir daugiasluoksnių struktūrų nusodinimo eksperimentams. 4.1.4 skyriuje

pateikiama struktūrinė vienasluoksnių HfO_2, Ta_2O_5, Nb_2O_5 ir SiO_2 dangų analizė. Nustatyta, kad pradinės moduliacijos atkartojamumas priklauso ne tik nuo nusodinimo technologinių parametrų, bet ir nuo pačios medžiagos savybių, pvz., molekulinio svorio. Lengvesni atomai yra labiau išbarstomi lekiant iš taikinio link bandinio paviršiaus ir netenka energijos susidūrę su dujomis kameroje, dėl ko formuojasi porėtesnis sluoksnis.

Sekančiame poskyryje (4.1.5) tyrinėjamos optinės vienasluoksnių HfO_2, Ta_2O_5, Nb_2O_5 ir SiO_2 dangų, nusodintų ant struktūrizuotų paviršių, savybės. Eksperimentinių sluoksnių pralaidumo spektrų tyrimai parodė, kad esant dideliam sluoksnio lūžio rodikliui, atsiranda rezonansinės sritys, kurios gali būti siejamos su Fano rezonansu arba – dviejų osciliavimų bangolaidinės ir Fabry-Perot modos surišimu (angl. coupling). Ta_2O_5 medžiagos vienasluoksnės dangos buvo ištirtos detaliau suformuojant 200 nm, 350 nm, 500 nm, 700 nm ir 900 nm fizinio storio dangas. Esant didesniam sluoksnio storiui, jame sužadinamos aukštesnių eilių bangolaidinės modos. Pagrindinė šio skyriaus išvada – periodiškai moduliuotas sluoksnis su dideliu lūžio rodikliu (n = 2.09), esantis mažo lūžio rodiklio aplinkoje ($n_{pagrindo}$ = 1.5 ir n_{oro} = 1), tenkina Fano rezonanso sąlygas ir pasižymi tiek erdviniu, tiek spektriniu prasklindančios spinduliuotės selektyvumu.

4.1.6 skyriuje tyrinėjamos daugiasluoksnės struktūros, nusodintos ant periodiškai moduliuotų padėklų bei pademonstruojamas jų erdvinis selektyvumas. Pirmiausia, didelis dėmesys buvo skirtas technologinių procesų optimizavimui. Atsižvelgiant į elemento konstrukciją, svarbu ne tik išlaikyti kuo vienodesnį moduliacijos gylį augant sluoksniams, bet taip pat svarbu išvengti struktūros šlyties.

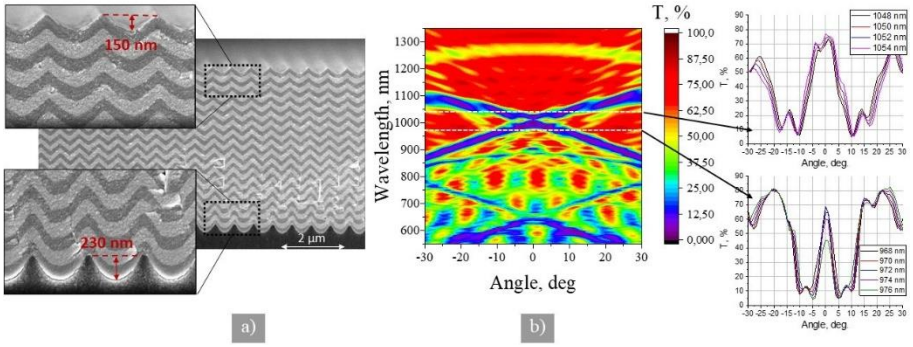

4 Pav. Daugiasluoksnės HfO_2-Nb_2O_5 dangos ant moduliuoto paviršiaus a) skerspjūvio SEM nuotrauka, b) pralaidumo žemėlapis ir pjūviai konkretiems bangos ilgiams.

Po optimizavimo eksperimentų ir tinkamų medžiagų parinkimo, buvo skaitmeniškai sumodeliuota tikslinė elemento konstrukcija, kuri suformuota 4.1.1 poskyryje. HfO_2-Nb_2O_5 dangos, nusodintos naudojant IBS technologiją, 33 sluoksnių skerspjūvis ir optinio pralaidumo žemėlapis pavaizduoti 4 Pav.

Erdviniu filtravimu pasižyminčios daugiasluoksnės dangos, nusodintos ant moduliuoto padėklo, suminis storis yra ~5 μm, tačiau moduliacijos gylis pasikeitė tik nuo 230 nm iki 150 nm. Nežymus struktūros užlygėjimas nesutrukdė pasiekti erdvinio filtravimo savybių. Iš spektrinių matavimų rezultatų matoma, kad pralaidumo juostos pusplotis (centrinis pralaidumas) siekia apie 2° ties 970 nm bangos ilgiu. Taigi, tokia fotoninio kristalo savybėmis pasižyminti struktūra, pagaminta optinių dangų tolygaus nusodinimo ant struktūrizuoto padėklo būdu, gali būti naudojama kaip elementas pasižymintis erdviniu selektyvumu. Toks elementas potencialiai gali būti taikomas kompaktiškose mikrolazerinėse sistemose.

Netolygus sluoksnių nusodinimas ant moduliuotų paviršių

Šiame skyriuje aprašomos periodiškos mikrostruktūros formavimo galimybės, dangą nusodinant ant periodiškai moduliuotų padėklų. Pristatomi tyrimai apjungiantys prieš tai aptartų metodų idėjas – SBD metodu nusodinamos dangos ant periodiškai struktūrizuoto paviršiaus. Eksperimentai buvo atliekami naudojant mažų energijų procesą – garinimą elektronų pluoštu ir garinimo kampu metodiką. Ši dvipusio garinimo dangų formavimo metodika yra analogiška anizotropinių dangų formavimo metodikai (3 skyrius).

Eksperimentai buvo atliekami esant dviems skirtingiems gardelės rėžių išdėstymams: lygiagrečiai ir statmenai medžiagos garavimo srautui. Norint formuoti dangą su periodine mikrostruktūra, rėžių padėtis turi būti statmena nusėdančių dalelių srautui. Iškilūs gardelės rėžiai sukuria šešėlį, į kurį negali patekti atlekiančios dalelės, ko pasėkoje formuojasi sluoksnis su individualių kolonų struktūra. Pasirenkant tinkamą garinimo kampą, galima valdyti besiformuojančių kolonų pločius. Kai garinimo kampas kinta nuo 50˚ iki 80˚, kolonos formuojasi su atitinkamai 0.55 iki 0.24 μm pradiniu pločiu. SiO_2 dangų skerspjūvių SEM nuotraukos pavaizduotos 5 Pav.

Šiame skyriuje pademonstruojama, kad, esant optimaliam 70° garinimo kampui, galima suformuoti mikrodarinius su individualia ir tvarkinga struktūra. Būtent šiuo kampu nusodinant SiO_2 medžiagą SBD metodu ant gardelės su 600 nm periodu, individualios kolonos iki 3 μm aukščio išlieka nesusijungusios.

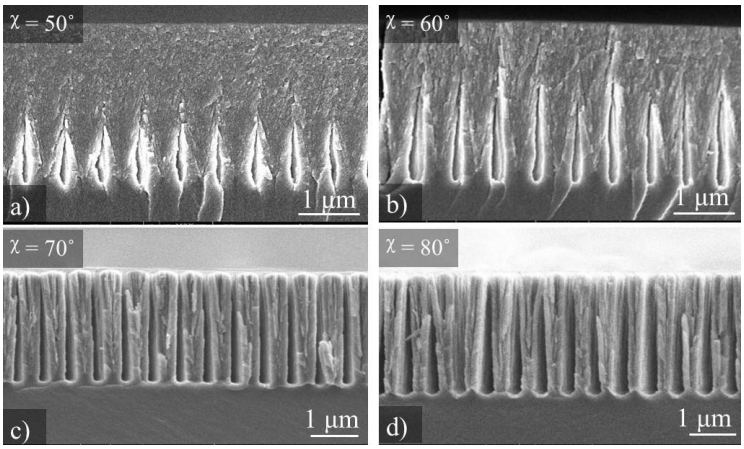

5 Pav. Vienasluoksnių SiO_2 dangų skerspjūvių SEM nuotraukos. Dangos suformuotos gardelės rėžiams esant statmenai garavimo srautui, SBD metodu skirtingais kampais χ a) 50°, b) 60°, c) 70° ir d) 80°

Periodinės nano- ir mikrostruktūros, turinčios didelį paviršiaus plotą ir valdomą vidinę geometriją/porėtumą, yra jautrios besikeičiančioms aplinkos sąlygoms. Todėl perspektyvoje gali būti taikomos įvairių jutiklių formavimui.

Pagrindiniai rezultatai ir išvados

Lazerio indukuoto pažaidos slenksčio matavimai rodo du kartus didesnį silicio dioksido nanostruktūrizuotų dangų optinį atsparumą, lyginant su aliuminio oksidu ar lantano fluoridu. Naudojant garinimo kampu metodiką, anizotropinių SiO_2 optinių dangų formavimui optimalus nusodinimo kampas, kuomet pasiekiama didžiausia struktūros anizotropija, yra 70°.

Darbe parodyta, kad tankus silicio dioksido sluoksnis, įterptas į koloninę silicio dioksido struktūrą, gali tarnauti dviem tikslams: padeda išvengti kolonų susijungimo ir yra tinkamas naujas plokščias pagrindas kitam nanostruktūrizuotam sluoksniui formuoti. Tai leidžia pagaminti aukštos kokybės fazines plokšteles, itin atsparias lazeriniam spinduliavimui (~40 J/cm^2) ir suformuoti jas ant praktiškai bet kokio plokščio pagrindo.

Statmenai sulygiuojant dviejų skirtingo anizotropiškumo silicio dioksido sluoksnių optines ašis buvo suformuotas poliarizatorius nulio laipsnių kampui. Toks elementas pasižymi dideliu lazerio indukuotu pažaidos slenksčiu (~39.0 J/cm^2 ir 48.5 J/cm^2 statmenoms tiesinėms poliarizacijoms) veikiant, 355 nm bangos ilgio nanosekundinės trukmės impulsais.

Išsamiai ištirtas dangų, pagamintų iš įvairių medžiagų (SiO_2, Ta_2O_5, Nb_2O_5 ir HfO_2), nusodintų ant moduliuoto paviršiaus naudojant jonapluoščio dulkinimo technologiją, formavimosi procesas. Pademonstruota, kad moduliuotas dielektrinis plonas sluoksnis, turintis aukštą lūžio rodiklį, ir esantis mažo lūžio rodiklio aplinkoje, tenkina rezonansinio ryšio sąlygas ir pasižymi spektriniu ir erdviniu selektyvumu. Tai gali būti pritaikoma erdviniam ir dažniniam šviesos filtravimui.

Nb_2O_5 ir HfO_2 medžiagų kompaktiška 5 μm storio daugiasluoksnė struktūra, tolygiai nusodinta ant periodiškai moduliuoto paviršiaus, pasižymi erdviniu selektyvumu. Toks elementas galėtų būti tinkamas kompaktiškoms mikrolazerinėms sistemoms.

Naudojant serijinio dvipusio garinimo metodą ir periodiškai moduliuotą padėklą, galima valdyti auginamų sluoksnių vidinę mikrostruktūrą. Nusodinant SiO_2 dangą SBD metodu 70° kampu ant statmenai garų srautui orientuotos 600 nm periodo gardelės, įmanoma suformuoti iki 3 μm aukščio individualių kolonų struktūrą.

PADĖKA

Niekada nesvajojau būti mokslininke ir niekada negalvojau, kad studijuosiu fiziką. Tačiau atėjus lemiamiems vidurinės mokyklos metams teko rinktis, ką veikti gyvenime toliau. Neturėdama aiškaus tikslo, pagalvojau, kad reikia studijuoti tai, kas būtų universalu ir pabaigus visi keliai būtų atviri. Pagalvojau, po tų keturių metų, tada nuspręsiu ką daryti toliau. Ir pasirinkau KTU taikomąją fiziką. Ir tai buvo pats geriausias sprendimas mano gyvenime!

Už tai pirmiausia norėčiau padėkoti savo šeimai, ypač tėvams, kad turėjau laisvą galimybę rinktis, kad besąlygiškai palaikė visur ir visada (kad ir kokie nesuprantami kartais būna tie sprendimai).

Noriu padėkoti savo bakalauro vadovui dr. Mindaugui Andrulevičiui, kad su hologramomis sužadino tą mokslininko gyslelę. Taip pat prof. Valentinui Snitkai ir visiems KTU kolegoms, kad turėjau galimybę magistro tiriamųjų darbų metu pasisemti daug patirties ir išmokti mokslininkui būdingo savarankiškumo.

Dėkoju savo doktorantūros vadovui dr. Ramučiui Drazdžiui už tai, kad dar magistrantūros studijų metu priėmė į Optidos ir FTMC Optinių dangų laboratorijos kolektyvą. Už laisvę pasirinkti mokslinę kryptį ir pagalbą rengiant disertacijos darbą. Taip pat už motyvuojantį posakį:

„Nori – tūkstantis galimybių, nenori – tūkstantis pasiteisinimų”

Ypatingai norėčiau padėkoti dr. Tomui Toleniui už tai, kad įvedė į skulptūrinių dangų pasaulį, dalinosi tiek idėjomis, tiek turima patirtimi ir lydėjo visą doktorantūros laikotarpį.

Norėčiau padėkoti prof. Kęstučiui Staliūnui už naują tematiką mano doktorantūros kelyje ir konsultacijas. Taip pat ir dr. Dariui Gailevičiui už palaikymą ir linksmas diskusijas.

Dėkoju savo studentams: Julianijai Nikitinai ir Karoliui Griciui už pagalbą atliekant eksperimentinius darbus.

Taip pat ypatingai dėkoju ir visam FTMC Optinių dangų laboratorijos kolektyvui, ypač Lukui Ramaliui, Audriui Valavičiui, Simui Melnikui, Ryčiui Buzeliui ir kitiems už malonią ir įkvepiančią atmosferą, smagias diskusijas ir pagalbą.

BIBLIOGRAPHY

1. S. Paetrow, Better Vision: Carl Zeiss Eyeglass Lenses 1912-2012, Verlag Hanseatischer Merkur ; Carl Zeiss Archives, (2012).
2. T. H. Maiman, "Stimulated Optical Radiation in Ruby," Nature **187**, 493–494 (1960).
3. F. J. McClung and R. W. Hellwarth, "Giant Optical Pulsations from Ruby," Appl. Opt. **1**, 103 (1962).
4. W. J. Hogan, E. I. Moses, B. E. Warner, M. S. Sorem, and J. M. Soures, "The National Ignition Facility," Nucl. Fusion **41**, 567–573 (2001).
5. J. J. Zayhowski and A. Mooradian, "Single-frequency microchip Nd lasers," Opt. Lett. **14**, 24 (1989).
6. M. Suzuki, T. Itoh, and Y. Taga, "Recent progress of obliquely deposited thin films for industrial applications," in A. Lakhtakia and R. F. Messier, eds., p. 94. (1999)
7. A. Lakhtakia, V. C. Venugopal, and M. W. McCall, "Spectral holes in Bragg reflection from chiral sculptured thin films: circular polarization filters," Opt. Commun. **177**, 57–68 (2000).
8. I. Abdulhalim, A. Karabchevsky, C. Patzig, B. Rauschenbach, B. Fuhrmann, E. Eltzov, R. Marks, J. Xu, F. Zhang, and A. Lakhtakia, "Surface-enhanced fluorescence from metal sculptured thin films with application to biosensing in water," Appl. Phys. Lett. **94**, 063106 (2009).
9. I. M. Thomas, "High laser damage threshold porous silica antireflective coating," Appl. Opt. **25**, 1481 (1986).
10. K. M. A. Sobahan, Y. J. Park, J. J. Kim, and C. K. Hwangbo, "Nanostructured porous SiO2 films for antireflection coatings," Opt. Commun. **284**, 873–876 (2011).
11. T. Tolenis, L. Grinevičiūtė, L. Smalakys, M. Ščiuka, R. Drazdys, L. Mažulė, R. Buzelis, and A. Melninkaitis, "Next generation highly resistant mirrors featuring all-silica layers," Sci. Rep. **7**, 10898 (2017).
12. S. Dhuey, A. Testini, A. Koshelev, N. Borys, J. R. Piper, M. Melli, P. J. Schuck, C. Peroz, and S. Cabrini, "Three-dimensional woodpile photonic crystals for visible light applications," J. Phys. Commun. **1**, 015004 (2017).
13. Y. Dahman, "Electronic and Electro-Optic Nanotechnology, By Yaser Dahman, Dang Le, Natasha Niznik, and Niroshitha Sadyathasan.," in Nanotechnology and Functional Materials for Engineers, Elsevier , pp. 191–206, (2017)
14. X. Yueshuang and C. Baoan, "Applications of Photonic Crystals in Medicine," Clin. Lab. **61**, (2015).
15. P. Halevi, A. A. Krokhin, and J. Arriaga, "Photonic crystals as optical components," Appl. Phys. Lett. **75**, 2725–2727 (1999).
16. M. Bass and Optical Society of America, eds., Handbook of Optics, 2nd ed, McGraw-Hill, (1995).

17. X. Zhang, F. Wu, L. Qi, X. Zhang, and D. Hao, "Phase Retardation and Birefringence of the Crystalline Quartz Plate in the Ultraviolet and Visible Spectrum," arXiv:1411.2811v1 [physics.optics], (2014).
18. G. G. Wells and C. V. Brown, "Multistable liquid crystal waveplate," Appl. Phys. Lett. **91**, 223506 (2007).
19. J. He, X. Fang, Y. Lin, and X. Zhang, "Polarization control in flexible interference lithography for nano-patterning of different photonic structures with optimized contrast," Opt. Express **23**, 11518 (2015).
20. D. J. Little, M. Ams, P. Dekker, G. D. Marshall, J. M. Dawes, and M. J. Withford, "Femtosecond laser modification of fused silica: the effect of writing polarization on Si-O ring structure," Opt. Express **16**, 20029 (2008).
21. M. Cerchez, R. Jung, J. Osterholz, T. Toncian, O. Willi, P. Mulser, and H. Ruhl, "Absorption of ultrashort laser pulses in strongly overdense targets," Phys. Rev. Lett. **100**, 1–4 (2008).
22. P. H. Tuan, M. C. Tsai, and Y. F. Chen, "Exploiting birefringent thermal lensing effect to manipulate polarization states of an Nd:YVO_4 self-mode-locked laser," Opt. Express **25**, 29000 (2017).
23. B. V. Romain Gaume, "Optical and thermo-mechanical properties of solid-state laser materials," Ann. Chim. Sci. Matér. **28**, 89–102 (2003).
24. V. Zhupanov, I. Kozlov, V. Fedoseev, P. Konotopov, M. Trubetskov, and A. Tikhonravov, "Production of Brewster angle thin film polarizers using a ZrO_2/SiO_2 pair of materials," Appl. Opt. **56**, C30 (2017).
25. L. Grinevičiūtė, M. Andrulevičius, A. Melninkaitis, R. Buzelis, A. Selskis, A. Lazauskas, and T. Tolenis, "Highly Resistant Zero-Order Waveplates Based on All-Silica Multilayer Coatings," Phys. Status Solidi A **214**, 1700764 (2017).
26. L. Grineviciute, L. Ramalis, R. Buzelis, and T. Tolenis, "Highly resistant all-silica polarizing coatings for normal incidence applications," Opt. Lett. **46**, 916 (2021).
27. P. M. Celliers, K. G. Estabrook, R. J. Wallace, J. E. Murray, L. B. Da Silva, B. J. MacGowan, B. M. Van Wonterghem, and K. R. Manes, "Spatial filter pinhole for high-energy pulsed lasers," Appl. Opt. **37**, 2371 (1998).
28. "https://www.optigrate.com/BragGrate_Spatial.html," (2021).
29. L. Maigyte, T. Gertus, M. Peckus, J. Trull, C. Cojocaru, V. Sirutkaitis, and K. Staliunas, "Signatures of light-beam spatial filtering in a three-dimensional photonic crystal," Phys. Rev. A **82**, 043819 (2010).
30. D. Gailevičius, V. Purlys, and K. Staliunas, "Photonic crystal spatial filters fabricated by femtosecond pulsed Bessel beam," Opt. Lett. **44**, 4969 (2019).
31. V. Purlys, L. Maigyte, D. Gailevičius, M. Peckus, M. Malinauskas, and K. Staliunas, "Spatial filtering by chirped photonic crystals," Phys. Rev. A **87**, 033805 (2013).

32. L. Maigyte, "Shaping of light beams with photonic crystals: spatial filtering, beam collimation and focusing," PhD Thesis (2014).
33. L. Grineviciute, C. Babayigit, D. Gailevičius, E. Bor, M. Turduev, V. Purlys, T. Tolenis, H. Kurt, and K. Staliunas, "Angular filtering by Bragg photonic microstructures fabricated by physical vapour deposition," Appl. Surf. Sci. **481**, 353–359 (2019).
34. L. Grineviciute, C. Babayigit, D. Gailevičius, M. Peckus, M. Turduev, T. Tolenis, M. Vengris, H. Kurt, and K. Staliunas, "Nanostructured Multilayer Coatings for Spatial Filtering," Adv. Opt. Mater. 2001730 (2021).
35. H. A. Macleod, Thin-Film Optical Filters, 3rd ed, Institute of Physics Pub, (2001).
36. A. Thelen, Design of Optical Interference Coatings, McGraw-Hill Optical and Electro-Optical Engineering Series, McGraw-Hill, (1989).
37. K. L. Chopra, Thin Film Phenomena, McGraw-Hill, (1969).
38. S. Kičas, "Daugiasluoksnių kintamo lūžio rodiklių sistemo su kontroliuojama dispersija formavimas, charakterizavimas ir taikymai," PhD Thesis (2016).
39. J. George, Preparation of Thin Films, M. Dekker, (1992).
40. J. Dudonis, Plonų Dangų Fizika Ir Nanotechnologijos, 1st-asis leid. ed. (2011).
41. O. Stenzel, J. Harhausen, D. Gäbler, S. Wilbrandt, C. Franke, R. Foest, and N. Kaiser, "Investigation on the reproducibility of optical constants of TiO_2, SiO_2, and Al_2O_3 films, prepared by plasma ion assisted deposition," Opt. Mater. Express **5**, 2006 (2015).
42. O. Stenzel, S. Wilbrandt, S. Du, C. Franke, N. Kaiser, A. Tünnermann, M. Mende, H. Ehlers, and M. Held, "Optical properties of UV-transparent aluminum oxide / aluminum fluoride mixture films, prepared by plasma-ion assisted evaporation and ion beam sputtering," Opt. Mater. Express **4**, 1696 (2014).
43. J. D. Musgraves, J. Hu, and L. Calvez, eds., Springer Handbook of Glass, Springer Handbooks (Springer International Publishing, 2019).
44. S. Tamulevičius, "Stress and strain in the vacuum deposited thin films," Vacuum **51**, 127–139 (1998).
45. C. Bundesmann and H. Neumann, "Tutorial: The systematics of ion beam sputtering for deposition of thin films with tailored properties," J. Appl. Phys. **124**, 231102 (2018).
46. "The image is taken from: https://optoman.com/show-inner-content/page-123.html," (2021).
47. K. Wasa, M. Kitabatake, and H. Adachi, Thin Film Materials Technology: Sputtering of Compound Materials (William Andrew Pub. ; Springer, 2004).
48. P.J.Martin, "Ion-based methods for optical thin film deposition," Journal of Materials Science volume 21, pages1–25 (1986).

49. N. Kaiser, "Review of the fundamentals of thin-film growth," Appl. Opt. **41**, 3053–3060 (2002).
50. M. Demchishin, A.V. B. A., "Structure and properties of thick condensates of nickel, titanium, tungsten, aluminum oxides, and zirconium dioxide in vacuum," (1969).
51. R. Messier, A. P. Giri, and R. A. Roy, "Revised structure zone model for thin film physical structure," J. Vac. Sci. Technol. Vac. Surf. Films **2**, 500–503 (1984).
52. C. R. M. Grovenor, H. T. G. Hentzell, and D. A. Smith, "The development of grain structure during growth of metallic films," Acta Metall. **32**, 773–781 (1984).
53. A. Anders, "A structure zone diagram including plasma-based deposition and ion etching," Thin Solid Films **518**, 4087–4090 (2010).
54. K. C. A. Smith and C. W. Oatley, "The scanning electron microscope and its fields of application," Br. J. Appl. Phys. **6**, 391–399 (1955).
55. P. M. Martin, ed., Handbook of Deposition Technologies for Films and Coatings: Science, Applications and Technology, 3. ed (Elsevier, 2010).
56. Y. Zhao, D. Ye, G.-C. Wang, and T.-M. Lu, "Designing nanostructures by glancing angle deposition," in A. Lakhtakia and S. Maksimenko, eds., pp. 59–73, (2003)
57. A. Lakhtakia and R. Messier, Sculptured Thin Films: Nanoengineered Morphology and Optics, Press Monograph Series No. v. no. PM143, SPIE Press, (2005).
58. C. Charles, N. Martin, and M. Devel, "Optical properties of nanostructured WO3 thin films by GLancing Angle Deposition: Comparison between experiment and simulation," Surf. Coat. Technol. **276**, 136–140 (2015).
59. D. Schmidt, "Generalized Ellipsometry on Sculptured Thin Films made by Glancing Angle Deposition," Theses Diss. Electr. Comput. Eng. (2010).
60. D. Schmidt, "Generalized Ellipsometry on Sculptured Thin Films made by Glancing Angle Deposition," University of Nebraska-Lincoln, Electrical & Computer Engineering, 143 (2010).
61. K. Robbie, "First thin film realization of a helicoidal bianisotropic medium," J. Vac. Sci. Technol. Vac. Surf. Films **13**, 2991 (1995).
62. K. Robbie and M. J. Brett, "Sculptured thin films and glancing angle deposition: Growth mechanics and applications," J. Vac. Sci. Technol. A **15**, 1460–1465 (1997).
63. S. Mukherjee and D. Gall, "Structure zone model for extreme shadowing conditions," Thin Solid Films **527**, 158–163 (2013).
64. A. Barranco, A. Borras, A. R. Gonzalez-Elipe, and A. Palmero, "Perspectives on oblique angle deposition of thin films: From fundamentals to devices," Prog. Mater. Sci. **76**, 59–153 (2016).

65. K. Robbie, G. Beydaghyan, T. Brown, C. Dean, J. Adams, and C. Buzea, "Ultrahigh vacuum glancing angle deposition system for thin films with controlled three-dimensional nanoscale structure," Rev. Sci. Instrum. **75**, 1089 (2004).
66. A. C. Van Popta, "Optical materials and devices fabricated by glancing angle deposition.," Library and Archives Canada, Bibliothèque et Archives Canada (2010).
67. M. M. Hawkeye, M. T. Taschuk, and M. J. Brett, Glancing Angle Deposition of Thin Films: Engineering the Nanoscale, John Wiley & Sons, Ltd, (2014).
68. I. Hodgkinson and Q. hong Wu, "Serial bideposition of anisotropic thin films with enhanced linear birefringence," Appl. Opt. **38**, 3621 (1999).
69. I. Hodgkinson, Q. hong Wu, B. Knight, A. Lakhtakia, and K. Robbie, "Vacuum deposition of chiral sculptured thin films with high optical activity," Appl. Opt. **39**, 642 (2000).
70. M. M. Hawkeye, M. T. Taschuk, and M. J. Brett, Glancing Angle Deposition of Thin Films: Engineering the Nanoscale, John Wiley & Sons Inc, (2014).
71. C. Charles, N. Martin, and M. Devel, "Optical properties of nanostructured WO3 thin films by GLancing Angle Deposition: Comparison between experiment and simulation," Surf. Coat. Technol. **276**, 136–140 (2015).
72. C. M. Zhou and D. Gall, "Surface patterning by nanosphere lithography for layer growth with ordered pores," Thin Solid Films **516**, 433–437 (2007).
73. H.-H. Jeong, A. G. Mark, J. G. Gibbs, T. Reindl, U. Waizmann, J. Weis, and P. Fischer, "Shape control in wafer-based aperiodic 3D nanostructures," Nanotechnology **25**, 235302 (2014).
74. Z. Huang and F. Bai, "Wafer-scale, three-dimensional helical porous thin films deposited at a glancing angle," Nanoscale **6**, 9401–9409 (2014).
75. M. O. Jensen and M. J. Brett, "Periodically Structured Glancing Angle Deposition Thin Films," IEEE Trans. Nanotechnol. **4**, 269–277 (2005).
76. M. M. Hawkeye, M. T. Taschuk, and M. J. Brett, Glancing Angle Deposition Optical Films (2014).
77. Jordan, Handbook of Deposition Technologies for Films Coatings, Vol. 53. (2013)
78. D. M. Mattox, Deposition (PVD) Processing Second Edition Dedication To My Wife Vivienne (2009).
79. H. K. V Latsch, Optical Interference Coatings, OIC 2016 (2014).
80. D. Ristau and H. Ehlers, Thin Film Optical Coatings (2012).
81. G. Balonek, "Coating a Grating Structure Using Various Deposition Techniques," http://www2.optics.rochester.edu/workgroups/cml/opt307/spr13/greg/.

82. C. L. S. James B. Oliver, Terrance J. Kessler, B. Charles, Fabrication of a Continuous-Enfolded Grating by Ion-Beam-Sputter Deposition (2015).
83. J. Oliver, "Characterization of Multilayer Optical Coatings on Microstructured Surfaces," http://www2.optics.rochester.edu/workgroups/cml/opt307/spr04/jim/index.html.
84. C. J. Stolz, M. D. Feit, and T. V. Pistor, "Laser intensification by spherical inclusions embedded within multilayer coatings," Appl. Opt. **45**, 1594 (2006).
85. P. Srinivasan, "Design and fabrication of space variant micro optical elements," PhD Thesis (2019).
86. A. Mehta, J. D. Brown, P. Srinivasan, R. C. Rumpf, and E. G. Johnson, "Spatially polarizing autocloned elements," Opt. Lett. **32**, 1935 (2007).
87. Y. Ohtera, T. Onuki, Y. Inoue, and S. Kawakami, "Multichannel Photonic Crystal Wavelength Filter Array for Near-Infrared Wavelengths," J. Light. Technol. **25**, 499–503 (2007).
88. N. Destouches, "Narrow band resonant grating of 100% reflection under normal incidence," 10 (2006).
89. S.-H. Chen, C.-K. Chen, Y.-C. Huang, and C.-C. Lee, "Omni-directional reflectors for deep blue LED using symmetric autocloning method," Opt. Rev. **20**, 141–144 (2013).
90. Y.-W. Yeh, T.-H. Chang, S.-H. Chen, and C.-C. Lee, "Etching effect of the autocloning structure using ion-assisted deposition," Opt. Rev. **16**, 222–225 (2009).
91. T.-H. Chang, S.-H. Chen, C.-C. Lee, and H.-L. Chen, "Fabrication of autocloned photonic crystals using electron-beam guns with ion-assisted deposition," Thin Solid Films **516**, 1051–1055 (2008).
92. I. S. catalogue International Organization for Standardization, 31.260 - Optoelectronics. Laser Equipment 21254-1:2011 (2011).
93. "https://lidaris.com/laser-damage-testing/1-on-1-test/," (2021).
94. G. Haugstad, Atomic Force Microscopy: Understanding Basic Modes and Advanced Applications (John Wiley & Sons, 2012).
95. W. Pong and C. S. Inouye, "Photoemission studies of LaF_3†," J. Opt. Soc. Am. **68**, 521 (1978).
96. E. O. Filatova and A. S. Konashuk, "Interpretation of the Changing the Band Gap of Al_2O_3 Depending on Its Crystalline Form: Connection with Different Local Symmetries," J. Phys. Chem. C **119**, 20755–20761 (2015).
97. A.-M. El-Sayed, M. B. Watkins, A. L. Shluger, and V. V. Afanas'ev, "Identification of intrinsic electron trapping sites in bulk amorphous silica from ab initio calculations," Microelectron. Eng. **109**, 68–71 (2013).

98. G. Ghosh, "Dispersion-equation coefficients for the refractive index and birefringence of calcite and quartz crystals," Opt. Commun. **163**, 95–102 (1999).
99. H. A. Macleod, Thin-Film Optical Filters, 4. ed, Series in Optics and Optoelectronics (CRC Press, 2010).
100. J. B. Oliver, T. J. Kessler, C. Smith, B. Taylor, V. Gruschow, J. Hettrick, and B. Charles, "Electron-beam–deposited distributed polarization rotator for high-power laser applications," Opt. Express **22**, 23883 (2014).
101. D. Ristau, Laser-Induced Damage in Optical Materials (2015).
102. L. Gallais, D.-B. Douti, M. Commandré, G. Batavičiūtė, E. Pupka, M. Ščiuka, L. Smalakys, V. Sirutkaitis, and A. Melninkaitis, "Wavelength dependence of femtosecond laser-induced damage threshold of optical materials," J. Appl. Phys. **117**, 223103 (2015).
103. Y. Zhao, K. Kita, K. Kyuno, and A. Toriumi, "Band gap enhancement and electrical properties of La2O3 films doped with Y2O3 as high-k gate insulators," Appl. Phys. Lett. **94**, 042901 (2009).
104. Thin Film Software: Https://Www.Optilayer.Com/ (OptiLayer GmbH).
105. T. Motohiro and Y. Taga, "Thin film retardation plate by oblique deposition," Appl. Opt. **28**, 2466 (1989).
106. C. Robertson, "Theory and practical recommendations for autocorrelation-based image correlation spectroscopy," J. Biomed. Opt. **17**, 080801 (2012).
107. W. Cai and V. Shalaev, Optical Metamaterials (Springer New York, 2010).
108. V. Vepachedu, P. D. McAtee, and A. Lakhtakia, "Nonexhibition of Bragg phenomenon by chevronic sculptured thin films: experiment and theory," J. Nanophotonics **11**, 1 (2017).
109. I. Hodgkinson and Q. hong Wu, "Serial bideposition of anisotropic thin films with enhanced linear birefringence," Appl. Opt. **38**, 3621 (1999).
110. S. Zhang, X. Zhang, H. Peng, L. Wen, G. Qiu, M. Hu, and C. Bai, "Structure Analysis of CaO–SiO2–Al2O3–TiO2 Slag by Molecular Dynamics Simulation and FT-IR Spectroscopy," ISIJ Int. **54**, 734–742 (2014).
111. S. Plimpton, "Fast Parallel Algorithms for Short-Range Molecular Dynamics," J. Comput. Phys. **117**, 1–19 (1995).
112. W. M. Brown, A. Kohlmeyer, S. J. Plimpton, and A. N. Tharrington, "Implementing molecular dynamics on hybrid high performance computers – Particle–particle particle-mesh," Comput. Phys. Commun. **183**, 449–459 (2012).
113. Humphrey, W., Dalke, A. and Schulten, K., “VMD - Visual Molecular Dynamics”, J. Molec. Graphics, Vol. 14, (1996). http://Www.Ks.Uiuc.Edu/Research/Vmd/.

114. H. Badorreck, M. Steinecke, L. Jensen, D. Ristau, M. Jupé, J. Müller, R. Tonneau, P. Moskovkin, S. Lucas, A. Pflug, L. Grinevičiūtė, A. Selskis, and T. Tolenis, "Correlation of structural and optical properties using virtual materials analysis," Opt. Express **27**, 22209 (2019).
115. A. Thelen, Design of Optical Interference Coatings, McGraw-Hill Optical and Electro-Optical Engineering Series, McGraw-Hill, (1989).
116. G. Abromavicius, R. Buzelis, R. Drazdys, A. Melninkaitis, and V. Sirutkaitis, "Influence of electric field distribution on laser induced damage threshold and morphology of high reflectance optical coatings," in G. J. Exarhos, A. H. Guenther, K. L. Lewis, D. Ristau, M. J. Soileau, and C. J. Stolz, eds. (2007)
117. L. Yang, X. D. Yuan, H. X. Deng, X. Xiang, W. G. Zheng, S. B. He, Y. Jiang, H. B. Lv, L. Ye, H. J. Wang, and X. T. Zu, "Influence of Ambient Temperature on Nanosecond and Picosecond Laser-Induced Bulk Damage of Fused Silica," Adv. Condens. Matter Phys. **2014**, 1–7 (2014).
118. T. Tolenis, L. Grinevičiūtė, R. Buzelis, L. Smalakys, E. Pupka, S. Melnikas, A. Selskis, R. Drazdys, and A. Melninkaitis, "Sculptured anti-reflection coatings for high power lasers," Opt. Mater. Express **7**, 1249 (2017).
119. T. Tolenis, L. Grinevičiūtė, R. Buzelis, L. Smalakys, E. Pupka, S. Melnikas, A. Selskis, R. Drazdys, and A. Melninkaitis, "Sculptured anti-reflection coatings for high power lasers," Opt. Mater. Express **7**, 1249 (2017).
120. I. Hodgkinson and Q. hong Wu, "Serial bideposition of anisotropic thin films with enhanced linear birefringence," Appl. Opt. **38**, 3621 (1999).
121. L. Grinevičiūtė, M. Andrulevičius, A. Melninkaitis, R. Buzelis, A. Selskis, A. Lazauskas, and T. Tolenis, "Highly Resistant Zero-Order Waveplates Based on All-Silica Multilayer Coatings," Phys. Status Solidi Appl. Mater. Sci. **214**, (2017).
122. M. Mende, L. O. Jensen, H. Ehlers, W. Riggers, H. Blaschke, and D. Ristau, "Laser-induced damage of pure and mixture material high reflectors for 355nm and 1064nm wavelength," Adv. Opt. Thin Films IV **8168**, 816821 (2011).
123. S. MacNally, C. Smith, J. Spaulding, J. Foster, and J. B. Oliver, "Glancing-angle-deposited silica films for ultraviolet wave plates," Appl. Opt. **59**, A155 (2020).
124. D. Gailevicius, "Photonic crystals for manipulation of spatial propagation of light beams," Thesis (2019).
125. T. Tolenis, S. E. Swiontek, and A. Lakhtakia, "Structural colours of nickel bioreplicas of butterfly wings," J. Mod. Opt. **64**, 781–786 (2017).
126. N. Pinna and M. Knez, eds., Atomic Layer Deposition of Nanostructured Materials, Wiley-VCH, (2012).

127. L. Grineviciute, J. Nikitina, C. Babayigit, and K. Staliunas, "Fano-like resonances in nanostructured thin films for spatial filtering," Appl. Phys. Lett. **118**, 131114 (2021).
128. J. J. Steele, M. T. Taschuk, and M. J. Brett, "Nanostructured metal oxide thin films for humidity sensors," IEEE Sens. J. **8**, 1422–1429 (2008).
129. M. M. Hawkeye and M. J. Brett, "Glancing angle deposition: Fabrication, properties, and applications of micro- and nanostructured thin films," J. Vac. Sci. Technol. Vac. Surf. Films (2007).

CURRICULUM VITAE

GENERAL INFORMATION

Name, Surname: **LINA GRINEVIČIŪTĖ**
Nationality: **Lithuanian** (EU)
Date and place of birth: **05 March 1991, Jurbarkas, Lithuania**

EDUCATION

- 2016 – 2020: **PhD studies in Material Science**, Centre for Physical Sciences and Technology (FMTC) and Vilnius University (VU)
- 2014 – 2016: **Master in Applied physics** Kaunas University of Technology
- 2010 – 2014: **Bachelor in Applied physics** Kaunas University of Technology

SCIENTIFIC AWARDS AND SCHOLARSHIPS

- Grant for the Research work at Molecular Foundry, Lawrence Berkeley National Laboratory project #5858.Work at the Molecular Foundry was supported by the Office of Science, Office of Basic Energy Sciences, of the U.S. Department of Energy under Contract No. DE-AC02-05CH11231. August 3 – September 30, **2019**
- Travel funding to do the research work at Molecular Foundry, Lawrence Berkeley National Laboratory "The project has received funding from European Social Fund (project No 09.3.3-LMT-K-712-14-0110) under grant agreement with the Research Council of Lithuania (LMTLT)." Aug. 3 – Sept. 30, **2019**
- Travel scholarship award for conference in New Mexico, US. "The project has received funding from European Social Fund (project No 09.3.3.-LMT-K-712-14-0138 under grant agreement with the Research Council of Lithuania (LMTLT)" June 2-7, **2019**
- Travel scholarship award from Research Council of Lithuania for conference in Prague, Czech Republic, 1-4 April, **2019**
- FizTeCh 2019, Vilnius, Lithuania, FTMC scientific conference for PhD students and young scientists (best oral presentation)
- FizTeCh 2018, Vilnius, Lithuania, FTMC scientific conference for PhD students and young scientists (best oral presentation)
- Young scientist award in recognition of the best poster presented „Anisotropic Nano-Structured Optical Interference Coatings for Polarization Control" // 19-th International Conference-School, AMT Palanga, Lithuania, Aug. 27-31, 2017

1 publikacija / 1st publication

Impact of deposition conditions on anostructured anisotropic silica thin films in multilayer interference coatings

L. Grineviciute, H. Badorreck, L. Jensen, De. Ristau, M. Jupe, A. Selskis, T. Tolenis.

Applied Surface Science **562,** 150167 (2021)

DOI: 10.1016/j.apsusc.2021.150167

Applied Surface Science 562 (2021) 150167

Contents lists available at ScienceDirect

Applied Surface Science

journal homepage: www.elsevier.com/locate/apsusc

Full Length Article

Impact of deposition conditions on nanostructured anisotropic silica thin films in multilayer interference coatings

Lina Grineviciute [a,*], Holger Badorreck [b,c], Lars Jensen [b,c], Detlev Ristau [b,c,d], Marco Jupé [b,c], Algirdas Selskis [a], Tomas Tolenis [a]

[a] Center for Physical Sciences and Technology, Savanoriu Ave. 231, LT-02300 Vilnius, Lithuania
[b] Laser Zentrum Hannover e.V., Hollerithallee 8, Hanover, Germany
[c] PhoenixD, Leibniz University Hanover, Germany
[d] Institute of Quantum Optics, Leibniz University Hanover, Germany

ARTICLE INFO

Keywords:
Sculptured thin films
Anisotropic coatings
Phase retardance
Effective refractive index
Surface filling
Molecular dynamics

ABSTRACT

Recent developments of nanostructured coatings have reached a point where extensive investigations within multi-layer systems are necessary for further implementation in novel photonic systems. Although sculptured thin films are explored for decades, no optical and structural measurements have been performed for anisotropic nanostructured multi-layer coatings with different deposition conditions of the dense layer. In this paper, we present extensive morphological analysis on silica nanostructured anisotropic films. Changing the deposition angle from 66° to 84°, indicate the changes in surface filling from 84% to 57%, respectively, while phase retardance has a maximal value of 0.032°/nm at 70° and 72° angles. We also present the investigation of covering such structures with the dense layer at different conditions. As a result, the technology for maintaining initial anisotropic properties is developed for extending spectral difference 1.6 times and phase retardation by 5% in anisotropic multi-layer coatings. Furthermore, we present simulations of growing silica layer using experimental conditions in the Virtual Coater framework resulting in virtual anisotropic films for comparison with measurements. The minimal impact on the anisotropy of porous layer is reached with the deposition of dense layer at 30° angle during constant substrate rotation.

1. Introduction

Advancements in nano-engineered coatings have extended the applications of thin films in virtually every topic. Telecommunications have benefitted from bottom-up surface modification techniques in many aspects [1]. Photovoltaics partly became the science of thin films and surface modification methods [2]. Optics and photonics also have their significant share in the usage of thin film technologies, mostly in optical coatings applications [3].

The GLancing Angle Deposition method (GLAD), which has been under constant development for more than 30 years, introduced the flexibility in thin films morphology. Based on self-shadowing effects, GLAD is capable to form nano-engineered coatings with slanted or vertical columnar, zig-zag [4], chiral [5,6], etc. nano-structures. Together with morphological changes, the characteristics of the films (optical properties, porosity, etc.) are also affected and used in developing advanced elements. A main example would be optical coatings, where the effective refractive index and even its birefringence can be controlled by changing the orientation of the substrate with regards to the vapor flux. Such developments have led to new types of optical components, e.g. coating-based waveplates [7,8], advanced anti-reflection coatings [9,10], Bragg mirrors with selectivity of circular polarization [11], polarization-active Bragg microcavities acting as wavelength retarders [12], etc. Combination of such nano-structures with liquid infiltration even allowed the development of switchable radial polarization converters based on sculptured thin films [13,14].

Recently, GLAD technology has been extended by combining nano-structured layers with dense thin films, resulting in even more complex multi-layer coatings. Changing the orientation of the substrate and the porosity, as a result, allows to obtain discrete layers with different optical properties using the same raw material. Major examples have been published during the last several years: all-silica anti-reflection coatings [9,10], mirrors [15], and waveplates [10,16]. All three components have demonstrated their extreme resistivity to laser radiation.

* Corresponding author.
E-mail address: lina.grineviciute@ftmc.lt (L. Grineviciute).

https://doi.org/10.1016/j.apsusc.2021.150167
Received 21 January 2021; Received in revised form 5 May 2021; Accepted 17 May 2021
Available online 23 May 2021

Despite the advanced properties of all-silica multi-layer coatings, new issues have appeared within the GLAD method. During the deposition of porous/dense layers, structural inhomogeneities lead to spectral errors and limitations for complex coating designs. This paper addresses these issues by extensively investigating 2-layer systems of silica formed by GLAD: Firstly, a nanostructured anisotropic layer, and secondly, this same layer with a dense layer on top. A modified sequence in the formation of multi-layer anisotropic coatings is presented.

The paper is divided as follows: section 2 describes experimental materials and methods; section 3 describes the results of detailed investigations of single- and multi-layer anisotropic layers; section 4 describes theoretical simulations of 2-layer systems and offers an interpretation of the interface evolution.

2. Materials and methods

An electron beam evaporation technique ("SIDRABE", Latvia) was used for all silica thin films deposition processes. Fused silica (FS) glasses with a diameter of 25.4 mm and Si plates were used as substrates. SiO_2 granules (Umicore) were used as evaporation source in each process. The distance between substrate and evaporation source is 34 cm. During the process, the layer growth rate was controlled with a crystal quartz monitor and maintained at 3 Å/s. Depositions were started at room temperature in a vacuum chamber at the pressure of 1.5×10^{-3} Pa. During the evaporation process, 2 sccm (the partial pressure of $2 \cdot 10^{-4}$ mbar) of oxygen gas was introduced into the chamber to ensure the oxidation of any non-oxidised particles in vapor flux.

A birefringent layer is obtained using one particular GLAD method – serial bi-deposition (SBD) [17]. During this process, the substrate was set at an oblique angle χ and rotated in half-turns (axial rotation α) around the surface normal without stopping the deposition process. The constant time period of half turns ($\alpha = 180°$) was induced in order to form structures, similar to chevrons, with 1–2 nm thickness sub-deposits (see Fig. 1). In this investigation, samples were coated by setting the angle χ to 66, 70, 72, 74, 76, 78, 80, and 84°and also various 2-layers, and 6-layer structures were fabricated and analyzed in detail by scanning electron microscopy (SEM), spectrophotometry and ellipsometry.

Transmission and phase delay difference between two perpendicular linear polarizations, namely in the shadowing plane (fast axis) and perpendicular to it (slow axis), are measured by a spectrophotometer ("Photon RT", Belarus) and spectrophotometric ellipsometer ("J. A. Woolam RC2", USA), respectively. The retardance difference is obtained by aligning the shadowing plane with one of the ellipsometry axes and then directly measuring the phase delay difference in transmission mode at 0° angle of incidence. The dispersions of the refractive indices of silica thin films were modeled by using the "Optilayer" software [18] and fitting transmission spectra (see Fig. 3(a)).

3. Results

Experimental research is divided into two parts: analysis of single- and multi-layers. The first part describes the optical and structural properties of anisotropic thin films deposited at different angles. The second part includes the detailed analysis of multi-layer structures, which are formed considering the results of the previous investigation.

3.1. Single-layers

A detailed investigation of optical and structural properties has been performed for anisotropic silica single-layers in order to determine the optimal deposition parameters to reach the highest anisotropy within the film. When increasing the deposition angle, the influence of the self-shadowing effect increases, which leads to more porous layer formation and, therefore in a lower effective refractive index of the film. Because the shadowing effect mostly dominates in one direction, when looking from the top, such structured layers indicate elliptical shape columns (see insert in Fig. 1). Therefore, optical anisotropy appears with a slow and a fast axis as in crystals with natural anisotropy, which allows the birefringent layer formation. Due to this SBD process the porosity increases differently in perpendicular directions and induces the formation of open cracks what is known as the bundling effect [12,19]. Since during low energy deposition, the surface morphology of the layer is the main factor for the formation of the secondary film, SEM images have been analyzed for the nanostructured thin films with thicknesses of 250 nm, deposited at different angles. The surface filling as a function of the deposition angle is presented in Fig. 2. The analysis indicates a continuous decrease of the surface filling when depositing at larger angles. Open pores strongly influence the deposition on top of such surfaces. This cannot only change the morphology of the secondary layer but can affect the first one as well.

Deposition at larger angles changes not only the nanostructure of thin films, but optical properties as well. Gradually increasing the deposition angle between the vapor flux and the substrate normally reduces the effective refractive index values due to an increasing self-shadowing effect, and therefore the porosity. Since the shadowing effect occurs only in one direction, the birefringence of silica films also depends on the deposition angle. Difference in refractive indices, for the thin film deposited at 70° angle, is lower compared to Smith et al. [20] and equals 0.028 at the wavelength of 350 nm. Difference can be influenced by humidity during the measurements and modelling of the spectra. SiO_2 anisotropic thin films exhibited the highest phase retardance of 0.032°/nm at the deposition angles of 70° and 72°. Similar

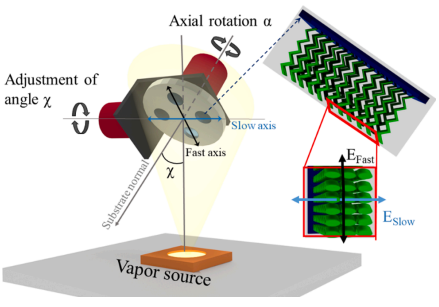

Fig. 1. The principal scheme of oblique angle deposition. χ indicates the angle between the vapor flux and the normal of the substrate surface.

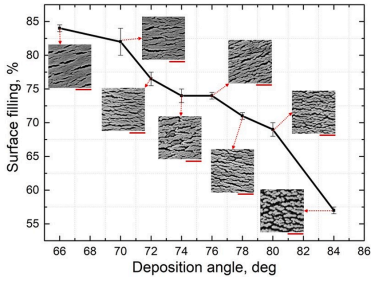

Fig. 2. Surface filling and SEM images of single layer anisotropic coatings (top view) deposited at different angles (Red bar under each SEM image is set at 500 nm). (For interpretation of the references to colour in this figure legend, the reader is referred to the web version of this article.)

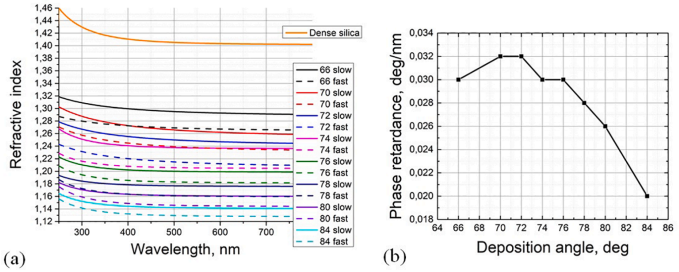

Fig. 3. (a) Refractive index dispersions of SiO_2 layers evaporated at different angles. slow axis - polarization perpendicular to shadowing direction, fast – polarization parallel to shadowing direction and (b) phase retardance of SiO_2 single layers evaporated at different angles.

tendencies were reported in other scientific publications, which were conducted for sculptured films made from materials like Ta_2O_5, WO_3 and Bi_2O_3 [7]. As stated above, optical analysis indicates that two deposition angles, namely 70° and 72°, are the most effective for the formation of anisotropic coatings, waveplates in our case. Additionally, surface structural investigations show (in Fig. 2) that thin films deposited at an angle of 70° have a higher filling factor of 5.5% compared to thin films deposited at 72° angle. This is preferable for multi-layer elements and for gaining better environmental stability due to less open areas within the coating, which can be exposed to contamination.

A deposition at 70°was chosen for further analysis as an optimal angle. Due to the competitive growth between fractions in the nanostructured layer, the expansion and coalescence of columns are present during the film growth [8]. The evolution of the film surface and optical anisotropy with increasing film thickness is shown in Fig. 4. The birefringence is influenced and changes with the thickness of the layer. Additionally, the increased size of the features can cause some negative side effects, such as optical scattering.

The surface analysis from SEM images indicates the decreasing surface filling of the films and the formation of wider cracks by increasing the film thickness, possibly due to the coalescence of the columns. The surface filling has decreased from 83.5% to 70% when the thickness of the film changed from 50 nm to 1500 nm, respectively. The mean area of the individual cracks has also increased from 86 nm^2 to 396 nm^2, accordingly. We can also observe from SEM images that cracks are increasing in both directions: fast and slow axis. After approximation of the elliptic form to each of the crack (please see Supplementary file), an increase of the largest minor axis within the surface of the film was determined: it changed from 20 nm to 81 nm when the thickness of the film changed from 50 nm to 1500 nm, respectively. Due to this structural gradient in the thin film growth axis, the optical anisotropy is affected as well. We can see the inhomogeneity of the normalized phase retardance dispersions of single layers with different thicknesses in Fig. 4(b). The phase retardation value at 350 nm wavelength for the film of 50 nm thickness is 0.025 °/nm. It increases 1.30 and 1.54 times when thickness increases to 400 nm and 1500 nm, respectively. According to our previous investigations of SiO_2, Al_2O_3, and LaF_3 nanostructured thin films, the cross-section of the plane perpendicular to the shadowing direction in the silica layers consists of columnar structures with gradually increasing diameters of individual columns as the film grows [8]. At the beginning of the film growth, the average widths of the columns are equal to ~29 nm. When film thickness reaches 400 nm, the coalescence of columns has started, and the width of the individual element extends to ~31 nm. Near the top of the layer (1.5 μm thickness), the width of the structural element increases to 70 nm. The expansion and later the coalescence of such columns leads to film inhomogeneity and light scattering for shorter wavelengths. Average phase retardation is similar in thin films with thicknesses from 200 nm to 400 nm. Layers of larger thickness are limited in quality and precision for coatings due to (i) inhomogeneous optical properties, (ii) optical scattering, (iii) wider crack formation, and (iv) mechanical instability. A multi-layer approach, i.e., the combination of porous anisotropic thin films with dense layers, has already been proven as a viable solution. Unfortunately, the deposition at close to normal incidence for dense thin film

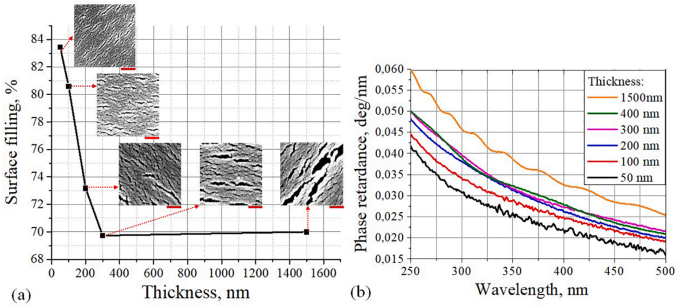

Fig. 4. The analysis of single-layer anisotropic coatings deposited at 70° angle by SBD method with different thicknesses. (a) Surface filling dependency on film thickness together with top-view SEM images (red bar under each SEM image is set at 200 nm), (b) normalized phase retardance. (For interpretation of the references to colour in this figure legend, the reader is referred to the web version of this article.)

formation still is highly influenced by larger voids in the porous layer. This can lead to larger inhomogeneities, therefore must be addressed.

3.2. Multi-layers

The combination of porous and dense layers with different inner structures allows to the creation of an interference coating using only one material. As it is shown in Fig. 3, depending on the deposition parameters, the same material can exhibit different effective refractive indices in a wide range (in case of SiO_2 from 1.41 to 1.13). Tailoring the nanostructures for individual layers induces Fresnel reflections in multi-layer coatings due to the difference in refractive indices, and therefore, various optical designs can be realized. For designs, which require high precision of optical properties, the combination of porous and dense layers must be controlled with high precision; therefore the investigation of the interface is crucial.

As the first step of multi-layer analysis, the 2-layer structures are fabricated and investigated in detail. The first layer (the base) is deposited at 70° angle with a thickness of 250 nm and is kept the same in all 2-layer coating experiments (see Fig. 5). The second layer is deposited with changed GLAD conditions: different deposition angles of incidence (χ) or different vapor flux directions. For three samples, a second layer with a thickness of 50 nm is deposited using constant rotation around the substrate axis and setting χ at 0, 30, and 50°. For the fourth sample, the second layer is deposited by the SBD method with an angle of $\chi = 50°$ and a time delay of 6 s between the half-rotations is maintained.

The qualitative SEM analysis was performed by combining cross-sections and top imaged to 3D images for the base layer and all 2-layer coating samples (Fig. 6). As it can be seen in Fig. 6(a), the base anisotropic layer surface structure consists of open cracks. As the second layer is being deposited on such base structure, some of the particles are penetrating inside the open voids and influence the optical properties of the first layer, therefore generating a transition zone. Furthermore, it is required for the dense layer to close the voids and to serve as a solid base for the next porous layer deposition. Depositing the secondary film at 0° and 30° closes most of the cracks (Fig. 6(b) and (c)), and it can be considered as a dense layer. Deposition at larger angles, 50° in our case, maintains open cracks and cannot be considered as a dense film for the multi-layer structure. Original SEM images of cross-sections of slow and fast axis can be found in Supplements Figs. S4 and S5.

Atomic Force Microscopy (AFM) measurements of surface roughness indicate that deposition at normal incidence also provides the lowest RMS values of 1.28 nm (Fig. 7(b)) in the experiment. Smooth surfaces after dense film deposition allow maintaining similar conditions in the growth of further porous anisotropic films and throughout all multi-layer formation. Depositions at 50° using constant substrate rotation or implementing SBD result in surfaces with open cracks and increased roughness of 1.60 nm and 1.68 nm, respectively. The comparison of the structural analysis between all 2-layers coatings indicates that only depositions at 0° and 30° angles are viable for the multi-layer formation and must be investigated further in order to determine their optical performance.

In order to enhance the spectral response to the multi-layer, consisting of nanostructured porous and dense layers, additionally, two 6-layer coatings were deposited. The anisotropic layers were the same in both designs, but the dense layers were deposited with constant rotation at different angles (0° and 30°), shown in Fig. 8(a). Both coatings are measured with the spectrophotometer and the ellipsometer (see Fig. 8 (b) and (c), respectively) for transmittance and phase retardance analysis. The multi-layer structure, which contains a dense layer deposited at a normal angle, exhibited a spectral difference in transmission of 3.9 nm (see Fig. 8(b)). For the dense layer deposited at 30° incidence, the spectral difference extended 1.6 times to 6.2 nm, indicating a larger optical anisotropy in the multi-layer coating. Additionally, the phase retardance is also evaluated for both experimental samples (see Fig. 8 (c)). The multi-layer, which contains layers deposited at 30°, exhibits a larger phase retardance value by ~5% throughout all UV spectra. Since dense films, deposited at both angles, are formed using constant substrate rotation, no birefringence is expected when light is irradiated at a normal angle. Therefore, phase retardance and spectral difference are present only due to the anisotropic layers, which are deposited at the same conditions in both cases. The difference in both optical properties, intensity and phase retardance, can be explained by considering the larger open cracks in anisotropic films surface. Deposition at a normal angle has a lower shadowing effect comparing to deposition at an incidence of 30°. Therefore, some part of the initial vapor flux can travel deeply into the pores and condensate in the initial film, and reduce its anisotropic properties. The transmission spectra of the multi-layer coating, deposited using 30° angle for dense films, is also shifted to the shorter wavelengths and has lower reflectance values near the Bragg zone. This behavior coincides with the multi-layer structure, which has lower refractive indices and a smaller difference between them. The refractive index of the dense film is slightly larger when deposited at 0° angle compared to the index of the film deposited at 30° angle. Therefore, the spectral changes of the Bragg zones depth are attributed to the reduced index of dense layers. The increased spectral difference of the Bragg zone for perpendicular polarizations is attributed to the larger anisotropy of the films deposited at 30° angle (when dense layers are deposited at 30° angles). Deposition of dense layers at 0° angle results in densifying the porous layer and reducing its anisotropy compared to the deposition of a dense thin film at 30° angle. In order to confirm this hypothesis, the growth of the coating was simulated and analyzed.

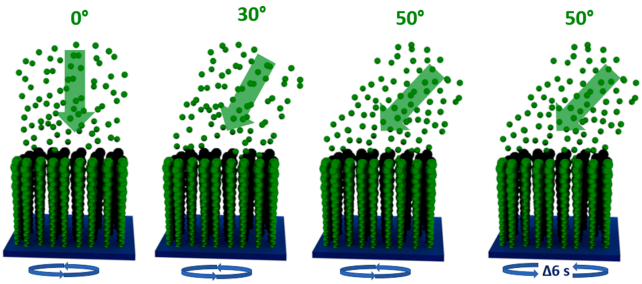

Fig. 5. The schematic representation of deposition conditions to form the second (dense) layer.

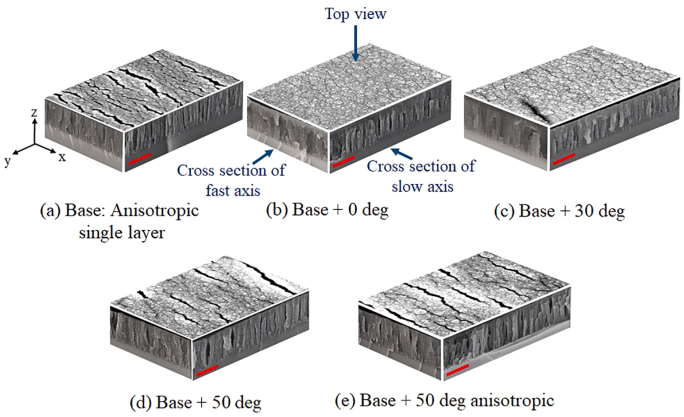

Fig. 6. 3D representation of SEM images combination of (a) single layer with 250 nm thickness, deposited at an angle of 70° and 2-layers structures with the second layer deposited at (b) 0°, (c) 30, (d) 50° and (e) 50°-anisotropic case. Red bar for each combination of SEM images is set at 250 nm. All structures are aligned the same way. Slow axis is parallel to *y* direction, fast axis is parallel to x direction. (For interpretation of the references to colour in this figure legend, the reader is referred to the web version of this article.)

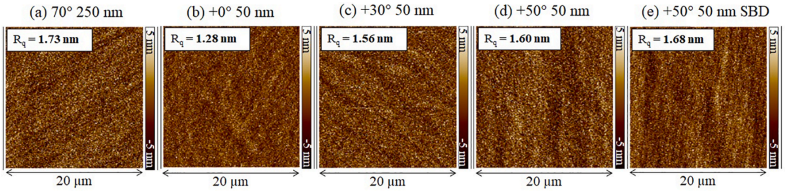

Fig. 7. AFM images of base single-layer (a) and 2-layer structures with top layer deposited at (b) 0°, (c) 30°, (d) 50°, and (e) 50° (anisotropic case).

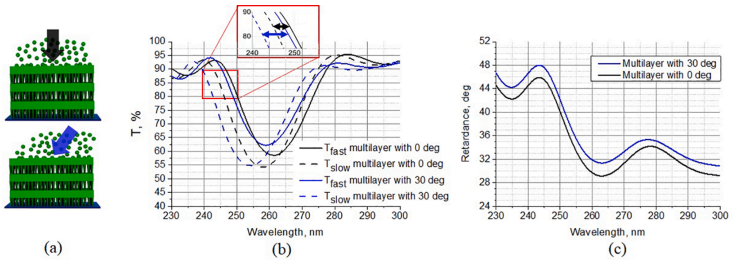

Fig. 8. (a) The schematic representation of a multi-layer structure with dense layers deposited at different angles, (b) transmission spectra of fabricated multi-layers for perpendicular polarizations (slow and fast axis), (c) the normalized retardance of fabricated multi-layer.

4. Atomistic thin film growth - molecular dynamics (MD)

For the growth simulation of SiO_2 multi-layers of anisotropic and dense films, the interaction potential from Zhang et al. [21] is used for the classical molecular dynamics (MD) performed with LAMMPS [22,23]. The simulation is performed for a substrate area size of x = 16 nm and y = 7 nm with lateral periodic boundary conditions. The first layer simulates a SBD coating (Fig. 9(a)) under an angle of $\chi = 70°$, where the angle α is flipped by 180° for every 1.5 nm of structure height (i.e., mean of the structure surface). The structure shown in Fig. 9(a) is grown with 10 flips of α. As deposition energy 0.3 eV is used throughout the simulation for silicon, while oxygen is deposited with no energy, i.e. it is adsorbed only in case of an attractive local potential on the surface. This method for oxygen serves as a simplified simulation of the common process of saturation in physical vapor deposition (PVD). For the purpose of simplicity, the deposition of more complex particles, like SiO_2 molecules, is only considered by the ratio between silicon and oxygen. The continuation on top of the zig-zag structure is done with more dense layers, deposited with an incidence of $\chi = 0°$, 30° and 50° in Fig. 9(b)–(d) during rotation of the structure by the azimuth angle α. The rotating

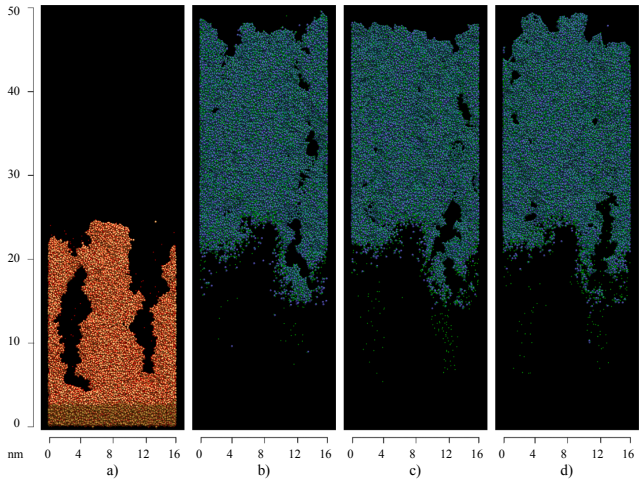

Fig. 9. Side view of simulated coatings (y-axis normal to paper plane), (a) the initial 1-layer zig-zag structure grown like SBD (red-yellow) with the substrate indicated by the shadowed area. The 2-layer structures with the second layer in blue-green continuing the first layer (not shown here) with different incidence angles χ during rotation of the azimuth α. (b) $\chi = 0°$, (c) $\chi = 30°$, (d) $\chi = 50°$. The filling of surface pores of the first layer is more pronounced for smaller angles χ. Graphics are generated with VMD [24]. (For interpretation of the references to colour in this figure legend, the reader is referred to the web version of this article.)

speed is 2.5 turns/nm.

Therefore, these simulations represent the digital twin of the experimental coatings shown in Fig. 6(a)–(d). As can be seen from Fig. 9 (a), the zig-zag layer exhibits a columnar structure. Although the simulation yields only two columns here due to the limited structure size and taking the periodic boundary into account, two major effects can already be observed. That is the beginning coalescence on the left side, while on the right an open pore and crack are build up. However, because the coalescence is not reproduced fully here, the columns widths are much smaller than observed in the experiment. With the continuation in Fig. 9(b)–(d), the closed pore on the left of each structure is nearly unchanged. In contrast, the open pore on the right is filled with additional material, which even leads to a closed small pore for 0°, while the impact on the initial layer decreases with increasing deposition angle as shown in Fig. 9(c) and (d). However, the second layer qualitatively changes the structure morphology, including only pores much smaller than the first layer. This is also viewed by the density profiles in the growth direction in Fig. 10. Here, the structure is divided into slices of 0.5 nm in the growth direction, and the density is calculated by counting the atomic masses for each slice resulting in a density profile. While the density does not change up to a height of about 14 nm, the range up to 19 nm for the 0° deposition shows a higher increase of the density than 30° and 50° due to filling the open pores with material from the second layer. The impact depth of material from the second layer can be considered to be about 5 nm. However, because the simulated structures are small compared to the experimental ones, resulting in smaller columns widths, the impact depth in the experiment is probably higher. The same initial structure reduces the high fluctuation in density seen for regions above 19 nm, therefore here the higher density can be considered significant, as also supported by the similar initial density for 30° and 50°, which is lost for 19 nm and above. For this region, the density grows by about 0.4 g/cm^3 while fluctuating by a non-negligible amount on the overall growth, but with no significant difference between the second layers.

Due to the structure morphology, an anisotropy for the first layer is expected and confirmed in the following by performing an anisotropic

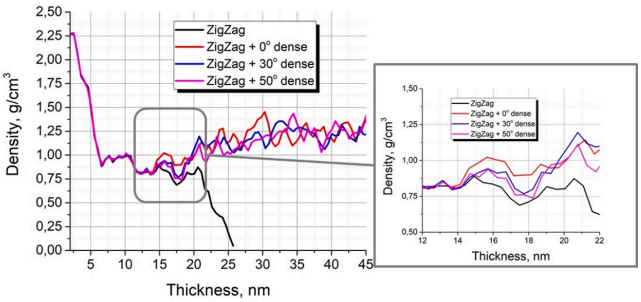

Fig. 10. Density profiles of anisotropic zig-zag single layer and its continuation with dense layers deposited with constant rotation at $\chi = 0°$, 30° and 50°

Table 1
Results of the anisotropic effective medium approximation analysis for the first layer, i.e. the structure height region between 7 and 20 nm, with the impact of the second layer. The uncertainty for the volume distribution is below ±3.6%, while for the birefringence Δn the uncertainty is about ±0.0017 for a 95% confidence interval (see also [26]).

	ZigZag	ZigZag + 0°	ZigZag + 30°	ZigZag + 50°
Volume distribution: material, pores	43.0%,57.0%	46.6%,53.4%	45.2%,54.8%	44.8%,55.2%
Refractive index of fast and slow axis	1.1925,1.2080	1.2128,1.2251	1.2055,1.2184	1.2029,1.2166
Δn	0.0155	0.0123	0.0129	0.0137
Normalized phase retardance @ 266 nm	0.0207°/nm	0.0167°/nm	0.0176°/nm	0.0185°/nm

effective medium approximation analysis as described in [25]. The results are viewed in Table 1 for a bulk refractive index of 1.5 for silica (at 266 nm). The distribution between the filled volume and pores is determined by dividing the structure into voxels of 0.2^3 nm^3. The voxels containing atoms contribute to the filled volume, while empty voxels contribute to the pores. The analysis of the first layer is taken for the growth height region of 7–20 nm, therefore excludes the substrate structure and upper surface region of the first layer but includes the height region impacted by the second layer. For this region, corresponding to the highest porosity, the highest birefringence for normal light incidence is observed for the solely first layer of $\Delta n = 0.0155$. Adding the second layer, the porosity decreases, which also leads to a rise in the value of the refractive index ellipsoid. However, due to the non-directional deposition of the second layer the birefringence decreases to 0.0123 for 0° and increasing again for larger deposition angles of 30° and 50° with 0.0129 and 0.0137, respectively, where the impact on the first layer is decreasing. The birefringence, i.e., the difference of the refractive indices of the slow and fast axis, mainly resembles the refractive index ellipsoid in x and y, because the ellipsoid is nearly aligned with the coordinate axes. The uncertainties for a 95% confidence interval are given in the caption of Table 1, however due to the small number of samples, these are probably overestimated [26].

Repeating the analysis for the growth height region between 25 nm and 47 nm (presented in Table 2), the results show a significantly lower amount of pores in the material. Because this region does not exist prior to the second layer, the influence of the first layer can only be indirect. With a lower number of pores, the refractive indices increase. The birefringence is much lower compared with the region between 7 and 20 nm. In general, for the second layer, a $\Delta n = 0$ can be expected so that the small values can be related to indirect effects from the first layer and/or statistical inaccuracies due to the limited simulated structure size in all dimensions.

Simulated nanostructures are also compared with experimental data and the same conclusions were found: deposition of dense coatings at 30° results in maintaining a more original anisotropy. Columns in simulated zig-zag are thinner than in the experiment, however also the coating thickness (15 nm mean height (~18 nm max)) is much less than in experiments, so columns probably have not fully joined. But within the periodicity of the simulation, the two columns already start joining. Also, the phase retardance of the simulation is by a factor of about 2 lower than in the experiment. Again, the thickness in the simulation is much lower (13 nm) than in the experiment with the smallest thickness (50 nm) – the coalescence of columns is not observed.

The deposition of dense silica thin films on top of porous layers influences the optical anisotropy of the first film. Birefringence is reduced in films with columnar structure when deposition of dense layer is performed at 0° angle and, therefore, the deposition of a dense coating at angles of 30° and 50° with rotating substrate around the normal axis were tested. The investigation was focused on the structural and optical analysis of the single layers, deposited at different angles and with different thicknesses. Afterward, different methods for over coating the porous anisotropic layer was tested. Since the changes of the structure at the interface between two distinct nanostructures is relatively small and difficult to analyze quantitatively, only the changes in optical performance, namely transmission and phase retardance, were measured. Nevertheless, optical measurements were targeted to measure the anisotropic properties – changes in transmission spectra and difference in phase delay for perpendicular polarizations at 0° angle of incidence. In all multi-layer samples, the anisotropic films were deposited at the same conditions, therefore, any changes in optical properties are attributed to the changes in porous layers nanostructure. In order to confirm this hypothesis, molecular dynamic simulations were performed. Results confirmed that different deposition conditions of dense layer influence the nanostructure of the porous layer and its optical anisotropy. Comparison between simulated refractive index differences for fast and slow directions between porous anisotropic and dense layers show similarities with transmission measurements of multilayer coatings. Differences are larger when dense layers are coated at 0° angle due to lower density of thin films deposited at 30° angle. At the same time, simulated birefringence of anisotropic film is larger when dense layer is coated at 30° angle, which explains the increased spectral difference of multilayer, consisted of porous anisotropic and dense isotropic layers coated at 70° and 30° angles, respectively.

Experimental results are limited to anisotropic SiO_2 films, deposited at 70°, but the same principles can be applied to other type of structures, namely columns with different nanostructure, chiral thin films, etc. Also, deposition of different materials by GLAD method may also lead to smaller cracks throughout nanostructured thin films surface. Depending on the size and number of cracks, lower deposition angles can be used for dense thin film formation.

Further research efforts are needed to simulate larger structures in order to compare them directly with experimental results, and investigations with other materials and nanostructures should be continued. We believe that we reported an investigation that can be reproduced with other known materials and nanostructures used in multi-layer optical coatings, thus expanding the capabilities of nanostructured thin films to be used in high performance optical components. Presented results can directly be applied for manufacturing coating-based advanced components such as zero-order waveplates and polarizers for zero angle of incidence, since remaining the anisotropic properties in the porous layer is essential. Also, interface analysis could be used in recently developed all-silica based interference coatings for

Table 2
Results of the anisotropic effective medium approximation analysis for the second layer, i.e. the structure height region between 25 nm and 47 nm. Here, the uncertainty for the volume distribution is below ± 6.8%, while for the birefringence Δn the uncertainty is below ± 0.0077 for a 95% confidence interval (see also [26]).

	ZigZag	ZigZag + 0°	ZigZag + 30°	ZigZag + 50°
Volume distribution: material, pores	–	63.3%,36.7%	61.8%,38.2%	62.0%,38.0%
Refractive index of fast and slow axis	–	1.3037,1.3078	1.2956,1.3002	1.2979,1.2999
Δn	–	0.0041	0.0046	0.0020
Normalized phase retardance @ 266 nm	–	0.0055°/nm	0.0063°/nm	0.0026°/nm

high-power lasers. Overall, any thin film based system, where strict interface is beneficial, could be improved by presented research.

5. Conclusion

In this work, the analysis of optical and structural properties of anisotropic silica thin films is presented, and the technology for maintaining such initial properties in multi-layer coatings when using dense layers is demonstrated. The largest anisotropy was obtained when the substrate was tilted at 70° angle. Phase retardation of such thin films changes during growth from 0.025°/nm to 0.038°/nm at thicknesses of 50 nm and 1500 nm, respectively. Such inhomogeneity of optical retardance is due to changes in films nanostructure: decreasing surface filling and expansion of cracks, which results in increased size of columns with elliptic cross-section during bundling effect. Experimental results indicate that in order to fully exploit such optical anisotropic properties of nanostructured silica thin films in multi-layer coatings, dense layers have to be deposited at 30° angle. Spectrophotometric and ellipsometric data show improved differences in optical response for perpendicular linear polarizations compared with multi-layers containing conventional dense films deposited at 0°. Molecular dynamics simulations of the thin film growth indicate that such behavior is caused by deeper penetration of vapor flux within the porous film in case of dense layer deposition at 0° angle. Therefore, the porosity and the birefringence of the anisotropic layers are reduced. Deposition at 30° angle, on the other hand, maintains a more original anisotropy.

Credit author statement

L. Grineviciute and T. Tolenis designed and carried out the experiments and measurements, H. Badorreck, L. Jensen, D. Ristau and M. Jupé performed the simulations and provided theoretical analysis. Algirdas Selskis performed SEM measurements. All authors participated in discussions, prepared and reviewed the manuscript.

Declaration of Competing Interest

The authors declare that they have no known competing financial interests or personal relationships that could have appeared to influence the work reported in this paper.

Acknowledgements

The authors thank the Deutsche Forschungsgemeinschaft (DFG) for funding within the cluster of excellence PhoenixD (390833453, EXC 2122).

Research also received funding from the Research Council of Lithuania (LMTLT), project UnCoatPower (agreement No S-MIP-20-61).

Appendix A. Supplementary material

Supplementary data to this article can be found online at https://doi.org/10.1016/j.apsusc.2021.150167.

References

[1] A.M. Urbas, Z. Jacob, L.D. Negro, N. Engheta, A.D. Boardman, P. Egan, A. B. Khanikaev, V. Menon, M. Ferrera, N. Kinsey, C. DeVault, J. Kim, V. Shalaev, A. Boltasseva, J. Valentine, C. Pfeiffer, A. Grbic, E. Narimanov, L. Zhu, S. Fan, A. Alù, E. Poutrina, N.M. Litchinitser, M.A. Noginov, K.F. MacDonald, E. Plum, X. Liu, P.F. Nealey, C.R. Kagan, C.B. Murray, D.A. Pawlak, I.I. Smolyaninov, V. N. Smolyaninova, D. Chanda, Roadmap on optical metamaterials, J. Opt. 18 (2016), 093005, https://doi.org/10.1088/2040-8978/18/9/093005.

[2] M. Coll, J. Fontcuberta, M. Althammer, M. Bibes, H. Boschker, A. Calleja, G. Cheng, M. Cuoco, R. Dittmann, B. Dkhil, I. El Baggari, M. Fanciulli, I. Fina, E. Fortunato, C. Frontera, S. Fujita, V. Garcia, S.T.B. Goennenwein, C.-G. Granqvist, J. Grollier, R. Gross, A. Hagfeldt, G. Herranz, K. Hono, E. Houwman, M. Huijben, A. Kalaboukhov, D.J. Keeble, G. Koster, L.F. Kourkoutis, J. Levy, M. Lira-Cantu, J. L. MacManus-Driscoll, J. Mannhart, R. Martins, S. Menzel, T. Mikolajick, M. Napari, M.D. Nguyen, G. Niklasson, C. Paillard, S. Panigrahi, G. Rijnders, F. Sánchez, P. Sanchis, S. Sanna, D.G. Schlom, U. Schroeder, K.M. Shen, A. Siemon, M. Spreitzer, H. Sukegawa, R. Tamayo, J. van den Brink, N. Pryds, F.M. Granozio, Towards Oxide Electronics: a Roadmap, Appl. Surf. Sci. 482 (2019) 1–93, https://doi.org/10.1016/j.apsusc.2019.03.312.

[3] D.T. Reid, C.M. Heyl, R.R. Thomson, R. Trebino, G. Steinmeyer, H.H. Fielding, R. Holzwarth, Z. Zhang, P. Del'Haye, T. Südmeyer, G. Mourou, T. Tajima, D. Faccio, F.J.M. Harren, G. Cerullo, Roadmap on ultrafast optics, J. Opt. 18 (2016), https://doi.org/10.1088/2040-8978/18/9/093006.

[4] R. Messier, T. Gehrke, C. Frankel, V.C. Venugopal, W. Otaño, A. Lakhtakia, Engineered sculptured nematic thin films, J. Vacuum Sci. Technol. A: Vacuum Surf. Films 15 (1997) 2148–2152, https://doi.org/10.1116/1.580621.

[5] K. Robbie, M.J. Brett, A. Lakhtakia, First thin film realization of a helicoidal bianisotropic medium, J. Vacuum Sci. Technol. A: Vacuum Surf. Films 13 (1995) 2991–2993, https://doi.org/10.1116/1.579626.

[6] M. Faryad, A. Lakhtakia, The circular Bragg phenomenon, Adv. Opt. Photon. 6 (2014) 225, https://doi.org/10.1364/AOP.6.000225.

[7] T. Motohiro, Y. Taga, Thin film retardation plate by oblique deposition, Appl. Opt. 28 (1989) 2466, https://doi.org/10.1364/AO.28.002466.

[8] L. Grinevičiūtė, M. Andrulevičius, A. Melninkaitis, R. Buzelis, A. Selskis, A. Lazauskas, T. Tolenis, Highly resistant zero-order waveplates based on all-silica multilayer coatings, Phys. Status Solidi A 214 (2017) 1700764, https://doi.org/10.1002/pssa.201700764.

[9] J.-Q. Xi, M.F. Schubert, J.K. Kim, E.F. Schubert, M. Chen, S.-Y. Lin, W. Liu, J. A. Smart, Optical thin-film materials with low refractive index for broadband elimination of Fresnel reflection, Nature Photon. 1 (2007) 176–179, https://doi.org/10.1038/nphoton.2007.26.

[10] T. Tolenis, L. Grinevičiūtė, R. Buzelis, L. Smalakys, E. Pupka, S. Melnikas, A. Selskis, R. Drazdys, A. Melninkaitis, Sculptured anti-reflection coatings for high power lasers, Opt. Mater. Express. 7 (2017) 1249, https://doi.org/10.1364/OME.7.001249.

[11] P.D. McAtee, A. Lakhtakia, Reflection and transmission of obliquely incident light by chiral sculptured thin films fabricated using asymmetric serial-bideposition technique, J. Nanophoton. 11 (2017), 043502, https://doi.org/10.1117/1.JNP.11.043502.

[12] M. Oliva-Ramirez, A. Barranco, M. Löffler, F. Yubero, A.R. González-Elipe, Optofluidic Modulation of Self-Associated Nanostructural Units Forming Planar Bragg Microcavities, ACS Nano 10 (2016) 1256–1264, https://doi.org/10.1021/acsnano.5b06625.

[13] M. Oliva-Ramirez, J. Gil-Rostra, M.C. López-Santos, A.R. González-Elipe, F. Yubero, Vapor and liquid optical monitoring with sculptured Bragg microcavities, J. Nanophotonics 11 (2017) 1, https://doi.org/10.1117/1.JNP.11.046009.

[14] M. Oliva-Ramírez, J. Gil-Rostra, A.C. Simonsen, F. Yubero, A.R. González-Elipe, Dye giant absorption and light confinement effects in porous bragg microcavities, ACS Photonics 5 (2018) 984–991, https://doi.org/10.1021/acsphotonics.7b01283.

[15] T. Tolenis, L. Grinevičiūtė, L. Smalakys, M. Ščiuka, R. Drazdys, L. Mažulė, R. Buzelis, A. Melninkaitis, Next generation highly resistant mirrors featuring all-silica layers, Sci. Rep. 7 (2017) 10898, https://doi.org/10.1038/s41598-017-11275-0.

[16] S. Macnally, C. Smith, J. Spaulding, J. Foster, J.B. Oliver, Glancing-angle–deposited silica films for ultraviolet wave plates, Appl. Opt. 59 (2020) A155–A161, https://doi.org/10.1364/AO.59.00A155.

[17] I. Hodgkinson, Q. Hong Wu, Serial bideposition of anisotropic thin films with enhanced linear birefringence, Appl. Opt. 38 (1999) 3621, https://doi.org/10.1364/AO.38.003621.

[18] Thin film software: https://www.optilayer.com/, OptiLayer GmbH, n.d. https://www.optilayer.com/.

[19] H. Vankranenburg, C. Lodder, Tailoring growth and local composition by oblique-incidence deposition: a review and new experimental data, Mater. Sci. Eng.: R: Rep. 11 (1994) 295–354, https://doi.org/10.1016/0927-796X(94)90021-3.

[20] C. Smith, S. MacNally, J.B. Oliver, Ellipsometric modeling of serially bi-deposited glancing-angle-deposition coatings, Appl. Opt. 59 (2020) A26, https://doi.org/10.1364/AO.59.000A26.

[21] S. Zhang, X. Zhang, H. Peng, L. Wen, G. Qiu, M. Hu, C. Bai, Structure Analysis of CaO–SiO2–Al2O3–TiO2 Slag by Molecular Dynamics Simulation and FT-IR Spectroscopy, ISIJ Int. 54 (2014) 734–742, https://doi.org/10.2355/isijinternational.54.734.

[22] S. Plimpton, Fast Parallel Algorithms for Short-Range Molecular Dynamics, J. Comput. Phys. 117 (1995) 1–19, https://doi.org/10.1006/jcph.1995.1039.

[23] W.M. Brown, A. Kohlmeyer, S.J. Plimpton, A.N. Tharrington, Implementing molecular dynamics on hybrid high performance computers – Particle–particle particle-mesh, Comput. Phys. Commun. 183 (2012) 449–459, https://doi.org/10.1016/j.cpc.2011.10.012.

[24] W. Humphrey, A. Dalke, K. Schulten, VMD – Visual Molecular Dynamics, J. Molec. Graphics 14 (1996). http://www.ks.uiuc.edu/Research/vmd/,.

[25] H. Badorreck, M. Steinecke, L. Jensen, D. Ristau, M. Jupé, J. Müller, R. Tonneau, P. Moskovkin, S. Lucas, A. Pflug, L. Grinevičiūtė, A. Selskis, T. Tolenis, Correlation of structural and optical properties using virtual materials analysis, Opt. Express. 27 (2019) 22209, https://doi.org/10.1364/OE.27.022209.

[26] H. Badorreck, L. Jensen, D. Ristau, M. Jupé, Statistical analysis on the structural size of simulated thin film growth with molecular dynamics for glancing angle incidence deposition, Coatings 11 (2021), https://doi.org/10.3390/coatings11040469.

2 publikacija / 2nd publication

Highly Resistant Zero-Order Waveplates Based on All-Silica Multilayer Coatings

L. Grineviciute, M. Andrulevičius, A. Melninkaitis, R. Buzelis, A. Selskis, A. Lazauskas, T. Tolenis.

Phys. Status Solidi A, **214**, 12, 1700764, (2017)

DOI: 10.1002/pssa.201700764

ORIGINAL PAPER

High Power Lasers

physica status solidi a

www.pss-a.com

Highly Resistant Zero-Order Waveplates Based on All-Silica Multilayer Coatings

Lina Grinevičiūtė, Mindaugas Andrulevičius, Andrius Melninkaitis, Rytis Buzelis, Algirdas Selskis, Algirdas Lazauskas, and Tomas Tolenis*

Waveplates, used to modify polarization state of light, are integral part of high-power lasers. Classical approach to waveplate manufacturing is based on combination of birefringent crystalline materials and deposition of nonpolarizing antireflection (AR) coatings. Their limitation to withstand maximal peak power is determined by laser-induced damage (LID) phenomena, mainly determined by low band-gap materials used in AR coatings. In this study, a novel multi-layer approach of high band-gap birefringent coatings was proposed and investigated to overcome this limitation. Three eligible candidate materials, namely LaF_3, Al_2O_3, and SiO_2 are investigated. Structural and optical analysis reveal superior properties of silica for UV spectral range. Zero-order thin film retarders based on all-silica nanostructures are fabricated by oblique angle deposition process. Low optical losses and high transparency ($T \sim 99\%$) are demonstrated while indicating potential to withstand high laser fluence of 40 J cm^{-2} in nanosecond regime at 355 nm wavelength. Such waveplates can essentially improve maximal tolerated peak power and thus allow production of more compact optical systems, even when high laser power is used.

1. Introduction

The performance of advanced high power optical systems depends on quality and sustainability of constituting optical components. Achieving high power in such modern laser systems is limited by laser-induced damage phenomena. Optical elements are constantly under investigation in order to increase the LID threshold parameter, described by ISO standard.[1] Today's most advanced modern laser facilities (LMJ,[2] ELI,[3] National Ignition Facility,[4] etc.) can produce extreme powers as a result of continuous development toward optical elements resistivity to laser light. Laser system parameters such as polarization state, peak intensity, spatial distribution of the pulse, etc. are often controlled by polarizing optical elements including waveplates (or phase retardation plates). Extensive studies of polymers, solid or liquid crystals, and other materials provided the "know-how" of today's waveplates.[5,6] Unfortunately, aforementioned materials suffer from environmental changes and has low resistivity to laser radiation.[7] Also, in order to apply typical waveplates in microsystems, additional mechanical challenges must be addressed.

In ideal case, true zero-order waveplates are desired by using birefringent material with minimal physical thickness, required to obtain necessary phase delay, e.g., $\pi/2$ or $\lambda/4$. Unfortunately, the fabrication and the handling are difficult for strongly birefringent materials such as calcite or quartz. Therefore, typically two multi-order waveplates are combined. One of possible solutions for zero-order waveplate with high LID threshold values is direct writing of nanogratings and inducing birefringence in silica glass using laser radiation.[8] Although, this novel method causes the formation of desirable phase delay, the features in the structure of nanogratings induce scattering, especially in UV region. The optical losses are 30% for the wavelength of 532 nm and >50% for the shorter wavelengths than 300 nm.[9] Aforementioned waveplates are also limited when applied in compact systems as they are separate optical elements. Also, antireflection coatings have to be deposited to obtain high transmission. Typical AR coatings consist of two materials with low and high refractive indexes. Latter has low optical resistivity due to low band-gap and limits the performance of the element.[10] Therefore, zero-order waveplates with high optical transmission and superior LID threshold performance are still an issue in compact high power laser systems.

In this research, sculptured thin films produced by oblique angle deposition (OAD) technique were introduced as a solution for zero-order waveplate formation.[11] The full-scale investigation was accomplished with three eligible candidates for UV

L. Grinevičiūtė, R. Buzelis, A. Selskis, T. Tolenis
State Research Institute Center for Physical Sciences and Technology
Savanorių ave. 231, LT-02300 Vilnius, Lithuania
E-mail: lina.grineviciute@ftmc.lt

M. Andrulevičius, A. Lazauskas
Institute of Materials Science
Kaunas University of Technology
K. Baršausko st. 59, LT-51423 Kaunas, Lithuania

A. Melninkaitis
Vilnius University
Laser Research Center
Saulėtekio ave. 10, LT-10223 Vilnius, Lithuania

The ORCID identification number(s) for the author(s) of this article can be found under https://doi.org/10.1002/pssa.201700764.

DOI: 10.1002/pssa.201700764

applications – LaF_3, Al_2O_3, and SiO_2. Structural (electron microscopy, X-ray diffraction, etc.) and optical (spectrophotometric and ellipsometric) measurements were performed and analyzed in detail. As a result, we present the conceptually novel approach to form sculptured thin films-based multilayer zero-order waveplates exhibiting low-loss and high resistivity to laser radiation.

The paper is organized as follows: experimental methods and measurement techniques, used in this work, are described in Section 2. Section 3 presents main results and is divided in two subsections: Subsection 3.1 shows characterization and analysis of different materials OAD single layers in order to select the most applicable one for waveplate production. Subsection 3.2 describes the modeled and implemented design of multilayer $\lambda/4$ waveplate based on sculptured thin films. Finally, section 4 provides concluding remarks.

2. Experimental Section

Three materials were picked for production of thin films with optical anisotropy: LaF_3, Al_2O_3, and SiO_2. All these materials have low absorption for the wavelength of 355 nm due to their wide band gaps (9.4,[12] 7.0,[13] and 8.9 eV,[14] respectively) and are widely used in optical coatings for UV spectral region.

2.1. Sample Preparation

Silicon plates and fused silica (FS) glasses with diameter of 24.5 mm were used as substrates. The great care was intended for their surface preparation before evaporation process. Firstly, substrates were carefully swabbed mechanically with ethanol and afterwards the ultrasonic cleaning in an aqueous surfactant with commercial alkaline cleaning solution was used. For the final process, plasma-etched FS sample was used and cleaned using the same method of surface preparation.

An in house modified electron-beam evaporation machine "Sidrabe" (Latvia) was used for thin films deposition processes. Coating materials were placed in copper crucible and evaporated on both silicon and FS substrates by focused electron beam. Layer growth rate was controlled with crystal quartz monitor and maintained at $3\,\text{Å}\,\text{s}^{-1}$ in all processes. Depositions were started at room temperature in vacuum chamber at the pressure of 1.5×10^{-3} Pa. During Al_2O_3 evaporation processes 2 sccm of oxygen gas was introduced into the chamber to ensure the oxidation of evaporated material. A birefringence of layers was obtained by using oblique angle deposition method. OAD technique allows to form thin film with oblique columnar structure by adjusting the vapor incident angle χ with respect to the normal of the substrate surface. Individual columns consist of elliptical cross-sections due to self shadowing effect occurring in one direction: shadowing plane (the plane between substrate normal and vapor flux). By also rotating the substrate around its normal axis (see **Figure 1**) various other artificial structures can be realized. The system with two stepper motors was used to set the glancing angle χ and to control the substrate rotation a around its normal.

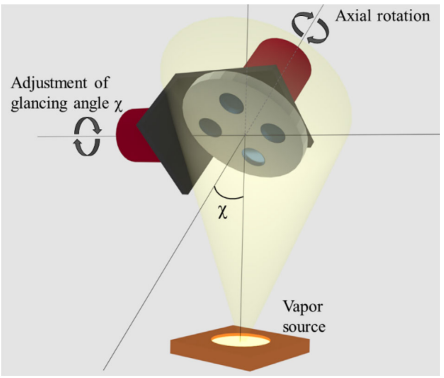

Figure 1. The principal scheme of oblique angle deposition: χ indicates the angle between the vapor flux and the normal of the substrate surface.

During our experiments one of the particular OAD method was used to increase the deposited thin films birefringence, namely serial bi-deposition (SBD).[15] Samples were fabricated by setting the deposition angle χ to 70°. During the deposition, substrate holder was periodically rotated around its axis by half turns ($a = 180°$). Rotation was performed every 5 s, which is similar to the deposition of zig-zag structures. Thin film contains of around 1000 sublayers, with each subdeposit of 1.5 nm thickness, therefore structural growth occurs in columns that are perpendicular to the substrate. Al_2O_3, SiO_2, and LaF_3 films with thickness of 1.5 μm were evaporated for optical and structural analysis. Additional samples of Al_2O_3 and SiO_2 with thicknesses of 1.5 μm and LaF_3 with 1 μm, evaporated on silicon wafers were used for SEM analysis.

2.2. Measurement Techniques

LIDT measurements. Two different set-ups were used for determination of laser induced damage threshold (LIDT). Both of them were operated according to 1-on-1 method described in ISO standard (ISO 21254:2011[1]). The basic measurement system equipped with the third harmonics (pulse duration 3.1 ns) Nd:YAG laser (NL 120 model Ekspla) was used for the comparative measurements for the wavelength of 355 nm using beam diameter of 60 μm.

The absolute value of LIDT was measured by using third harmonic of pulsed Nd:YAG InnoLas Laser: SpitLight Hybrid laser (linear polarization, pulse duration 5.4 ns). The absolute value of laser induced damage in formed waveplate was measured according also to S-on-1 test procedure, which is in compliance with ISO 21254-2 standard. Two different diameters of laser beam were used for testing: 220 μm, as specified in ISO standards, and 59 μm to reduce the influence of film defects. LIDT evaluation consisted of online scattered light damage

detection and offline inspection of damage detection using Nomarski microscopy (up to 100×).

Ellipsometric measurements were performed by spectroscopic ellipsometer (RC2, J.A. Woollam Co, Inc.). The dispersion of phase delay measurements in all deposited anisotropic films were performed in transmission mode at 0° incident angle.

Spectroscopic measurements were performed by spectrofotometer Photon RT (Essent Optics, Belarus). It was employed to measure the transmission of linearly polarized light at 0° incident angle in two perpendicular directions: P polarization – parallel to the plane of evaporation and substrates normal, S polarization – perpendicular to it.

X-Ray photoelectron spectroscopy (*XPS*) *measurements* were made by Thermo Scientific ESCALAB 250Xi spectrometer and monochromatized Al K_α radiation ($h\nu = 1486.6$ eV) as excitation source. Base pressure in the analytical chamber was better than 2.7×10^{-7} Pa. Survey and detailed spectra acquired using hemispherical electron energy analyzer with pass energy of 40 and 20 eV, respectively. Energy scale of the system was calibrated according to Au 4f7/2, Ag 3d5/2, and Cu 2p3/2 peaks position. Charge neutralizer was used during analysis of all samples. Relative atomic concentrations calculations were performed using original ESCALAB 250Xi Avantage software and relevant sensitivity factors. The peak fitting procedure was accomplished using Gauss-Lorentz product with Gauss/Lorentz mix value of 30%.

The X-ray diffraction (*XRD*) *measurements* at grazing incidence (XRDGI) were performed using a D8 Discover diffractometer (Bruker) with Cu K_α ($\lambda = 1.54$ A) X-ray source. Parallel beam geometry with 60 mm Göbel mirror was used. Processing of the resultant diffractograms was performed with DIFFRAC.EVA software. Refinement procedures were performed with expo v1.14.10 program for automatic solution of crystal structures.[16] The non-structural parameters were refined with Le Bail method; background was described with Chebyshev polynomial function, while the Pearson VII was used as a peak shape function.[17]

3. Results and Discussion

3.1. Single- Layer Analysis

Detailed investigation of optical and structural properties has been performed for single-layers to determine the necessary deposition conditions needed for low-loss waveplates with high optical resistivity. Dispersions of phase delay difference between two perpendicular polarizations, namely in shadowing plane (fast axis) and perpendicular to it (slow axis), were measured by spectrophotometric ellipsometer. Results of phase retardance, normalized to individual film thickness of LaF_3, Al_2O_3, and SiO_2 nano-sculptured layers, are presented in **Figure 2**a. LaF_3 and Al_2O_3 columnar thin films exhibit similar phase retardance of 0.043 and 0.042° nm^{-1}, respectively, for 1 nm layer physical thickness at the wavelength of 355 nm. SiO_2 film of the same thickness indicates slightly smaller phase delay difference – 0.038°. Materials with higher bulk refractive indexes indicate larger phase delay difference in columnar structure, as was experimentally shown by Hodkinson.[15] As an example, crystal quartz has a birefringence in the range of 0.01 at the wavelength of 355 nm.[18] Such difference of refractive indexes in perpendicular directions would result a phase retardance of 0.01° nm^{-1}. Comparing with this crystal, all nano-structured layers exhibit few times larger phase delay difference. According to these results, all three materials can be considered to form $\lambda/4$ waveplates by depositing 2.09, 2.14, and 2.37 μm thickness films of LaF_3, Al_2O_3, and SiO_2, respectively. Analysis of optical transmission has been performed by measuring each 1.5 μm thickness experimental sample. Spectra are shown in Figure 2b. The reflection from the backside of fused silica substrate was neglected.

The green solid line in Figure 2b shows the modeled transmission of the bare substrate with refractive index of 1.476 at the wavelength of 355 nm. The program "OptiLayer" was used to model transmission and determine refractive indexes of anisotropic single layers deposited at 70° oblique angle. Refractive indexes were found to be 1.164 and 1.321 in

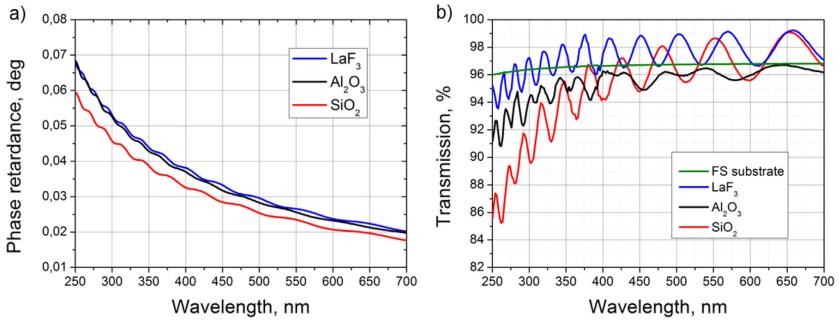

Figure 2. a) The dispersions of phase retardance and b) transmission measurements of LaF_3 (blue line), Al_2O_3 (black line) and SiO_2 (red line) single layer anisotropic thin films for polarization in fast axis.

shadowing plane and perpendicular to it for LaF_3 material, respectively, and for SiO_2 material indexes were 1.211 and 1.231, respectively. The transmission value of single-layer and the substrate system increases when films refractive index is lower than the index of the substrate and optical losses are absent in the film itself.[19] The spectrophotometric measurements by polarized light in fast axis of nano-sculptured films show that only the transmission of LaF_3 film is at the same level as the bear substrate and has optical losses in UV spectral range. The transmission of SiO_2 layer, despite relatively low refractive index, is lower, indicating optical losses throughout all measured spectral region. Difference between substrate and alumina transmission with varying levels of interference peaks and valleys indicate optical losses and inhomogeneity in Al_2O_3 thin film. Therefore, the effort to characterize refractive index values for this material was not effective. In next section, the main causes of optical losses in transmission spectra will be investigated in detail.

3.1.1. Structural and Elemental Analysis of Nano-Sculptured Thin Films

Deviations from ideal stoichiometry can induce absorption and inhomogeneity in thin films. Therefore, X-ray photoelectron spectroscopy measurements were performed to ascertain the elemental compositions and possible chemical bounds of all deposited layers. The atomic concentrations of analyzed films are shown in **Table 1**.

Small amount of adsorbed carbon contamination on the film surfaces was detected for all experimental samples (2.2, 4.8, and 2.6% atomic concentrations for silica, alumina, and lanthanum fluoride, respectively), because of the exposure to the atmosphere after the deposition processes. Therefore, during stoichiometry determination it was neglected and is not included in Table 1. The analysis of silica film XPS spectra showed composition of Si and O elements with atomic concentrations equal to 38.6 and 61.4%, respectively. This corresponds well to the theoretical stoichiometric ratio of SiO_2, which is equal to 33.3 and 66.6%, respectively for Si and O. The composition in alumina film consisted of 41.1% Al and 58.9% O. Measured ratio also is in agreement with its theoretical value for Al_2O_3, where Al:O is 40 and 60%, respectively. It should be noted that only one peak was detected in oxygen spectra in O 1s region (see Figure S1, Supporting Information) for silica film indicating low amount of adsorbed oxygen. While in case of alumina, additional peak with lower intensity was also detected and it indicates increased amount of adsorbed oxygen as described in Supporting Information. Insert in Figure S1, Supporting Information shows high-resolution spectra in Si 2p and Al 2p regions with narrow and symmetrical peaks for both oxides, indicating stoichiometric oxide composition for both films. The XPS survey spectra of LaF_3 film indicated additional lanthanum composition with oxygen. The XPS spectrum of $La_{x1}F_{y1}/La_{x2}O_{y2}$ layer is shown in **Figure 3**.

Table 1. The atomic concentrations of SiO_2, Al_2O_3, and LaF_3 nano-sculptured thin films.

Sample	Atomic concentration				
	Si (%)	Al (%)	La (%)	O (%)	F (%)
SiO_2	38.6	–	–	61.4	–
Al_2O_3	–	41.1	–	58.9	–
LaF_3	–	–	33.2	8.2	58.6

The XPS spectra analysis of LaF_3 film indicated additional minor lanthanum composition with oxygen. Analysis of detected peaks showed that the film deposited by e-beam evaporation process consisted of La (33.2%), F (58.6%), and O (8.2%). Oxygen in lanthanum fluoride films appear due to residual gases in vacuum chamber[20–22] and due to exposure of samples to air after deposition. Oxygen is present in two forms as indicated in O 1s spectra: oxygen bound to lanthanum at 529.2 eV and adsorbed oxygen contaminants (O_2, OH, O-C) at 531.6 eV on binding energy scale (see Figure S2, "A" and "B", Supporting Information, respectively). Estimated binding energy values for lower energy peak "A" are in good agreement with the values reported in literature for oxygen bounded to lanthanum: 528.9, 528.5, and 528.8 eV.[21–23] In the same way, the "B" peak position is close to binding energy values for adsorbed hydroxides/oxygen reported in literature: 532.5,[20] 531.0/532.5,[22] 530.75/531.9 eV.[21] Insert in Figure 3 indicates peaks of $La4d_{5/2}$ and $La4d_{3/2}$ states, found at 104.4 and 107.4 eV, respectively, which corresponds to LaF_3 and coincides with values 104.4 eV and 107.5 eV for LaF_3.[23] Less intense peaks detected at 102 eV and 106 eV were assigned to $La4d_{5/2}$ and $La4d_{3/2}$ states in La_2O_3 material.[23,24] Therefore it can be stated that deposited LaF_3 coating contains small, but not negligible amount of La_2O_3. The band gap of La_2O_3 is relatively narrow (5.3 eV) and may cause the optical losses in UV spectral region. This finding is in agreement with results of other scientists.[20,25] In order to reduce residual oxygen during LaF_3 evaporation cost-ineffective solutions are required – the pressure in vacuum chamber should be maintained at least at 10^{-5} Pa[21] in combination with use of various getters.[26]

Crystallinity and inner nano-structure in thin film material can also cause optical losses.[27] Therefore, scanning electron

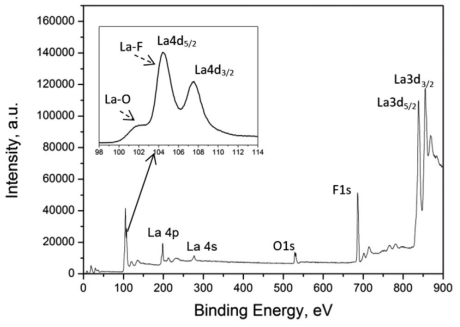

Figure 3. XPS spectrum of LaF_3 layer (the insert shows detected peaks of La_xF_y and La_xO_y compositions).

microscopy (SEM) and X-ray diffraction were used for analysis of the inner structure of nano-sculptured thin films.

XRD diffractogram of the LaF_3 was recorded and analysis indicated that LaF_3 has a hexagonal scalenohedral crystal structure – space group $P\bar{3}c1$ (group number = 165) with a unit cell parameters $a = b = 7.19$ Å, $c = 7.38$ Å, $\alpha = \beta = 90°$, and $\gamma = 120°$. Crystallographic planes orientations (1 1 0), (1 1 1), (3 0 0), (1 0 4), (2 2 3), (4 1 1), (4 1 3), (3 3 2), and (5 2 0) were observed. The crystallite sizes for corresponding reflexes were determined to be 45.6, 64.0, 42.7, 29.1, 44.0, 38.6, 48.7, 67.6, and 41.2 Å. With reference to XRD measurements, additional scattering losses can be assumed in LaF_3 films transmission spectra due to presence of crystalline structure. The sizes of crystallites in films were less than 7 nm and had low impact on optical losses in visible spectral region. Analyses of Al_2O_3 and SiO_2 thin film diffractograms indicated amorphous structure.

SEM images of Al_2O_3, LaF_3, and SiO_2 films, evaporated by SBD method at oblique angle set to 70°, are shown in **Figure 4**a–c. Samples were cleaved to observe the cross section of the shadowing plane.

Analysis of thin films cross-sections indicates that inner structures consist of vertical columns with different features depending on each material (see Figure 4a–c). Characteristic feature sizes of relatively densely packed columns (width ≈40 nm) remain constant only during the LaF_3 growth. SiO_2 and Al_2O_3 layers consist of columnar structure with gradually increasing diameters of individual columns as the film grows. In the beginning of the film growth, average widths of the columns were equal to 29 nm for silica and 20 nm for alumina. When films thicknesses reached 400 nm, the coalescence of columns has been started and the width of the individual element extended to 31 and 88 nm for SiO_2 and Al_2O_3, respectively. Near the top of the layer (1.5 μm thickness) the width of the structural element increases to 70 nm for silica and 120 nm for alumina. Both, the expansion and later the coalescence of such columns could lead to film inhomogeneity and light scattering. This phenomenon also was shown by other scientific group who conclude that photometric measurements of silica OAD films indicated poor performance, because of optical scattering, with losses of 10–15%.[28]

Optical resistivity to laser radiation was analyzed by measuring the laser-induced damage threshold (LIDT) in nano-sculptured films of each material. Comparative laser damage testing measurements were performed in single shot mode for SiO_2, Al_2O_3, and LaF_3 thin films and indicated thresholds of 6.5 a. u., 3.0 a. u., and 3.0 a. u., respectively, at the wavelength of 355 nm. Silica layer exhibited the largest optical resistivity: LID threshold was more than two times larger if compared to lanthanum fluoride or alumina. In pulsed nanosecond regime, the LIDT is closely related to thermal properties (thermal capacity, heat conduction and melting point) and dielectric breakdown effects (multiphoton absorption and avalanche ionization) of materials.[29] The tendency was shown, that materials with larger bandgap are less efficient absorbers (by the means of multiphoton absorption) and thus are more resistant to laser damage.[30] The band gap of bulk SiO_2 is ≈9 eV, which is higher than that of Al_2O_3 (≈7 eV). Pure LaF_3 material has even higher bandgap value than silica, however, deposited LaF_3 film consisted not only of pure LaF_3 but also contains La_2O_3, which distinguishes band gap value of 5.3 eV.[25] This composition of LaF_3 and La_2O_3 indicates defected areas with lower effective bandgap value than pure LaF_3, thus significantly reduced LIDT values.

LID threshold measurements of single layer experimental samples indicate better optical resistance of silica thin films if compared to alumina or lanthanum fluoride. However, nano-sculptured silica films also exhibited significant optical losses in transmittance, which must be addressed prior using such waveplates in practice. In present work, a novel approach of nano-sculptured SiO_2 evaporation was devised to overcome this drawback. Combination of anisotropic and homogenous all-silica thin films (see **Figure 5**b) resulted in suspended expansion and coalescence of columns.

In the beginning of film growth, the average width of the columns was ≈29 nm. When film thickness reached 400 nm, the width of the columns increased up to ≈31 nm. In order to suspend the further spread of cone-like structure, dense SiO_2 layer is introduced at this moment. This interlayer serves for two purposes: it suppresses the expansion of columns and serves as the new flat base for the next layer with columnar structure. The anisotropic film growth on such interlayer is then continued in the same as grown on a substrate. By doing so the average width of the columns is kept about 29 nm and expands only by 2 nm when films thickness reaches 400 nm.

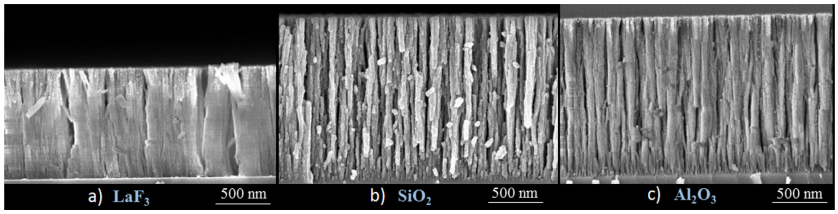

Figure 4. Cross-sectional SEM images of LaF_3, SiO_2, and Al_2O_3 thin films deposited by serial bi-deposition technique at 70° angle.

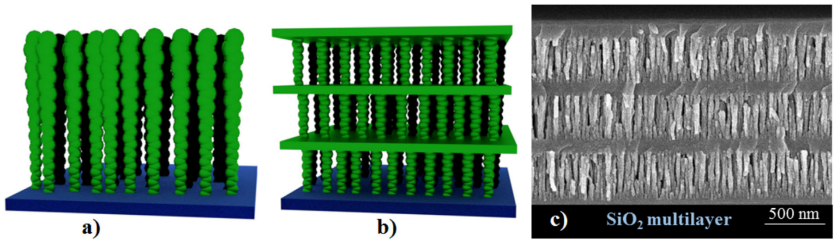

Figure 5. The schematic representation of the formation mechanism during the evolution of nano-sculptured SiO_2 thin film: a – the spread and coalescence of the columns with 1.5 nm thickness subdeposits, during single layer growth, b – multilayer approach using dense interlayers, c – SEM image of deposited multilayer SiO_2 coating.

3.2. Multilayer Analysis

3.2.1. Nano-Sculptured Silica Layers

Fresnel reflections between interfaces are inseparable in optical systems with different refractive indexes. Even reducing the columnar broadening in anisotropic silica film (using chevronic thin film structure[31] with, possibly, lower birefringence[15] would result in interference between the porous silica layer and the fused silica substrate. Also, the final waveplate must contain at least two layers: anisotropic film for retardance and a dense layer on top for mechanical protection. To obtain a transparent optical element with deposited relatively thick film (≈3–4 μm) is difficult due to intense interference oscillations. Therefore, multilayer approach allows more freedom in varying the thickness of individual layers resulting in broad spectral region of transmittance.

Conventional antireflection (high-transmission) or high-reflection optical elements are formed by combining iterative pairs of high and low refractive index materials films with optical thickness equal to quarter-wave or half-wave.[32] To reach optimal transmission of the waveplate the great care must be intended to model the design of interference coating, consisting of porous and dense silica layers. Initially the dispersions of refractive indexes were characterized using "OptiLayer" program for dense layer and anisotropic layer for two perpendicular polarizations: F and S (in fast and slow axis, respectively). For the wavelength of 355 nm the refractive index of dense SiO_2 layer is equal to 1.41, of anisotropic layer for F and S polarization – 1.211 and 1.231, respectively. Therefore, maintaining the evaporation structure design, dense and porous anisotropic films can be approached as high and low refractive index materials. The aim of the waveplate design is to have the smallest number of layers in order to reach the highest transmission and to keep thicknesses of individual anisotropic layers thinner than 400 nm to avoid scattering effect. In this way, high transmittance can be reached and, by keeping the sum of anisotropic layers at the proper thickness, necessary phase delay can be achieved. The modeled design of λ/4 waveplate, where distribution of electromagnetic field $|E|^2$ is presented across coating thickness, is shown in **Figure 6**a. This evaporation design

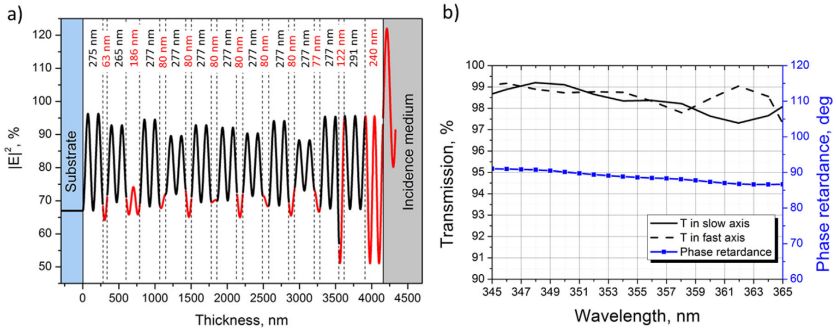

Figure 6. a) Theoretical calculations of multilayer waveplate *E*-field distribution and design. b) Optical measurements of deposited multilayer waveplate: transmission spectra of the element in slow and fast axes are plotted in black solid and dashed curves, respectively; the dispersion of phase delay difference is indicated by blue solid curve.

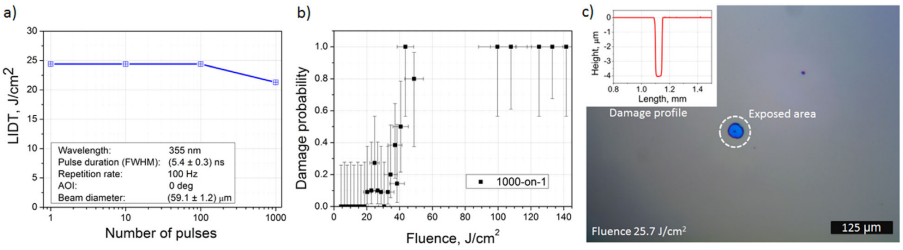

Figure 7. The results of LIDT measurements: a – the characteristic damage curve, b – the damage probability curve, c – microscopy image of typical damage morphology at the fluency level of 25.7 J cm^{-2} after 1 pulse.

was implemented and both, the transmission and phase delay dispersion, are shown in Figure 6b.

Optical resistivity of the waveplate evaporated according to the presented design was tested at the wavelength of 355 nm in nanosecond regime. Using laser beam diameter of 220 μm, the damage threshold reached 11.5 J cm^{-2} in 1-on-1 and slightly decrease in S-on-1 test method. Comparable LIDT value (10.4 J cm^{-2}) was obtain for silica nano-sculptured single layer film by Oliver group.[28] However, this value possibly is restricted by contamination and surface cleanliness. The same evaporated waveplate was damage tested with laser beam diameter of 59 μm to reduce the irradiated area and possibility of interaction with defects within the coating or between it and the substrate. The LIDT value was equal to 24.4 J cm^{-2} using 1-on-1 test method and slightly decreased by using S-on-1 test method (**Figure 7**a). According to damage probability curve (Figure 7b), this value is still restricted by the layer defects and has more potential to be raised even till 40 J cm^{-2}. Damage morphology, presented in Figure 7c, also shows damage site, initiated by defect. Profiler measurements, shown in the legend, indicate the depth of the damage to reach 4 μm. This value matches with the total thickness of multilayer coating confirming that defects on the substrate are partly responsible for the damage initiation.

Although, bulk-fused silica indicates LIDT value about 23 J cm^{-2} for the wavelength 355 nm, the tendency was shown that nano-sculptured evaporated silica layers indicate higher LIDT values due to increasing porosity while evaporating at glanced angle.[33,34] Porous structures are less restricted in density when material is expanding in volume due to the thermal effects. However, as it was shown earlier in Figure 6a, one of the intensive peaks of the E-field coincided with dense SiO_2 layer, what encourages to extend future work in optimizing E-field distribution in nano-sculptured coating layers for even better results.

4. Conclusions

In this work, the conceptually novel multilayer nano-sculptured thin film evaporation-based approach has been presented for production of zero-order λ/4 waveplate operating at 355 nm wavelength. In pulsed nanosecond regime (at the wavelength of 355 nm) comparative analysis of its building blocks – porous single layers with columnar structure indicated superior optical resistivity of silica material if compared with alumina and lanthanum fluoride thus making it best candidate for multilayer coating. The concept of insertion additional dense interlayers in porous anisotropic amorphous silica films allowed to minimize optical scattering by reducing coalescence and spreading effects of the columnar structure. Multilayer design was then successfully optimized to reach high transparency ($T \sim 99\%$) of experimental waveplate. Optical resistance of multilayer component has been tested in nanosecond regime at the wavelength of 355 nm. LIDT values of 11.5 and 24.4 J cm^{-2} have been reached using laser beam diameter of 220 and 59 μm, respectively. Damage morphology images and profiler measurements confirm resistivity limitations due to defects in the coating and on the substrate. A total of 15% damage probability at 40 J cm^{-2} indicates the potential to withstand higher laser fluency for proposed design of all-silica-based waveplate coating.

Supporting Information

Supporting Information is available from the Wiley Online Library or from the author.

Conflict of Interest

The authors declare no conflict of interest.

Keywords

evaporation, high power lasers, optical coatings, sculptured thin films, waveplates

Received: October 6, 2017
Revised: November 9, 2017
Published online:

[1] International Organization for Standardization, ISO Standards catalogue, **2011**, 31.260 – Optoelectronics. Laser equipment, ISO 21254-1:2011.
[2] J. Ebrardt, J. M. Chaput, *J. Phys: Conf. Ser.* **2008**, *112*, 032005.
[3] Nature Publishing Group, *Nat. Mater.* **2016**, *15*, 1.

[4] C. A. Haynam, P. J. Wegner, J. M. Auerbach, M. W. Bowers, S. N. Dixit, G. V. Erbert, G. M. Heestand, M. A. Henesian, M. R. Hermann, K. S. Jancaitis, K. R. Manes, C. D. Marshall, N. C. Mehta, J. Menapace, E. Moses, J. R. Murray, M. C. Nostrand, C. D. Orth, R. Patterson, R. A. Sacks, M. J. Shaw, M. Spaeth, S. B. Sutton, W. H. Williams, C. C. Widmayer, R. K. White, S. T. Yang, B. M. Van Wonterghem, *Appl. Opt.* **2007**, *46*, 3276.
[5] M. M. Wefers, H. Kawashima, K. A. Nelson, *J. Chem. Phys.* **1998**, *108*, 10248.
[6] G. G. Wells, C. V. Brown, *J. Mater. Sci. Mater. Electron.* **2009**, *20*, 175.
[7] J. Wang, H. Wang, P. R. Goode, T. J. Spirock, C.-Y. Lee, N. M. Ravindra, J. Ma, C. J. Denker, *Opt. Eng.* **2001**, *40*, 1016.
[8] R. Desmarchelier, B. Poumellec, F. Brisset, S. Mazerat, M. Lancry, *World J. Nano Sci. Eng.* **2015**, *05*, 115.
[9] M. Lancry, R. Desmarchelier, K. Cook, B. Poumellec, J. Canning, *Micromachines* **2014**, *5*, 825.
[10] X. Fu, A. Melninkaitis, L. Gallais, S. Kičas, R. Drazdys, V. Sirutkaitis, M. Commandré, *Opt. Express* **2012**, *20*, 26089.
[11] A. Lakhtakia, R. Messier, *Sculptured Thin Films: Nanoengineered Morphology and Optics*. SPIE Press, Bellingham, Washington, USA **2005**, p. 336.
[12] W. Pong, C. S. Inouye, *J. Opt. Soc. Am.* **1978**, *68*, 521.
[13] E. O. Filatova, A. S. Konashuk, *J. Phys. Chem. C* **2015**, *119*, 20755.
[14] A. M. El-Sayed, M. B. Watkins, A. L. Shluger, V. V. Afanas'ev, *Microelectron. Eng.* **2013**, *109*, 68.
[15] I. Hodgkinson, Q. H. Wu, *Appl. Opt.* **1999**, *38*, 3621.
[16] A. Altomare, C. Cuocci, C. Giacovazzo, A. Moliterni, R. Rizzi, N. Corriero, A. Falcicchio, *J. Appl. Crystallogr.* **2013**, *46*, 1231.
[17] L. B. McCusker, R. B. Von Dreele, D. E. Cox, D. Louër, P. Scardi, *J. Appl. Crystallogr.* **1999**, *32*, 36.
[18] G. Ghosh, *Opt. Commun.* **1999**, *163*, 95.
[19] H. A. Macleod, *Thin- Film Optical Filters*. CRC Press, Tuscon, Arizona, USA **2010**, p. 332.
[20] G. Liu, H. He, Y. Jin, Z. Fan, *Appl. Surf. Sci.* **2010**, *256*, 2343.
[21] Y. Taki, K. Muramatsu, *Thin Solid Films* **2002**, *420–421*, 30.
[22] H. Yu, Y. Shen, Y. Cui, H. Qi, J. Shao, Z. Fan, *Appl. Surf. Sci.* **2008**, *254*, 1783.
[23] Y. A. Teterin, A. Y. Teterin, *Russ. Chem. Rev.* **2002**, *71*, 347.
[24] M. F. Sunding, K. Hadidi, S. Diplas, O. M. Lovvik, T. E. Norby, A. E. Gunaes, *J. Electron Spectrosc. Relat. Phenom.* **2011**, *184*, 399.
[25] Y. Zhao, K. Kita, K. Kyuno, A. Toriumi, *Appl. Phys. Lett.* **2009**, *94*, 042901.
[26] A. Heidary Moghadam, V. Dashtizad, A. Kaflou, H. Yoozbashizadeh, *Vacuum* **2015**, *111*, 9.
[27] T. Tolenis, L. Grinevičiūtė, L. Mažulė, A. Selskis, R. Drazdys, *J. Nanophotonics* **2016**, *10*, 036003.
[28] J. B. Oliver, T. J. Kessler, C. Smith, B. Taylor, V. Gruschow, J. Hettrick, B. Charles, *Opt. Express* **2014**, *22*, 23883.
[29] R. M. Wood, in *Laser-Induced Damage in Optical Materials*, Section I (Ed. D. Ristau), CRC Press, Boca Raton, USA **2015**, pp. 9–25.
[30] L. Gallais, D. B. Douti, M. Commandré, G. Batavičiūtė, E. Pupka, M. Ščiuka, L. Smalakys, V. Sirutkaitis, A. Melninkaitis, *J. Appl. Phys.* **2015**, *117*, 223103.
[31] V. Vepachedu, P. D. McAtee, A. Lakhtakia, *J. Nanophoton.* **2017**, *11*, 036018.
[32] A. Thelen, *Design of Optical Interference Coatings*. McGraw-Hill, California, USA **1989**, p. 255.
[33] L. Yang, X. D. Yuan, H. X. Deng, X. Xiang, W. G. Zheng, S. B. He, Y. Jiang, H. B. Lv, L. Ye, H. J. Wang, X. T. Zu, *Adv. Condens. Matter Phys.* **2014**, *2014*, 308918.
[34] L. Tolenis, L. Grinevičiūtė, R. Buzelis, L. Smalakys, E. Pupka, S. Melnikas, A. Selskis, R. Drazdys, A. Melninkaitis, *Opt. Mater. Express* **2017**, *7*, 1249.

3 publikacija / 3rd publication

Highly resistant all-silica polarizing coatings for normal incidence applications

L. Grineviciute, L. Ramalis, R. Buzelis, T. Tolenis

Optics letters, **46**, 4, (2021)

DOI: 10.1364/OL.414392

Optics Letters

Highly resistant all-silica polarizing coatings for normal incidence applications

LINA GRINEVICIUTE,* LUKAS RAMALIS, RYTIS BUZELIS, AND TOMAS TOLENIS

State Research Institute Center for Physical Sciences and Technology, Savanoriu Ave. 231, LT-02300 Vilnius, Lithuania
**Corresponding author: lina.grineviciute@ftmc.lt*

Received 9 November 2020; revised 15 January 2021; accepted 15 January 2021; posted 19 January 2021 (Doc. ID 414392); published 12 February 2021

Several fundamental restrictions limit the implementation of microlasers in high power systems, low resistivity of coatings and compactness of elements, especially if control of polarization is necessary. Thin-film-based coatings with extremely high optical resistivity and polarizing properties for normal incidence could become a preferable solution. In this Letter, a novel multilayer approach to form all-silica polarizing coatings for normal incidence angle applications is proposed. Laser induced damage thresholds (test one-on-one) at the wavelength of 355 nm were 39 J/cm^2 and 48.5 J/cm^2 for the reflected and transmitted polarizations, respectively. Such elements can essentially improve tolerated radiation power and allow for production of more compact laser systems.

https://doi.org/10.1364/OL.414392

Polarization control in modern laser systems is essential in several current applications: interference lithography [1], refractive index modulations in transparent materials [2], absorption enhancement in laser–matter interactions [3], etc. For solid state lasers, birefringent crystals (such as YVO_4) can be used as gain media and generate linear polarization [4], but, for microchip lasers, isotropic materials are more preferable due to their exclusively better properties [5]. Additional consideration must also be included when higher averaged powers and ultrashort pulses are used, or compact solutions with shorter resonators are needed. Optical components and especially coatings have to withstand extreme intensities without losing their optical performance. Therefore, compact, preferably coating-based solutions for high power polarized laser emission are highly desirable.

Several different methods, mostly implemented using glancing angle deposition (GLAD) technology, have been realized for low band-gap thin-film-based polarizing components. For circular polarization selectivity, chiral nanostructures can be formed with helical non-homogeneity along a fixed axis [6]. For transformation to linear polarization, nematic structures of sculptured thin films can be employed, namely, zig-zag nanostructures, which are similar to biaxial crystals and have three characteristic refractive indices [7]. When such a film is irradiated at a zero angle of incidence (AOI), two principal axes are present, the fast and slow axes, which are parallel and perpendicular to the shadowing plane, respectively [8]. The shadowing plane is the plane parallel to the α rotation axis and vapor flux direction [see Fig. 1(a)]. Birefringence of anisotropic thin film depends on deposition angle χ. Specifically selected combinations of anisotropic thin films in a multilayer structure can lead to novel components. Changing the orientation of an individual film's optical axis results in a polarizer with highly reflected (R) linear polarization and highly transmitted (T) perpendicular polarization. A few such designs have been realized using TiO_2, Ta_2O_5, and WO_3 materials [9,10]. The combination of both nanostructures also was implemented for more complex optical coating, capable of inverting polarization in the transmission mode [11]. All of aforementioned investigations describe polarizing coatings, but all of them used materials with comparatively low optical resistivity, limiting their applications in high power laser systems. Mainly, two microlaser configurations could benefit from polarizing coating: (i) by applying the coating instead of an output coupler, the unwanted polarization can be diminished by lowering the reflectivity for that polarization; (ii) vice versa requirements are needed when a zero angle polarizer is used within the cavity—high transmittance is required for the preferable polarization, and small reflections for the perpendicular polarization would diminish it. Therefore, a flexible method is needed for covering a wide range of laser systems [12].

During the last 5 years, a new approach has been presented for coatings with extreme resistivity to laser radiation. All-silica-based high reflectivity mirrors showed the potential to reach more than 60 J/cm^2 LIDT at a 355 nm wavelength in the pulsed nanosecond regime [13]. Afterwards, anisotropic all-silica multilayer coatings have been implemented for waveplate formation, which showed impressive performance under high laser power density (laser induced damage threshold, LIDT = 24.4 J/cm^2) [8].

In this Letter, we present a new all-silica coating polarizer, which is also capable of withstanding high density radiation. In order to demonstrate the versatility of the presented approach, several coating designs have been modeled, and two of them are fabricated together with the full-scale measurements and analysis necessary for the implementation of polarizres into high power microlaser systems. Two polarizing coatings at the wavelength of 355 nm have been formed using two stepper motors

0146-9592/21/040916-04 Journal © 2021 Optical Society of America

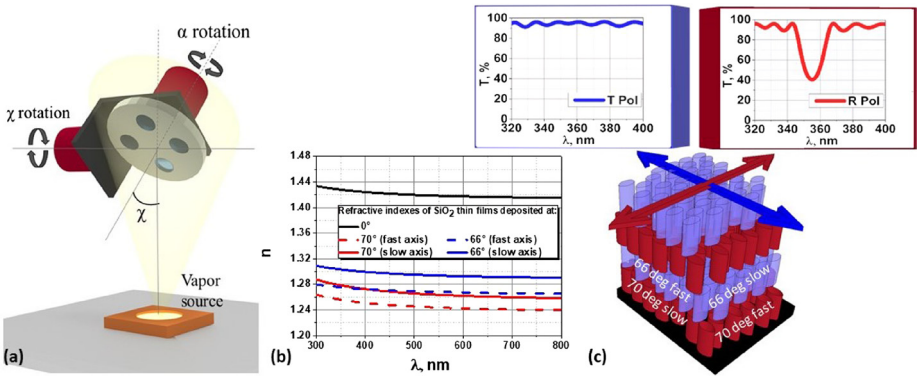

Fig. 1. (a) Principle scheme of the GLAD system, (b) effective refractive index dispersions of silica films deposited by the GLAD system at 0°, 66°, and 70° angles, and (c) principal scheme of the cross section of the high-contrast polarizer multilayer coating consisting of anisotropic layers with perpendicularly aligned optical axes.

based on the GLAD system [Fig. 1(a)]. Afterwards, optical and structural analyses have been performed including spectrophotometric, atomic-force microscopy (AFM), scanning electron microscopy (SEM), and optical resistivity measurements.

Thin films, formed by the GLAD method, can virtually exhibit any refractive index ranging from bulk material to air [14]. Additionally, birefringence of the layers can also be tuned by changing the deposition angle and the thickness of zig-zag subdeposits [15]. In present research, for the formation of anisotropic thin films, depositions at glancing angles (in this case 66° and 70°) were performed using the so-called serial bideposition technique [15]. Substrates were rotated every 6 s in half-turns around its axis for the formation of columnar thin films with orientation perpendicular to the substrate plane with elliptical shape cross sections. The effective refractive indices of silica thin films, deposited at angles of 0°, 66°, and 70°, are presented in Fig. 1(b). A relatively dense silica layer, deposited at a 0° angle, exhibits the isotropic refractive index of 1.43. Effective refractive indices of anisotropic layers for the plane between vapor flux and substrate normal have lower values compared to the perpendicular plane due to the self-shadowing effect during thin-film growth. Therefore, the aforementioned plane performs a function of the "fast axis" and the plane in the perpendicular direction is the "slow axis". As shown in Fig. 1(b), refractive indices match in the fast and slow directions for thin films deposited at 66° ($n_{\text{fast}}^{66} = 1.27$) and 70° ($n_{\text{slow}}^{70} = 1.27$) angles, respectively. For opposite directions of the films, the same layers have the difference in refractive indices of 0.054. Therefore, deposition of both single layers sequentially and misaligning their optical axis by 90° with respect to each other would result in a difference of spectral performance. The principal scheme of sequentially misaligned layers with elliptically shaped cross sections is presented in Fig. 1(c). Fixing the optical thicknesses of all layers in the presented multilayer coating will result in two distinct spectral performances for two perpendicular linear polarizations. For T polarization, the refractive indices match, and minimal Fresnel reflections occur between the interfaces of the coating. For perpendicular polarization, namely, R polarization, indices differ, and spectral performance depends on the thicknesses of individual layers.

The obtained dispersions of effective refractive indices [in Fig. 1(b)] of silica thin films were used in modeling multilayer coatings. The multilayer coating consists of layers sequentially depositing at angles of 66° and 70° and changing the orientation of the films' optical axis by 90°. Such a sequence results in matched indices for T polarization. Therefore, optical thicknesses of individual layers have low impact on transmittance/reflectance for this linear polarization. For R polarization, indices have the largest difference, and, therefore, optical thicknesses have a high impact on optical performance. In order to gain the maximal reflectance in R polarization at the wavelength of 355 nm, each layer was set at one quarter wavelength optical thickness (QWOT). Therefore, the physical thickness of films, deposited at angles of 66° and 70°, were 68.1 nm and 70.7 nm, respectively. Choosing 12 layers (six pairs of films, deposited at angles of 66° and 70°) as one stack, several designs were modeled for demonstration of the high-contrast polarizer's principal idea [see Fig. 2(a)]. Modeled transmission spectra indicate high transmission for T polarization, which is independent of the number of stacks in the coating. As for R polarization, the reflectivity increases by increasing the number of stacks within the coating to virtually any value. It is worth mentioning that dense layers (deposited at a 0° angle) were inserted between the stacks in order to strengthen the coating structure and increase the mechanical resistivity. Since the optical thickness of each dense thin film was two QWOTs, it had minimal influence on spectral performance. As can be seen from the figure, the presented approach allows us to gradually control the transmittance of R polarization and stabilize it for T polarization at the same time. In order to gradually vary the transmittance of T polarization, additional modifications were added to the design. The modification means that for the multilayer design three pairs of anisotropic layers are removed, and one high reflective pair (angle of 70° and dense silica layer of QWOT) is added. Figure 2(b) indicates how transmittance of the R polarization

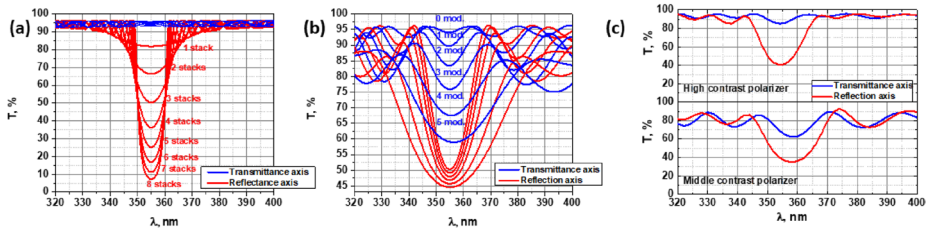

Fig. 2. (a) Modeled transmittances for R and T polarizations of the high-contrast design depending on the number of the stacks (including the back side of the component), (b) modeled transmittances of the middle-contrast design depending of the number of modifications, and (c) measured transmittance for R and T polarizations at zero AOI of fabricated polarizers.

remains stable, and it can gradually be changed for T polarization. The presented approach indicates how transmittance for each polarization can be tuned independently to perpendicular polarization by choosing one of the two paths. Two modeled designs of high- and middle- contrast polarizers were experimentally verified and characterized in great detail.

Both designs were deposited using a SIDRABE electron-beam evaporation plant and measured with spectrophotometer PhotonRT with polarized light at 0° (AOI). Measured transmittance graphs are presented in Fig. 2(c). The high-contrast sample consisted of four stacks and exhibited the transmission of 40.4% and 85.3% for R and T polarizations, respectively. The obtained difference in transmission values differs by almost 10% from the theoretical due to experimental errors in the physical thicknesses and refractive indices of the coatings. Also, nano-sculptured layers can exhibit inhomogeneities in structure and optical properties as a consequence [8]. The middle-contrast experimental sample of three stacks and three modifications exhibited the transmission of 35.1% and 62.5% for R ant T polarizations, respectively. The obtained values again differ by almost 10% from the theoretical due to experimental errors in the coatings' physical thicknesses and refractive indices. However, such discrepancies between the modeled and experiment results do not preclude the demonstration of the concept.

Structural analysis of the experimental samples has been performed in order to investigate the possible causes of optical losses and structural inhomogeneity. The surface morphology and inner structure of the high-contrast polarizer is shown in Fig. 3. Two SEM images are combined in Fig. 3(a): on the left side of the multicolor bar, the cross section is parallel to the R polarization direction, and, on the right side, the cross section is perpendicular to the R polarization direction (parallel to T polarization).

The multilayer structure consists of nanostructured thin films, deposited at angles of 66° and 70° by the serial bideposition method and dense layers inserts. In the beginning of the film growth, the average width of the individual columns is around 25 nm. The tangible shape of the columns cannot be distinguished due to the spread and the coalescence of the columns at interfaces. Previous research indicates that cross sections of the nano-columns, formed by deposition at either 66° or 70° angles, have elliptical cross sections [16]. The cross section of the multilayer parallel to R polarization consists of relatively densely packed columns in thin films, coated at a 66° angle, and more porous layers, coated at a 70° angle. Alternatively, anisotropic

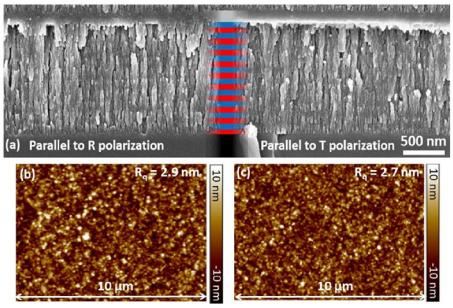

Fig. 3. Structural investigation: (a) SEM images of high-contrast polarizer (the colors of the marked central bar indicate substrate (black); layer deposited at 70° (red); layer deposited at 66° (blue); dense layer (gray)) and AFM images of (b) high-contrast and (c) middle-contrast polarizers morphologies.

single layers, deposited at a 70° angle, with the thickness of more than 400 nm, have thicker columns, which may cause increased optical scattering [8]. Such a phenomenon was not observed when individual anisotropic films were deposited in an orthogonal orientation. Scattering from the relatively large features (25 nm and more) can still cause some optical losses in the UV spectral range. Additionally, the dense interlayers were embedded after each stack for better mechanical robustness.

The surface roughness of the fused silica (FS) substrates used in experiments did not exceed 0.5 nm. GLAD is known to increase the surface roughness of the optical coatings [8,14]. Analysis of AFM images indicates that the surface roughness of the high-contrast and middle-contrast polarizers is 2.9 nm and 2.7 nm, respectively. Comparatively large surface roughness can also be considered as the essential reason for optical losses.

The high-contrast polarizer was tested by high power laser radiation in order to determine the LIDT value. An EKSPLA NL220 pulsed nanosecond Nd:YAG laser was used for the evaluation of damage probability at the wavelength of 355 nm using the one-on-one test method [17]. Pulse duration of ~3 ns and microfocus approach with focused beam diameter of 60 µm were chosen in order to separate damages on local defects from intrinsic resistance of investigated surfaces. Damage probability versus radiation fluence for the R and T polarizations is presented in Fig. 4(a). The errors of LIDT measurements did

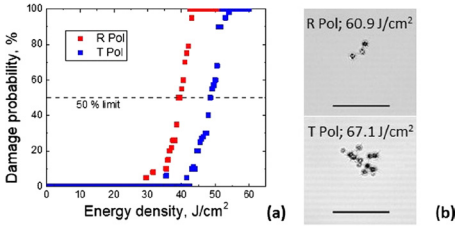

Fig. 4. Resistance to laser radiation of the high-contrast polarizer: (a) damage probability for T and R polarizations and (b) optical microscopy (black bars represent 100 μm) images representing typical damage morphologies.

not exceed ±5% of the measured values. The lowest fluence level, at which damage initiation occurred, was 29.5 J/cm^2, when the experimental sample was irradiated in R polarization. For T polarization, the lowest fluence, at which the damaged site was observed, was at the level of 35.5 J/cm^2. In order to evaluate the intrinsic resistivity of the coating more accurately, damage thresholds were also evaluated at 50% probability level, therefore neglecting the influence of low resistivity defects [18]. Re-evaluated values were 39.0 J/cm^2 and 48.5 J/cm^2 for the R and T polarizations, respectively. All of the damaged sites were inspected with optical microscopy and measured by a profilometer in order to determine the possible causes for induced damage. Two typical damaged sites are presented in Fig. 4(b). Several spots are visible in both cases, indicating the defect-based damage morphology. Both images were taken of damaged spots at the fluency level with probability of 100%. Afterwards, damaged sites were measured by a profilometer for depth determination. For R polarization, the depth of the damaged sites increased from 234 nm to 523 nm when the energy fluence was changed from 42.7 J/cm^2 to 65.1 J/cm^2. For T polarization, no tendency for the depths of the damaged sites was found. Measured depths varied from around 500 nm to 3000 nm at similar levels of fluence.

The presented research demonstrates the polarizer, which operates at a zero AOI and is highly resistive to laser radiation. Instead of forming a Brewster type design, GLAD technology enabled us to form anisotropic layers. Accordingly, instead of isotropic films with high and low refractive indices, only silica material has been used by varying the inner structure of individual layers and, therefore, obtaining necessary birefringence for polarizing functions at a zero AOI. However, few issues still have to be addressed for technological implementation in microlaser systems.

The main concern regarding the presented component is its porous structure. The coating is sensitive to environmental changes due to open voids of the silica structure. Several investigations indicate the adsorption of water on the structures of silica films [19]. One of the main applications of the presented polarizers is to deposit them on the active medium. Typically, such components are sealed or otherwise protected from the environment. Therefore, only handling throughout the transportation must be addressed.

Other concern is regarding the mechanical stability of the coating. Single layer columnar structures are extremely fragile and mechanically unstable. The presented coatings are covered with a dense silica layer as the last film of the coating. It provides the mechanical endurance during the mechanical cleaning of residues after the deposition process. For very thick multilayer coatings of polarizers, the top dense coating can be insufficient. Therefore, dense silica layers can be incorporated within the overall coating design without drastically affecting the spectral properties or optical resistivity.

All of aforementioned issues have to be tackled in the future works.

Current research presents an all-silica polarizing coating, which can be applied on virtually any substrate. Spectral performance can be controlled individually for each perpendicular polarization by changing the number and thickness of isotropic and anisotropic layers. Since all films consist of the same material, namely SiO_2, overall coating can withstand extreme laser radiation power densities without any damage, hence, opening new possibilities for high power compact solid state laser systems.

Funding. Lietuvos Mokslo Taryba ((LMTLT) Project No. S-M-ERA.NET-20-2).

Acknowledgment. We thank Dr. Algirdas Selskis from the Center for Physical Sciences and Technology for the SEM images.

Disclosures. The authors declare no conflicts of interest

REFERENCES

1. J. He, X. Fang, Y. Lin, and X. Zhang, Opt. Express **23**, 11518 (2015).
2. D. J. Little, M. Ams, P. Dekker, G. D. Marshall, J. M. Dawes, and M. J. Withford, Opt. Express **16**, 20029 (2008).
3. M. Cerchez, R. Jung, J. Osterholz, T. Toncian, O. Willi, P. Mulser, and H. Ruhl, Phys. Rev. Lett. **100**, 245001 (2008).
4. P. H. Tuan, M. C. Tsai, and Y. F. Chen, Opt. Express **25**, 29000 (2017).
5. B. V. R. Gaume, Ann. Chim. Sci. Matériaux **28**, 89 (2003).
6. K. Robbie, M. J. Brett, and A. Lakhtakia, J. Vac. Sci. Technol. A **13**, 2991 (1995).
7. I. Hodgkinson, Q. H. Wu, and J. Hazel, Appl. Opt. **37**, 2653 (1998).
8. L. Grinevičiūtė, M. Andrulevičius, A. Melninkaitis, R. Buzelis, A. Selskis, A. Lazauskas, and T. Tolenis, Phys. Status Solidi A **214**, 1700764 (2017).
9. A. Doucet, G. Beydaghyan, P. V. Ashrit, and J.-F. Bisson, Appl. Opt. **54**, 8326 (2015).
10. I. Hodgkinson, Q. H. Wu, A. Lakhtakia, and R. Messier, Opt. Photon. News **10**(12), 30 (1999).
11. Y. J. Park, K. M. Sobahan, J. J. Kim, and C. K. Hwangbo, Opt. Express **17**, 10535 (2009).
12. P. Laporta, S. Taccheo, S. Longhi, O. Svelto, and C. Svelto, Opt. Mater. **11**, 269 (1999).
13. T. Tolenis, L. Grinevičiute, L. Smalakys, M. Ščiuka, R. Drazdys, L. Mažule, R. Buzelis, and A. Melninkaitis, Sci. Rep. **7**, 10898 (2017).
14. T. Tolenis, L. Grinevičiūtė, R. Buzelis, L. Smalakys, E. Pupka, S. Melnikas, A. Selskis, R. Drazdys, and A. Melninkaitis, Opt. Mater. Express **7**, 1249 (2017).
15. I. Hodgkinson and Q. H. Wu, Appl. Opt. **38**, 3621 (1999).
16. H. van Kranenburg and C. Lodder, Mater. Sci. Eng. R **11**, 295 (1994).
17. International Organization for Standardization, "31.260—Optoelectronics. Laser Equipment," ISO 21254-1:2011 (2011).
18. M. Mende, L. O. Jensen, H. Ehlers, W. Riggers, H. Blaschke, and D. Ristau, Proc. SPIE **8168**, 816821 (2011).
19. S. MacNally, C. Smith, J. Spaulding, J. Foster, and J. B. Oliver, Appl. Opt. **59**, A155 (2020).

4 publikacija / 4th publication

Angular filtering by Bragg photonic microstructures fabricated by physical vapour deposition

L. Grineviciute, C. Babayigit, D. Gailevičius, E. Bor, M. Turduev, V. Purlys, T. Tolenis, H. Kurt, K. Staliunas.

Applied Surface Science, **481**, 353-359, (2019)

DOI: 10.1016/j.apsusc.2019.03.082

Applied Surface Science 481 (2019) 353–359

Contents lists available at ScienceDirect

Applied Surface Science

journal homepage: www.elsevier.com/locate/apsusc

Full length article

Angular filtering by Bragg photonic microstructures fabricated by physical vapour deposition

Lina Grineviciute[a], Ceren Babayigit[b], Darius Gailevičius[c,d,*], Emre Bor[b,e], Mirbek Turduev[e], Vytautas Purlys[c,d], Tomas Tolenis[a], Hamza Kurt[b], Kestutis Staliunas[f,g]

[a] Center for Physical Sciences and Technology, Savanoriu Ave. 231, LT-02300 Vilnius, Lithuania
[b] Department of Electrical and Electronic Engineering, TOBB University of Economics and Technology, Söğütözü Str. 43, 06510 Ankara, Turkey
[c] Vilnius University, Faculty of Physics, Laser Research Center, Sauletekio Ave. 10, Vilnius, Lithuania
[d] Femtika LTD, Sauletekio Ave. 15, LT-10224 Vilnius, Lithuania
[e] Department of Electrical and Electronic Engineering, TED University, Ziya Gökalp Str. 48, 06420, Ankara, Turkey
[f] Institució Catalana de Recerca i Estudis Avancats (ICREA), Passeig Lluís Companys 23, 08010 Barcelona, Spain
[g] Universitat Politècnica de Catalunya (UPC), Rambla Sant Nebridi 22, 08222 Terrassa, (Barcelona), Spain

ARTICLE INFO

Keywords:
Spatial filtering
Photonic crystals
Physical vapour deposition
Glancing angle deposition
FDTD
Surface grating

ABSTRACT

We propose and experimentally demonstrate spatial filtering by photonic crystals in a Bragg configuration. Compared to the Laue configuration, where spatial filtering was already demonstrated before, the Bragg configuration is more technologically challenging, as the longitudinal periods of such structures must be shorter than the operational wavelength. The proposed configuration is designed and analyzed by FDTD simulations and the multilayer structure is fabricated by physical vapour deposition on the microstructured substrate. The measurements of the angle/wavelength transmission of the fabricated structure show the signatures of the angular filtering.

1. Introduction

The idea of the angular/spatial filtering by photonic crystals (PhCs) relies on selective diffraction of light from the double-periodic photonic structures. The angular components of the incident light at resonance with the transverse and longitudinal periodicities of the structure diffract efficiently and they are removed from the zero-diffraction order of the transmitted beam. On the other hand, the angular components that are out of the resonance propagate unaffected or weakly affected by the photonic structure. Therefore, the angular/spatial filtering (low-angle-pass or high-angle-pass filtering) can be obtained by a proper interplay between the longitudinal and transverse periodicities, i.e., by a suitable geometry of the PhCs.

The spatial filtering by the PhCs was theoretically predicted [1–3] and experimentally demonstrated [4,5]. In particular, the PhCs filtering has been already implemented for intracavity angular filtering in microchip lasers, where the beam spatial quality was substantially improved and the brightness of the emission was increased [6]. Due to small dimensions, mechanical stability, and no need for focusing or additional optical elements, such PhC filtering shows itself as an attractive alternative solution for conventional techniques, where the filtering is achieved by a confocal arrangement of lenses with the filtering diaphragm in a focal plane.

On the other hand, apart from conventional filtering, there have been attempts to apply more sophisticated schemes for the light manipulation, in particular by using passive [7,8] or light-induced [9–11] Bragg gratings. However, the latter approach uses an additional laser source. To the best of author's knowledge, the filtering was demonstrated only using cold gases, which limits its applicability in the microoptical systems. Population density gratings can also be induced by using optical pulses in a nonlinear medium that does not require an additional laser source [12]. These alternative methods, however, require complex designs and additional optical components that limit their applications, especially in the microlaser systems. On the contrary, the PhCs based angular filters are extremely compact. Hence, they are especially promising solutions for the intracavity use in the microlasers.

The PhC filters so far were designed and fabricated to work in Laue diffraction regime where the waves diffract predominantly in a forward direction as schematically illustrated in Fig. 1(a). In general, the Laue regime occurs for $d_z > \lambda$. In this case, no full photonic band gap exists. As the wave propagates through the PhC in Laue regime, the periodic revivals called Rabi oscillations occur between the zero- and first-

* Corresponding author at: Vilnius University, Faculty of Physics, Laser Research Center, Sauletekio Ave. 10, Vilnius, Lithuania.
E-mail address: darius.gailevicius@ff.stud.vu.lt (D. Gailevičius).

https://doi.org/10.1016/j.apsusc.2019.03.082
Received 15 October 2018; Received in revised form 12 February 2019; Accepted 10 March 2019
Available online 12 March 2019
0169-4332/

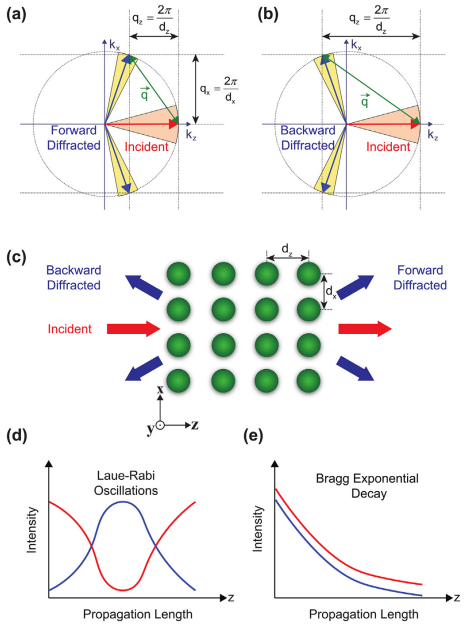

Fig. 1. The principles of PhC angular filtering in (a) Laue and (b) Bragg configurations. The incident wave, with the wavevector indicated by red arrow (k_x, k_z) = (0, k_0), diffracts from the double-periodic structure in (c) with the wavevectors (q_x, q_z). The diffraction is efficient if the grating is at resonance, meaning that the wavevectors of the diffracted wave (blue arrows) are on the light-circle (or light-sphere in 3D). The diffracted waves in Laue configuration propagate in a forward direction and result in periodic energy exchange between the zero and first diffraction orders (d), whereas the waves in a Bragg configuration diffract backward, and thus result in an exponential decay (and correspondingly the stop-bands) of the incident wave (e).

diffracted orders (Fig. 1(d)). For this reason, the length of the structure must be selected precisely for to get efficient filtering. The advantage of the Laue regime is that the lattice periods are well achievable by optical fabrication techniques in organic/inorganic materials [13–15], as the PhC periods along the optical axis d_z are in the range of tens of microns, and along the transverse directions $d_{x,y}$ - of several microns.

The spatial filtering is also possible in the so-called Bragg regime (Fig. 1(b)). Here the length of the structure is less critical, as the Rabi oscillations between filtered and unfiltered modes do not appear, and, instead, exponential decay of the filtered modes occurs (Fig. 1(e)). In the Bragg regime $d_z < \lambda$ (most typically $d_z \approx \lambda/2$), the optical fabrication techniques can be hardly implemented. Holographic methods, despite promising experiments [16,17], require ultraviolet sources and complicated optical designs. Therefore, their use for the PhC fabrication is very restricted, especially when the two-dimensional (2D)/three-dimensional (3D) volume gratings are required. Here, the physical vapour deposition method can be considered as a promising alternative solution for fabrication of such spatially filtering photonic structures in Bragg regimes. The thin film deposition methods have been demonstrated to be able to control the thickness and optical parameters at high accuracy [18]. Additionally, evaporation techniques, equipped with glancing angle deposition method, showed promising results in forming microstructures on structured substrates [19].

Other approaches of spatial filtering by photonic microstructures include the use of resonant gratings [20], 1D and 2D PhCs [21–24], graded index PhCs [25], metallic grids [26] and bi-dimensional doubly periodic gratings [27]. However, all these approaches are still lacking reasonable technological implementations.

The figure illustrates the high-angle-pass filter for simplicity, however evidently, a variation of the periods or wavelength results in a low-angle-pass filter.

In the presented study, we provide an experimental demonstration of the signatures of angular filtering in the Bragg configuration for the first time. We fabricate the PhCs on micro-textured substrates using physical vapour deposition method. The results experimentally prove the concept of spatial filtering but they do not lead to the ideal filtering performance yet, wherein the filtered waves are 100% attenuated. The main reason for that has become apparent in the process of the theoretical/experimental studies and is basically caused by too large transverse periods, and too small depth of the structures (too few longitudinal periods). Therefore, in concluding part of the article, we performed the finite-difference time-domain (FDTD) calculations with "*improved*" geometrical parameters and showed that the presented angular filtering principle works and leads to enhanced spatial filtering that can be applied for selected practical applications. However, the designed structure with enhanced geometrical properties was beyond the available fabrication facilities.

The article is organized in the following way: after the derivation of the Bragg band-gap conditions, we present the FDTD numerical simulation results of the light propagation through the structure. For the proper understanding of the experimental results, we calculated three versions of multilayered PhC structures for spatial filtering. The first version is based on a harmonically modulated substrate profile, and the second one is based on a blazed grating (triangular) substrate. Both versions can be realized by conformal dielectric coatings on a substrate with a periodic surface profile. The ideal case for spatial filtering would be a harmonic (wavy) one, yet the structure with a sufficient modulation depth and the smallest available period was the blazed one. Moreover, the real fabricated structure when starting from a blazed surface grating develops a smoother, almost sinusoidal character towards the outer layers. Therefore, the final result is a combination of the both, blazed and sinusoidal modulated versions. In this regard, the blazed-rounded structure was also calculated.

2. Positions of the band-gaps

The conditions for the Bragg bandgaps can be derived from the resonant scattering condition by using the simple geometric approach. All waves must satisfy the momentum and energy conservation laws. According to the latter, the wave with the wave-vector $\vec{k}_0 = (k_{0,x}, k_{0,z})$, and modulus $|\vec{k}_0| = \omega/c$ after diffracting in a periodic structure with reciprocal lattice vector $\vec{q} = (q_x, q_z)$, results into a diffracted wave with $\vec{k} = \vec{k}_0 + \vec{q}$. The components of the lattice vector are $q_{x,z} = 2\pi/d_{x,z}$ (see Fig. 1. for the definition of the transverse/longitudinal periods $d_{x,z}$). For efficient diffraction, the new wave with wave-vector $\vec{k}$ must satisfy the energy conservation law too, i.e., must satisfy $|\vec{k}| = \omega/c = |\vec{k}_0|$. This means that in an isotropic medium the initial, as well as the final wave-vectors, must lie on the "light ring": $|\vec{k}|^2 = (\omega/c)^2$, as illustrated in Fig. 1(a) and (b). As a result, a simple geometrical consideration allows us calculating the angles at which the Bragg diffraction is most efficient.

An incident wave propagating at the angle θ_i to the optical axis $\vec{k}_0 = (k_0 \sin(\theta_i), k_0 \cos(\theta_i))$, diffracting on a grating with $\vec{q} = (q_x, q_z)$, results in diffracted wave $\vec{k} = \vec{k}_0 + \vec{q} = (k_0 \sin(\theta_i) + q_x, k_0 \cos(\theta_i) - q_z)$. The resonance condition $|\vec{k}| = |\vec{k}_0|$ then leads to the following implicit condition for the Bragg diffraction angle:

$$|\vec{k}| = \frac{q_x^2 + q_z^2}{2q_z\cos(\theta_i) - 2q_x\sin(\theta_i)}. \quad (1)$$

The Eq. (1) is a convenient tool to interpret the angular diffraction map, i.e., the dependence of diffracted wavelength on the incidence angle of θ_i. It shows one Bragg diffraction curve in diffraction map, i.e., the diffraction due to the main harmonics $\vec{q} = (q_x, q_z)$ of the periodic structure. Considering that the gratings have different harmonics of periodicity: $\vec{q}_{n,m} = (m_x q_x, m_z q_z)$, different Bragg-diffraction branches appear:

$$|\vec{k}|_{mx,mz} = \frac{m_x^2 q_x^2 + m_z^2 q_z^2}{2m_z q_z\cos(\theta_i) - 2m_x q_x\sin(\theta_i)}. \quad (2)$$

Here $m_x = \ldots, -2, -1, 0, 1, 2, \ldots$ corresponds to the diffraction order in the transverse direction, and $m_z = 1, 2, \ldots$ corresponds to the harmonics of longitudinal periodicity. The Eq. (2) bears an orientational character, showing the qualitative tendencies in the diffraction map. In order to quantitatively compare the precise FDTD calculations with the experimental results, the Eq. (2) is calibrated by the averaged refraction indices of the environments. Corresponding results are given in the following sections.

3. Design approach and numerical results

The design of multilayered PhC structure for spatial filtering is schematically represented in Fig. 2. The structure consists of alternating multilayers on a substrate where the interfaces of the layers are modified as a periodic array of sinusoidal wavy curves. It is important to note that for efficient spatial filtering the photonic structure must be periodically modulated in both longitudinal and transverse directions. Therefore, due to the wavy surface of the substrate, the modulation of the refractive index occurs not only in vertical but also in horizontal direction, resulting in a 2D PhC structure. Refractive indices of the high (H), low (L) index layers and substrate (Sub) are $n_H = 1.42$, $n_L = 1.33$ and $n_{Sub} = 1.5$, respectively. The thicknesses of the high and low refractive index layers are both equal to $d_z/2 = 120$ nm, where the d_z corresponds to the longitudinal period of the structure. The transverse lattice constant (period of wavy curves) is fixed to $d_x = 1.67$ μm and the number of layers is equal to $N_L = 33$.

The commercial FDTD software was used for the light-matter interaction analysis in the designed structure [28,29]. Due to the periodicity of the structure in the *x*-direction, time domain calculations were conducted via the supercell approach by assigning periodic boundary conditions in the *x*-direction. The dashed green frame in Fig. 2(b) shows the supercell boundaries. Here, the FDTD method solves the Maxwell's equations by infinitely repeating the defined periodical supercell in the *x*-direction. In order to observe the angular filtering property, the proposed structure is illuminated with *P*-polarized plane wave source at a variable angle ($-40° < \theta_i < 40°$) and the corresponding zero-order transmission is calculated in the range of the wavelengths between 450 nm and 850 nm. Note that if radiation from a wide spectral bandwidth source is incident at an oblique angle, a phase shift occurs in the frequency domain [30]. Hence, to obtain the wideband response with an oblique incident plane wave, the Broadband Fixed Angle Source Technique (BFAST) is used in the supercell calculations [31]. The calculated transmission efficiencies evidencing the angular dependence are given as a map in Fig. 3(a).

As mentioned above, the fabrication of the layered structure was initiated on the blazed grating substrate. By considering the fabrication process, we first analyzed a blazed layered structure of the same periods. The blazing angle was adjusted as 10° and the obtained transmittance map is given in Fig. 3(b). However, in the corresponding map, the angular filtering profile was broader in comparison with the presented map for wavy structure in Fig. 3(a). Next, the blazed-rounded structure was calculated, Fig. 3(c). Here, one can see the obtained

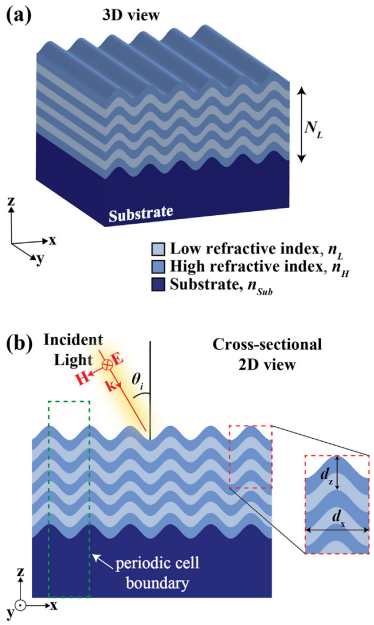

Fig. 2. Schematic representation of the design approach. (a) 3D view and (b) 2D cross-sectional view. Number of layers of the structure is represented by N_L, d_z corresponds to the vertical period and d_x denotes the horizontal period. The structure is illuminated with obliquely incidence source, and the incidence angle is represented by θ_i.

transmittance wave preserves the characteristics of the sinusoidal and blazed structures. Furthermore, for all cases, a cross-sectional profile of the intensity transmittance maps is extracted at $\lambda = 582$ nm (denoted by the black solid line). The obtained results are given for sinusoidal, blazed and blazed-rounded layered structures in Fig. 3(d), (e) and (f), respectively. For the sinusoidal wavy structure, at zero incidence angle, we obtain transmission efficiency as high as 96%, and filtering bands are present for angles at $\theta_i = -10°$ and 10°, where transmission efficiency is decreased to 62%. However, for the blazed case, there is no sign of explicit filtering between $-10°$ and 10° degrees. For the blazed-rounded structure, there is an asymmetric behavior as expected. Nevertheless, the filtering characteristic angles at $\theta_i = -10°$ and 10° are preserved.

In order to quantitatively compare FDTD-calculated Bragg-diffraction branches with analytical predictions, as stated previously, we calibrated Eq. (2) by the averaged refraction indices of the photonic structure. Obtained results are superimposed with transmission maps for both wavy and blazed structures in Fig. 3(a) and (b), respectively. Analytically calculated Bragg-diffraction branches are denoted by colored dashed lines on the transmission maps, showing good agreement with FDTD results.

4. Experimental study

4.1. Fabrication and measurement

The fabrication of the designed structure involved three main steps.

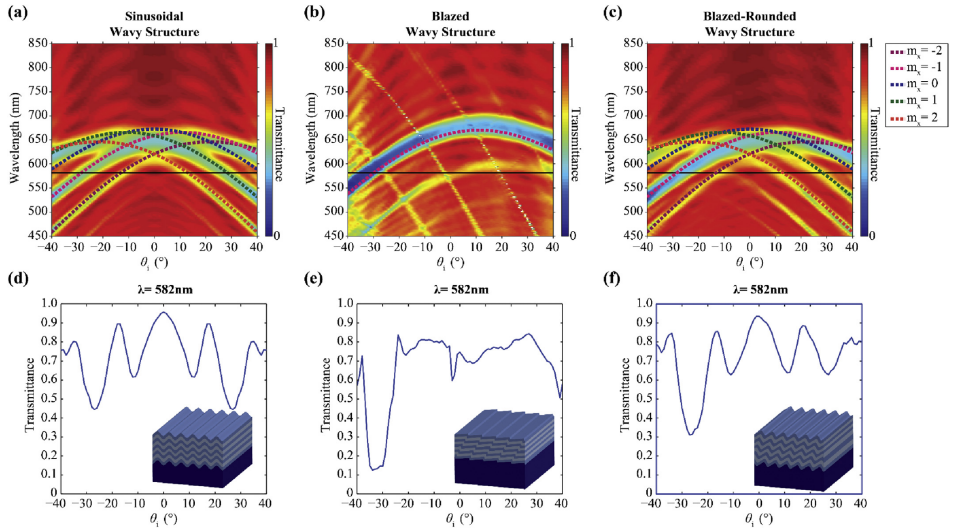

Fig. 3. Zero-order calculated transmittance maps for incidence angle θ_i and wavelength λ for structures with d_z = 240 nm and d_x = 1.67 μm for (a) sinusoidal, (b) blazed and (c) blazed-rounded wavy layered structures. Analytically calculated Bragg-diffraction branches are indicated by dashed curves. Cross-sectional profiles are shown for the wavelength λ = 582 nm for (d) sinusoidal, (e) blazed and (f) blazed-rounded wavy layered structures. The black solid line indicates the wavelength of interest. Schematically representations of the sinusoidal and blazed wavy layered structures are given as insets in the figure plots.

First, a PDMS mold of a commercially available diffraction grating (with a pitch of d_x = 1.67 μm) was made [32]. Second, a base grating was stamped on soda-lime glass slides using a UV curable hybrid polymer (OrmoComp, n_{ref} = 1.52) as the material for the replica. Finally, the multilayer coatings were deposited on the base grating, by alternating high and low refractive index thin films.

"Sidrabe" coating system equipped with glancing angle deposition (GLAD) technology was used in all evaporation processes. GLAD method allowed us to modulate the porosity of the thin films by changing the deposition angle between the substrate normal and evaporation flux. This enabled us to vary the refractive index of individual layers easily and with high precision [33]. During the coating process, the corrugated substrates were placed in a holder constantly rotating around its axis to ensure the conformal evaporation. Theoretical modeling indicates that the refractive index difference between high and low index layers for optimal spatial filtering should be around 0.12. To reach the desired refractive index contrast the deposition angles between the substrate normal and the vapour flux were 0° and 65° for n_H = 1.42 and n_L = 1.30 respectively. Based on the calculations, the designed structures with N_L = 33 and N_L = 39 layers were deposited starting with the higher refractive index material. The physical thickness of each layer was equal to 120 nm (value for $d_z/2$) and controlled with a quartz crystal monitor. The coating processes were started at room temperature, in high vacuum of $p_0 = 1.7 \times 10^{-5}$ mbar and 2 sccm of oxygen gas were introduced into the chamber to ensure the oxidation of evaporated material. The deposition rate was maintained at 3 Å/s.

Surface morphology of the grated substrate was measured by Dimension Edge atomic force microscope (AFM) by Bruker. Height distribution measurements of 20 × 20 μm^2 surface areas were performed in tapping mode and in ambient conditions. A commercial silicon probe with a tip diameter of < 10 nm (force constant – 40 N/m) was used.

The inner structure of the samples was characterized using a scanning electron microscope (SEM) workstation Helios Nanolab 650. The cross sections were made by ion beam milling procedure and later analyzed by SEM. The spectroscopic measurements were performed by spectrophotometer Photon RT (Essent Optics). Linearly polarized light was used for two perpendicular polarizations: S and P, where S polarization is perpendicular to the grating lines on the substrate. The transmission was measured in the spectral region from 450 nm to 850 nm at different angles of incidence. The angle between the mean plane of grating and the detector was changed from −40° to 40° by steps of 2°.

For characterization, we tested the N_L = 39 layer structure by probing it with a divergent beam to make sure that the filtering effect can be observed not only for plane waves but also for beams with curved wavefronts. We focused an S-polarized Gaussian beam with a wavelength of λ = 532 nm with a 2.5 cm focal length cylindrical lens. The beam was characterized by a full divergence angle of ~6°. The transmittance was measured onto the sample which we mounted on a rotating conical mount. The sample was mounted at 21° angle to the incident beam to approximate an effective wavelength of λ_{eff} = 570 nm. The filtered beam was projected directly on the matrix of a CCD camera at the far-field. The angle between the mean plane of grating and the detector was changed from −40° to 40° by steps of 1°, and the total spatial transmittance spectrum has been averaged for overlapping angular positions.

4.2. Experimental results

According to the AFM measurements, the produced blazed substrate pitch was d_x = 1.67 μm and the peak to valley height was 150 nm (Fig. 4(a)). After depositing the alternating high and low refractive index layers, the blazed surface gradually changed to a smooth sinusoidal surface, as can be seen in Fig. 4(b) SEM image of the sample

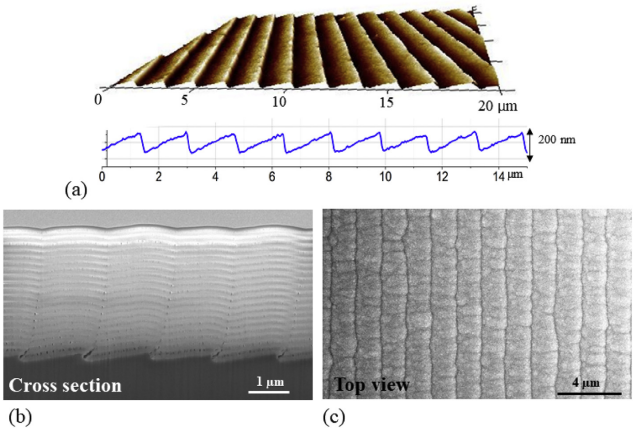

Fig. 4. (a) AFM 3D plot with its height distribution of the corrugated substrate surface. SEM images of fabricated PhC structure (b) cross-section and (c) top view.

cross-section. Although the surface is changing, the horizontal periodicity d_x of the structure remains unchanged.

The measurements of zero-order angular transmittance profiles are summarized in Fig. 5. In Fig. 5(a) and (b) we show the complete transmittance map of the structures having 33 and 39 layers. As expected, the selective decrease in transmittance is more pronounced for the structure with a larger number of longitudinal periods. Also, when comparing the general trend with the numerical results from Fig. 3, we see a qualitative similarity with the predicted results for a harmonic template profile, although there is some asymmetry induced by the blazed profile. Ultimately, the result coincides with superimposed maps from Fig. 3(a) and (b). We interpret this as a result of the continuous change of each individual layer from the blazed to a more harmonic profile (see Fig. 4(b)).

In Fig. 5(c) we see explicit evidence for the hybrid blazed-to-harmonic structure and how much the asymmetry is expressed. For the particular wavelength of $\lambda = 572$ nm, 4 filtering bands are apparent that correspond roughly to $\pm 15^{\circ}$ and $\pm 28^{\circ}$. The smaller angle filtering band minimum transmittance is 60%. The larger angle resulting from the Bragg condition is asymmetric. Transmittance is reduced to 30%

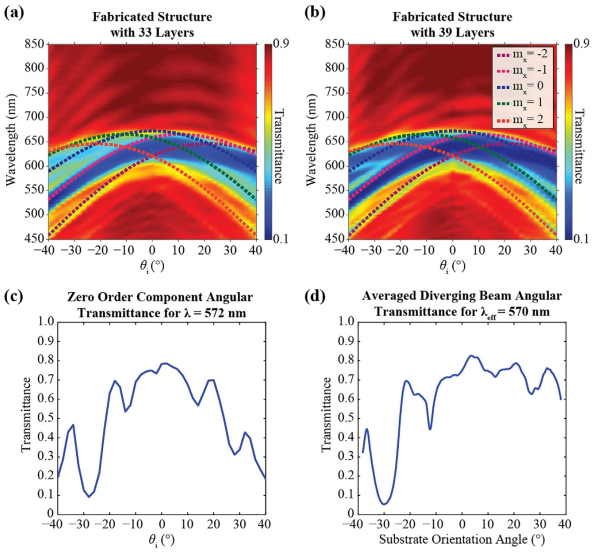

Fig. 5. Zero-order spatial transmittance maps measured using a collimated beam for a fabricated $N_L = 33$ (a) and $N_L = 39$ (b) layer structure. (c) Spatial transmittance profile (horizontal cross-section of the map in (b)) measured for the fabricated structure with $N_L = 39$ layers, (d) averaged angular transmittance of a sample at a constant tilt 21° angle illuminated by a diverging beam with fixed wavelength $\lambda = 532$ nm, which is equivalent to the normal incidence with an effective wavelength of $\lambda_{eff} = 570$ nm. Dashed lines indicate the analytical dependencies according to Eq. (2).

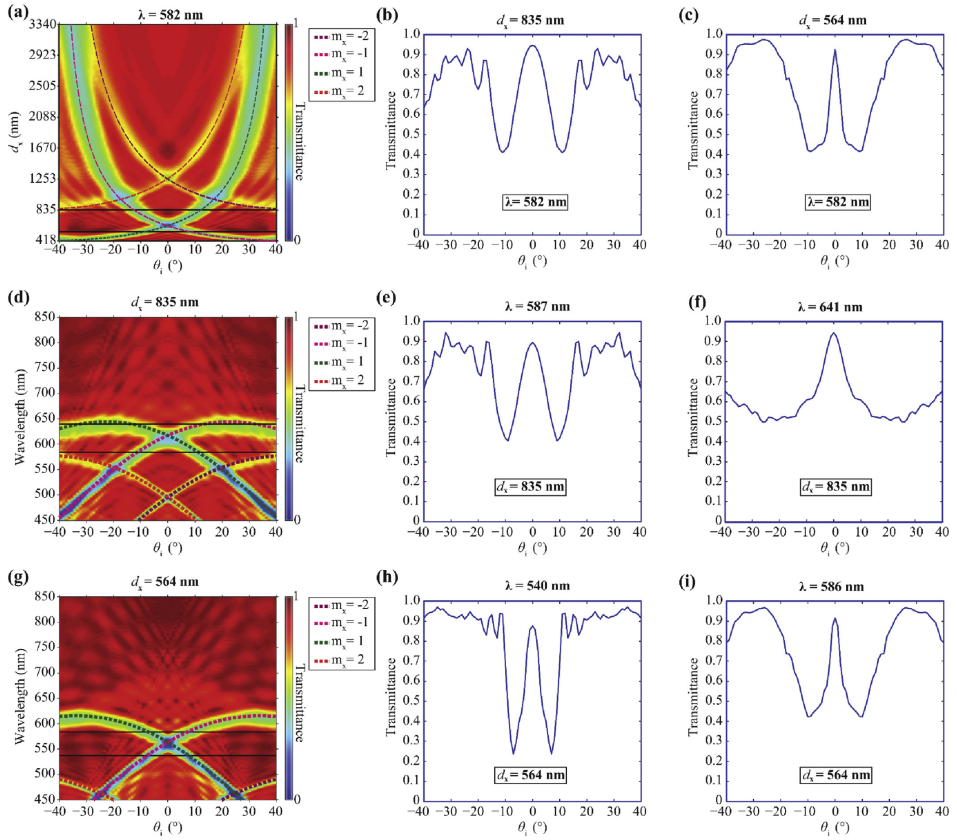

Fig. 6. Zero-order angular transmittance maps (a) for the transverse period d_x, when the probing wavelength λ is fixed at λ = 582 nm, (d) for λ, when d_x = 835 nm, (g) for λ, when d_x = 564 nm. The middle and right columns show corresponding selected transmittance graphs for (b) λ = 582 nm and d_x = 835 nm, (c) λ = 582 nm and d_x = 564 nm, (e) λ = 587 nm and d_x = 835 nm, (f) λ = 641 nm and d_x = 835 nm, (h) λ = 540 nm and d_x = 564 nm, (i) λ = 586 nm and d_x = 564 nm. For all structures: d_z = 240 nm, n_H = 1.42, n_L = 1.33, N_L = 33. Dashed lines indicate the analytical dependences, Eq. (2).

and 10%, whereas the zero-angle transmittance is at around 80%. Fig. 5(d) shows the result when the sample is probed with a diverging beam. The transmittance profile is even more clearly asymmetric. The bands for positive angles feature transmittance values comparable to the zero-angle component, whereas the positive angle bands are in correspondence to Fig. 5(c). However, all the cases show that we created selective attenuation in a form of photonic band gap operation.

5. Perspectives

Filtering performance of the multilayered wavy structure can be improved by further tuning the periods and the contrast of the refractive indexes, which is beyond the current fabrication possibilities. To observe and understand the effect of changing the transverse period d_x, we performed numeric simulations of wavy structures having structural parameters same as in section 3. In this regard, operating wavelength is fixed as λ = 582 nm and the zero-order transmission is computed for transverse periods d_x between 835 nm and 3340 nm. Corresponding incidence angle θ_i versus transverse period d_x transmission map is given in Fig. 6(a). The angular filtering effect increases with the decrease of the transverse period for the specified wavelength value. For a better comparison, a cross-sectional profile of the transmittance map is calculated at d_x = 835 nm and d_x = 564 nm, which are represented in Fig. 6(b) and (c). When the profiles in Fig. 6(b) and (c) are compared with the profile in Fig. 3(c) (structure with d_x = 1.67 μm), we see that the low-pass transmittance peak (between −10° and 10°) is getting sharper with the decrease of the transverse period.

Thereafter, the zero-order transmittance angular filtering characteristic was computed for the structures with d_x = 835 nm and d_x = 564 nm. Results for varied wavelengths are shown in Fig. 6(d) and (g). For both cases, the cross sectional profiles are calculated for selected wavelengths (denoted by black solid lines) and presented in Fig. 6. An even narrower transmittance peak is observed at λ = 641 nm

for $d_x = 835$ nm. The cross-sectional profile is presented in Fig. 6(f). Here, the filtering bands are broader and extend well beyond the incidence angles $|\theta_i| > 10°$. Hence, for a more pronounced filtering effect that is appropriate for practical applications in the optical regime, the transverse periods should be $\lesssim 2$ times smaller than our experimental test value $d_x = 1.67$ μm.

6. Conclusions

Here, we demonstrated the signatures of spatial filtering in Bragg regime, based on periodic photonic microstructures fabricated by physical vapour deposition. Further developments need to be made for such structures to be of practical use, however the principle of angular filtering has been convincingly demonstrated. The main reason for the relatively weak filtering performance of our structures is the relatively large transverse periods. As evidenced by the Eq. (2), the filtering parabolas for each Bragg component cross at small angles; therefore, the narrow low-angle-pass transmission peaks could not be obtained. In order to show the potential, we present the calculations using the structures beyond the technological fabrication possibilities currently available by us. The master gratings required for these structures can be potentially fabricated using more advanced techniques, such as electron beam lithography. In this regard, the presented results in Section 5 show a promising case and evidences a perspective of practical application of the spatial filters being developed based on the idea promoted in the current article. The presented technology is highly flexible: the transverse period can be controlled from tens of nanometers to micrometers using different methods. Longitudinal period and optical constants can also be tuned precisely with thin film deposition methods. Additionally, the proposed spatial filter can be applied as a coating to any surface, indicating its high suitability to complex microlaser systems.

Acknowledgments

K.S acknowledges support by the EUROSTARS Project E!10524 HIP-Lasers, as well as by Spanish Ministerio de Ciencia e Innovación, and European Union FEDER through project FIS2015-65998-C2-1-P. D.G. and V.P. acknowledge the financial support from “FOKRILAS” (Project No. P-MIP-17-190) from Research Council of Lithuania. Authors are grateful to dr. Algirdas Selskis from State research institute Center for Physical Sciences and Technology for SEM measurements.

Declarations of interest

None.

References

[1] K. Staliunas, V.J. Sánchez-Morcillo, Spatial filtering of light by chirped photonic crystals, Phys. Rev. A 79 (5) (2009) 053807.
[2] E. Colak, A.O. Cakmak, A.E. Serebryannikov, E. Ozbay, Spatial filtering using dielectric photonic crystals at beam-type excitation, J. Appl. Phys. 108 (11) (2010) 113106.
[3] Z. Luo, Z. Tang, Y. Xiang, H. Luo, S. Wen, Polarization-independent low-pass spatial filters based on one-dimensional photonic crystals containing negative-index materials, Appl. Phys. B Lasers Opt. 94 (4) (2009) 641–646.
[4] L. Maigyte, T. Gertus, M. Peckus, J. Trull, C. Cojocaru, V. Sirutkaitis, K. Staliunas, Signatures of light-beam spatial filtering in a three-dimensional photonic crystal, Phys. Rev. A 82 (4) (2010) 043819.
[5] V. Purlys, L. Maigyte, D. Gailevičius, M. Peckus, M. Malinauskas, K. Staliunas, Spatial filtering by chirped photonic crystals, Phys. Rev. A 87 (3) (2013) 033805.
[6] D. Gailevicius, V. Koliadenko, V. Purlys, M. Peckus, V. Taranenko, K. Staliunas, Photonic crystal microchip laser, Sci. Rep. 6 (1) (2016) 34173.
[7] A.A. Skorynin, V.A. Bushuev, B.I. Mantsyzov, Dynamical Bragg diffraction of optical pulses in photonic crystals in the Laue geometry: diffraction-induced splitting, selective compression, and focusing of pulses, J. Exp. Theor. Phys. 115 (1) (2012) 56–67.
[8] S.E. Svyakhovskiy, A.A. Skorynin, V.A. Bushuev, S.V. Chekalin, V.O. Kompanets, A.I. Maydykovskiy, T.V. Murzina, B.I. Mantsyzov, Experimental demonstration of selective compression of femtosecond pulses in the Laue scheme of the dynamical Bragg diffraction in 1D photonic crystals, Opt. Express 22 (25) (2014) 31002.
[9] H.Y. Ling, Y.Q. Li, M. Xiao, Electromagnetically induced grating: homogeneously broadened medium, Phys. Rev. A - At. Mol. Opt. Phys. 57 (2) (1998) 1338–1344.
[10] A.W. Brown, M. Xiao, All-optical switching and routing based on an electromagnetically induced absorption grating, Opt. Lett. 30 (7) (2005) 699.
[11] L. Zhao, W. Duan, S.F. Yelin, All-optical beam control with high speed using image-induced blazed gratings in coherent media, Phys. Rev. A-At. Mol. Opt. Phys. 82 (1) (2010) 1–8.
[12] R.M. Arkhipov, A.V. Pakhomov, M.V. Arkhipov, I. Babushkin, A. Demircan, U. Morgner, N.N. Rosanov, Population density gratings induced by few-cycle optical pulses in a resonant medium, Sci. Rep. 7 (1) (2017) 1–21.
[13] S. Maruo, O. Nakamura, S. Kawata, Three-dimensional microfabrication with two-photon-absorbed photopolymerization, Opt. Lett. 22 (2) (1997) 132.
[14] G.D. Marshall, M. Ams, M.J. Withford, Femtosecond inscription of wavelength specific features in optical waveguide structures, in Integrated Optics, Silicon Photonics, and Photonic Integrated Circuits, G. C. Righini, ed. 6183 (2006) 61830Q.
[15] M. Malinauskas, A. Žukauskas, S. Hasegawa, Y. Hayasaki, V. Mizeikis, R. Buividas, S. Juodkazis, Ultrafast laser processing of materials: from science to industry, Light Sci. Appl. 5 (8) (2016) e16133.
[16] M. Campbell, D.N. Sharp, M.T. Harrison, R.G. Denning, A.J. Turberfield, Fabrication of photonic crystals for the visible spectrum by holographic lithography, Nature 404 (6773) (2000) 53–56.
[17] C.K. Ullal, M. Maldovan, E.L. Thomas, G. Chen, Y.-J. Han, S. Yang, Photonic crystals through holographic lithography: simple cubic, diamond-like, and gyroid-like structures, Appl. Phys. Lett. 84 (26) (2004) 5434–5436.
[18] S. Wilbrandt, O. Stenzel, N. Kaiser, Experimental determination of the refractive index profile of rugate filters based on in situ measurements of transmission spectra, J. Phys. D. Appl. Phys. 40 (5) (2007) 1435–1441.
[19] R.J. Martín-Palma, C.G. Pantano, A. Lakhtakia, Replication of fly eyes by the conformal-evaporated-film-by-rotation technique, Nanotechnology 19 (35) (2008) 355704.
[20] A. Sentenac, A.-L. Fehrembach, Angular tolerant resonant grating filters under oblique incidence, J. Opt. Soc. Am. A 22 (3) (2005) 475.
[21] Young Ju Lee, Junho Yeo, R. Mittra, Wee Sang Park, Application of electromagnetic bandgap (EBG) superstrates with controllable defects for a class of patch antennas as spatial angular filters, IEEE Trans. Antennas Propag. 53 (1) (2005) 224–235.
[22] H. Iizuka, N. Engheta, S. Sugiura, Extremely small wavevector regime in a one-dimensional photonic crystal heterostructure for angular transmission filtering, Opt. Lett. 41 (16) (2016) 3829.
[23] J.G. Mutitu, A. Barnett Shouyuan Shi, D.W. Prather, Angular selective light filter based on photonic crystals for photovoltaic applications, IEEE Photonics J. 2 (3) (2010) 490–499.
[24] Q. Qian, C. Xu, C. Wang, All-dielectric polarization-independent optical angular filter, Sci. Rep. 7 (1) (2017) 16574.
[25] P.V. Usik, A.E. Serebryannikov, E. Ozbay, Spatial and spatial-frequency filtering using one-dimensional graded-index lattices with defects, Opt. Commun. 282 (23) (2009) 4490–4496.
[26] O.F. Siddiqui, G.V. Eleftheriades, Resonant modes in continuous metallic grids over ground and related spatial-filtering applications, J. Appl. Phys. 99 (8) (2006) 083102.
[27] A.-L. Fehrembach, A. Talneau, O. Boyko, F. Lemarchand, A. Sentenac, Experimental demonstration of a narrowband, angular tolerant, polarization independent, doubly periodic resonant grating filter, Opt. Lett. 32 (15) (2007) 2269.
[28] A. Taflove, S.C. Hagness, Computational Electrodynamics (Boston, Artech House), (2005).
[29] "Lumerical FDTD Solutions, Inc., http://www.lumerical.com for high performance FDTD-method Maxwell solver for the design, analysis and optimization of nano-photonic devices, processes and materials.," (n.d.). Retrieved on 11th of February 2019.
[30] B. Liang, M. Bai, H. Ma, N. Ou, J. Miao, Wideband analysis of periodic structures at oblique incidence by material independent FDTD algorithm, IEEE Trans. Antennas Propag. 62 (1) (2014) 354–360.
[31] "Lumerical Inc. https://kb.lumerical.com/en/ref_sim_obj_sources_bfast.html for Broadband Fixed Angle Source Technique (BFAST), which only applies to the periodic structures illuminated with a broadband source at an angle," (n.d.). Retrieved on 11th of February 2019.
[32] Y. Xia, G.M. Whitesides, Soft lithography, Angew. Chemie Int. Ed. 37 (5) (1998) 550–575.
[33] T. Tolenis, L. Grinevičiūtė, R. Buzelis, L. Smalakys, E. Pupka, S. Melnikas, A. Selskis, R. Drazdys, A. Melninkaitis, Sculptured anti-reflection coatings for high power lasers, Opt. Mater. Express 7 (4) (2017) 1249.

5 publikacija / 5th publication

Nanostructured Multilayer Coatings for Spatial Filtering

L. Grineviciute, C. Babayigit, D. Gailevičius, M. Peckus, M. Turduev, T. Tolenis, M. Vengris, H. Kurt, K. Staliunas.

Adv. Optical Mater. **9***,* 2001730, (2021)

DOI: 10.1002/adom.202001730

ADVANCED OPTICAL MATERIALS
www.advopticalmat.de

Nanostructured Multilayer Coatings for Spatial Filtering

Lina Grineviciute, Ceren Babayigit, Darius Gailevičius, Martynas Peckus, Mirbek Turduev, Tomas Tolenis, Mikas Vengris, Hamza Kurt, and Kestutis Staliunas**

Spatial filtering is an important mechanism to improve the spatial quality of laser beams. Typically, a confocal arrangement of lenses with a diaphragm in the focal plane is used for intracavity spatial filtering. Such conventional filtering requires access to the far-field domain. In microlasers, however, conventional filtering is impossible due to the lack of space in microresonators to access the far-field. Therefore, a novel concept for more compact and efficient spatial filtering is necessary. In this study, a conceptually novel mechanism of spatial filtering in the near-field domain is proposed and demonstrated, by a nanostructured multilayer coating—a 2D photonic crystal structure with a periodic index modulation along the longitudinal and transverse directions to the beam propagation. The structure is built on a nanomodulated substrate, to provide the transverse periodicity. The physical vapor deposition is used to provide self-repeating modulation in the longitudinal direction. A 5 µm thick photonic multilayer structure composed of nanostructured multiple layers of alternating high- and low-index materials providing spatial filtering in the near-infrared frequencies with 2° low angle passband is experimentally demonstrated. The proposed photonic structure can be considered as an ideal component for intracavity spatial filtering in microlasers.

1. Introduction

Spatial filtering of light beams is an essential procedure in laser science and technology. Cleaning of the spatial distortions of the laser beams can be performed in postprocessing of the laser radiation to ensure the tight focusing or precise/controlled collimation of the light. However, even more important is the intracavity beam filtering inside of the laser resonators which enables the emission of maximally "clean" beam directly from the laser. In many kinds of lasers, the spatial distortions of the radiation are cleaned naturally due to the low aspect ratio of the system, when the longitudinal extent of the resonator is substantially larger than its transverse size, or due to resonators' curved mirrors with naturally occurring apertures. On the other hand, additional spatial filtering is sometimes performed by the intracavity spatial filter—a confocal lens arrangement with the aperture in the focal plane, which blocks higher-angle wave components (i.e., higher-order transverse modes) of the intracavity radiation. However, still for a large class of microlasers, such as semiconductor edge-emitting lasers, vertical-cavity surface-emitting lasers (VCSEL), microchip lasers, the intracavity spatial filtering is an unresolved issue. The natural beam cleaning mechanism is absent due to large aspect ratio of such microresonators, and the artificial filtering arrangement is impossible due to extremely small resonator dimensions (cavity length is in the order of millimeters, or in case of VCSEL—micrometers). A search for novel, efficient and convenient spatial filtering mechanisms, working in the near-field domain is crucial for the further development of such microlaser systems.

The spatial filtering in principle can be provided by photonic crystals (PhCs)—the structures with a periodically modulated refractive index on a wavelength scale, both longitudinally

L. Grineviciute, Dr. T. Tolenis
Center for Physical Sciences and Technology
Savanoriu Ave. 231, Vilnius LT-02300, Lithuania
E-mail: lina.grineviciute@ftmc.lt
C. Babayigit, Prof. H. Kurt
TOBB University of Economics and Technology
Söğütözü Str. 43, Ankara 06510, Turkey

The ORCID identification number(s) for the author(s) of this article can be found under https://doi.org/10.1002/adom.202001730.

DOI: 10.1002/adom.202001730

Dr. D. Gailevičius, Dr. M. Peckus, Prof. M. Vengris, Prof. K. Staliunas
Laser Research Center
Faculty of Physics
Vilnius University
Sauletekio Ave. 10, Vilnius LT-10223, Lithuania
E-mail: kestutis.staliunas@icrea.cat
Dr. D. Gailevičius
Femtika
Sauletekio Ave. 15, Vilnius LT-10224, Lithuania
Dr. M. Turduev
TED University
Ziya Gökalp Str. 48, Ankara 06420, Turkey
Prof. K. Staliunas
ICREA
Passeig Lluís Companys 23, Barcelona 08010, Spain
Prof. K. Staliunas
Departament de Fisica
Universitat Politècnica de Catalunya (UPC)
Rambla Sant Nebridi 22, Terrassa, Barcelona 08222, Spain

and transversely to the beam propagation direction.[1–4] Here, the filtering effect is based on the photonic bandgaps (BGs) of periodic media. Well known are the BGs in the frequency domain, which are due to the Bragg diffraction in layered (e.g., 1D index modulated) media, where the first BG occurs for the periods of modulation at around half-wavelength $\lambda/2$. Less evident is that also the angular BGs can occur in double-periodic (e.g., 2D index modulated) media, where the refraction index is modulated simultaneously in the longitudinal and transverse directions.[5]

The principal possibility of spatial filtering by PhCs already has been discussed,[1–4] but the experimental realization of the efficient spatial filters is still an unresolved issue. Volume refractive index modulation with the periods of around the $\lambda/2$ is technologically a great challenge. We note that the modulation must occur in 2D for 1D (cylindrical) spatial filtering, and in 3D for full (axisymmetric) spatial filtering. As the beams of several millimeter widths are to be cleaned in typical applications, the modulation must be perfectly uniform across the photonic structure over the ranges of millimeters. The transverse/longitudinal periods of the modulation must also be perfectly matched to provide the filtering on a given wavelength. Combining all these ingredients into one compact optical element is an unresolved challenge. Some attempts to fabricate spatial filters were made by direct laser writing in glasses,[6,7] and although they even were successfully integrated into microlasers,[8,9] they did not lead to spectacular improvement of the spatial structures of the radiation (the brightness increased 3 times in microchip lasers,[8] and 1.5 times in edge-emitting lasers[9]).

There are also alternative ideas on compact spatial filtering in metasurfaces, which can also provide angular sensitivity for plane waves reflecting/transmitting through the structure.[10] Various angular dispersion properties were demonstrated giving rise to incident-angle-selective meta-absorber, an angle-multiplexed meta-polarizer, an angle-multiplexed wavefront controller, and angle-multiplexed broadband metasurface sensor.[11,12] The aforementioned works are promising in perspective; however, they are still far from the technological applications in real photonic systems and high-power microlasers.

In this study, we propose and realize the spatial filtering effect based on the mechanism of the angular BGs in double-periodic photonic structures (see the schematic of the structure in **Figure 1**). Practically, the transverse periodicity results in a translation-invariant behavior, therefore such filters should be easy to align considering the fact that aligning optics precisely can be a very challenging task. From the technological viewpoint, the work combines lithographical methods to provide the seed of transverse modulation and the physical vapor deposition approach for longitudinal refractive index modulation. The transverse modulation was obtained by structuring the surface of the substrate by laser interference lithography, and the ion-beam sputtering process was used to conformally deposit multilayer coating on pre-microstructured substrates. There were also previous attempts to coat the microstructured substrates,[5,13] but no implementation has been presented. The thin films replicate the transverse seed modulation of the substrate and, as a result, the double-periodical modulation of the refractive index is obtained, which is a necessary ingredient for the PhC spatial filtering. The present article elaborates on the physical idea of filtering with its technological idea of

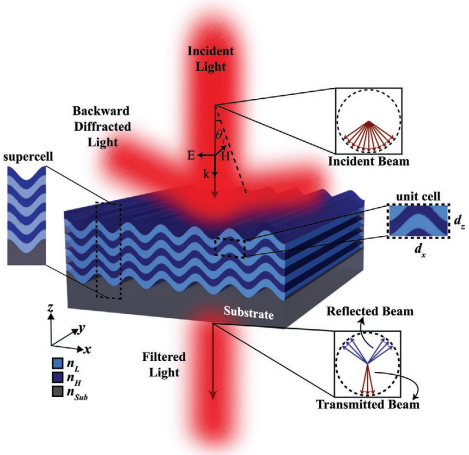

Figure 1. Photonic structure consisting of a self-replicating curved multilayer coating on a periodically modulated substrate. The insets show the elementary cell to calculate the photonic band diagrams, and the supercell used to calculate (angle, wavelength) diagrams of field transmission through the structure. The insets also illustrate the double-refraction based angle-selectivity of the transmission, providing the spatial filtering. Electric field is oriented for s-polarization case.

fabrication. Moreover, the study presents a systematic search of the optimum geometry by simulations in finite-difference time-domain (FDTD) and plane-wave expansion (PWE) methods, an analytical approach of the design, fabrication using lithographic methods, multilayer coatings, and experimental measurements of spatial-angular transmission of the design. One of the main messages of the article is the first experimental demonstration of the functional 2D PhC spatial filter of several micrometer thicknesses for the near-infrared radiation.

2. Design

The geometry of the photonic structure is schematically shown in Figure 1. The structure consists of alternating thin films with high and low refractive indices on a modulated substrate. The curved thin films replicate the surface modulation of the substrate, providing the refractive index modulation in both, the longitudinal (z-axis) and transverse (x-axis) directions. Note that the refraction from such a structure can be classified as the generalized Bragg one, since the refracted components propagate in a backward direction. The condition for the back-refraction is that the longitudinal component of the index modulation should have a periodicity of $\lambda/2 < d_z < \lambda$. This results in very compact dimensions of the filtering structure. For instance, 15 periods (30 layers) of modulation result in layered coatings of approximately 10 λ thickness, which, for the near IR, considering the refractive index of the material, is around 5 μm.

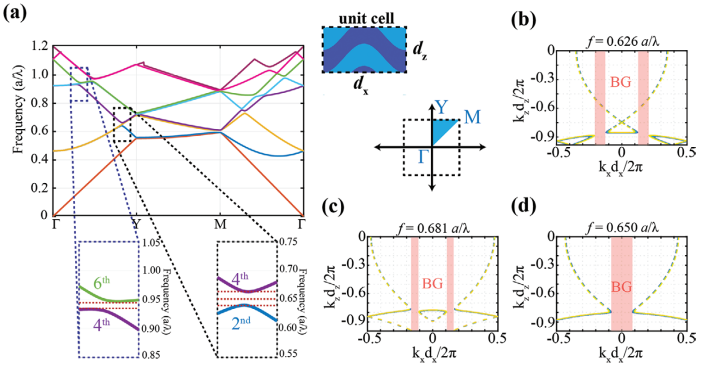

Figure 2. a) Band diagram of the (infinitely extended) periodic structure for the s-polarized electromagnetic field, with the regions of interest zoomed out (only second, and fourth bands indicated in the first, and fourth, and sixth bands in the second inset window). IFCs combined from second, third, and fourth bands, indicating high-angle-pass filtering at the middle of d) the first frequency BG, and low-angle-pass filtering below and above b,c) the first BG, respectively. Here, the Γ Y and M directions conventionally represent the points of high symmetries of 2D structures: Γ represents the center of the Brillouin zone, Y represents the center of a face along the light propagation direction, while M represents the corner point. These symmetry points are used to define the direction of the *k*-vectors. Parameters: transverse period $d_x = 600$ nm, longitudinal period $d_z = 301$ nm, modulation depth 150 nm, refractive indices $n_L = 1.99$ and $n_H = 2.24$. The wavelength is normalized to the lattice constant $a = d_x$.

This is a significant advantage of our filtering principle compared with the spatial filters in Laue configuration,[3,4,8,9] where the thickness of the spatial filter is of the order of 1 mm. Moreover, in Laue forward refraction configuration no "true" BGs are possible—just the quasi-BGs appear, as the refraction is directed predominantly in the forward direction. Furthermore, this thin arrangement of the filtering layers can support resonant wave-guiding modes if the coating has a higher refractive index than its surrounding media. Depending on the incidence angle and the wavelength of the incoming light, waveguiding modes can lead to enhanced/reduced transmission as a result of constructive/destructive interference and may improve the BG-based filtering effect.

The idea of the angular BGs filtering is first explored by the calculations of the band diagrams of the proposed structure by using the standard PWE method. To represent the band diagram of the structure in the reciprocal-space, we follow first the ΓY trajectory (i.e., along the beam propagation direction), then YM, and then back MΓ, see **Figure 2**a. Here, the BGs along the optical axis (ΓY-direction) are important for the filtering effect (see the inset dashed windows in the band-diagram, Figure 2a). In the middle of the axial BG, evidently, the axial components are blocked, which hints on the high-angle-pass spatial filtering effect. However, for the frequencies slightly below and above the axial BG the low-angle-pass filtering can be expected.

The scenario has been explored by calculating the isofrequency contours (IFCs) for the frequencies around the axial BG. We focus on the s-polarized electromagnetic field, where the electric field is directed parallel to the groves, in the main part of the article. The IFCs in Figure 2b–d are combined from the second, third, and fourth photonic bands, since the same frequency IFCs can be found in different bands. Indeed, for the frequencies inside the axial BG, the high-angle-pass filtering is obtained, see Figure 2d. For the frequencies slightly below and above the BG, the low-angle-pass filtering occurs as can be seen in Figure 2b,c, respectively. A complete collection of IFCs is presented in Suppl. 1 (Supporting Information). The filtering angular bandgaps actually consist of low angle pass areas, with the angles bounded from below by the isolines from second and fourth photonic bands, and the high angle pass area, with the angles bounded from above by isolines from third photonic bands at larger angles. In Figure 2b–d, the "relevant" isolines are indicated by the solid lines and "irrelevant: ones, which correspond to the "deaf" or "silent" modes, are shown by dashed lines. These "deaf" modes formally exist, but are not excited by the incident plane wave, since they are orthogonal, or almost orthogonal to the incident plane waves, and the incident radiation does not project into these modes.

Interestingly, the same scenario of low-high-low angle-pass filtering occurs also around the second frequency BG, although to a lesser extent, as indicated in Figure 2a and documented in Suppl. 1 (Supporting Information).

Next, we explore numerically the transmission of the plane waves through the photonic structure depending on their incidence angle and the wavelength. Due to the transverse periodicity, we used the supercell analysis of the field propagation by the FDTD method, with Bloch-periodic boundary condition on the lateral boundaries of the supercell.[14,15] Corresponding results are summarized in **Figure 3**a. Here, we present the results only for the s-polarized incident wave (electric field orientation is parallel to the fringe direction, i.e., parallel to the *y*-axis). The p-polarization gives qualitatively the same response, see Suppl. 2 (Supporting Information). Furthermore, analytically calculated angular-frequency bandgaps are presented and superimposed in Figure 3b (for detailed analytical derivations see Suppl. 3, Supporting Information). Also, the cross-sectional profiles of the transmittance maps are extracted for wavelengths of $\lambda = 1051$ and $\lambda = 972$ nm in Figure 3c,d, respectively.

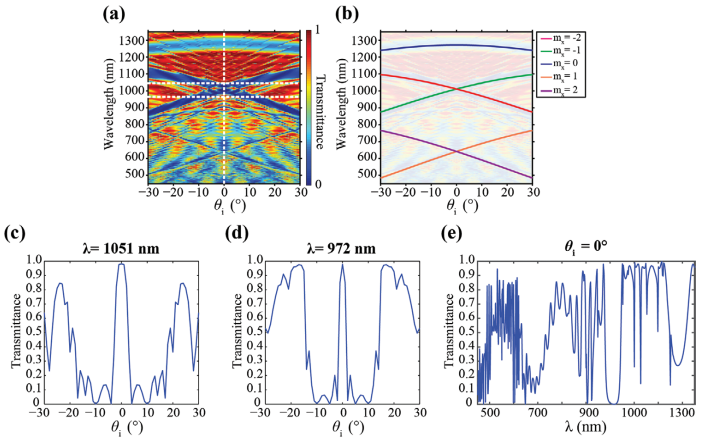

Figure 3. a) Map of transmission dependence on incidence angle and the wavelength extracted from the FDTD numerical calculations on a supercell. Two "crosses" of Bragg reflection lines are visible indicating the first and the second axial BG. Two dashed lines indicate cross-sectional transmission profiles of $\lambda = 1051$ nm and $\lambda = 972$ nm. b) Analytically calculated Bragg bandgap positions. Angular dependences of transmissions at different wavelengths of c) $\lambda = 1051$ nm and d) $\lambda = 972$ nm (horizontal cross-sections of the map) showing efficient spatial filtering at around the first filtering BG. e) Vertical cross-section at the incidence angle $\theta_i = 0°$ at the transmission map in (a). Here, the structural parameters are the same as in Figure 2 and the number of layers equal to $N = 33$.

Additionally, a vertical cross-sectional profile indicating the frequency BGs at the incidence angle $\theta_i = 0°$ is presented in Figure 3e. As can be seen from Figure 3c,d, almost perfect transmission occurs within small incidence angles and the waves at slightly larger angles are strongly suppressed in the transmitted light. Interestingly the second frequency BG also provides spatial filtering but with comparably lower efficiency, at around the wavelength of $\lambda = 620$ nm, however, a detailed study was not performed.

The overall filtering pattern (i.e., angular BGs positions presented in Figure 3a) corresponds well with the analytically calculated ones (Figure 3b), see the Suppl. 3 (Supporting Information). However, additionally, the transmission spectrum in the map was overlaid by the fringed structure. Vertical fringing is evidently related to the Fabry-Perot resonances of the coating structure, as the frequency separation between the fringes corresponds to the resonances of the structure of 5 µm geometrical thickness (10 µm optical thickness). The origin of the horizontal part of fringing is more sophisticated. We identify them as the resonances of the first-order diffracted modes trapped in the planar structure of a relatively high refraction index. The corresponding waveguided modes are calculated in Suppl. 4 (Supporting Information), resulting in a correct angular period of fringes. In addition to the main mechanism of the angle-selective refraction effect on a grating, the waveguiding effect can increase/decrease spatial filtering depending on the parameters (essentially on the thickness parameter of the coating). Further optimization of this additional effect can be used to improve the filtering performance of this type of spatial filter.

3. Fabrication and Characterization

The substrates with periodically transversally modulated surfaces were fabricated by laser interference lithography and nanoimprint technology. A chain of technological processes was applied to fabricate the samples. The fabrication process consists of the following steps: i) preparation of the master copy using the interference method in a photoresist ii) imprinting of the master structure on the substrate (using the UV imprint polymer); iii) physical vapor deposition on the modulated substrate to form the multilayered structure. The details are provided in the experimental section as well as in Suppl. 5 (Supporting Information).

The inner structure of the sample was characterized by using scanning electron microscope (SEM). In order to analyze the cross-sections, samples were cut by a laser beam and broken in the middle of the sample. Additionally, surface morphology was measured by atomic force microscope (AFM) before and after depositions of the coating to precisely determine the depths of the curved structure modulation, see **Figure 4**a.

Transmission maps for the fabricated sample were recorded by spectrophotometric measurements. Here, linearly polarized light was used for two perpendicular polarizations: s- and p-, where s-polarization is parallel to the grating lines on the sample. The angle between the main plane of the grating and the detector was varied from -30° to 30° by steps of 1°. The resulting transmission map is presented in Figure 4b.

The transmission maps correspond quantitatively to the ones obtained by numerical FDTD simulations. The main feature of the map—the crossings of the Bragg-reflection lines, is evident.

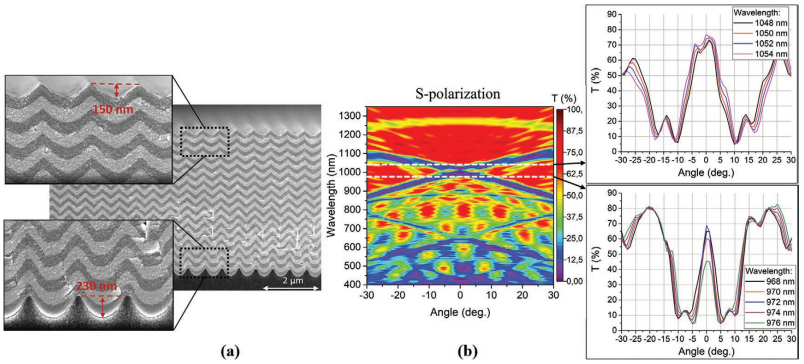

Figure 4. a) SEM images of the cross-section of the structure. b) Transmission map (transmission depending on the angle (horizontal axis) and wavelength (vertical axis)), together with cross-sections of the map (angular transmission curve) for characteristic wavelengths in the insets.

Also, the fringing is visible in the measured map. Similarly, to the numerical results, two crossings of the Bragg-reflection lines were observed, the main cross indicating the strong spatial filtering associated with the first BG and the weaker one associated with the second BG.

It should also be noted that SEM images of the cross-sections indicate a general tendency where the curving amplitude of the layers decreases with an increasing number of layers (see the inset cross-sections in Figure 4a). Typically, the modulation of the substrate with the amplitude of ≈220 nm decreases to the amplitude in the range of 110–150 nm at the top layer surface. The influence of the sweep of the modulation amplitude was also examined with the FDTD supercell analysis, and the obtained outcome showed that it did not essentially affect the results. The FDTD simulations with the modulation sweep lead to a weak deformation of the transmission maps without leading to essential modifications. The comparison is provided in Suppl. 6 (Supporting Information).

The main quantitative difference between numerical results and spectroscopic measurements of the fabricated structure is that the filtering lines in the latter case were less deep and more blurred. This can be attributed to the imperfections of fabricated structure—the corrugation of the substrate modulation on a range of around 10 μm and, subsequently, the corrugation of the whole structure. The influence of these large-scale imperfections is estimated in Suppl. 7 (Supporting Information).

4. Direct Proof of Spatial Filtering

Finally, the fabricated sample was illuminated by a cylindrically focused laser beam of a tunable picosecond laser (details of the laser device are provided in the experimental section). **Figure 5**a,b compares the far-field (angular) profiles of the incident probe beam and the resulting filtered beam for slightly different wavelengths. The narrowing of the angular spectra in the transmission is evident—angular divergence of the beam at FWHM is ≈2°. This is the main result of the article—specifically direct experimental proof for the spatial filtering effect by nanostructured multilayer coating.

For a more detailed analysis, a transmission map was reconstructed by dividing the measured angular intensity profile of the filtered beam by the reference (unfiltered) one. For comparison, we show the reconstructed transmission map in Figure 5c together with the one that obtained from spectrophotometric data in Figure 5d. Angular transmission spectra for two wavelengths of $\lambda = 968$ nm and $\lambda = 972$ nm are shown in Figure 5e,f for an additional comparison. The first case shows a transmission curve for a more bell-shaped profile with a higher transmission loss at the low angle values. On the other hand, the second case shows a lower loss case with a flat top resembling case. The detailed record of measurement data is provided in Suppl. 8 (Supporting Information). It is notable that the transmission through the structure did not exceed 80% whereas 100% would be more preferable for practical use at the angular intensity transmission bands. Here, both components of fabricated photonic structure: the substrate and the multilayer coating, are made of transparent, nonabsorbing materials for Vis-IR range. Since optical losses arise from the scattering and reflections, it can be controlled by using an optimized design of multilayer coating (including antireflective properties).

5. Discussion

The main message of the article is the demonstration of pronounced functional spatial filtering by thin nanostructured multilayer coating and with detailed numerical, analytical and experimental data, we are able to demonstrate such filtering of light. However, some imperfections still prevent the filter from technical applications, which should be discussed below and could be tackled in future work.

One issue is the broadening of the filtering lines due to the technical artifacts—the corrugation of the substrate on a large scale, and of the structure itself. With the current technology of the substrate fabrication, this limits the half-width of the filtering

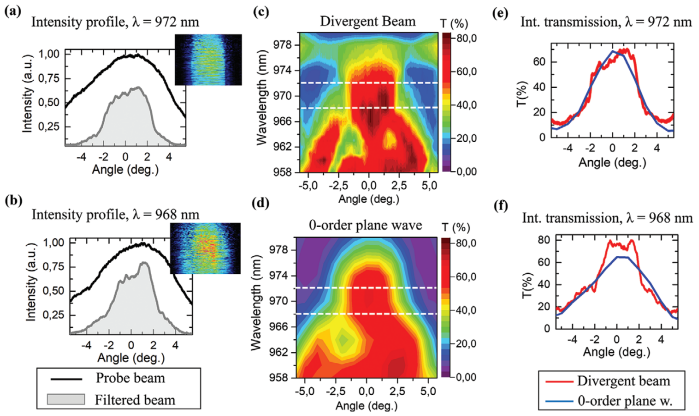

Figure 5. Experimental data for spatial filtering of a divergent probe beam. a,b) Transmission of a reference beam and filtered beam evidencing 1D (cylindrical) spatial filtering for two different wavelengths. Insets show the 2D intensity profiles of the filtered beam, registered on a CMOS camera. c) The corresponding transmission map, where the sample was illuminated with a divergent probe beam. Wavelengths of interest are marked with dotted lines. d)The zoomed-in range from Figure 4b corresponding to a zero-order plane wave transmission spectral-angular map. e,f) The intensity transmission profiles for wavelengths 972 and 968 nm for both measurement methods.

line approximately to 2°. As numerical simulations show, the removal of corrugation would allow reducing the half-width of filtering lines to approximately 1° for the current configuration.

The other issue is that the demonstrated filtering is a cylindrical one. The extension to 2D is, however, straightforward and consists in a change of the substrate modulation geometry (to square, hexagonal, concentric, etc.). The filtering geometry depends solely on the substrate, as the subsequent coating of layers in the vertical direction is independent of the geometry of the modulation of the substrate.

Hence, the fabricated multilayer structure (1D filtering, 2θ half-angle) could be well applied for broad area semiconductor edge emission lasers, where the reduction of the beam divergence from typical 5°–10°, to desired 1°–2° would be very profitable. The filters for the other relevant systems can require different angular widths of the transmission. To reduce the width (to obtain narrower angular transmission lines) generally the index contrast of deposited layers should be decreased, and the number of layers is increased.

6. Experimental Section

A variety of methods were used to achieve the main result—the demonstration of spatial filtering.

Design of the structure is based on numerical simulations using standard methods: plane wave expansion in a perfectly periodic structure to calculate the frequency isolines; FDTD simulations on a supercell to calculate the (angle, wavelength) transmission maps. Both are well-established methods.[15,16] For the proof of the spatial filtering, the full FDTD simulations on a complete structure were performed, which is also a well-established method.

Fabrication: The laser interference lithography, employing the third harmonics of Nd:YAG laser radiation, was used to form the master grating. Subsequently, the master was used in a typical soft nanoimprint lithography process,[17,18] where an intermediate soft polydimethylsiloxane imprint was taken from it and used for UV cured polymer (OrmoComp, $n_{ref} = 1.52$) copies production. The resulting samples with sinusoidally modulated surfaces (600 nm transverse period and 220 nm modulation depth) were used as the substrate for multilayer coating. The coating consists of alternating high and low refractive index thin films, deposited by the Ion Beam Sputtering method. Specifically, hafnia and niobia materials were used with refractive indices $n_L = 1.99$ and high $n_H = 2.24$, respectively. The multilayer structure consists of 33 layers, whose optical thicknesses were equal for both the high and low refractive index layers—317 nm ($d_z = 301$ nm with the geometric thicknesses—141.8 and 159.2 nm, respectively). More technical details are provided in Suppl. 5 (Supporting Information).

Characterization was performed by the AFM analysis of the surface's morphology of the substrate and of the upper layer of the fabricated structure. SEM was used to explore the cross-section of the fabricated structure. Finally, the spectroscopical measurements of the transmission were performed in order to build the (angle, wavelength) transmission maps.

Demonstration of spatial filtering by recording the far-field profiles of the transmitted beam from a tunable picosecond laser source, tuned in the wavelength range of 958 nm $\leq \lambda \leq$ 980 nm using a monochromator with a spectral bandwidth of approximately $\Delta\lambda \approx 1$ nm. Focusing provides the angular divergence of the beam of ≈9.7° at FWHM (full width at half maximum) in the horizontal direction. The resulting filtered beam was registered with a CMOS beam profiler camera while imaging the beam directly onto the sensor.

Supporting Information

Supporting Information is available from the Wiley Online Library or from the author.

Acknowledgements

This project has received funding from European Social Fund (project No 09.3.3- LMT-K712-17- 0016) under grant agreement with the Research Council

of Lithuania (LMTLT), D.G. and M.P. acknowledge the financial support from "FOKRILAS" (Project No. P-MIP-17-190) from Research Council of Lithuania. Authors are grateful to Dr. Algirdas Selskis from State research institute Center for Physical Sciences and Technology for SEM measurements.

Conflict of Interest

The authors declare no conflict of interest.

Author Contributions

K.S. supervised the project and provided theoretical analysis. C.B., M.T., H.K. performed the simulations. L.G. and D.G. fabricated modulated substrates, L.G., T.T., and D.G. designed and carried out the experiments and measurements. M.P. and M.V. performed measurements with a divergent laser beam. All authors participated in discussions and reviewed the manuscript.

Data Availability Statement

The data that supports the findings of this study are available in the supplementary material of this article.

Keywords

metamaterials, microlasers, photonic crystals, physical vapor deposition, spatial filtering

Received: October 8, 2020
Revised: February 17, 2021
Published online:

[1] K. Staliunas, V. J. Sánchez-Morcillo, *Phys. Rev. A* **2009**, *79*, 053807.
[2] E. Colak, A. O. Cakmak, A. E. Serebryannikov, E. Ozbay, *J. Appl. Phys.* **2010**, *108*, 113106.
[3] L. Maigyte, T. Gertus, M. Peckus, J. Trull, C. Cojocaru, V. Sirutkaitis, K. Staliunas, *Phys. Rev. A* **2010**, *82*, 043819.
[4] V. Purlys, L. Maigyte, D. Gailevičius, M. Peckus, M. Malinauskas, K. Staliunas, *Phys. Rev. A* **2013**, *87*, 033805.
[5] L. Grinevičiūtė, C. Babayigit, D. Gailevičius, E. Bor, M. Turduev, V. Purlys, T. Tolenis, H. Kurt, K. Staliunas, *Appl. Surf. Sci.* **2019**, *481*, 353.
[6] L. Maigyte, K. Staliunas, *Appl. Phys. Rev.* **2015**, *2*, 011102.
[7] D. Gailevičius, V. Purlys, K. Staliunas, *Opt. Lett.* **2019**, *44*, 4969.
[8] D. Gailevicius, V. Koliadenko, V. Purlys, M. Peckus, V. Taranenko, K. Staliunas, *Sci. Rep.* **2016**, *6*, 34173..
[9] S. Gawali, D. Gailevičius, G. Garre-Werner, V. Purlys, C. Cojocaru, J. Trull, J. Montiel-Ponsoda, K. Staliunas, *Appl. Phys. Lett.* **2019**, *115*, 141104.
[10] J. Cheng, S. Inampudi, H. Mosallaei, *Sci. Rep.* **2017**, *7*, 12228.
[11] N. Born, I. Al-Naib, C. Jansen, R. Singh, J. V. Moloney, M. Scheller, M. Koch, *Adv. Opt. Mater.* **2015**, *3*, 642.
[12] A. Leitis, A. Tittl, M. Liu, B. H. Lee, M. B. Gu, Y. S. Kivsha, H. Altug, *Sci. Adv.* **2019**, *5*, eaaw2871.
[13] J. B. Oliver, T. J. Kessler, B. Charles, C. Smith, presented at *SVC Techcon*, Chicago, IL, May 2014.
[14] A. Taflove, S. C. Hagness, *Computational Electrodynamics: The Finite-Difference Time-Domain Method*, Artech House, Norwood, MA **2005**.
[15] B. Liang, M. Bai, H. Ma, N. Ou, J. Miao, *IEEE Trans. Antennas Propag.* **2014**, *62*, 354.
[16] S. G. Johnson, J. Joannopoulos, *Opt. Express* **2001**, *8*, 173.
[17] T. Tamulevičius, S. Tamulevičius, M. Andrulevičius, E. Griškonis, L. Puodžiukynas, G. Janušas, A. Guobienė, *Exp. Tech.* **2008**, *32*, 23.
[18] Y. Xia, G. M. Whitesides, *Annu. Rev. Mater. Sci.* **1998**, *28*, 153.

6 publikacija / 6th publication

Fano-like Resonances in Nanostructured Thin Films for Spatial Filtering

L. Grineviciute, J. Nikitina, C. Babayigit, K. Staliunas.

Applied Physics Letters **118**, 131114, (2021)

DOI: 10.1063/5.0044032

Applied Physics Letters

Fano-like resonances in nanostructured thin films for spatial filtering

Cite as: Appl. Phys. Lett. **118**, 131114 (2021); https://doi.org/10.1063/5.0044032
Submitted: 13 January 2021 . Accepted: 11 March 2021 . Published Online: 02 April 2021

Lina Grineviciute, Julianija Nikitina, Ceren Babayigit, and Kestutis Staliunas

Applied Physics Letters ARTICLE scitation.org/journal/apl

Fano-like resonances in nanostructured thin films for spatial filtering

Cite as: Appl. Phys. Lett. **118**, 131114 (2021); doi: 10.1063/5.0044032
Submitted: 13 January 2021 · Accepted: 11 March 2021 ·
Published Online: 2 April 2021

View Online Export Citation CrossMark

Lina Grineviciute,[1,2] Julianija Nikitina,[1,2] Ceren Babayigit,[3] and Kestutis Staliunas[1,4,5,a)]

AFFILIATIONS

[1]Vilnius University, Faculty of Physics, Laser Research Center, Sauletekio Ave. 10, Vilnius, Lithuania
[2]Center for Physical Sciences and Technology, Savanoriu Ave. 231, LT-02300 Vilnius, Lithuania
[3]TOBB University of Economics and Technology, Söğütözü Str. 43, 06510, Ankara, Turkey
[4]ICREA, Passeig Lluís Companys 23, 08010, Barcelona, Spain
[5]UPC, Dep. de Fisica, Rambla Sant Nebridi 22, 08222, Terrassa (Barcelona) Spain

[a)]**Author to whom correspondence should be addressed:** kestutis.staliunas@icrea.cat

ABSTRACT

Fano-like resonant coupling of electromagnetic radiation with planar waveguiding modes of nanostructured thin films is proposed and realized experimentally. Different from conventional Fano coupling to compact resonators with the discrete spectrum, we report Fano-like coupling to infinitely extended planar waveguiding modes of the spatially unbound system. We fabricated the films by the ion beam sputtering method on nano-modulated substrates. The observed Fano-like process shows extremely strong sensitivity with respect to the wavelength and especially to the incidence angle of the radiation and can potentially be used for frequency and spatial filtering of light in transmission/reflection through/from such nanostructured thin films.

Fano resonances are widespread in nature and technology. After their first observation around 90 years ago[1] and their universal mathematical description 60 years ago,[2] Fano resonances found application in different physical systems. Specifically, the growth of interest in Fano resonances was boosted by rapidly developing micro- and nanophotonic technologies during the last decade.[3,4]

Fano resonances can be interpreted within a simple model of two coupled oscillators: a driven oscillator with a broad spectrum coupled to the second oscillator with a discrete spectrum. When the frequency of the driving force is tuned around the resonance frequency of the second oscillator, sharp changes occur in the response of the first driven oscillator. Importantly, the first oscillator shows a vanishing response to the driving force in the vicinity of the resonance of the second oscillator—the impedance of the system turns to infinity—and all the energy of the driving force reflects. Potentially, the Fano resonances can impose high sensitivity in the system: the absorption and scattering can be efficiently engineered in extremely narrow frequency ranges.[3,4]

Typically, the Fano resonances are encountered in coupling of extended wave systems with compact oscillators, like dielectric or plasmonic nanoparticles, micro-nano-circuits, meta-atoms, and other compact resonators,[5–7] possessing discrete spectra of their spatially bound modes. For instance, plasmonic resonances in nanoparticles can play the role of the secondary oscillators, whereas non-resonant background corresponds to the driving force.[8,9] Not only do such plasmonic structures suffer from ohmic, intrinsic, and radiative heating losses, but their damage threshold is also highly sensitive to the fabrication quality. Alternatively, all-dielectric metamaterials are also proposed to support Fano resonances.[10–12] Here, the secondary oscillator uses multiple,[11] distinct,[10] or broken symmetry[13] compact dielectric structures.

Fano resonances due to coupling with the localized oscillators are especially attractive since they allow to realize local responses and, thus, allow to structurize incoming beams on demand,[5–13] which boosted the increasing popularity of the field. However, less attention was paid to similar resonances due to the coupling with the unbound modes of the secondary, infinitely extended, oscillator. Early work in the field[14] predicts such nonlocal resonances, in general, and the most recent studies[15–17] consider such nonlocal Fano resonance basically in relation to the image processing via coupling to the leaky surface modes.

In this manuscript, we propose to use such a Fano-like coupling with the unbound planar waveguiding modes of thin dielectric films in order to manipulate the reflection/transmission properties of the beam

radiation incident in the near-to-normal direction of the film. We show that such an unbound system is mathematically equivalent to conventional compact Fano-resonant systems. We fabricate a nanostructured thin film, measure the Fano-like resonances, and demonstrate high angle-wavelength sensitivity of transmission/reflection.

The idea of Fano-like coupling in a nanostructured thin film is sketched in Fig. 1(a). The radiation, incident in a near-to-normal direction to the film, excites the Fabry–Perrot (FP) modes of the film, with the refraction index larger than that of the environment. Such planar modes are not leaky, as in Refs. 15–17, but perfectly bound in the absence of the modulation. In order to couple these planar modes to the FP modes, the surfaces of the film are periodically structured on a wavelength scale along its surface, as shown in Fig. 1(a). If the planar structure supports the waveguiding modes with the propagation wavenumber k_m for a given frequency $\omega_0 = ck_0$ (here, the wavenumber $k_0 = 2\pi/\lambda$) and if the period of the film modulation is d_x (the reciprocal modulation wavenumber is $q_x = 2\pi/d_x$), then the resonant coupling to the right/left propagating modes occurs for the incidence angles θ such that $k_0 \sin(\theta) \pm q_x = \pm k_m$.

The propagation wavenumbers of the planar modes, k_m, do not have explicit analytical expressions in general; however, in the limit of strongly confining planar waveguides, corresponding to tight binding approximation, the mode propagation numbers can be estimated as $k_m = m\sqrt{(nk_0/m)^2 - (\pi/d_z)^2}$, with $m = \pm1, \pm3, \pm5, \ldots$ for symmetric modes and $m = \pm2, \pm4, \pm6, \ldots$ for antisymmetric modes, where the sign of m indicates the mode propagation direction. This results in a relatively simple expression for the Fano-like resonances in the angle-wavelength domain,

$$\lambda_m(\theta) \approx \frac{d_x n}{\sqrt{1 + \left(\frac{md_x}{2d_z}\right)^2}} \pm \frac{d_x \sin(\theta) sgn(m)}{1 + \left(\frac{md_x}{2d_z}\right)^2}. \quad (1)$$

Relation (1), although being an approximation, gives insight into the structure of the resonant curves in the plane of (θ, λ). It consists of symmetric branches of the resonances, with respect to the angle θ, corresponding to the excitation of the right/left propagating waveguiding modes [see Fig. 1(b)]. The branches cross in the plane (θ, λ), thus introducing a strong angular transmission/reflection sensitivity.

Fano resonances are universally interpreted by a driven coupled oscillator system.[2] In our case, the role of the primary oscillator is in the FP mode of the thin film, driven by an external field, incident in the near-to-normal direction to the film surface. Such FP modes have broad angular and frequency spectra for weak reflections from the interfaces of the film. The secondary oscillators in our case are the unbound planar waveguiding modes of the film. In the mean field approximation, the time evolution of the FP field $A(x, \tau)$ is described by

$$\frac{dA}{d\tau} = A_0 t - A\left(1 - r^2 \exp(i\varphi)\right) + \sum_m i s_m B_m. \quad (2a)$$

Here, A_0 is the amplitude of the external driving field and $t = \sqrt{2n}/(n+1)$ is the transmittivity through the interface (in terms of the amplitude), which is related to the reflection $t^2 + r^2 = 1$. We consider the same reflectivity/transmission from the both interfaces of the thin film, to make the analytical estimations simpler (in numerical studies, we consider exact values). $\varphi = 2nd_z k_{0,z}$ is the phase accumulation of the plane wave on a cavity round trip with the round trip length $2\,d_z$. The time τ is normalized to the photon round trip time in the FP resonator. The FP field $A(x, \tau)$ is coupled with the waveguiding modes of the film $B_m(x, \tau)$, where the coupling coefficients s_m depend on the character of modulation and on a spatial profile of the mode, and cannot be rigorously calculated in the general case. Rough estimation in the shallow modulation limit $h_0 \ll \lambda$ gives $s_m \approx h_0(n-1)/\lambda$, where h_0 is the amplitude of the surface modulation of the film: $h(x) = h_0/2 \cos(qx)$. The time evolution equation for the amplitudes of the waveguide modes reads

$$\frac{dB_m}{d\tau} = i s_m A + i\Delta\omega_m B_m. \quad (2b)$$

$\Delta\omega_m$ are the normalized detuning of each excited mode from its resonance frequency. In terms of the wavelength, the detuning reads $\Delta\omega_m = -4\pi d_z \Delta\lambda_m/\lambda^2$, where $\Delta\lambda_m$ is the wavelength detuning from the corresponding resonances given by (1).

The stationary solution of (2a) and (2b) straightforwardly leads to the transmission coefficient through the thin film,

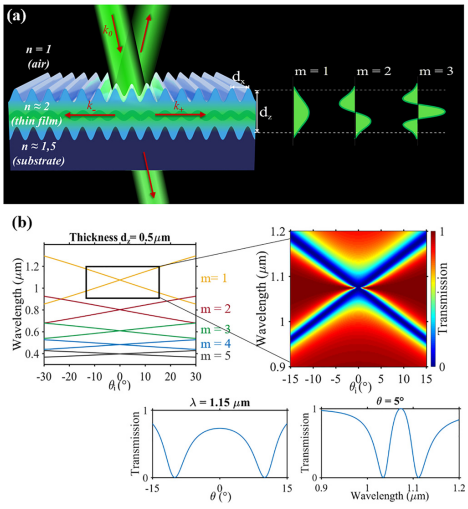

FIG. 1. (a) Schematic representation of the proposed geometry for the resonant coupling between the Fabry–Perrot and planar waveguiding modes: the incident radiation at normal angle θ couples with left/right propagating waveguiding mode with $+k_m$ or $-k_m$. (b) Resonant wavelength dependence with respect to the incidence angle, which is obtained using Eq. (1) with $m = \pm1, \ldots, \pm5$ c) and transmission map in the θ plane (θ, λ) together with its characteristic vertical and horizontal cross sections obtained using Eq. (3) for the left-right propagating modes with $m = \pm1$. The parameters are $s = 0.1$, $d_x = 0.6\,\mu$m, $d_z = 0.5\,\mu$m, $h_0 = 0.2\,\mu$m, and $n = 2$.

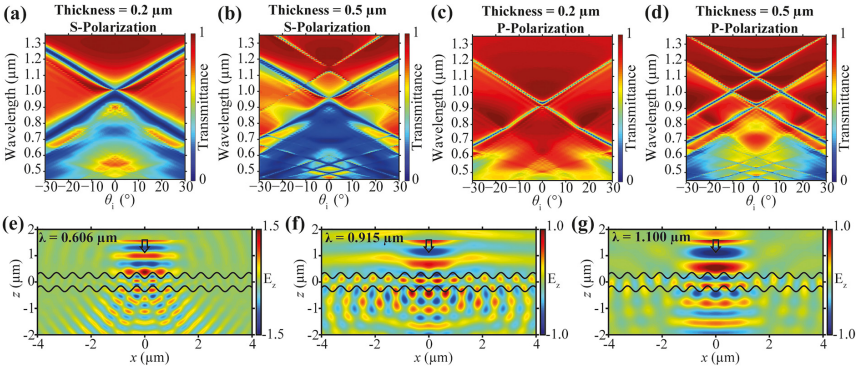

FIG. 2. (a)–(d) Transmission maps in a plane (θ, λ) for different polarizations of the incident field and for different thicknesses of the film (obtained from supercell FDTD calculations). (e)–(g) Instantaneous field distributions obtained from full-sample FDTD results at different wavelengths illustrating strong and weak excitation of the waveguiding modes at and out of the Fano resonances. The parameters are transverse period d_x=0.6 μm, amplitude modulation = 0.22 μm, and refractive index n = 2.086. For the full-sample FDTD calculations, the thickness of the structure is d_z=0.5 μm and the film is illuminated with an s-polarized Gaussian beam of width 3 μm.

$$t_R = \frac{1}{\left(1 - r^2 \exp\left(i\varphi\right)\right)/t^2 + i\sum_m s_m^2/\left(\Delta\omega_m t^2\right)}. \quad (3)$$

Figure 1(c) shows the transmission function (3) considering the left and right propagating lowest order modes with $m = \pm 1$. Eq. (3) coincides with the Fano scattering function[2] with the Fano factor equal to zero, i.e., in the absence of the internal losses of the secondary oscillator. In accordance with the general theory of Fano resonances, the transmission (3) becomes exactly zero at the resonance of the secondary oscillator. As checked below by numerical simulations (see Fig. 2) and by experimental measurements (see Fig. 3), the transmission indeed drops to zero at the resonances.

Numerical proof of the idea is presented in Fig. 2. Here, the numerical analysis comprises supercell Finite Difference Time Domain (FDTD) analysis and full-structure FDTD calculations.[18,19] Transmission maps evidence the Fano-like resonances, in qualitative accordance with Eqs. (1)–(3). Moreover, Fig. 2, e.g., represents the electric field profile calculations of the thin film at the specific wavelength values, which correspond to strong and weak excitation of waveguide modes for the parameters close- and far away from the resonances.

Further, the substrates with the modulated profile were fabricated by the laser interference lithography and nano-imprint technology. First, the gratings with a period of 600 nm and a modulation depth of 220 nm were manufactured in a photoresist by laser interference. Then, the fabricated grating was used to imprint the structure on the highly transparent substrate (the UV curable hybrid polymer, OrmoComp, with a refraction index of $n = 1.52$). Finally, the dielectric material (Ta_2O_5, $n = 2.086$) was deposited by the ion beam sputtering technique on the modulated substrate to form the nanostructured thin film. We refer to Refs. 20 and 21 for fabrication details.

The inner structure of the sample was explored using a Scanning Electron Microscope (SEM): the samples were cut by a laser beam and

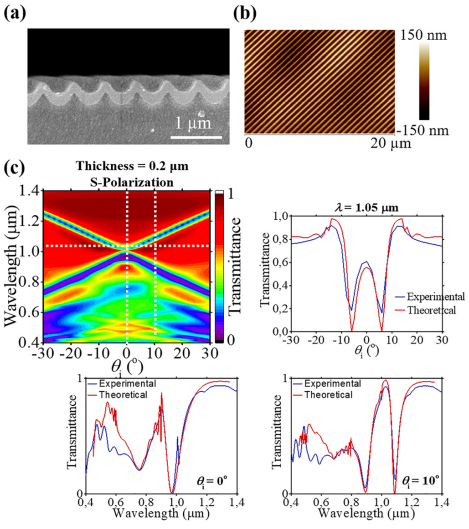

FIG. 3. (a) SEM image of the cross section of the fabricated sample. (b) AFM image of the film surface and (c) transmission maps in a plane (θ, λ) together with corresponding cross sections, compared with numerical calculations.

broken in the middle of the sample. Additionally, the surface profiles were measured using an Atomic Force Microscope (AFM) before and after depositions of the thin film. The thickness of the fabricated films varied from 200 nm to 900 nm. Here, we report the measurements of the 350 nm-thick films. The SEM and AFM images of the reported film after fabrication are summarized in Figs. 3(a) and 3(b). The AFM images, however, indicate a weak large-scale corrugation of the surface: on top of the main modulation with the 600 nm period and 220 nm amplitude, some weak random modulation with a spatial scale of $\geq 10\,\mu$m and the maximum depth of ≤ 50 nm is visible.

Transmission maps for the fabricated samples were obtained by spectrophotometric measurements. The linearly polarized light in the range of 0.4–1.4 μm wavelengths was used in two perpendicular polarizations. The S/P polarization corresponds to the electric field parallel/perpendicular to the grating lines.

The spectroscopic measurements of the transmission maps, which are represented in Fig. 3(c), show good correspondence with the numerically calculated maps. The cross sections of the map show sharp transmission lines, both in frequency and in angle, in accordance with the Fano resonance theory, Eqs. (1)–(3). One should note that slight blurring of the transmission lines was observed, due to the weak $\geq 10\,\mu$m large scale corrugation of the film. Due to these fabrication imperfections, exact zeroes were not reached in experiments. We checked this interpretation by FDTD numerical analysis of the deliberately corrugated films on a large space scale (not presented in the Letter) and observed the blurring of resonances in accordance with the experimental observations.

The results promise efficient and narrow-band filters in both wavelength and angle domains. It should be noted that in the case of Bragg structures, the resonances are always of flat-top and flat-bottom shape (not of a type of single zero), which result in substantially broadened filtering lines.[20,21]

Moreover, the width of the Fano resonant lines $\Delta\omega$ depends primarily on the coupling coefficient between the FP modes and the planar waveguide modes: $\Delta\lambda \sim s^2$ as follows from Eq. (3). To check the predicted scaling analytically, we performed FDTD supercell numerical simulations for different amplitudes of the modulations of the film. The calculated dependences in Fig. 4 are in good correspondence with the analytically estimated scaling in the limit of shallow modulations.

Simulations also allowed us to calibrate the proportionality coefficient in scaling since the analytically predicted dependence of $\Delta\lambda$ on the amplitude of the surface modulation h_0 is just indicative due to the absence of knowledge of the exact waveguiding mode shapes and exact couplings between FP and waveguiding mode. In terms of the wavelength, the estimation reads $\Delta\lambda = ch_0^2/d_z$, with the calibration constant on the order of unity ($c = 0.5$ and 0.2 for two different planar modes with $m = 1$ and 2). This means that shallow modulation could allow extremely narrow transmission gaps in terms of the wavelength. For instance, modulation amplitude $h_0 = 30$ nm should result in the transmission gap with the width on the order of $\Delta\lambda \approx 1$ nm at around $\lambda = 1\,\mu$m. In terms of the incidence angle, the width of the gap reads $\Delta\theta = \Delta\lambda/d_x\left(1 + \left(md_x/(2d_z)\right)^2\right)$. The estimate for shallow modulation is $\Delta\theta = ch_0^2/(d_x d_z)$, with the same calibration constant c. The modulation amplitude $h_0 = 30$ nm should result in the transmission angular gap with the width on the order of $\Delta\theta \approx 1$ mrad.

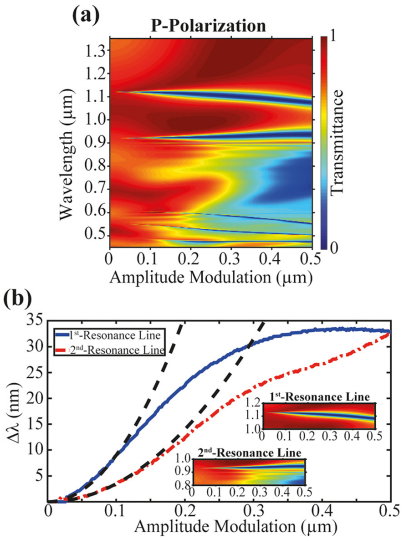

FIG. 4. The dependence of the width of the Fano-like resonance on the amplitude of the modulation h obtained from the supercell FDTD calculations (solid blue and red lines) for first and second planar modes together with the analytically proposed scaling (dashed lines). The thickness of the structure is $d_z = 0.5\,\mu$m with other parameters remaining as in Fig. 2.

The above estimations were performed when a single Fano resonance is considered. This occurs away from the cross point of the resonance lines, i.e., for the incidence angle $\theta \neq 0$. What is interesting is the case around the cross of two resonance lines, when two Fano resonances are in action simultaneously. In the wavelength domain, this results in the double width of the gap, compared with the single resonance case, as directly follows from (3) for the angle $\theta = 0$, i.e., does not lead to quantitative differences. However, in the angle domain, the width of the transmission gap (and the width of the reflection peak, respectively) becomes

$$\Delta\theta^2 \approx \frac{s^2\lambda_0^2\Delta\lambda}{2\pi t^2 d_z d_x^2}, \tag{4}$$

which is valid close to the center of the cross of the resonance lines. Having in mind that $d_x \approx \lambda_0$ for the first cross, the following estimation can be obtained: $\Delta\theta \sim s\sqrt{\Delta\lambda/d_z}$, which shows the singular character with respect to the wavelength detuning $\Delta\lambda$. This predicts a principal possibility to obtain extremely narrow angular transmission gaps (and reflection peaks) even for finite modulation depth h_0 by tuning the wavelength close to the double resonance point.

In summary, the following key conclusions follow from our study:

(i) We find sharp resonances in transmission through the nano-modulated thin film structure, in both wavelength and angle domains, and identify them as Fano-type resonances. Different from conventional Fano resonances occurring due to the coupling with bound modes of coupled compact resonators, in our case, the resonant coupling with unbound planar modes of the extended system is at the basis.

(ii) We indicate high transmission selectivity in terms of wavelength and angle. The width of the resonance lines scales as the square of the amplitude of the modulation h_0^2.

(iii) The angular transmission function is extremely sharp at the cross of two resonant lines. The width of the angular transmission dip (and correspondingly or reflection peak) scales as $\Delta\lambda^{1/2}$ with respect to the detuning from the double resonance. This means that even for a finite modulation amplitude, the spatial filtering lines can, in principle, be arbitrarily narrow. Note that the spatial filters based on Laue or Bragg diffraction[22–25] in periodic structures always result in the finite angular width of the filtering line, with the minimum width proportional to the index contrast (equivalent to the modulation amplitudes). In this way, the Fano effect-based spatial filters offer qualitative differences with the Bragg-type devices. The latter observation offers huge potential of a technical outcome: the high angular sensitivity offers compact spatial filters. Together with the properties as the position invariance, compactness, and convenience to integrate into photonic systems, this could lead to new optical components for modern photonics.

Finally, as a future perspective, a natural extension can be considered for Fano resonances in higher dimensions, considering the square, hexagonal lattices or even quasiperiodic lattices with higher symmetries (octagonal, etc.) of the substrate modulation. Such structures are expected to provide two-dimensional spatial filtering suitable for the lasers with two lateral dimensions in relevant (VCSELs or microchip lasers) coordinates. The real challenges in this 2D modulation case occur in the process of nano-fabrication of the substrates, whereas the thin film formation should be analogous to the 1D modulation case reported in the present Letter.

AUTHORS' CONTRIBUTIONS

K.S. supervised this research and performed analytical studies, L.G. and J.N. fabricated the structure and performed experimental measurements, and C.B. performed numerical simulations. All the authors contributed to interpretation of the results and preparation of this article.

This work received funding from the European Social Fund (Project No. 09.3.3-LMT-K712–17-0016) under grant agreement with the Research Council of Lithuania (LMTLT), from Horizon 2020 ERA.NET-COFUND program project MiLaCo (Project No. S-M-ERA.NET-20–2) under grant agreement with the Research Council of Lithuania (LMTLT), and also from the Spanish Ministerio de Ciencia e Innovacion under Grant No. 385 (PID2019–109175GB- 288 C21).

DATA AVAILABILITY

The data that support the findings of this study are available from the corresponding author upon reasonable request.

REFERENCES

[1]U. Fano, Nuovo Cimento **12**, 154 (1935).
[2]U. Fano, Phys. Rev. **124**, 1866 (1961).
[3]M. F. Limonov, M. V. Rybin, A. N. Poddubny, and Y. S. Kivshar, Nat. Photonics **11**, 543 (2017).
[4]E. Kamenetskii, A. Sadreev, and A. Miroshnichenko, *Physics and Applications Springer Series in Optical Sciences* (Springer Nature Switzerland AG, 2018), Vol. 219.
[5]L. Stern, M. Grajower, and U. Levy, Nat. Commun. **5**, 4865 (2014).
[6]M. V. Rybin, K. B. Samusev, I. S. Sinev, G. Semouchkin, E. Semouchkina, Y. S. Kivshar, and M. F. Limonov, Opt. Express **21**, 30107 (2013).
[7]P. Fan, Z. Yu, S. Fan, and M. L. Brongersma, Nat Mater. **13**, 471 (2014).
[8]S. Campione, D. de Ceglia, C. Guclu, M. A. Vincenti, M. Scalora, and F. Capolino, Appl. Phys. Lett. **105**, 191107 (2014).
[9]N. Yu and F. Capasso, Nat. Mater. **13**, 139 (2014).
[10]Y. Yang, W. Wang, A. Boulesbaa, I. I. Kravchenko, D. P. Briggs, A. Puretzky, D. Geohegan, and J. Valentine, Nano Lett. **15**, 7388 (2015).
[11]X. Long, M. Zhang, Z. Xie, M. Tang, and L. Li, Opt. Commun. **459**, 124942 (2020).
[12]H. Liu, C. Guo, G. Vampa, J. L. Zhang, T. Sarmiento, M. Xiao, P. H. Bucksbaum, J. Vučković, S. Fan, and D. A. Reis, Nat. Phys. **14**, 1006 (2018).
[13]S. Campione, S. Liu, L. I. Basilio, L. K. Warne, W. L. Langston, T. S. Luk, J. R. Wendt, J. L. Reno, G. A. Keeler, I. Brener, and M. B. Sinclair, ACS Photonics **3**, 2362 (2016).
[14]S. S. Wang and R. Magnusson, Appl. Opt. **32**, 2606 (1993).
[15]H. Kwon, D. Sounas, A. Cordaro, A. Polman, and A. Alù, Phys. Rev. Lett. **121**, 173004 (2018).
[16]A. Cordaro, H. Kwon, D. Sounas, A. F. Koenderink, A. Alù, and A. Polman, Nano Lett. **19**, 8418 (2019).
[17]H. Kwon, A. Cordaro, D. Sounas, A. Polman, and A. Alù, ACS Photonics **7**, 1799 (2020).
[18]A. Taflove and S. C. Hagness, *Computational Electrodynamics* (Artech House Norwood, 2005).
[19]Lumerical FDTD Solutions, Inc., see http://www.lumerical.com for the high performance FDTD-method Maxwell solver for the design, analysis, and optimization of nanophotonic devices, processes, and materials.
[20]L. Grinevičiūtė, C. Babayigit, D. Gailevičius, E. Bor, M. Turduev, V. Purlys, T. Tolenis, H. Kurt, and K. Staliunas, Appl. Surf. Sci. **481**, 353 (2019).
[21]L. Grineviciute, C. Babayigit, D. Gailevičius, M. Peckus, M. Turduev, T. Tolenis, M. Vengris, H. Kurt, and K. Staliunas, Adv. Optical Mater. 2001730 (2021).
[22]K. Staliunas and V. J. Sánchez-Morcillo, Phys. Rev. A **79**, 053807 (2009).
[23]E. Colak, A. O. Cakmak, A. E. Serebryannikov, and E. Ozbay, J. Appl. Phys. **108**, 113106 (2010).
[24]L. Maigyte, T. Gertus, M. Peckus, J. Trull, C. Cojocaru, V. Sirutkaitis, and K. Staliunas, Phys. Rev. A **82**, 043819 (2010).
[25]L. Maigyte and K. Staliunas, Appl. Phys. Rev. **2**, 011102 (2015).

Vilnius University Press
9 Saulėtekio Ave., Building III, LT-10222 Vilnius
Email: info@leidykla.vu.lt, www.leidykla.vu.lt
Print run copies 25